Towards data assimilation in the Catalan continental shelf

From data analysis to optimization methods

by Gabriel Jordà Sánchez

Laboratori d'Enginyeria Marítima

LIM/UPC - Barcelona

Pôle d'Océanographie Côtière de

POC - Toulouse

A la memoria de mi padre, porque el defecto más grande
de esta tesis es no haber estado acabada a tiempo.

"Mira'm als ulls que cap fosca no venç ..."
(Miquel Martí i Pol)

"La tesis, la tesis, ... "
(Gabriel Mª Jordà)

Towards data assimilation in the Catalan continental shelf

From data analysis to optimization methods

MEMÒRIA

per optar al títol de Doctor en Ciències del Mar
Programa de Doctorat en Ciències del Mar UPC – UB – CSIC
Realitzada al Laborator d'Enginyeria Marítima LIM/UPC
i al Pôle d'Océanographie Côtière de Toulouse
defensada a
Barcelona el Juny de 2005

Per

Gabriel Jordâ Sánchez

This thesis has been supervised by

Dr. Manuel Espino

Dr. Pierre De Mey

Dr. Patrick Marsaleix

Granted by an FPU grant of the Ministerio de Educacion and
a SOCRATES grant from the UPC

Supported by PRECARIOS, a postgraduate's organization whose dedication and effort contribute to improve young scientists working conditions in Spain: www.precarios.org

Cover design: Carles Llull (carlesllull@wanadoo.es)

Clàusula de bon ús

"Queda absolutament prohibida la utilització, recerca i desenvolupament, de manera directa o indirecta, de qualsevol de les aportacions científiques pròpies de l'autor que es presenten en aquesta memòria, per part de qualsevol exèrcit del món o per part de qualsevol grup armat, per a qualsevol ús militar i per a qualsevol altre ús que atempti contra els drets humans o contra el medi ambient, si no és amb el permís escrit de totes les persones del món."

Good Use Right

"It is strictly prohibited to use, to investigate or to develop,in a direct or indirect way, any of the scientific contributions of the author contained in this work by any army or armed group in the world, for military purposes and for any other use which is against human rights or the environment, unless a written consent of all the persons in the world is obtained"

Campanya per la Pau: No a la investigacio militar
http://www.prouinvestigaciomilitar.org

ABSTRACT

The goal of this thesis is to implement a data assimilation scheme into a hydrodynamic model of the catalan continental shelf. This system would allow us to combine the information provided by measured data with the information coming from the numerical models in order to find the best approach, from a statistical point of view, of reality.

To reach this objective it is needed, in a first moment, to have a good knowledge of the region and of the physical processes therein. The next step is to have a numerical model able to reproduce in a realistic way the dynamics of the area. Afterwards, the error sources of the system and the error dynamics should be characterized to, finally, implement a data assimilation system well suited for the problem.

Following this way we can take profit of the data available and the tools developed to deepen in the the knowledge of the dynamics in the catalan continental shelf from different approaches.
-The analysis of the measures obtained in the frame of the research projects FANS and YOYO have allowed us to characterize the region dynmics, to study the origin of the slope current variability in the high and low frequencies, to study the processes over the shelf and to see the water mass evolution.
-The implementation of the hydrodynamical model SYMPHONIE has been done carefully applying a new initialization technique (the modal potential vorticity method) and has been validated agains real data to obtain a complet and realistic model. Once we had this part done, we have used it to study the evolution of a topographic Rossby wave over the continental shelf, the wind effects over the 3D dynamics and the exchanges shelf-slope induced by the wind and the slope current.
-The stochastic modelling has been used to describe the dynamics of the errors associated to the slope current characterization and the wind field. We have determined that the former are stationary but non linear while the last are non stationary but highly linear. From these results we have also defined the EOFs base which defines the reduced order space where the data assimilation will be carried on.
-Taking profit of the above mentioned elements, we have implemented the SEQUOIA data assimilation system with an analysis kernel based in the reduced order optimal interpolation. After evaluationg its behaviour we have used a twin experiments protocol to compare the performance of different observational networks to correct different model errors.

Altough all the work have been done in the frame of the catalan continental shelf, most of the obtained results and the techniques used could be applied to other shelf-slope regions with similar characteristics.

RESUM

L'objectiu d'aquesta tesi és implementar un sistema d'assimilació de dades a un model hidrodinàmic de la plataforma continental catalana. Aquest sistema ens permetrà combinar la informació proporcionada per les dades mesurades amb la informació que prové dels models numèrics per tal de fer la millor estimació posible, en termes estadístics, de la realitat.

Per arribar a aquesta fita cal en un primer moment tenir un bon coneixement de la regió d'estudi i dels processos físics que hi tenen lloc. La següent passa és disposar de un model numèric que sigui capaç de reproduir de manera realista la dinàmica de la zona. Acte seguit cal identificar i caracteritzar les fonts d'errors del sistema i la seva dinàmica per, finalment, poder implementar un sistema d'assimilació de dades adequat al problema que tractam.

Seguint aquest camí podem aprofitar les dades i les eines desenvolupades per aprofondir en el coneixement de la dinàmica a la plataforma continental catalana desde diversos plantejaments.

-L'estudi de les mesures obtingudes en el marc dels projectes FANS i YOYO ens ha permés caracteritzar la dinàmica de la regió, estodiar l'origen de la variabilitat del corrent de tal.lús tant per altes com per baixes freqüències, estodiar els processos sobre la plataforma i veure l'evolució de les masses d'aigua.

-La implementació del model hidrodinàmic SYMPHONIE s'ha fet amb cura aplicant una novedosa tècnica d'inicialització i s'ha validat amb dades reals per tal d'obtenir un model complet i realista. Un pic aconseguit això l'hem emprat per estodiar l'evolució d'una ona topogràfica de Rossby sobre la plataforma continental, l'efecte del vent en la dinàmica tridimensional i els intercanvis plataforma-tal.lús induits pel vent i per oscil.lacions del corrent de tal.lús.

-L'ús de la modelització estocàstica ens ha permés descriure la dinàmica dels errors associats a la caracteritzacio del corrent de tal.lús i al camp de vents podent veure que els primers són no lineals pero estacionaris mentre que els segons són lineals pero no estacionaris. A partir d'aquests resultats també hem definit la base d'EOFs que defineix l'espai d'ordre reduit on es farà l'assimilació de dades.

-Aprofitant els elements mencionats abans hem implementat el sistema d'assimilació de dades SEQUOIA amb un nucli d'anàlisi basat en interpolació òptima d'ordre reduit. Després d'avaluar el seu comportament hem utilitzat un protocol d'experiències bessones per comparar l'efectivitat de diverses xarxes de mesura per corregir diversos errors del model.

Malgrat tot el treball s'ha centrat a la plataforma continental catalana gran part dels resultats obtinguts i de les tècniques emprades són aplicables a qualsevol altra regió amb característiques similars.

ACKNOWLEDGMENTS

"Es de bien nacidos el ser agradecidos"
(Refranero popular)

"Mi patria son los amigos"
(Alfredo Bryce Echenique)

Maybe, for the intrepid reader who ventures into the pages of this thesis, this part of acknowledgments is not essential and even avoidable.

Maybe he is right.

However, for me it is a great success that this section is as long as whatever scientific section of this book: this means that during these years I have got the chance of meeting a lot of people who have marked me in some ways. At the end, over all that can be written, these traces will remain to remind us that we are what we lived.

In other and more traditional words ... “¡Qué me quiten lo bailao !”.

The first acknowledgments are for my three supervisors, who contributed to this "happy end", each one in a different way.

Querría agradecer a Manuel Espino su apoyo en todas las iniciativas que se me ocurrieron durante estos años y el haber provisto su mejor voluntad en los múltiples problemas que fueron apareciendo.

Je voudrais remercier Pierre de Mey pour sa générosité, pour m'avoir accueilli dans son groupe et pour tout le temps qu'il m'a consacré. Pendant mon séjour à Toulouse j'ai, grâce à lui, appris bien plus de choses que de simplement assimiler des données.

Un grand merci aussi à Patrick Marsaleix qui, un jour, a accepté de me passer son modèle sans savoir qu'il dirigerait ma thèse par la suite. Ça a eté un grand plaisir travailler avec lui.

I would also like to thank other people who helped me in different moments sharing with me their scientific skills, always unselfishly.

Ao Paulo Leitão e Ramiro Neves que suportaram com muita paciência os meus problemas e as gafes numéricas durante a minha estadia no MARETEC.

Un grand merci à Claude, Francis et Florent toujours prêts à donner un coup de main.

A en Jordi Salat, per les enriquidores discusions i per tenir sempre la porta oberta.

Finally, the most important part of the acknowledgments is reserved for all the people who were there for the daily battles, always available to help, encourage or simply laugh. Without them I have never finished this thesis.

A tota la gent que fa que es pugui arribar a enyorar el LIM. A en Joan (exemple de savi dels temps moderns i de qui s'amistat és un bén preciat), a na Mar (mira que anar a trobar una mallorquina tan ben parida a Barcelona ...), a César (pinche compadre, fue una suerte que te echaran de Méjico y que acabaras por aquí), a n'Eric (camarada de

penes, viatges, exilis i unes quantes xerrades de les que arreglen el món), a n'Anna (la xiqueta més entranyablement divertida de la vila del pingüí), a en Dani (company de despatx per antonomàsia, malgrat les nostres discrepàncias en l'ús del tippex), a Jose (Pep Alsina para los amigos, por el buen rollete y las sesiones de catarsis - ¡¡ mierda de L@#@M !!), a Erika (ay, que haré yo sin oir Bielsito, Bielsito, ...) y a todo el resto de personajes que se pasean o han paseado por allí (Rodolfo, Manel, Walter, Fede, Jesús, Marta, ...)

A toute la faune du POC et des alentours : Merci que d'avoir accueilli si chaleureusement ce catalan insulaire qui parle français comme une vache espagnole (ehem,ehem,...). J'espère n'oublier personne : Julien et Guillaume (Ah, le chaud-time des premiers mois dans le bureau 41), Laurent (toujours la dernière visite du soir), Sylvain (et ses expériences musicales tellement bizarres et attirantes), Erika (toujours un sourire pour illuminer la fin de la thèse), Baptiste (qui est en train de conquérir Barcelone), Claire (la parfaite colocatrice de bureau, je vous la recommande) et aussi Pieter, Thierry, Celia, Kenshi, Ivane et Caroline.

À Fátima, muito mais que uma anfitriã. Ainda me lembro daquele Outono na Parede e de tudo o que aprendi, quase sem querer. Quando menos esperares apareço por ai outra vez!

A n'Andreu punt de referència musicatalà a Toulouse, pel seu bon humor i ser un gran exemple per a la vida després de la tesi.

A n'Ananda i en Simon, per una amistat conreada amb la calma de Mallorca i regada amb l'aigua del Midi-Pyrénées.

Més que un agraiment, un pensament molt, molt especial per a na Susana, probablement la historiadora que sap més d'oceanografia de tota Mallorca. Gràcies infinites per tot el camí que hem fet junts i per una morna trista que em vas deixar escrita al vent i que de tant en tant encara em ronda pel cap.

Als amics de Nou Romancer (Jaume, Tolo, Migue i Pere), per tenir sempre un assaig gastronòmico-musical preparat per quan jo arribava a s'illa.

À Martine, pour tout ce que nous avons partagé et tous les moments que tu m'as offert. Une des meilleurs choses de cette thèse c'est qu'elle m'a permis de te rencontrer… et c'est une véritable chance.

Per a acabar, i molt especialment ...

A Gabriel y a Juana,
dos personas admirables
dos amigos que redescubro día a día ...

mis padres.

CONTENTS

1 INTRODUCTION 1-1

2 STUDY OF THE CATALAN CONTINENTAL SHELF DYNAMICS FROM FIELD MEASUREMENTS 2-1

2.1 INTRODUCTION 2-1
2.2 DATA 2-3
2.3 GENERAL BEHAVIOUR 2-7
2.3.1 Slope 2-7
2.3.2 Shelf 2-9
2.4 CHARACTERIZATION OF CURRENT VARIABILITY 2-11
2.4.1 Slope 2-11
2.4.2 Shelf 2-18
2.5 WATER MASSES EVOLUTION 2-21
2.5.1 Slope 2-23
2.5.2 Shelf 2-27
2.6 HIGH FREQUENCY CURRENT VARIABILITY 2-29
2.6.1 Slope 2-29
2.6.2 Shelf 2-35
2.7 STUDY OF THE LOW FREQUENCY CURRENT VARIABILITY USING DYNAMICAL BALANCES 2-37
2.8 INFLUENCE OF WIND AND ATMOSPHERIC PRESSURE OVER THE LOW FREQUENCY CURRENT VARIABILITY 2-43
2.8.1 Slope 2-43
2.8.2 Shelf 2-50
2.9 EVIDENCES OF THE IMPORTATION OF DYNAMICAL VARIABILITY 2-51
2.9.1 Waves 2-52
2.9.2 Eddies 2-54
2.10 CONCLUSIONS 2-59

3 NUMERICAL MODELLING OF THE EBRE REGION DYNAMICS 3-1

3.1 INTRODUCTION 3-1
3.2 MODEL IMPLEMENTATION 3-2

3.2.1 SYMPHONIE model description 3-2
3.2.2 Model domain and forcings used 3-8
3.2.3 Model initialization technique 3-10
3.2.4 Description of data used to validate the model. 3-15
3.2.5 Summary and justification of runs 3-15
3.3 MODEL VALIDATION 3-19
3.3.1 Comparison with real data. 3-19
3.3.2 Description of model results 3-25
3.3.3 Sensitivity of the model to different parameters 3-29
3.4 NON LINEAR ADJUSTMENT OF THE SLOPE CURRENT 3-32
3.5 ROLE OF THE WIND IN THE SHELF AND SLOPE DYNAMICS 3-41
3.5.1 No wind 3-42
3.5.2 Migjorn (S) wind 3-42
3.5.3 Gregal (NE) wind 3-47
3.5.4 Llevant (E) wind 3-49
3.5.5 Mestral (NW) wind 3-51
3.6 SHELF-SLOPE EXCHANGES 3-63
3.6.1 Exchanges induced by the slope current variability 3-64
3.6.2 Exchanges induced by the wind 3-68
3.6.3 Residence time 3-71
3.7 CONCLUSIONS 3-74

4 DATA ASSIMILATION METHODOLOGY 4-1

4.1 FORMULATION OF THE DATA ASSIMILATION PROBLEM 4-1
4.2 DEFINITION OF THE ENSEMBLE RUNS 4-10
4.2.1 Definition of error sources 4-11
4.2.2 Definition of typical scenarios 4-13
4.3 EXPERIMENTAL PROTOCOL OF THE ENSEMBLE RUNS 4-15
4.3.1 Reference run configuration 4-15
4.3.2 Description of the perturbation technique 4-16
4.4 ANALYSIS OF THE RESULTS 4-22
4.4.1 Physical description of the reference run 4-22
4.4.2 Statistical moments 4-25
4.4.3 Is the system response linear? 4-37
4.4.4 Memory time 4-40
4.5 INFLUENCE OF OBSERVATIONS 4-42

4.6 ENSEMBLE MULTIVARIATE EOF ANALYSIS 4-50
4.6.1 Technical details of the multivariate EOF computation. 4-50
4.6.2 Results of EOF computation..... 4-59
4.6.3 Ensemble statistical diagnostics using EOFs..... 4-65
4.7 THE EOF BASE FOR ASSIMILATION 4-68
4.7.1 What do we demand from the EOF base? 4-68
4.7.2 Mixed EOFs..... 4-69
4.8 SINGLE MODE EXPERIMENTS 4-73
4.9 CONCLUSIONS..... 4-77

5 DATA ASSIMILATION IN THE EBRE REGION. PERFORMANCE OF DIFFERENT OBSERVATIONAL NETWORKS 5-1

5.1 INTRODUCTION..... 5-1
5.2 EXPERIMENTS PROTOCOL..... 5-1
5.3 DIAGNOSTIC TOOLS 5-4
5.4 OBSERVATIONAL NETWORKS..... 5-9
5.5 RESULTS REGIME 1-CORRECTION OF SLOPE CURRENT ERRORS 5-14
5.6 RESULTS REGIME 2-CORRECTION OF WIND ERRORS 5-24
5.7 RESULTS OF REGIME MIXED..... 5-33
5.8 SENSITIVITY OF THE RESULTS 5-38
5.8.1 Assimilation period 5-38
5.8.2 EOF base..... 5-39
5.8.3 Forecast error 5-41
5.8.4 Is the EnKF a good alternative? 5-44
5.8.5 Observational errors..... 5-46
5.8.6 Use of smoother/filter mode 5-48
5.9 DISCUSSION 5-49
5.10 CONCLUSIONS 5-55

6 CONCLUSIONS, PERSPECTIVES AND FINAL THOUGHTS

REFERENCES

APPENDIX : VALIDATION OF ARPEGE WIND AND PRESSURE FIELDS

INTRODUCTION

"Cette lettre est plus longue que de coutume,
mais c'est parce que je n'ai pas eu le temps
d'en écrire une plus courte".
(B. Pascal)

" - ¿Por dónde empezarías a resolver
el problema más complicado?
-¡Vaya pregunta!. ¿Por dónde va a ser,
hombre?, ¡Pues por el principio! ".

1 INTRODUCTION

General Context

The sea has always been key in most of the societies around the world. For lots of people, it has been the source from where life comes, and, from a social point of view, the sea has been at the same time an element of isolation and of communication between civilizations.

Nowadays, that historical importance is still in force by several reasons. On one hand, the ocean state has a strong influence into the global climate, which is extremely sensible due to the human action in the last century, as it is a controlling factor of the thermal and carbon balances. Also, it is a basic link in the hydrological cycle. On the other hand, an important percentage of the human activities gravitate around the sea (fisheries, transport, tourism,…).

It is also true that in the last century the pressure over the ocean has increased as a result of what is called the "progress", and the present equlibrium is seriously menaced because the over-explotation of fish stocks, loss of marine ecosystem habitats or contamination, for instance. In consequence, the sustanaible development of coastal areas, the management of marine resources (off-shore activities and fisheries) and the control of pollution is (or should be) a serious concern. Any action in that sense goes through the proper knowledge of the sea and the development of some capabilities to monitorize and forecast its state.

To reach these goals is not easy at all. The description of the ocean dynamics is 'per se' a complex problem, specially over the continental shelf and slope, which represents the natural border between the open sea and the coastal regions. The spatial scales are small (~10-100km) as well as the temporal ones (~1-10 days), and there are multiple processes interacting through non-linear relations.

The most natural way to understand the ocean behaviour is to use the information it provides measuring the relevant parameters. The problem is that to obtain data in the sea is though and expensive and, usually, the available measurements are limited in space and/or time. Thus, sophisticated analysis techniques are needed to obtain the maximum benefit of the sparse information.

A different possibility is to use numerical models to solve the physical equations that describe the ocean dynamics. This is a powerful tool if used properly. It can provide complete 3D pictures of the sea state and of its temporal evolution but their quality depends on the suitability of the basic equations and the methods used to solve them.Thus, as the numerical results are just mathematical descriptions of reality, it becomes basic to validate those results against real data to be confident on their quality.

In summary, these two approaches (observations and numerical modelling) provide different pieces of information which are useful but limited by their characteristics and their

reliability. Consequently, it seems natural to try to combine those sources of information to obtain the best possible picture of the sea state at the same time that the problems associated to each of them are reduced. The technique that allows to join the numerical models with the observations is called ***data assimilation***. The potential of this technique is very interesting because it allows to correct the model trajectories looking forward obtaining the best approximation to reality, or, from another point of view, to interpolate in space and time the available observations in a physically coherent way. The inclusion of real data into the modelling system would contribute to improve the process-oriented models, to enrich the monitoring systems and to increase the accuracy of the marine forecasts.

Previous work

The study area is located in the North Western Mediterranean sea, in the Catalan continental shelf, in particular in its southern part (see Fig 1. 1). This domain has the typical characteristics of coastal and shelf areas in the Mediterranean sea, so we expect that most of the results obtained during this thesis could be extrapolated to other regions.

The dynamics in this region is dominated by a quasi-permanent slope current, the Northern Current (NC; Millot, 1999). The NC is a geostrophic current which flows over the continental slope in a cyclonic path around the Western Mediterranean sea, from the Ligurian Sea to the Balearic basin. In summer, this slope current is relatively wide and shallow and displays a reduced mesoscale variability while in winter it becomes thicker and narrower and tends to flow closer to the slope. Also in that season, the NC developes intense mesoscale meanders with amplitudes and wavelengths from few tens to one hundred kilometers. This behaviour is present all along its path and namely in the Balearic sea (Font et al., 1995). The main difference in this area respect to other regions (i.e. the Gulf of Lions) is that the wind has a low influence over the slope current. Font (1990) showed that the winds in the area are too weak and variable to modify significatively the structure of the current.

The southern Catalan shelf is characterized by its sudden widening (see Fig 1. 1). The differences of width at the north and the south of the Ebre delta provides different dynamical characteristics at both areas (Sánchez-Arcilla and Simpson, 2002). In particular, the wide shelf acts as a buffer zone which isolates the nearshore from the slope dynamics and allows the appearance of new dynamical patterns which don't need to be related with the slope or the nearshore processes.

Over the shelf, the circulation at the north of the Ebre delta is completely dominated by the slope circulation while at the south the situation is more complex. In the wide shelf, the system is drived by the interaction of the slope current, the wind effects and the Ebre river discharges. Salat et al. (1992) and Rippeth et al. (2002) have showed the importance of the wind on the

circulation over the shelf while Espino et al. (1998) and Maidana et al. (2002), using numerical models, studied the joint effect of the river plume with the wind forcing . All those works can be summarized in the sketch presented in Fig 1. 1. The Northern Current flows over the slope acting as a border between the open sea processes and the shelf. The region of freshwater influence (the ROFI area) of the Ebre river is limited to 20-30km but it is variable depending on the river runoff. Finally, the wind climate in the region is dominated by the Mestral (NW) winds, channelled by the Ebre valley, and the Llevant (E) wind, much broader as it blows from the open sea.

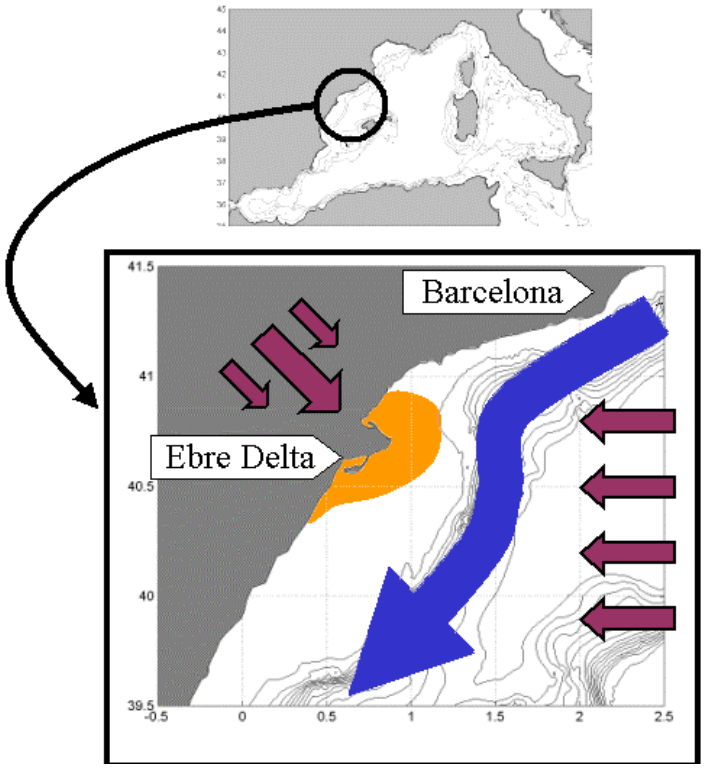

Fig 1. 1: Location and principal dynamical forcings in the southern Catalan continental shelf. The blue arrow represents the Northern Current, the orange spot is the ROFI of the Ebre river, and the magenta arrows sketch the narrow Mestral winds (NW) and the wide Llevant winds (E).

It must be noted that the study of the mesoscale variability in this region presents the difficulty of an important lack of exhaustive programs which would provide dense datasets. In consequence, the available measurements usually do not have a spatial and/or temporal coverage good enough to properly characterize the different processes, specially the 3D dynamical structures, and their temporal evolution.

The complement to this lack of data could be the numerical modelling but most of the previous works in that field presented some important shortcomings. The works of Espino et al.

(1998) and Maidana et al. (2002) didn't consider the river outflow and were just based on the wind-driven circulation. Naudin et al (2002) and Mestres et al. (2003) included the Ebre river plume but their studies where very local and didn't describe the general patterns. Finally Xing and Davies (2002) used a larger domain model but in an idealized configuration. In summary, there have been few numerical works in the region and no one planned to study the whole shelf-slope region in a realistic configuration.

Finally, to our knowledge, there is no published work on data assimilation in the Balearic sea. In addition to that, few studies of data assimilation in coastal and shelf areas have been presented in the scientific community. Assimilation at regional scales is an immature field which presents lots of difficulties, specially because it needs a different approach from the one used at global scales.

Most of the present data assimilation schemes are based in a linear estimation where the correction of the model state **x** using observations is done through a linear relation:

$$\delta \mathbf{x} = \mathbf{K}\, \delta \mathbf{y}$$

where **y** represent the observations, δ**y** represents the differences observation-model and **K** is the gain matrix which defines the way the correction is done. This gain matrix is constructed from the error covariance matrices which describe the structure of the errors associated to observations and the errors of the model forecasts. Formaly this is:

$$\mathbf{K} = \mathbf{P}^{\mathbf{f}}\mathbf{H}\left[\mathbf{HPH} + \mathbf{R}\right]^{-1}$$

where **R** is the observational error covariance matrix, **H** is an observatior operator and $\mathbf{P}^{\mathbf{f}}$ is the forecast error covariance matrix. This forecast error is defined as the difference between the model results and the truth (note that it is obviously not possible to know it, but what is intended to know is its statistics).

To sum up, assimilation translates the difference between the model results and the measured data into corrections of the model state. To do this, the information about the uncertainties of the model and the observations is used.

The key point of the assimilation and what limits the quality and optimality of the different schemes, is the way the error covariance matrices are defined. Specially, the forecast error covariance matrix, which describes the structure of the errors in the forecast, is completely unknown. In open sea implementations, some simplifications as isotropy, homogeneity or stationarity are assumed to define those covariances but in coastal regions these assumptions are no longer acceptable. Namely, Echevin et al. (1999) showed that the influence functions in a

coastal model of the Gulf of Lions were highly non-homogeneous and anisotropic. Mourre et al. (2004) highlighted the non-stationarity of the errors structures in a barotropic model of the Northern Sea. Finally, Auclair et al. (2003) proposed the ensemble modelling to define the error dynamics in a coastal model. These few examples enlight the fact that data assimilation in regional scales is not at all a trivial issue and must be carefully treated. The work associated is quite extensive, demands a strong scientific background and must be carefully done following several steps

First of all, it is basic to have a good knowledge of the dynamics of the region of study. It is important to have a good idea about the dominant processes and their variability in order to be able to evaluate the quality of the modelling work and to better understand the results obtained. The second step is to have a reliable numerical model able to produce good estimates of the sea state and its variability. The model must be as complete as possible and should be carefully validated against real data. The third step is to characterize the error sources of our modelling system. We need to know not only what are the main errors but also what is their structure and their temporal evolution. Finally, with all those elements, we have to implement a data assimilation system that must be well suited for the problems we face, namely, the 3D circulation in the shelf-slope region.

Our proposal

Once the general context has been presented, we can talk about the particular history of this thesis. This work was launched in the frame of the Laboratori d'Enginyeria Marítima of the Universitat Politècnica de Catalunya (LIM/UPC), a lab which traditionally has been interested on the dynamics in the Balearic Sea and the Catalan continental shelf (NW Mediterranean). All the studies done in the LIM until now have been based either on observations or on numerical models but nothing has been done joining both. On the other hand, the group is involved in several projects which focus on the improvement of monitoring and forecasting skills at regional scales as MFS (Mediterranan Forecasting System), ESEOO (Establecimiento de un Sistema Español de Oceanografía Operacional) or the CAMCAT (Marine Pollution Emergency Plan of the Generalitat de Catalunya). In consequence, it was proposed, as a natural continuation of the work done by the group and to face the new worklines, to develop the suitable tools to merge observations and numerical models in the Catalan coastal region.

The main objective of this thesis is, thus, **to implement, in a 3D numerical model of the Catalan continental shelf, a data assimilation system well suited for the coastal region**.

In addition to that, and in order to take profit of all the technical and conceptual efforts done along that path, a secondary objective arises: **To improve the knowledge of the coastal and**

shelf region dynamics using different approaches: data analysis, numerical modelling and statistical tools.

To adquire the adequate skills to do this work, part of the thesis has been developed in the Pôle d'Oceanographie Cotière (POC, Toulouse). This group has been working for a long time in modelling the shelf and coastal regions and in developing data assimilation schemes. Thus, its expertises were very useful for the development of the work.

In this context, we defined the way towards implementing a data assimilation system in the Catalan continental shelf as follows.

In a first stage, we needed to characterize the dynamical processes in the region in order to establish a solid base for all the subsequent numerical work. Instead of simply doing a bibliographical research we preferred to rescue some underused datasets and to use them to confirm and complement the main results already obtained in the region by other authors. Thus, we have used current meter data obtained in the frame of the FANS and YOYO projects in the 1996-1999 period to characterize the principal dynamical patterns both over the slope and the shelf. We have carried on several analysis to obtain a general picture of the circulation and, specially, of its variability. We have studied both the high and the low frequency bands in order to have a complete picture of the processes that take place in the region, and we have tried to relate them to several forcing factors to understand the origin of the variability. All this work is based, basically, on statistical tools, so we wanted to show some special events that escaped from the mean behaviour but that are interesting as the effects of a strong winter on the water masses evolution or the advection of isolated structures.

The second stage was to implement a 3D coastal model able to reproduce the principal processes observed. To do that, high resolution is needed as well as a correct description of the vertical processes, a good atmospheric forcing must be available and a correct definition of the initial and boundary conditions is basic. The model chosen is the SYMPHONIE model, which is a 3D primitive equations model largely and successfully tested in coastal and shelf implementations. It is, basically a state-of-the-art model but which includes some added attractives as the hybrid vertical coordinate system or the modal potential vorticity (MPV) initialization method. In fact, the main handicap of limited area models is the correct prescription of the initial and boundary conditions. It is not trivial to define an initial state which reproduces the desired features and which is in equilibrium with the model equations. On the other hand, the model interior solution is really sensitive to the boundary conditions so they have to be treated very carefully. The MPV method allowed us to precisely define the dynamical situation that best adjusts to the picture provided by observations.

Once the coastal model has been implemented in a realistic configuration and validated against real data, we decided to take advantage of it to complement the studies done in the

region. In consequence, we have studied the propagation of a topographic wave over the shelf, the 3D circulation patterns induced by the wind and the exchanges shelf-slope.

The third stage of the thesis has been to develop the assimilation tools suitable for the coastal region. We use the SEQUOIA data assimilation system with the MANTA analysis kernel, which is a Reduced Order scheme. Once the assimilation schem is chosen, the key point is to characterize the dynamics of the main sources of error of our modelling system, namely the wind and the slope current. To do that we use stochastic modelling based in the work of Evensen (1994) and Auclair et al. (2003). From ensemble modelling we can explore the dynamics of the errors looking at the dispersion of the results of an ensemble of model runs where some parameters have been perturbed. Using this approach we can look at the spatial structure and the temporal evolution of the errors and we can describe their dynamics with statistical tools.

The last stage of the work was to couple the data assimilation scheme with the numerical model and to test it in a realistic framework. We need to know the skills of the system and specially its limitations. The way to test this has been the study of the performance of different observational networks to correct errors in the modelling system. We have used the twin experiments strategy in order to obtain the maximum flexibility and control over the assimilation procedure.

This manuscript is organized as follows. The characterization of the region dynamics and its variability is presented in *chapter 2*. The implementation and validation of the SYMPHONIE model and it application to process oriented studies is done in *chapter 3*. The data assimilation methodology and the characterization of the error dynamics is carried on in *chapter 4*. The practical implementation of the SEQUOIA data assimilation system to study the performance of different observational networks is showed in *chapter 5*. Finally the global conclusions of the thesis and the perspectives that arise from it are presented.

STUDY OF THE CATALAN CONTINENTAL SHELF DYNAMICS FROM FIELD MEASUREMENTS

"Comprendre les coses que ens envolten
és la millor preparació per entendre
les coses que hi ha més enllà".
(*Hipatia)*

2 STUDY OF THE CATALAN CONTINENTAL SHELF DYNAMICS FROM FIELD MEASUREMENTS

2.1 Introduction

The goal of this chapter is to characterize the dominant physical processes in the Catalan continental shelf (see Fig 2. 1) as a previous step to the numerical studies and the data assimilation exercises in the region. First of all, we are interested in the characterization of the general (climatological) behaviour of the permanent dynamical processes and their variability. On the other hand we are also interested into enlighting the atypical behaviours that sometimes appear and to define its importance in the region dynamics.

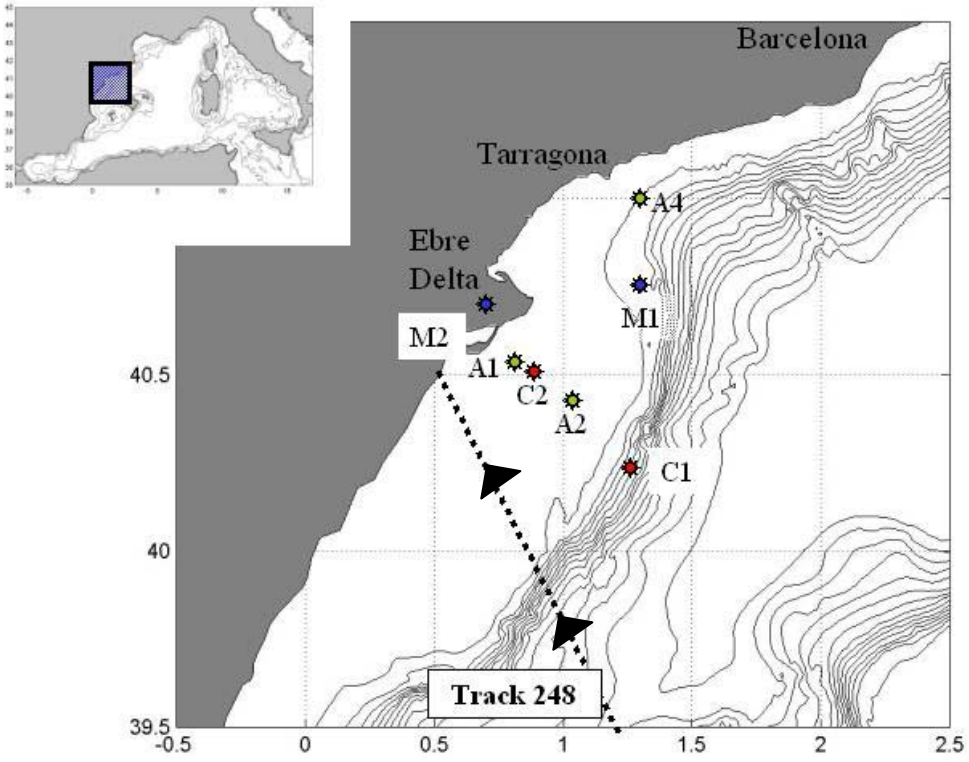

Fig 2. 1: Mooring positions (A-C), meteorological stations (M) and the altimetric track. Isobaths separation is of 100m

The region is strongly marked by the specific features of the bathymetry. Namely, its most relevant characteristics are the steep slope, which changes from 200m to 2000m in 20km (α=dh/dx~0.01) and the abrupt change of the shelf width, which evolves from 15km in the northern part to 65km in the south. This shelf widening has important consequences over the dynamics: The drastic change of the slope orientation is favorable to the generation of topographic waves (Gjevik et al., 2002) and to induce current meandering. On the other hand, the differences of the shelf width lead to different dynamical properties at the north and the south of the slope bending (Sánchez-Arcilla and Simpson, 2002).

About the slope dynamics, the most relevant thing is the presence of a quasi-permanent slope current. This current, the so-called Northern Current (Millot, 1999) is in geostrophic equilibrium due to the density differences between waters in the interior part of the basin and the coastal waters, less dense due to continental processes. Also, Echevin et al. (2004) have recently suggested that the slope current could be established by a Kelvin wave propagating along the slope.

The wind climate is dominated by the southerly and southwesterly wind during summer while in winter the predominant winds come from the northwest. The wind bursts rarely last more than two days and their intensity is usually lower than 15m/s. Its influence over the shelf is of first order of importance (Salat et al., 1992), while its effects over the slope dynamics at subinertial frequencies seem negligible.

Over the shelf, another important factor is the Ebre River. This river has associated a mean outflow of 300 m^3/s with some peaks than can reach 2000 m^3/s during winter (source: Confederación Hidrogràfica del Ebro). Its importance is based on the fact that it is a source of buoyancy, key for the dynamics, and of sediments. Usually, the extension of the Ebre river plume is about 20-30km and it is limited by the shelf width. Nevertheless, the fact that it is located in the widening area favors than, under certain conditions, the river plume is able to reach the slope and even modify the slope current (Xing and Davies, 2002).

In spite of the fact that lot of work has already been done in this region, both over the shelf and the slope, the data collected in the frame of the FANS and YOYO projects and the use of some analysis techniques never used before in the region, can help us to complement the past studies. In section 2.2 we present the ensemble of the available data sets and the data processing applied. Afterwards, we characterize the general behaviour (section 2.3) and its variability (section 2.4) in the shelf and slope from long time series (more than a year) of current measurements. Later, we focus in the time evolution of the water masses (section 2.5) and we study the high frequency variability (section 2.6). The next step is to deepen in the low variability processes using the dynamical balances (section 2.7) and studying the effects of wind

and pressure over that frequency range (section 2.8). Finally, we show some evidences of the import of variability (section 2.9).

2.2 Data

This study is mainly based in data collected during the FANS project (Fluxes Across Narrow Shelves: The Ebre Delta case) and the YOYO project (development of an autonomous multisensor profiler)

At the end of 1996, the FANS project was launched with the objective of studying the water and particle and nutrient fluxes in narrow continental shelves. With this aim, an extensive program of measurements was carried on over the Catalan shelf and slope. Namely, a series of moorings were deployed (see Fig 2. 1) during different periods between November 1996 and July 1998. At the end of this period, the YOYO project began, maintaining some of the moorings until summer 1999. In Table 2. 1, it is summarized the mooring positions, the current meter depths and the measurement periods.

The current meters used are rotor based Aanderra RCM7 in positions C1 and C2 with a frequency sampling of 30 minutes. The Doppler current meters are wide band acoustic profilers with a sampling frequency of 10 minutes and a bin size of 4 meters. Temperature was obtained with termistors located in the same positions as the current meters and with a termistor chain between 100 and 200 meters during a special period of the YOYO project (see Table 2. 1).

The FANS current meter data is characterized by having lot of gaps in the series due to maintenance while in the YOYO project those gaps were much less important. In consequence the YOYO data is more suitable for studying the general behaviour and to compute statistical quantities.

All the time series have been cleaned following visual and objective criteria. To fill the gaps in the series, simply linear interpolation has been used when gaps are shorter than 6 hours while for the longer gaps we have used the Joseph's spectral method. Finally, a low-pass 6 hours filter have been used to remove noise and all velocity series have been rotated 50º so the x (y) component represents de along (across) slope direction. It must be noted that the difference with the angle obtained from the principal component analysis is never greater than 10º, so the use of a constant rotation angle for all series is justified.

Position	Bottom	Depth	*1996*	*1997*	*1998*	*1999*
C1	**600**	*100*		*** *** ***	** ******	********
		300	**	*** *** ***	** ******	********
		500	**	*** *** ***	** ******	********
C1 - Termistor chain	**600**	*100-200*			**	*****
C2	**60**	*15*	**	*** *** ***	** ******	********
		55	**	*** *** ***	** ******	********
A1	**50**	*8:4:44*		***		
A2	**80**	*14:4:74*		***		
A4	**90**	*11:4:79*		***		
Ebre Runoff	**-**	-	**********	**********	**********	**********
M1-Meteo Casablanca	**-**	-	**	** ** *****	** ****	****
M2-Meteo Ampolla	**-**	-		**********	**********	**********

Table 2. 1: Measurement periods for moorings, meteo stations and Ebre runoff series.

In order to complement the current data, we have used several coastal meteorological stations and one located in the open sea (see Fig 2. 1). The coastal stations belong to the XAC (Xarxa Agrometeorològica de Catalunya) and to XIOM (Xarxa d'Instrumentació Meteorològica i Oceanogràfica) and provide, among other parameters, wind velocity at 2m and atmospheric pressure. The Casablanca station in the open sea belongs to the Repsol oil company and provides atmospheric pressure and wind velocity at 50m. In order to make all measurements comparable, we have used the Large and Pond (1981) algorithm to transfer those values to the standard 10m height and we have applied the same cleaning procedure than for the current and temperature time series. Finally, in some comparisons, we have used the wind stress computed from:

$$\tau = \rho C_D W |W| \qquad \textbf{(2.1)}$$

where ρ is the air density (0.0012 g / cm ^{3}), C_D is the drag coefficient and W the 10m wind velocity. The drag coefficient is computed as a function of wind velocity following Wu (1980):

$$C_D = (0.8 + 0.065W)10^{-3} \qquad \textbf{(2.2)}$$

It must be noted that the coastal meteorological stations present the handicap that they are not completely representative of what happens over the sea (Estournel et al. 2001). At the same time, the only measurement point in the open sea has often technical problems, so making difficult to have continuous measurement of atmospheric conditions over the sea.

To solve the above mentioned problems, we decided to use the wind and pressure information provided by the atmospherical model ARPEGE run by Méteo France (*www.meteofrance.fr*) to complement the available data. The main advantage of the models is that they provide information with a good coverage both in time (3-6 hours) and in space (1/10º of horizontal resolution). On the other hand their results must be validated before be used. To do this, we compared the model results with observed data from the available meteo stations (see appendix 1). This comparison shows a good agreement suggesting that numerical results could be used when no real data is available.

From this dataset we can identify the wind climate in the region (see Fig 2. 2). The results are in good agreement with García and Ballester (1984). The Mestral (NW) winds dominate with a significative contribution of the west and north-northeast winds. Depending on the station position (open sea/coast) there are some differences in the results due to the fact that the coastal stations are affected by the local topography. In consequence, winds in the Casablanca station (see Fig 2. 2) are stronger and more variable in direction than those measured in the Ampolla station. On the other hand it is interesting to note that, in general, the duration and intensity of wind bursts are weaker than in other regions of the NW Mediterranean (i.e. The Gulf of Lions).

Finally, other datasets have been occasionally used to complement some parts of the work. During the FANS project, three CTD campaigns were also carried on in different seasons (Salat et al., 2002). In our case, we use this data to get information about the temperature, salinity and density profiles and to have a complete 3D picture of the water mass distribution in different moments.

We also use satellite information of the sea surface temperature (SST) images provided by the AVHRR (Advanced Very High Resolution Radar) sensors installed in the NOAA satellites. Images were obtained from the free web site of the DLR (German aeronautic center: http://eoweb.dlr.de:8080). Details about the acquisition and data treatment can be found in its web site. A comparison of the SST images with surface temperature measured in the Tortosa

buoy of the XIOM network shows strong disagreements in terms of bias between both pieces of information. This is probably due to the algorithms used to do the atmospheric corrections for the satellite images. Therefore, we use these images to identify spatial structures and not to obtain precise measurements.

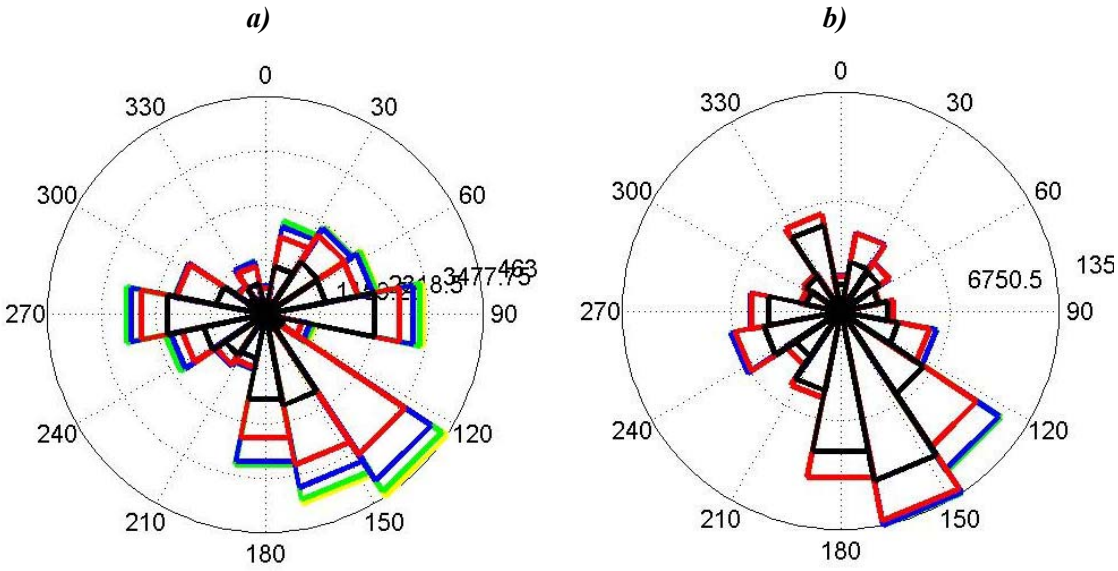

Fig 2. 2: Wind distribution for (a) the Casablanca meteo station (open sea) and (b) l'Ampolla meteo station (coast) in 1997. Wind are represented following the oceanographic convention and colours denote different bands of wind speed: black >0-5m/s, red >5-10m/s, blue >10-15m/s and green > 15-20m/s

To complement SST images and to have a direct measure about the Ebre river plume, we use chlorophyll data provided by the SeaWifs sensors. Images were obtained with a spatial resolution of 2km and already treated from the Joint Research Center (JRC) Marine Environment Unit (ME) -Space Applications Institute (SAI) web site. It must be noted that the high values observed in the images are not always the signal of high chlorophyll concentrations. High sediments concentrations or shallow regions can generate a signal that can be mistaken for chlorophyll maximum.

Finally, we also used altimeter data from TOPEX/Poseidon satellites in order to get some estimations of the sea surface anomalies. We have used measurements over the 248 track (see Fig 2. 1) treated by the Laboratoire d'Etudes Geophysiques (LEGOS - Toulouse) team.

2.3 General behaviour

To study the general behaviour of the circulation in the Ebre region, we use the YOYO data because it is the longest continuous time series available (August 1998-September 1999). The Northern Current and its variability have been tracked with current meters located in C1 over a 600m bottom. This mooring is placed in an ideal position because it is considered than the slope current flows over the 800-900 isobath being 30-50 km wide, so it is expected that current meters clearly capture its signal.

Over the shelf, we can get a good picture about processes there thanks to the C2 mooring, which is placed over the 60m isobath in the widening shelf area.

2.3.1 Slope

Over the slope, the shallowest current meter is at 100m depth but it can be considered representative of the more superficial circulation because Font et al. (1995), using data between surface and 100m depth, showed that the slope current in this region has a strong barotropic character. In consequence, we can consider that variability measured by our current meter is representative of what happens between surface and 100m depth.

Data obtained in C1 show that the mean velocity is not too strong (~10 cm/s at 100m and just 3cm/s at 500m) but that variability is quite important, as it is shown by the marked oscillations at all depths (see Fig 2. 3).

During December and January, the maximum values are found. Velocities can reach 40cm/s at 100m and 300cm/s at 300m depth. This sudden increase of current intensity has also been observed in 1998 with the FANS data (not shown) confirming the seasonality of the Northern Current intensity already evidenced by other authors (i.e. Font et al., 1995). During this period, there are some important wind events in the region but it doesn't seem that they are directly responsible of the observed intensification. It is rather the consequence of the seasonal variability of the general circulation in the Western Mediterranean: In winter, the Northern Current is accelerated due to the homogeneization of the water column, the generation of winter deep water in the Gulf of Lions and the intensification of winds in that area (Millot, 1999).

Usually, this intensification takes place in the Gulf of Lions simultaneously at all depths but as velocities are not the same in the whole water column, the acceleration reaches our region with a different lag depending on the depth. This would be why the maximum at 300m depth is delayed.

From the progressive vector of every current meter (see Fig 2. 4), it can be observed a clear predominance of currents directed towards the southwest with a weakening in depth. The constant tick separation in Fig 2. 4 until November indicates a near constant velocity while the greater separation (greater displacements) during winter are due to the above commented

intensification. It is important to note that current is predominant to southwest during all the year. This means that most of the time, the cyclonic circuit of the Western Mediterranean (Millot, 1999) is continuous and present in this region, contrary to what is usually found in the numerical studies of the general circulation in the Mediterranean where the current path until the Eivissa channel is not reproduced (Fernández et al., 2004; Demirov and Pinardi, 2002)

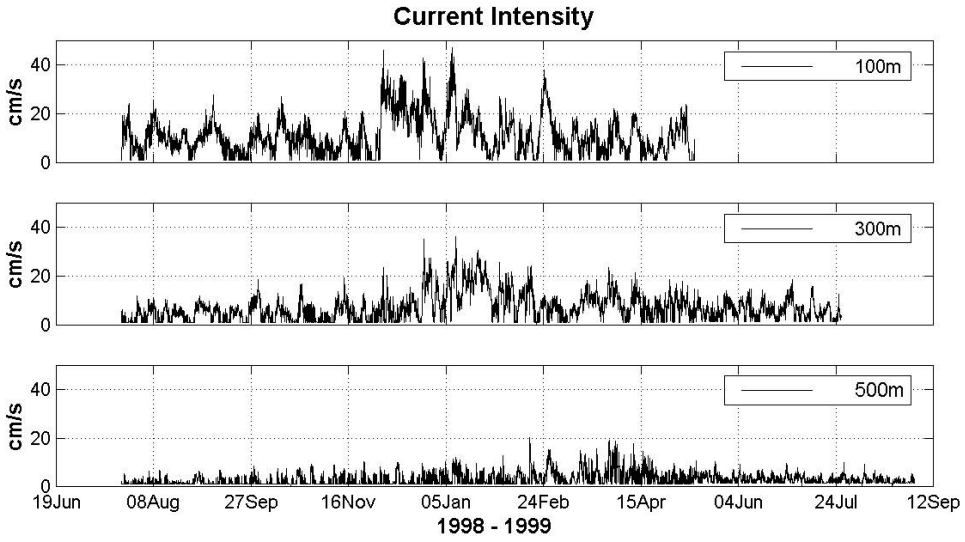

Fig 2. 3: Current intensity at different depths (a) 100m (b) 300m and (c) 500m.

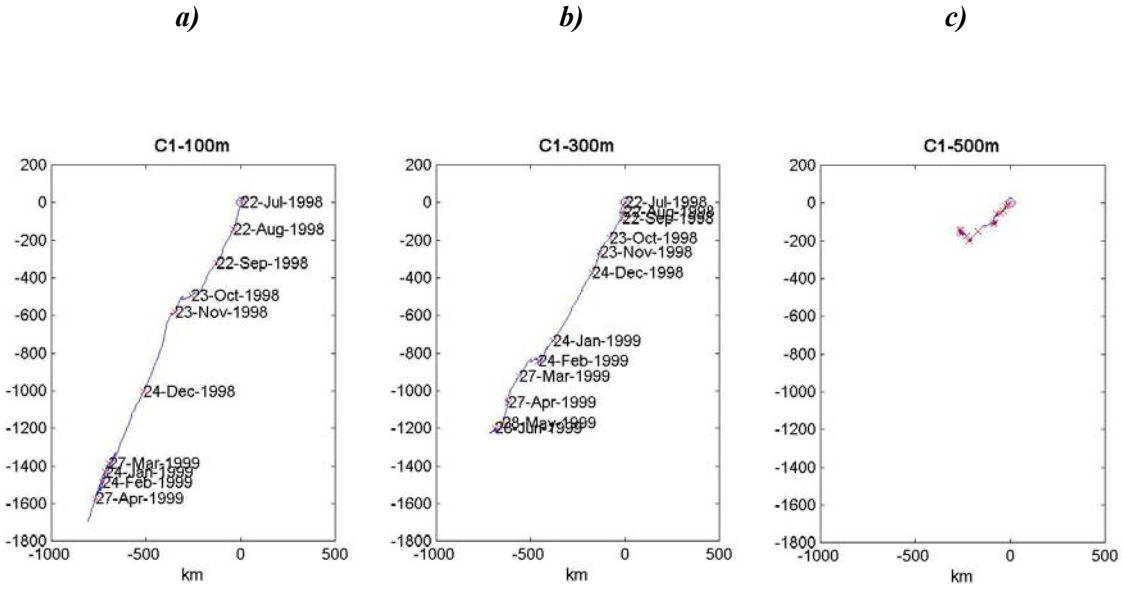

Fig 2. 4: Progressive vector of the current meters located over the slope (C1) at a) 100m, b) 300m and c) 500m. Ticks are placed every 31 days and for clarity dates are not included in the 500m plot.

Overimposed to this predominant current there are frequent series of cyclonic-anticyclonic oscillations that are the reflex of the current meandering (see Fig 2. 5) and can be found all the year. On the other hand, during the whole period, there are also several 2-5 days current interruptions linked, probably, to mesoscale structures advected by the slope current. At the end of the period (February-March 1999), there is an important inversion of the current that will be commented later on (see section 2.9). It must be noted that this kind of inversions, where the current interruption lasts for more than 10 days, are not at all frequent, at least at this depth. During the FANS and YOYO periods, where we have ~2 years of validated data, we have just found two inversions like that.

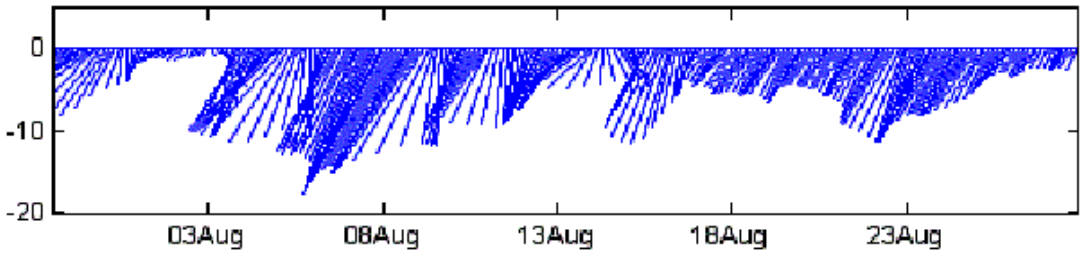

Fig 2. 5: Stick diagram of the currents over the slope at 100m depth during August 1999.

2.3.2 Shelf

Over the continental shelf, the mean current is about 8cm/s in the whole water column and, similarly to what happens over the slope, the standard deviation is important being 6cm/s at 15m depth and 5cm/s near the bottom. During all the period, several peaks of intensity have been observed where the current reach maximum values of 50cm/s near the surface and 30cm/s near the bottom (see Fig 2. 6).

As it can be seen in the progressive vectors diagram (see Fig 2. 7), there is no clear pattern of displacement and the only significative seasonal variation is around June where the surface current is intensified while the bottom layers loss energy. This is probably due to the formation of the thermocline which inhibites the energy transfer from wind in surface layers to the bottom.

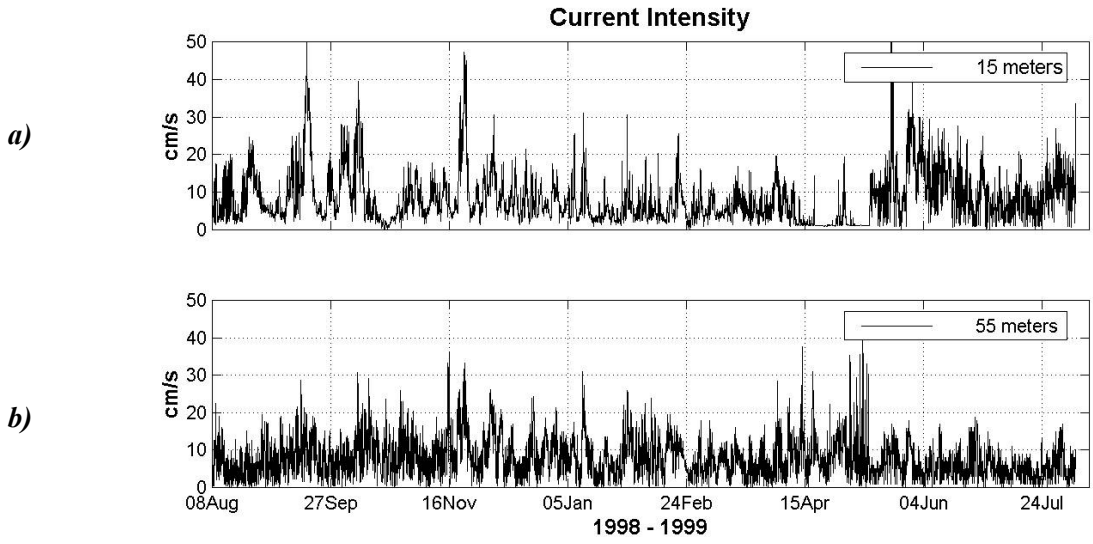

Fig 2. 6: Current intensity over the shelf (a) 15m and (b) 55m

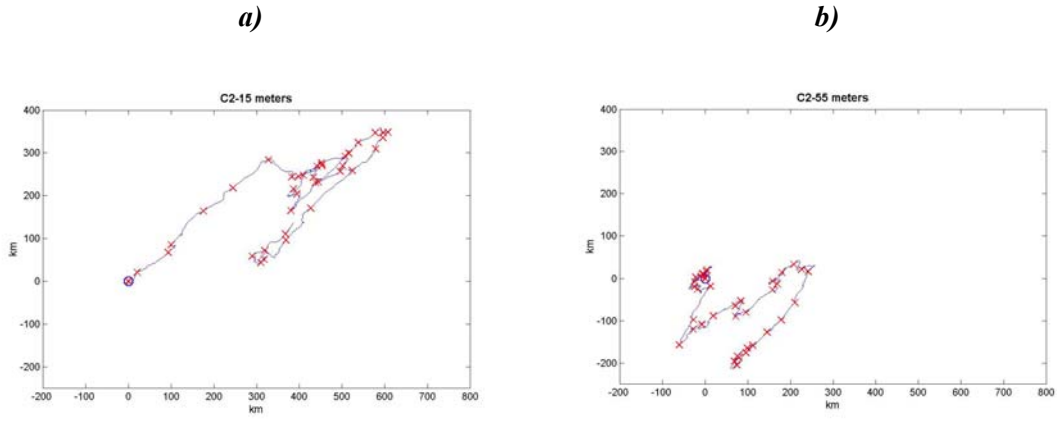

Fig 2. 7: Progressive vectors of shelf currents at 15m and 55m over a bottom of 60m between August '98 and July '99. Each mark (*) indicates an increment of 31 days (for clearity we don't include the dates).

2.4 Characterization of current variability

2.4.1 Slope

If we look to the dispersion diagrams and we compute the axes of the variance ellipses (see Fig 2. 8), it is clear than the current variability is important (see the size of the cloud) and it is very polarized: More than the 80% of the variance is linked to the principal axe. In addition to that, the angle of the variance ellipses is in good agreement with the slope direction (around 50º) suggesting than variability is topographically controlled. The most energetic oscillations are along-slope while the movements across-slope are restricted by the bottom slope.

Another interesting point is that there is an anticyclonic rotation of the principal axe with depth. At 100m it has an inclination of 66º, at 300m is 53º and at 500m is 40º. The explanation of this rotation is maybe linked to a topographic effect. Deeper is the layer, a greater control of the bathymetry over the dynamics is expected, so a stricter alignment with the isobaths.

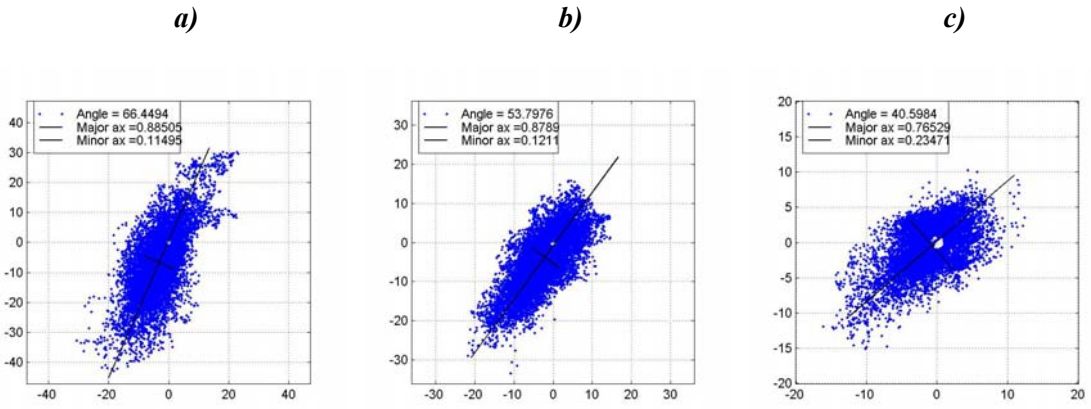

Fig 2. 8: Dispersion diagrams and variance ellipses axes for the different current meters over the slope a)100m b)300m and c)500m

The evolution of the variability along the year can be characterized looking at the evolution of the mean kinetic energy (averaged every week) and its standard deviation (see Fig 2. 9). As it was mentioned before, the energy suddenly increases between November and February with a maximum in December. The energy decreases with depth and it must be noted that the maximum peaks at different depths are not in phase, suggesting some degree of independence between processes at different levels.

The kinetic energy variance (Fig 2. 9) follows the same tendency than the mean energy with a maximum during winter even if it is not as abrupt. It is interesting to note than at 500m the variance values exceed the mean energy values.

If we compare these results with those presented by Font et al. (1995) for shallower levels between 1987 and 1992, we find a good agreement with the dates of variation and the maximum values of energy variance.

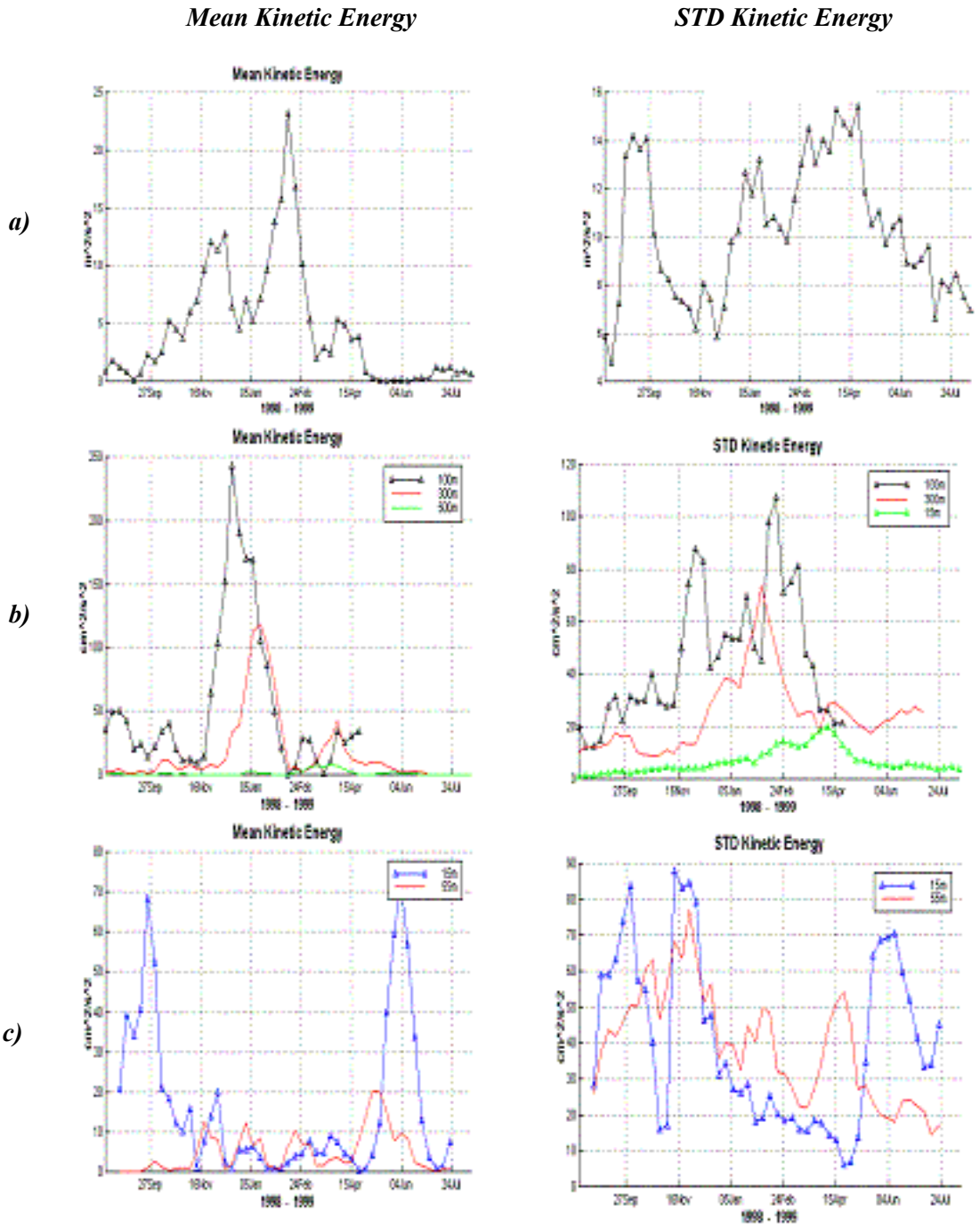

Fig 2. 9:Time evolution of the mean kinetic energy and the kinetic energy STD computed in a 7days interval for (a) wind in the Ampolla station, (b) currents over the slope and (c) currents over the shelf.

In order to gain an insight into the relations between processes at different levels, we have performed an EOF analysis (Empirical Orthogonal Functions) of the low frequency velocities

filtered with a low-pass filter of 1 day. The technique used is the same used by Kundu and Allen (1976) and Noble and Ramp (2000), and it is useful to find statistical relations of the variability at different levels.

The vertical structure of movements alongslope presents a dominance of the barotropic behaviour (see Fig 2. 10), where the first mode explains the 76.2% of the variance. The second mode explains the 15.5% of the total variance, it has a baroclinic character and clearly unlinks the processes at 100m depth with those below. On the other hand, if we look to the local variance associated to those modes we find that they are enough to explain almost all the variability at 100m and 300m. Finally, processes in the deeper layer (500m) are mainly controlled by the third mode but with a significative effect of the other two modes. This is in good agreement with the idea that measurements at 500m are near the base of the Northern current and depending on the dynamical regime they are more or less influenced by it, so showing more or less correlation with upper levels.

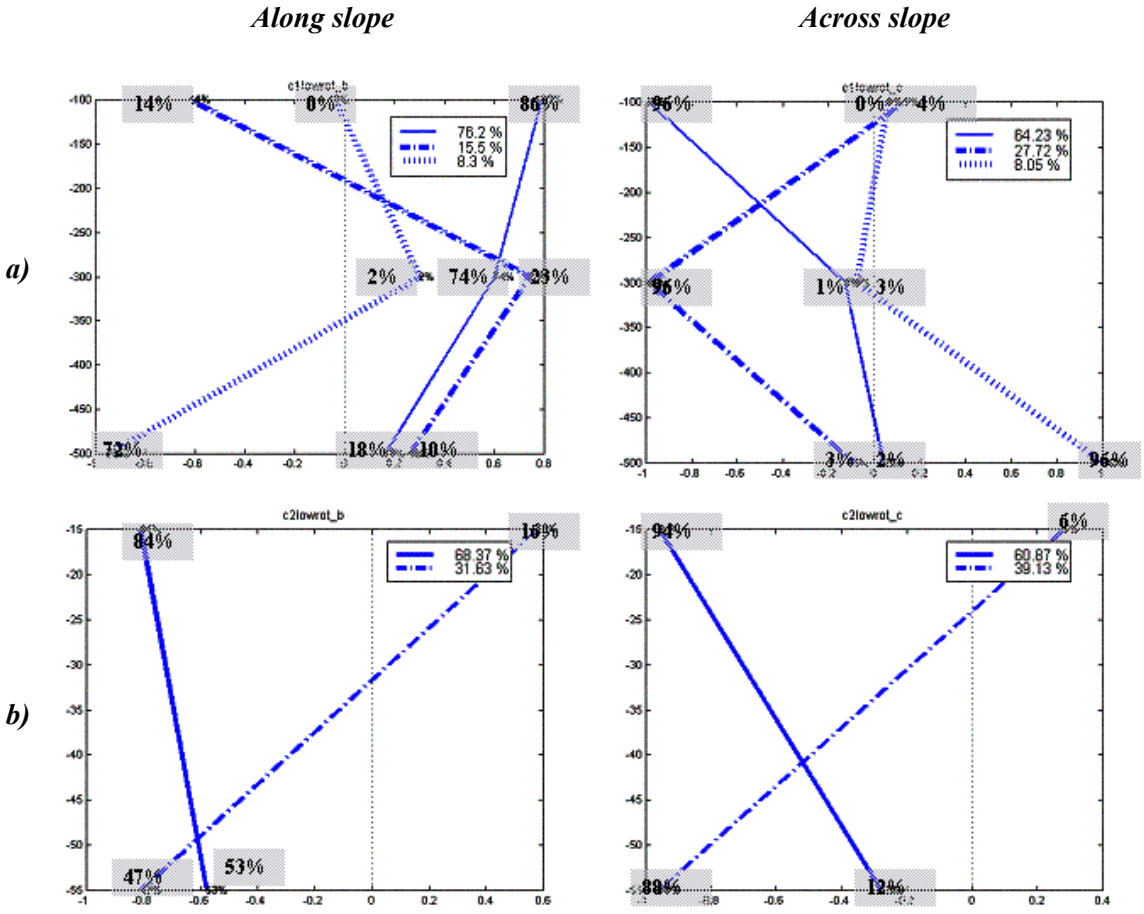

Fig 2. 10: Vertical structure of the EOFs a) over the slope and b) over the shelf. For each depth it is marked the local variance associated to each mode.

If we look at the structure of the movements perpendiculars to the slope, it can be seen a clear independence about what happens at each level. For each measurement point there is just one mode that explains almost all the variability. This could be explained because the processes, which induce across-slope movements, are independent at each level or because there is some kind of lag between different depths, which makes the EOF computation less effective. Linked to this, Pinot et al. (2002) observed at the Eivissa channel that the meandering of the Northern current affected all levels but with some phase lag, which in our case would induce low correlations. They proposed baroclinic instability as the mechanism, which would generate these current oscillations.

Finally, we also have find that the EOF computation at different seasons don't change the modal structure found and only the explained variance by each mode slightly changes.

The EOFs give an idea about the vertical structure of the movement from a statistical point of view. An alternative to study that structure is to use the normal or Kelvin modes obtained analytically from a density profile (Gill, 1982). These modes are function of the stratification and describe the vertical structure of the velocity associated to the different Kelvin modes. They can be used to evidence the nature of current fluctuations depending on the dominant modes. Even if they are a theoretical approximation, Alberola et al. (1995) showed that the Northern current before coming into the Gulf of Lions is well represented by the barotropic and the first baroclinic mode. Until our knowledge, a similar analysis has never been done in our region although, a priori, the behaviour observed by Alberola et al. upstream doesn't need to be maintained all along its path. Instability processes, changes in stratification and the topographic influence, among others, could contribute to modify the vertical structure of the current. In consequence, it seems interesting and justified to compare the empirical modes with the normal modes.

In order to do a good enough comparison, it would be necessary a distribution of velocities in the vertical denser than what we have during the YOYO period to compute the EOFs. In this case, we use ADCP measurements obtained in the position A4 (the northern part of the domain) between March and October, the spring-summer period, of 1997 . This measurement point is near the shelfbreak and it can be consider that it captures the coastal edge of the Northern current. On the other hand, the normal modes are computed using a typical density profile in the region obtained from the summer FANS campaign (see Fig 2. 16a). The fact of using other density profiles slightly change the zero crossing position but the structure is qualitatively the same.

In Fig 2. 11, it is presented the comparison between the empirical and the normal modes. The first EOF corresponds to the barotropic mode and it is not shown. The amplitude is not

important and just the structure is significative. As it can be seen, there is a striking good correlation between the theoretical modes and the empirical modes in the vertical structure but also in the zero crossing position. In the shallower levels, the wind effect degrades the quality of the comparison because some of the hypotheses done in the development of the normal modes are severely violated. Nevertheless, we can take profit of the statistical information provided by the EOFs to say that the vertical structure of the Northern current in the Balear Sea is barotropic in a 70%, a 15% is adjusted to the first baroclinic mode and a 4% to the second.

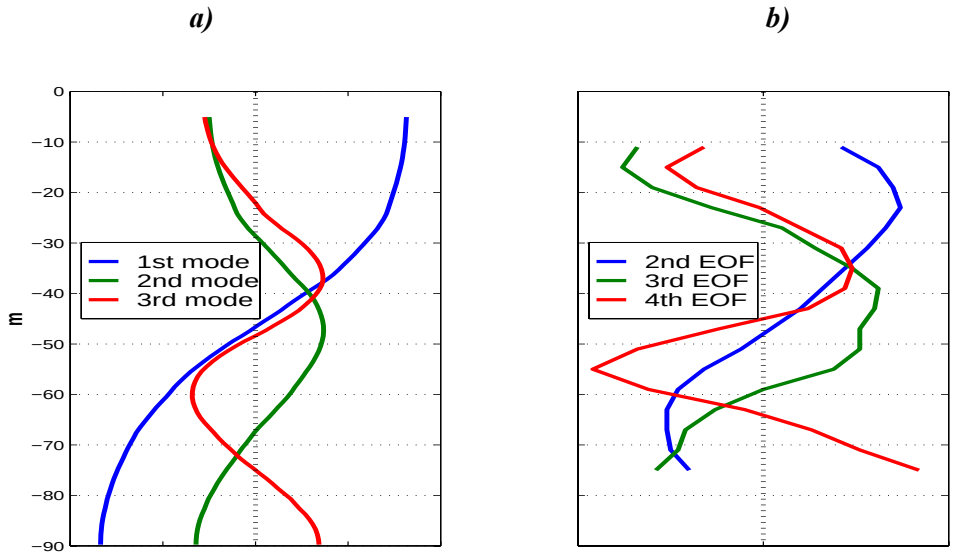

Fig 2. 11: Comparison of the vertical structure of the first (a) normal modes and (b) empirical modes (EOFs) computed at position A4 between march and october 1997. The explained variance associated to the first mode (not drawn) is 70%, the second 15%, the third 4% and the fourth 2%.

To finish with the comparison, it must be said that results using other density profiles lead to the same qualitative results. Unfortunately we do not have winter ADCP data over the slope to look at the seasonal evolution of the vertical structure of the current.

In order to better characterize the variability evidenced in the dispersion diagrams, we do a spectral analysis of each velocity component (along and across the slope) and of the rotational spectrum (see Fig 2. 12).

The analysis has been done using the Welch method where an average of the spectra is done by sections. If a great number of sections are used, the statistical confidence will be greater but also the frequency resolution will be lower. In our case, we have used 10 sections because we have enough data to reach a reasonable statistical confidence. This allows us to identify a series

of peaks in the 1-10 days band associated to processes that takes place in different moments of the year.

At all depths, we find that the most energetic processes have periods of 3,6 and 14 days and also near the inertial frequency (18.45h) and the tide signals at 12 and 24 hours. In the 2-5 days band, there are relatively important peaks that would collapse to the 3 days peak if we had use more sections in the computation of the spectrum. If we look at the spectra at different seasons the results qualitatively similar being the only difference that, during winter, the inertial oscillations are more energetic.

The near inertial peak at 100m is clearly anticyclonic dominating the spectrum but when depth increases its relative importance decreases at the same time that it begins to polarize in the slope direction. We will talk about this point in section 2.6.

Concerning to the subinertial processes along the slope, it is interesting to note that their energy is aproximately the same at 300m than at 100m while in deeper levels (500m) it decreases outstandingly. This is coherent with the above mentioned idea that the two first current meters are inside the slope current and capture the barotropic variations of it while, at 500m, it just captures the current variability sometimes.

The peaks in the 2-6 days band could be associated to a same process which slightly varies its period along the year provoking that it presents different multiple peaks in the spectrum. In fact, the Northern current meandering is well known and Sammari et al. (1995) estimated that in the Ligurian sea the meandering has a 3-6 days period and a wavelength of 30-60km. In our case the meandering is present at different moments (see Fig 2. 5) even if they are much more energetic during the winter season. In consequence it is quite possible that the current meandering is the responsible of those peaks in the 2-6 days band.

The origin of those meanders has been traditionally explained with the baroclinic instability (Crépon et al., 1982; Sammari et al., 1995). Flexas et al. (2002) applied an analytical model of the Northern current in the Gulf of Lions, showed that the variability in the 6-7 days periods could be due to baroclinic instability. Their model limitations avoided to give more insight into the origin of the 3 days oscillations. More recent works using physical models (Flexas et al., 2004a) and numerical models (Flexas et al., 2004b) propose the shear barotropic instability as a possible cause for the current meandering with a period around 3.3-3.8 days and a wavelength of 50-75km.

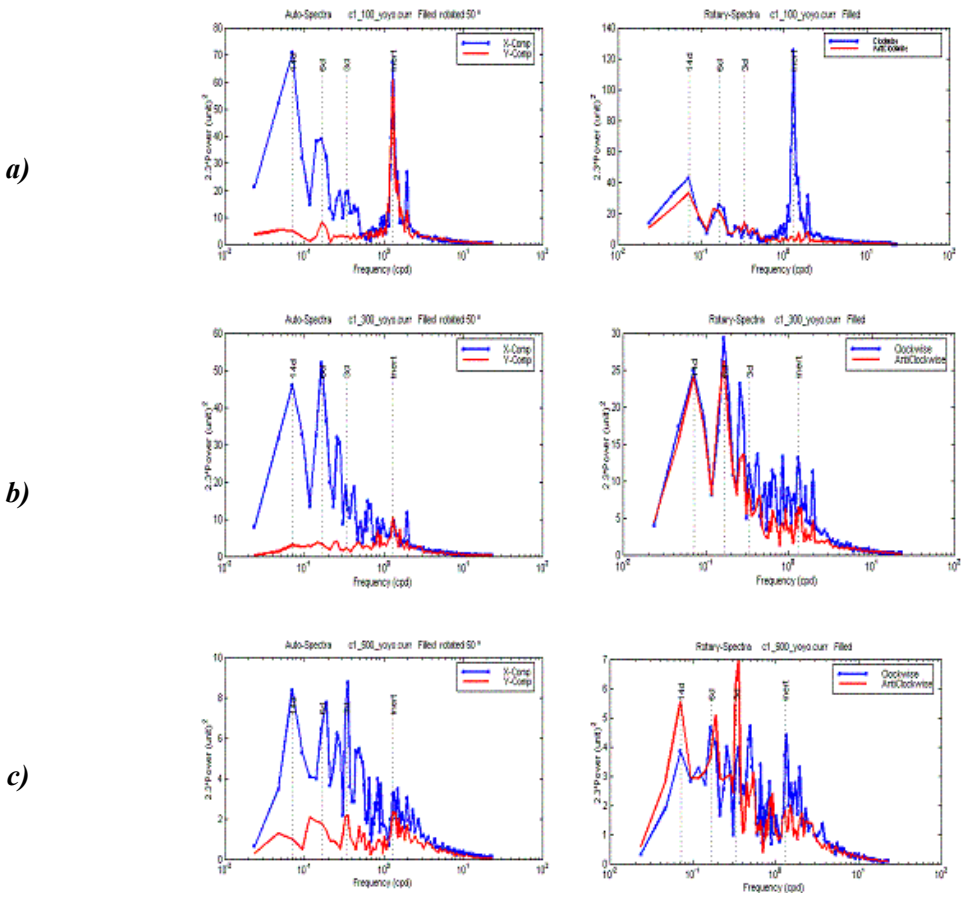

Fig 2. 12: Variance preserving energy spectra of the slope current at (a) 100m, (b) 300m and (c) 500m. Left: Alongslope (x-comp) and across-slope (y-comp). Right: Rotational spectra.

Another possible explanation for the 3days peak proposed by other authors (Millot, 1985; Sammari et al., 1995), is that it can be associated to a trapped topographic wave propagating along the slope. Palanqués et al. (2004), using a long-wave model, which includes friction and topography (Brink and Chapman, 1987), found that it could exist a topographic wave for a period around 3 days and a wavelength of 100km. In our case, the fact of finding the signal at all depths will inforce their hypothesis that it would not be a bottom trapped wave.

About the 14 days peak, Alberola and Millot (1995) found than for the Northern current near Nice, the energy found in the 10-20 days was dominant but they didn't propose any explanation. In our case, we have found a good correlation between these oscillations and the atmospheric pressure and we will come back to this issue in section 2.8.1.

Unfortunately, as we only have punctual information we cannot establish the wavelength and the horizontal structure of the oscillations, so we cannot advance further to find the origin of the subinertial variability measured during 1999.

2.4.2 Shelf

In the shelf, the variance ellipses present the same angle than the coast direction but they are much less elongated than over the slope (see Fig 2. 13). In other words, even if the topographic and coastline control over the current variability is evident, this control is less restrictive than over the slope and the movements appear less polarized. This is logical if we take into account that the topographic control over the dynamics depends on the bottom slope, which is much less important over the shelf than over the slope.

a) ***b)***

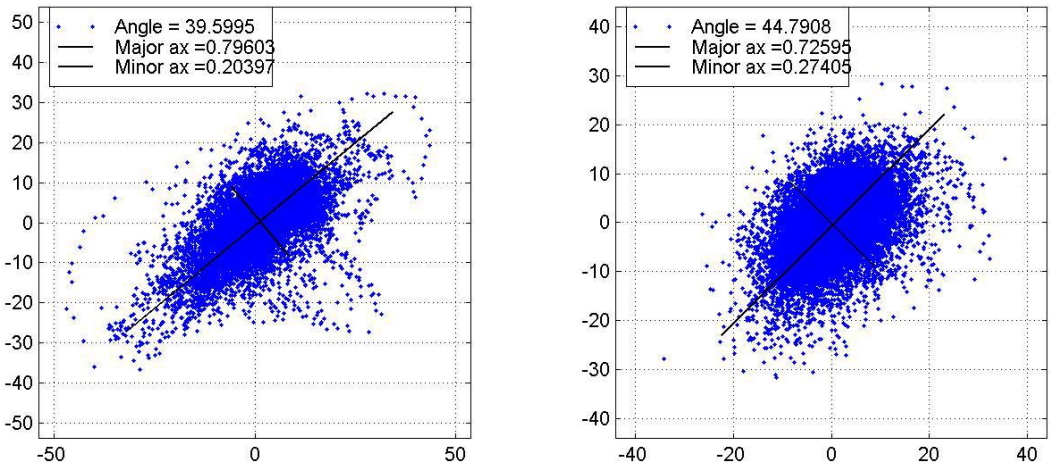

Fig 2. 13: Dispersion diagrams and variance ellipses axes for the different current meters over the shelf (a) 15m and (b) 55m.

If we look at the kinetic energy evolution along the year (see Fig 2. 9) there is no clear evidence of the winter intensification found over the slope. Far from it, it seems that energy during the winter period is reduced. What is probably happening is that along the year there is no process over the shelf with a seasonal signal that affects the current. On the other hand, the baroclinic character of the stratified season implies that energy coming from the wind stays in the shallower levels, producing the clear peaks of energy in the summer period.

As it has been done previously, we use the EOFs to characterize the statistical relations between different depths (see Fig 2. 10b). The modal structure can be interpreted as a barotropic mode and a baroclinic one which unlinks what is happening at different depths, both for alongcoast and across-shelf movements. The main interest of this analysis is to look at the time evolution of the explained variance of each mode along the year. It can be seen (Table 2. 2) that

the importance of the barotropic mode increases significatively during winter. If we look at the variance explained by this mode at each depth, we see that during the stratified season there is an important difference between 15m and 55m. This means that the movement in both layers is mainly unlinked. This situation changes during autumn and winter when the coordinate variability in the whole water column dominate

Barotropic Along-coast movements				
%	***Summer***	Autumn	Winter	Spring
Mode variance	64	77	80	64
Var. at 15m	93	80	60	97
Var. at 55m	21	73	91	8
Barotropic Across-shelf movements				
%	***Summer***	Autumn	Winter	Spring
Mode variance	65	67	70	74
Var. at 15m	80	98	58	99
Var. at 55m	24	9	80	2

Table 2. 2: Seasonal evolution of the percentage of explained variance by the barotropic mode over the shelf and at each depth.

Now, we compare the EOFs with the normal modes as it has been done with the slope data. We use the ADCP measurements obtained in the A2 position during winter 1997 to compute the EOFs and we compare them with the dynamical modes obtained from a typical density profile measured in the FANS winter campaign. In Fig 2. 14, it can be seen that the correspondence is as good as what was found over the slope. The barotropic mode represents a 60% of the shelf variability while the first baroclinic mode represents a 25%. The following modes have a minor importance being never over the 6%.

The spectral analysis of the velocity time series over the shelf (see Fig 2. 15) shows a dominance of the anticyclonic inertial band with a secondary peak at 1 day. These peaks are probably induce by the wind, as it will be shown in section 2.8.2. On the other hand, there is also a peak at 3 days which has special importance in the bottom velocities. These oscillations are specially important during autumn and the beginning of the summer period, while during the winter period they are not too much significative. Another peak in the 6-7 days band is also specially intense during autumn.

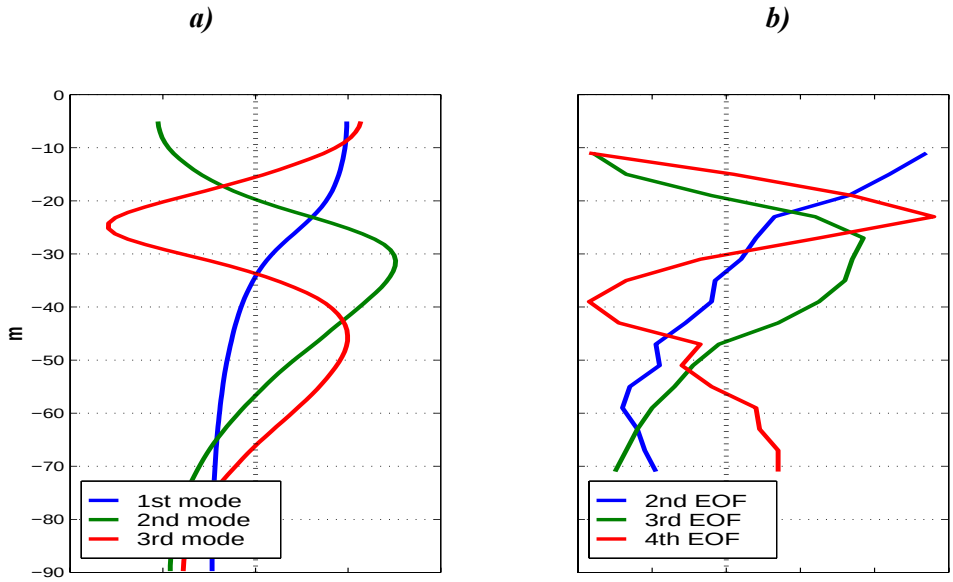

Fig 2. 14: Comparison of the vertical structure of the first (a) normal modes and (b) the empirical modes (EOFs) computed over the shelf in the A2 position from data obtained during winter 1997. The explained variance by the first EOF (not shown) is 60%, the second is 25 %, the third 6% and the fourth 4%.

The origin of those peaks are not too clear but they are maybe linked with the slope current. It is not illogical to think that through the shelf widening, where the separation between the shelf and the slope is reduced (see Fig 2. 1), the oscillations of the slope current could affect the shelf circulation. If we compare the shelf and slope currents filtered in the 2-7 days band, we find some agreement in certain periods but it is not a general behaviour. Unfortunately, the data distribution and its time coverage is not enough to go further with this hypothesis.

Finally, the 12-15 days peak it is not linked to any oscillation but to a concrete event in mid-November. It is a sudden evolution of the current which passes from a near-rest state to a southwesward current of 30cm/s. This event is not linked to the wind or the river runoff, so it is reasonable to think that it is due to the slope current but again we have not enough data to confirm this.

a)

b)

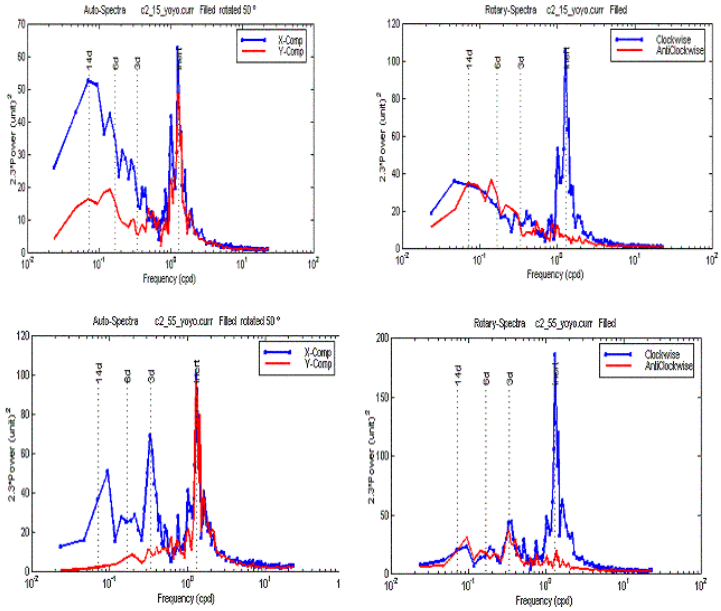

Fig 2. 15: Variance preserving energy spectra of currents over the shelf at (a) 15m and (b) 55m. Left: Alongcoast (x-comp) and across-shelf (y-comp). Right: Rotational spectra.

2.5 Water masses evolution

During the YOYO and FANS projects, the moorings were equipped with thermistors which provide a continuous measure of the water temperature at different depths. Even if we do not have salinity measurements which could allow to precisely define the water masses, we can obtain interesting information about their evolution along the year and in special events.

To complement the temperature measurements and to put them in the context of the water mass distribution in the region, we look at the temperature and salinity profiles from the FANS CTD campaigns (see Fig 2. 16). Altough these campaigns are not contemporary to the thermistor measurements, they are representative enough of the water mass distribution along the year in the region. An in-depth explanation of these campaigns is presented in Salat et al. (2002).

The water column structure can be understood as a three-layers system (Salat and Cruzado, 1981) with a shallow layer until 150-300m, an intermediate layer until 600-800m and a deep layer reaching the bottom. The last layer is formed by WMDW (Winter Mediterranean Deep Water) with a potential temperature (θ) between 12.7-12.9 ºC and salinity (S) between 38.42-38.46 psu. The intermediate layer is occupied by LIW (Levantine Intermediate Water), which is characterized by a relative maximum in temperature and salinity. In our region it can be traced by θ= 13.0-13.4 ºC and S=38.48-38.54 psu. Finally, the surface layer is the most variable one because it is where the thermocline is found as well as the contribution of the continental and

atmospheric fresh water. This layer is occupied by waters with Atlantic origin, which suffered different mixing processes along its path in the western Mediterranean basin. Waters formed by winter convection in the North-Western Mediterranean shelves, the WIW (winter intermediate waters), occupy the deeper part of the surface layer and can be identified by low temperatures and salinities (θ= 12.5-12.8 ºC and S=38.1-38.3 psu). Waters of Atlantic origin can also be found in the interior of the basin, which are saltier and warmer, and waters of the same origin over the continental shelf with lower salinities due to the effect of continental contributions. Finally, in the shallower layers, waters with very low salinities (S<37.5) directly influenced by the Ebre river are also present.

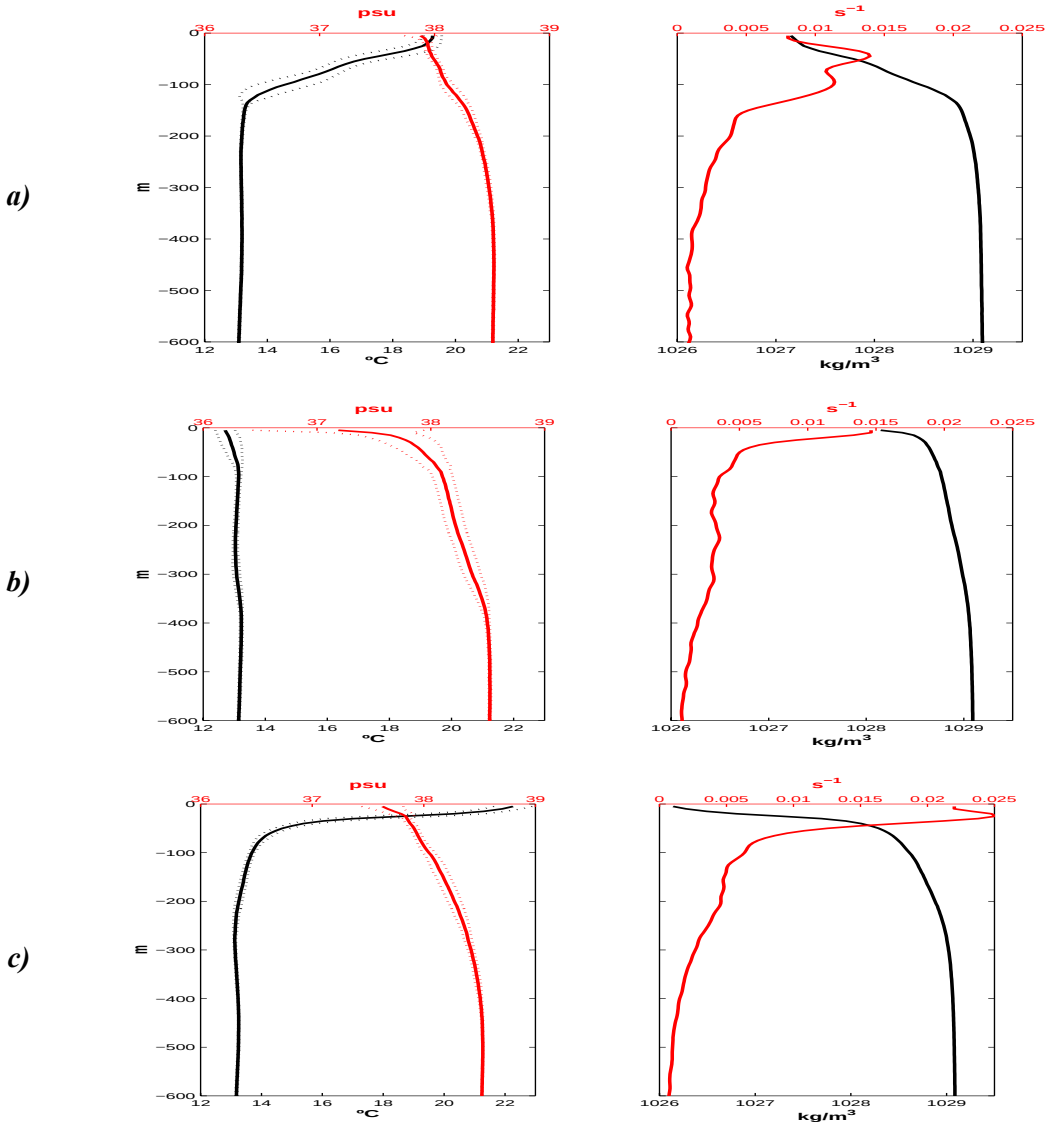

Fig 2. 16 : Average profiles of potential temperature and salinity (left) and density and buoyancy (right) for the different CTD campaigns. (a) FANS I- autumn 96 (b) FANS II-winter 97 and (c) FANS III - summer 97. The dotted lines indicate the dispersion limits of the profiles.

2.5.1 Slope

The FANS and YOYO temperature time series, at 100,300 and 500m, allow seeing the evolution of the thermal vertical structure for a period of near three years (see Fig 2. 17). The fact that the first measurement is at 100m implies that the seasonal variability in the shallower levels cannot be captured but nevertheless they provide new information about the evolution of water masses in the deep layers.

At 100m, we are placed in the deeper part of the surface layer commented above but the seasonal effects are hardly captured. The mean temperature is 13.5 $\pm$ 0.7 ºC and it seems that this depth is in the limit between the surface waters and the Levantine waters, so depending on the period, a different water mass is measured. During the winter months the temperature shows an increase due to the seasonal homogeneization linked to the current acceleration. The magnitude of this increase depends on the year (see the difference between 1997 and 1998). At 300m we are well placed in the LIW layer, so the temperature becomes more constant with a values range of 13.25 $\pm$ 0.15 ºC. Finally, at 500m, the Levantine waters are also measured with a mean value of 13.25ºC but with lower variations than at 300m.

Concerning to the correlations between different levels, it seems that there is no great relation between different depths except in punctual moments. The variability at 100m is induced by processes that do not affect the deeper levels, especially when what is measured are the surface waters (SW). In the periods when the shallower level is occupied by Levantine waters (from January), it seems that there is a good correlation until 300m but still unlinked with the deepest levels, which needs some weeks to follow the tendence. This can be explained if we think that there is an advection of Levantine water from the north, probably from the Gulf of Lions region: Currents at 100m and 300m have a comparable intensity and the advected waters reach simultaneously the measurement point while the low velocities in the deepest level imply a delay of several weeks at it has been observed. Afterwards, this water occupies the whole water column between 100 and 500m and behaves in a more or less homogeneous way. Finally, in march 1999; there is a sudden decrease of the temperatures at all levels, which will be commented later on.

If we look carefully to the time series, we find that between August and October, at 500m there are temperature oscillations with an amplitude of ~0.2ºC and a period of 20-25 days that seem linked to deep current oscillations and which are decorrelated from what happens in shallower levels. These temperature oscillations are probably due to the fact that current advects Levantine waters from the interior of the basin to the slope. This water is "younger" than waters over the slope, so slightly warmer because they have not interacted with the adjacent waters. The reason why these oscillations are found at 500m and not at 300m is maybe because an

oscillation of the density front is being captured in depth. As this front (with the corresponding temperature gradient associated) is tilted in the vertical, it is possible that it is nearer the measurement point near the bottom than in the intermediate level, so the current variations would be more noticed in the temperature measurements at 500m than at 300m.

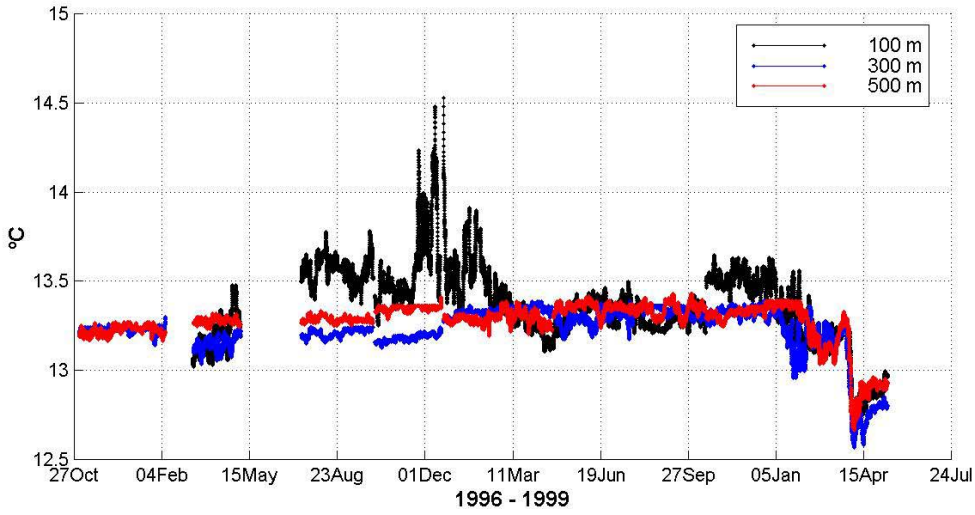

Fig 2. 17: Time evolution of temperatures over the slope (C1) at different depths between October 1996 and June 1997.

A clearer image of the temperature variability can be obtained combining the available temperature measurements with the measurements obtained by the thermistors chain between 100-200m between October 98 and May 99, and comparing them with the 100m velocities (see Fig 2. 18). The first thing that can be observed is that the warmer surface waters (SW) occupy the first 150m and then they gradually disappear leaving the place to the Levantine intermediate waters which are already occupying the deeper levels. Near the day 1120, there is a relative minimum of temperature (T<13º) centered at 300m depth which lasts for 30 days and which can be associated to the passage of a winter intermediate water (WIW) generated in the north. At the end of the period, the sudden temperature decrease at all levels is also evident showing a minimum near 300m. These two last observations, suggest that the WIW generated over the shelf in the north flows towards the southwest centered at a depth of 300m where its buoyancy must equilibrate with the surroundings.

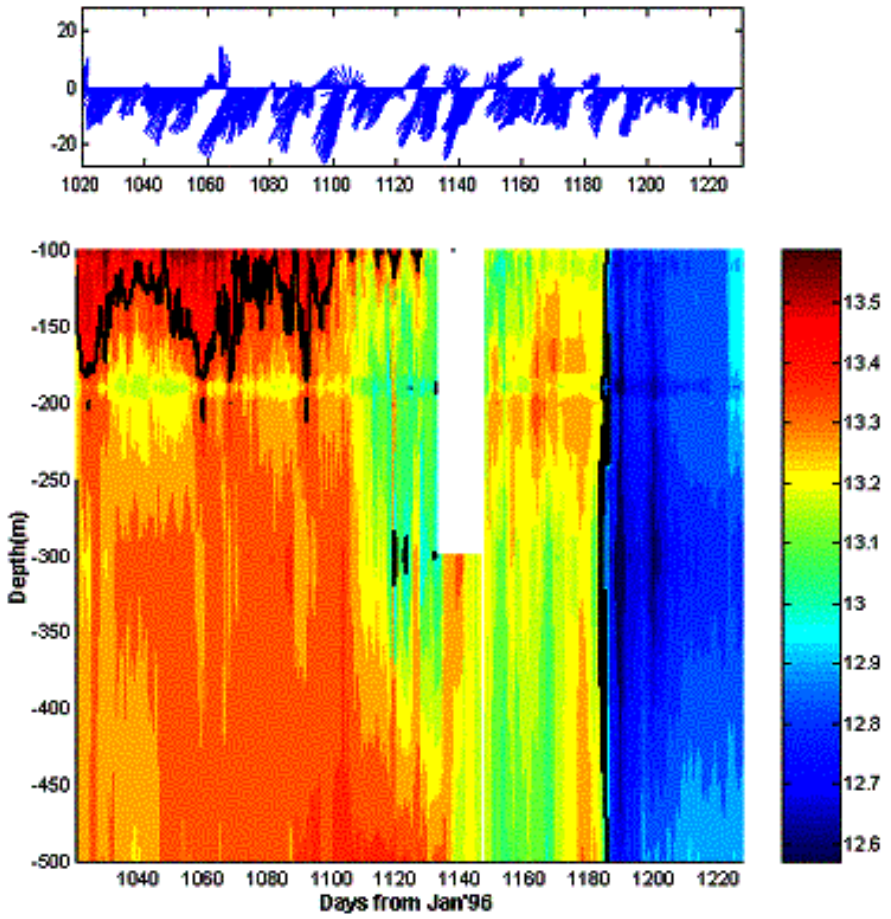

Fig 2. 18: Comparison of 100m velocities (top) and temperature distribution between 100 and 500m (bottom) measured over the slope. The black lines limit the water masses as they have been defined in the text.

On the other hand, it must be noted that in the levels where the interface between Levantine intermediate waters and the surface waters is placed, current oscillations provoke important temperature changes. For instance, during the period between days 1105-1130, there are some current oscillations with a 5 day period that induce temperature variations of around 0.3ºC and until 200m depth. These fast changes would be probably more important in the shallower levels, as far as the temperature gradients associated to the slope front are more important there, but we can't confirm this due to the lack of data.

Finally, we comment the sudden presence of winter intermediate waters at the end of the period because it is uncommon the great quantity of WIW which reaches the region and the velocity at which this is done. Between the 26 March and 6 April (days 1180-1190 in figure), the temperatures suddenly decreased 0.6ºC simultaneously between 100 and 500m. This is a

variation much more important than all the other variations observed during the FANS and YOYO period and corresponds to the arrival of WIW advected from the North. It is also interesting to note that the current inertial oscillations in the moment of the temperature decrease induce temperature oscillations of 0.2ºC in just 9 hours. The simmetry of the temperature peaks suggests that the WIW mass is advected in a wedge shape centered over the slope.

To understand the origin of this situation it is needed to place in the hydrodinamic context of the Balear Sea during winter 1999. Pascual et al. (2002) found than in September 1998 an intense anticyclonic eddy was generated in the northern part of the Balear Sea, between Barcelona and Menorca (see Fig 2. 36c). This structure stayed until March 1999, and it is believed that during that period it bloked the water transport from the Gulf of Lions to the Eivissa channel. During the life of the eddy, the measurements in the south, in position C1 at 100m depth, don't show any significative variation neither of the current nor of the temperature. This is not in contradiction with the bloking hypothesis as far as the current can be maintained by the local geostrophical equilibrium.

On the other hand, the Catalan continental shelf in the north of Barcelona is a favourable place to generate winter intermediate waters due to the cooling and convection of dense waters. Usually, the waters generated by this process are advected downstream, as it is done with the waters generated in the Gulf of Lions, but the eddy bloking prevent them to leave the generation place.

The winter 1999 was especially strong and an important quantity of intermediate waters was generated in the Gulf of Lions (Béthoux et al., 2002), so it is expected that the same thing happened in the Catalan shelf. On the other hand, due to the eddy bloking, this water mass didn't displace and was accumulated during the winter months over the shelf. When the eddy dissipated in March, the current circuit was restablished and the cold waters accumulated began to be advected southwards. Looking at a chlorophyll SeaWifs images for the 3 March (see Fig 2. 19) it can be observed the signal of the eddy but also the high chlorophyll concentration in the northern part of the Catalan coast. This concentration gives an indication of the shelf origin of those waters reinforcing the hypothesis of the accumulation of waters over the shelf during the bloking period.

An idea of the vertical structure of this water mass is found comparing the temperature and salinity profiles in the core of the eddy before and after the strong storms which induced the eddy displacement (see figure 14 of Pascual et al.; 2002). In those profiles it can be observed how, in just 10 days, the profile suddenly changes being completely homogeneous between 150 and 1000m. This change is too abrupt in the whole water column to be generated in few days and it is more probable that it was due to an accumulation of WIW, which is suddenly released.

On the other hand, if we consider than the current velocity is about 15-20cm/s, and we consider than the bloking is dissipated the last days of February, the advection time of the intermediate waters from its generation place (north of Barcelona) until the measurement point is about 25-30 days, which coincides with the fact that the temperature decreasing is observed the 26 March.

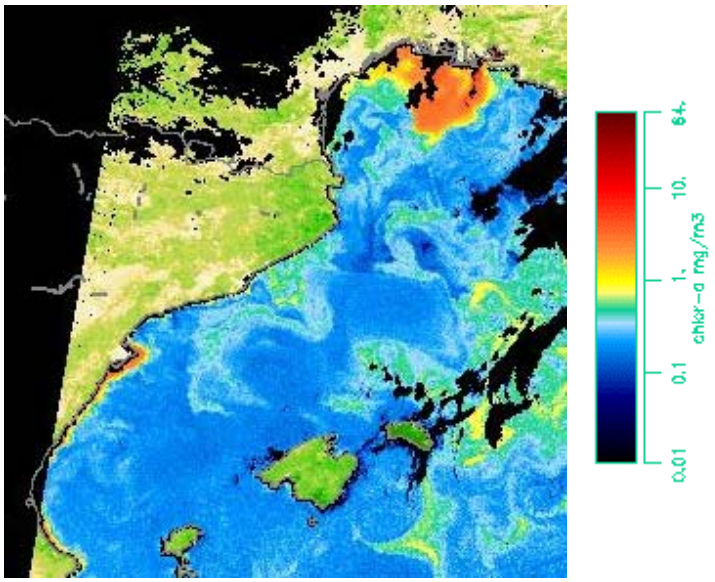

Fig 2. 19 : Chlorophyll SeaWifs image for 3 March 1999

2.5.2 Shelf

Over the shelf, the predominant water mass is what was previously defined as surface waters (modified Atlantic waters), much more affected by the continental contributions of fresh water. The sea surface temperature satellite images during the winter period show a clear distinction between shelf and slope in terms of temperature differences. This is due to the fact that over the shelf the heat fluxes effect is inforced because the water column height is smaller than in the open sea (i.e. there is less water to be cooled). In addition to that the residence time of waters is greater so they have more time to be cooled than in the open sea. During the summer period, the SST images are not reliable to track the water masses as the superficial warming masks the evolution of what is happening in depth.

The seasonal evolution of the stratification is quite clear looking at the temperature time series (see Fig 2.). Near the end of summer, the shallower layer (15m) reaches a maximum temperature of 26ºC and an important temperature gradient ($\Delta T \sim 12$ºC) between surface and

bottom is established. Afterwards, the surface waters begin to cool and, the first days of November, a temperature increase near the bottom can be felt due to the winter homogenization. In December, the entire water column is homogenized and the cooling continues at all depths until reaching a minimum of 12-13ºC in February. It is interesting to note than the mixing process takes place in just 10 days (15-25 November).

The general tendency of the temperature is the result of the heat fluxes where some punctual modifications induced by the hydrodynamics are overimposed. One of these modifications takes place in September 17th, where the temperature varies 0.5ºC in 24 hours due to a current intensity peak of 50cm/s induced by the wind. Other examples as this one are easily found along all the period and, doing and approximate calculation, we can conclude that wind bursts of 0.1 N/m^2 induce temperature variations of 1ºC in 2-3 days. The temperature variations have a phase lag of about 20 hours, which coincides with f^{-1}, the inertial response time. These effects in depth are more evident during the periods where the water column is more homogeneous while in the stratified periods they are hardly felt

About the river influence, it must be said that the available measurements, which begin at 15m depth, are out of the region of fresh water influence, the ROFI area (see Naudin et al., 2002), so it is logical than we don't see a clear relation between temperature and variations of the river runoff.

a)

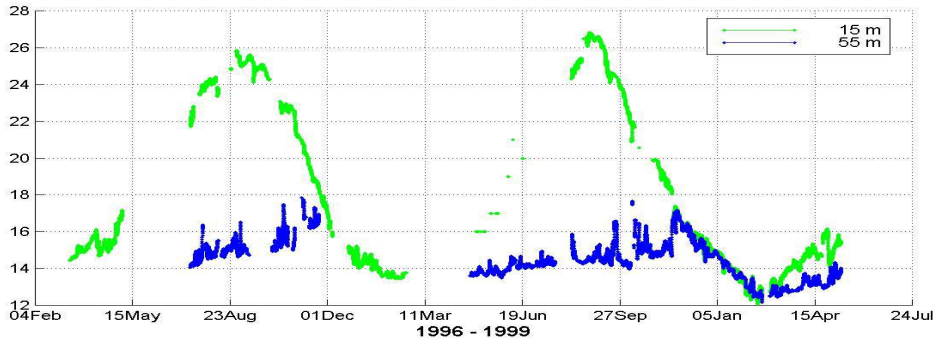

b)

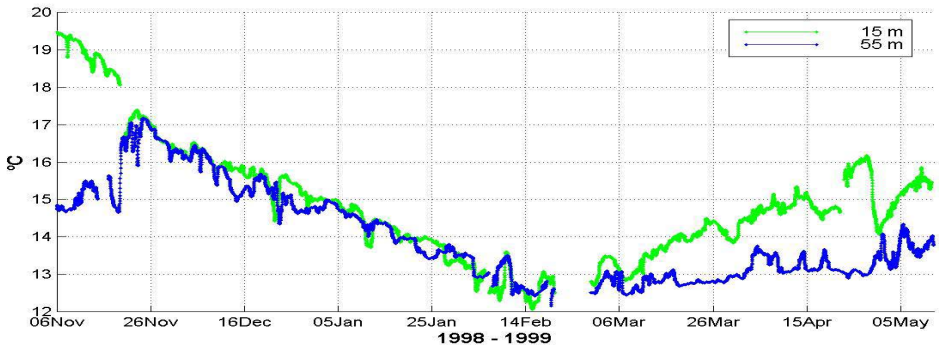

Fig 2. 20: Time evolution of temperatures over the shelf (C2) at different depths between (a) October 1996 and June 1999 (b) Zoom for the YOYO period.

2.6 High frequency current variability

2.6.1 Slope

As it was shown in section 2.4.1, the current variability over the slope has a dominant component near the inertial frequency. The first thing that seems interesting is that this energy peak doesn't change significatively along the year and it is placed at 18.4 hours, the local inertial period. This means that the current meters are not located in a region with a significative vorticity, which could change the effective inertial period, which is defined after Mooers (1975) as:

$$f_{eff}^2 = f\left(f + V_x\right) \qquad \textbf{(2.3)}$$

In consequence we can consider than the measurements were obtained in the core of the slope current where the relative vorticity is minimum.

The filtered series for periods lower than 28 hours (see Fig 2. 21) show that the near inertial currents at 100m depth have velocities around 3-5cm/s reaching a maximum of 5-10cm/s. At 300m, the mean values are about 2-4cm/s reaching a maximum of 5-7cm/s. At 500m, the currents at the inertial period are rarely perceived except in punctual moments where they reach 5cm/s.

Salat et al. (1992) studied the near-inertial movements in the same region and found that the wind was at the origin of these movements and that these represented between 35% and 54% of the energy spectra between 100 and 15m, respectively. It has been often suggested in the literature (Kroll, 1975; Maas, 2001) than most of the energy near the inertial frequency is transported between the surface and the deeper levels through internal waves. In our case we are interested into see if the wind effect can be felt until 100-500m and in which conditions.

If we look to the filtered series and we compare them with the wind (see Fig 2. 21), we see that there is certain relation between the increase of inertial oscillations at 100m and the wind altough in most cases there is not a clear response. The cases where a good relation is found are present when an isolated wind peak is produced (i.e. 20 Dec). Doing a gross estimation we find that the energy is transferred from surface to deeper layers with a velocity of 100m/day, which more or less coincides with the 0.2cm/s estimated by Salat et al. (1992).

Except in these situations it is difficult to find a significative correlation between the inertial oscillations at different depths. This is maybe because the mechanism of energy transfer is not always the same (different stratifications or the passage of water masses that modify the energy propagation), and thus the correlations between depths are altered, or just simply because what

is being measured correspond to different processes. To deepen into this is quite complicated with the available vertical resolution.

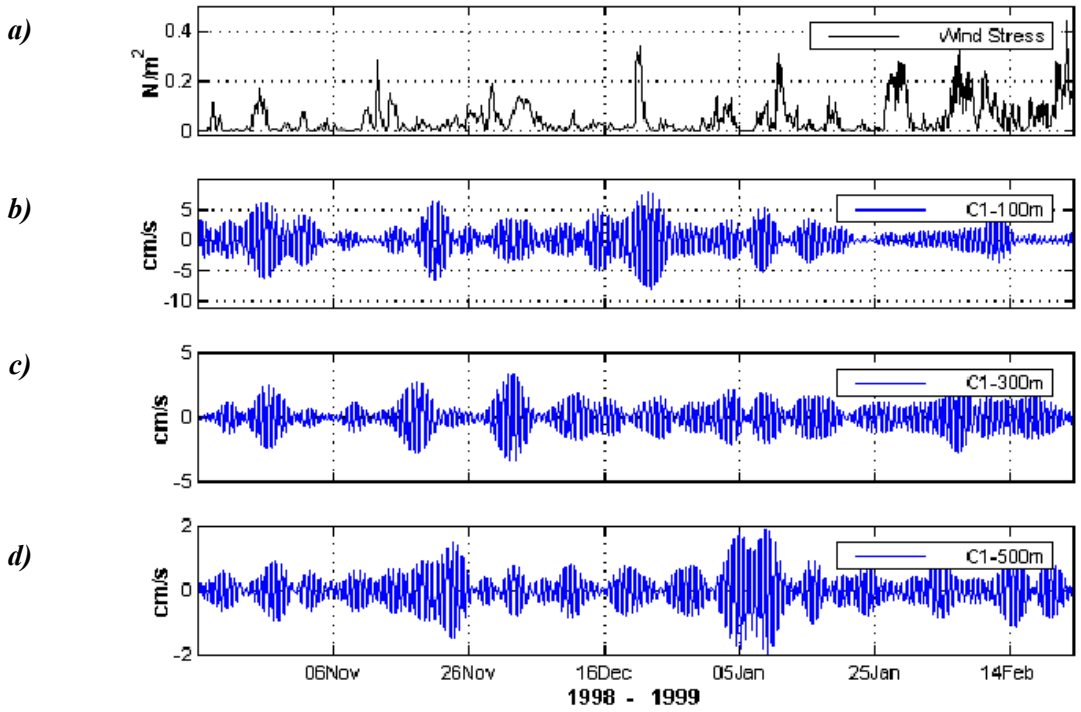

Fig 2. 21 : Temporal series of (a) wind and currents filtered around the inertial period over the slope at (b)100m (c)300m and (c)500m

Another point that should be considered is that as depth increases, the inertial oscillations loss their clear anticyclonic behaviour. In order to objectively quantify this, we can define the rotation coefficient as $C_R = (S_+ - S_-)/(S_+ + S_-)$ where S_+ and S_- are, respectively, the anticyclonic and cyclonic rotational spectra (see Fig 2. 15). This coefficient will give a value of 1 for the perfectly anticyclonic oscillations and 0 for the random movements or the perfectly rectilinear oscillations. Doing the calculation for different measurements over the slope, we find that at 100m the rotational coefficient is near 0.95, at 300m is 0.5 and at 500m it is just 0.3.

The reason of this polarization in depth could be explained because the across shelf movements are more inhibited in deeper levels. In other words, being nearer the bottom the topographic effect over the dynamics would more noticeable. In this case, the oscillations at the inertial period would be polarized along the slope. This hypothesis is reinforced by the fact that

the oscillations associated to the M2 tide component (12 hours) are also polarized in depth in a similar way (see below).

Another possibility can be suggested after looking at the hodographs of the velocity time series filtered near the inertial frequency (see Fig 2. 22). It can be seen how, as the depth increases, the oscillation are less circular becoming more elongated. Recently van Haren and Millot (2003) identified as gyroscopic oscillations the oscillations measured in the near-inertial band in regions with low stratification in the NorthWestern Mediterranean.

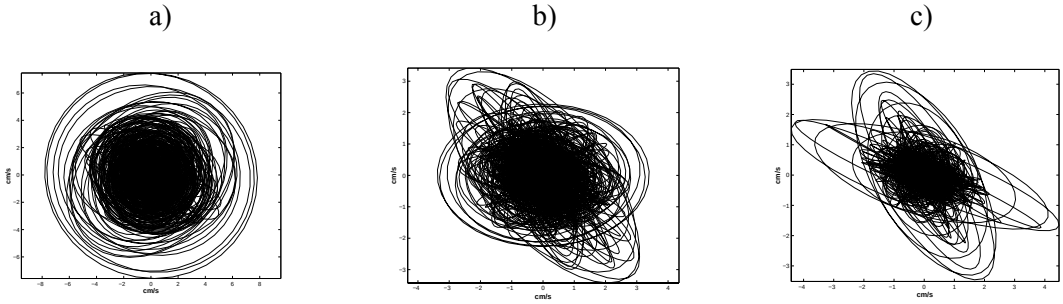

Fig 2. 22: Hodographs of the currents in the near inertial band over the slope at (b) 100m (c) 300m and (c) 500m.

When the stratification becomes weak (Brunt-Väisala frequency (N) comparable to f or less), the classic formulation for the internal waves where the hydrostatic approximation is done is insufficient. If the complete equations are used, an expression for the maximum and minimum limits of the inertio-internal and inertio-gravitational waves is obtained (LeBlond and Mysak, 1978):

$$\begin{aligned} \nu &= \arctan(\sin 2\varphi / (\cos 2\varphi + (N/2\Omega)^2))/2 \\ \sigma_{low} &= 2\Omega(\sin^2\varphi\cos^2\nu - (\sin 2\varphi \sin 2\nu)/2 + (\cos^2\varphi + (N/2\Omega)^2\sin^2\nu)^{0.5} \\ \sigma_{high} &= 2\Omega(\sin^2\varphi\sin^2\nu - (\sin 2\varphi \sin 2\nu)/2 + (\cos^2\varphi + (N/2\Omega)^2\cos^2\nu)^{0.5} \end{aligned} \qquad \textbf{(2.4)}$$

where Ω is the earth rotation, φ the latitude and ν the angle between the wave vector perpendicular to the oscillation plane of the internal waves and the gravity ($\nu = \widehat{(g, k_3)}$). If N $\rightarrow$0 the rotation plane is no longer perpendicular to g and the projection of the circular oscillations over the horizontal plane has an elliptical shape. In other words, when $\nu \rightarrow 90^o$ what is measured by the current meters (which measure in the horizontal plane) tends to have a rectilinear behaviour. In normal stratification conditions as during the FANS periods (see Fig 2. 16) ν is near 0, so we wouldn't expect to find this kind of waves. On the other hand what can be

happening is that in certain moments just a part of the water column can be homogenized with N becoming weaker. An example of this situation could be the passage of WIW cores where the water is quite homogeneous therein. In fact, if we look at the hodographs at different moments during the year, we find that the near-inertial oscillations have a very elongated elliptical shape in certain cases. These cases coincide with the moments identified in section 2.5 where temperature between different levels converges to a same value, denoting a homogeneization of part of the water column.

It is also interesting to note that this kind of oscillations are very effective in the vertical mixing processes because they present circular movements in inclinated planes respect to the vertical, so inducing significative vertical movements that will enhance the mixing.

For frequencies higher than the inertial period, what we find is the typical spectrum of free internal waves. Garret and Munk (1972) proposed that for the internal wave band $f << \sigma << N$, the free wave spectrum should be $P(\sigma) \sim N \sigma^{p}$, where $-2.5<p<-1.5$. As it can be seen in Fig 2. 23 the spectra at all depths are in the limits proposed by them, so it seems that the high frequencies are dominated by the free internal waves.

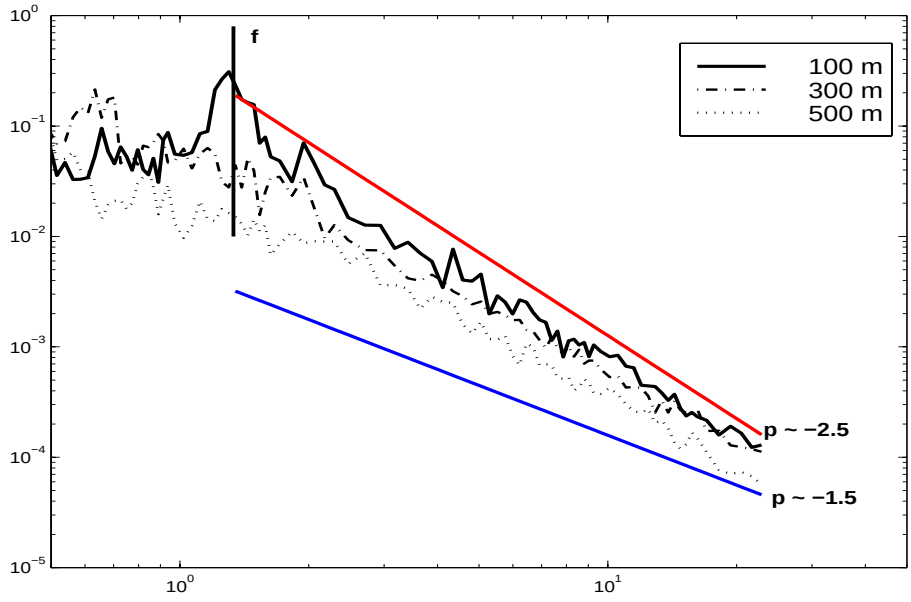

Fig 2. 23: Zoom of the energy spectra for the high frequencies with the Garret and Munk adjustment overimposed.

Finally, to finish with this section, we will look at the tidal signal over the currents. Traditionally it has been considered than the region has a microtidal regime and it is usual to

neglect their importance. Nevertheless, in order to have a complete overview of processes in the region, we are interested into quantify this concept and to see the contribution of the tides over the velocity. To do that we perform a harmonic analysis of the current series to identify the phase and amplitude of the principal tidal components with a well-known period. If we represent the effect of the tidal wave over the velocity as $v_{tide} = A\sin(wt+\varphi)$ where w is the frequency number and t is the time. This velocity is completely described by the amplitude A and the phase φ . The analysis looks for the amplitudes and phases combinations that best adjust to the complete set of data for a set of 75 different tide components. A summary of the results for the most significative components at high frequencies can be found in Table 2. 3. This analysis is very precise and useful for the high frequencies because we have a long enough time series that allows us to distinguish very close peaks as P1, S1 or K1, which have periods of 24.07h, 24.0h and 23.93h respectively.

As it was expected, the associated velocities to the tides are quite low being never greater than several mm/s. Even when all the tide components are combined they have a significative effect as it is observed in Fig 2. 24 where we have overimposed the 66 high frequency tide components (T< 28h) over the current in the slope and the shelf.

a)

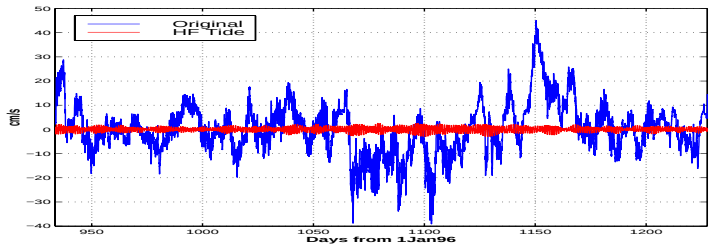

b)

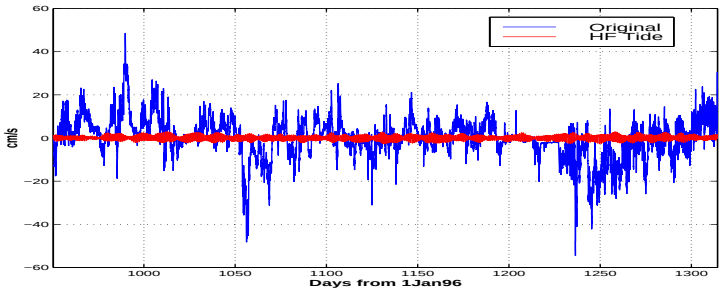

Fig 2. 24: Tide currents overimposed to the total current for the (a) alongslope currents at 100m and (b) the alongcoast currents over the shelf at 15m.

Along slope/Along coast component

Wave	Period (hours)	*C1 100m*		*C1 300m*		*C1 500m*		*C2 15m*		*C2 55m*	
		Amp(cm/s)	*Phase(º)*	*Amp(cm/s)*	*Phase(º)*	*Amp(cm/s)*	*Phase (º)*	*Amp(cm/s)*	*Phase (º)*	*Amp(cm/s)*	*Phase (º)*
Sig1	*27,85*	*0,19*	*197,04*	*0,32*	*217,76*	*0,07*	*165,36*	*0,18*	*359,39*	*0,21*	*97,66*
Q1	*26,87*	*0,25*	*177,05*	*0,21*	*303,76*	*0,05*	*22,92*	*0,12*	*71,12*	*0,11*	*341,01*
Ro1	*26,72*	*0,25*	*336,21*	*0,19*	*122,02*	*0,07*	*75,08*	*0,07*	*233,1*	*0,25*	*293,05*
P1	*24,07*	*0,29*	*323,37*	*0,12*	*26,85*	*0,07*	*349,6*	*0,68*	*241,38*	*0,33*	*32,19*
S1	*24*	*0,34*	*206,82*	*0,26*	*246,58*	*0,06*	*235,47*	*0,49*	*99,36*	*0,79*	*179,8*
K1	*23,93*	*0,16*	*50,85*	*0,15*	*105,29*	*0,05*	*37,43*	*0,59*	*235,9*	*0,38*	*145,3*
Tta1	*23,21*	*0,21*	*40,83*	*0,12*	*83,91*	*0,05*	*252,39*	*0,07*	*131,41*	*0,09*	*22,36*
OO1	*22,31*	*0,19*	*77,8*	*0,24*	*206,7*	*0,12*	*150,57*	*0,48*	*315,42*	*0,85*	*58,71*
KQ1	*21,58*	*0,31*	*252,92*	*0,04*	*69,07*	*0,05*	*76,98*	*0,43*	*23,34*	*0,07*	*101,86*
OQ2	*13,17*	*0,23*	*19,99*	*0,13*	*310,65*	*0,06*	*141,2*	*0,1*	*180,3*	*0,23*	*0,54*
N2	*12,66*	*0,16*	*90,04*	*0,07*	*165,82*	*0,07*	*116,66*	*0,07*	*91,59*	*0,17*	*129,79*
MSK2	*12,46*	*0,35*	*297,64*	*0,1*	*131*	*0,09*	*149,09*	*0,19*	*44,84*	*0,12*	*49,49*
M2	*12,42*	*0,79*	*127,04*	*0,57*	*161,18*	*0,15*	*142,6*	*0,32*	*121,38*	*0,69*	*133,69*
S2	*12*	*0,17*	*165,45*	*0,1*	*185,44*	*0,05*	*207,31*	*0,24*	*179,27*	*0,23*	*151,12*
K2	*11,97*	*0,28*	*127,95*	*0,05*	*249,33*	*0,02*	*158,07*	*0,14*	*100,98*	*0,18*	*235,81*

Across slope/ across shelf component

Sig1	*27,85*	*0,03*	*192,41*	*0,21*	*74,92*	*0,04*	*326,43*	*0,2*	*232,71*	*0,14*	*17,12*
Q1	*26,87*	*0,18*	*81,67*	*0,04*	*60,74*	*0,06*	*205,71*	*0,04*	*280,67*	*0,19*	*180,35*
Ro1	*26,72*	*0,12*	*219,32*	*0,07*	*165,65*	*0,03*	*225,67*	*0,21*	*84,86*	*0,14*	*343,24*
P1	*24,07*	*0,1*	*189*	*0,17*	*296,36*	*0,04*	*220,48*	*0,33*	*152,79*	*0,13*	*99,89*
S1	*24*	*0,33*	*95,59*	*0,06*	*91,12*	*0,05*	*111,26*	*0,49*	*293,61*	*0,87*	*144,16*
K1	*23,93*	*0,09*	*23,52*	*0,1*	*297,14*	*0,06*	*254,25*	*0,24*	*137,73*	*0,18*	*141,53*
Tta1	*23,21*	*0,13*	*219,84*	*0,12*	*275,45*	*0,02*	*4,4*	*0,07*	*151,74*	*0,07*	*340,5*
OO1	*22,31*	*0,35*	*336,87*	*0,09*	*0,11*	*0,04*	*335,5*	*0,13*	*226,39*	*0,32*	*353,06*
KQ1	*21,58*	*0,28*	*156,35*	*0,06*	*266,01*	*0,03*	*125,37*	*0,2*	*345,62*	*0,17*	*336,38*
OQ2	*13,17*	*0,06*	*163,34*	*0,13*	*150,91*	*0,04*	*10,3*	*0,14*	*57,17*	*0,3*	*292,18*
N2	*12,66*	*0,08*	*142,55*	*0,02*	*154,53*	*0,03*	*17,19*	*0,04*	*156,31*	*0,09*	*108,57*
MSK2	*12,46*	*0,13*	*213,6*	*0,15*	*45,12*	*0,06*	*105,22*	*0,16*	*349,37*	*0,12*	*309,47*
M2	*12,42*	*0,14*	*336,8*	*0,12*	*61,2*	*0,11*	*349,93*	*0,09*	*317,9*	*0,15*	*94,54*
S2	*12*	*0,05*	*225,12*	*0,08*	*0,15*	*0,03*	*234,95*	*0,19*	*142,24*	*0,06*	*323,6*
K2	*11,97*	*0,15*	*27,57*	*0,05*	*67,16*	*0,05*	*238,04*	*0,18*	*308,57*	*0,25*	*158,43*

Table 2. 3: Phase and amplitude of the most significative tide components for the YOYO curren meters over the slope (C1) and over the shelf (C2). The low frequency components (T>28hores) are not included.

2.6.2 Shelf

The energy spectra over the shelf shows a dominant peak near the inertial frequency (see Fig 2. 15). This peak is linked to the anticyclonic oscillations induced by wind bursts. The inertial velocities are around 4-5cm/s reaching 8-10cm/s both near the surface and the bottom (see Fig 2. 25). It is interesting to notice that the velocities at 55m are often higher that near the surface and they are not always linked to a 15m signal. It must be noted that Gjevik and Moe (2002) computed the period of the barotropic shelf waves for this region and found that it is around 20-22 hours, so they could be mistoken with what is observed in the near-inertial frequency.

Rippeth et al. (2002) studied the inertial oscillations and at the diurnal period with ADCP measurements in the same region during the spring of 1997. These authors showed from observations and analytical models that the energy provided by the wind is transferred from surface to the bottom and that there is a phase lag between both layers of 180º. This phase difference is sudden in the pycnocline and can be interpreted as the result of the zero-flux in the coast, which would induce a current inversion. They also evidenced that the oscillations become more energetics further from the coast and they interpreted this as the result of the stronger winds in the open sea.

We can also look to the river runoff and compare it with the near-inertial currents. The highs of the Ebre river don't seem to be directly responsibles of the current oscillations but it seems that they affect the sea response to the wind. Between December and April there was a significative increase of the river runoff passing from 100 m^3/s to 400 m^3/s. During this period the response to the wind bursts is very damped in comparison to the rest of the year: even if the winds are stronger, the inertial oscillations are reduced to the half. Font et al. (1995) showed that there was a seasonal maximum of energy in the near inertial band at the end of spring and in summer, which coincides with our observations where we consider than in winter there is a decrease of the energy in that band.

The explanation for this energy decrease during winter can be linked to the increase of river runoff as the measurement point is in the ROFI area. Even if the Ebre plume doesn't reach the 15m depth where the current meter is placed, in surface it reachs the mooring position. So, it could be imagined that in some way, the fresh water input from the river increases the stratification generating a shallow pycnocline which would difficult the energy transfer from surface to the deeper layers.

Another possible explanation is that the increase of the river runoff and the decrease of the velocities coincide with the seasonal homogeneization. The fact that the water column is homogeneous implies that the sea adjusts to the sea as a unique layer behaving as a 2D system.

In this configuration, it can be thought that the wind has more difficulties to induce the movement over the whole water column than in a stratified period and bottom friction plays a more important role.

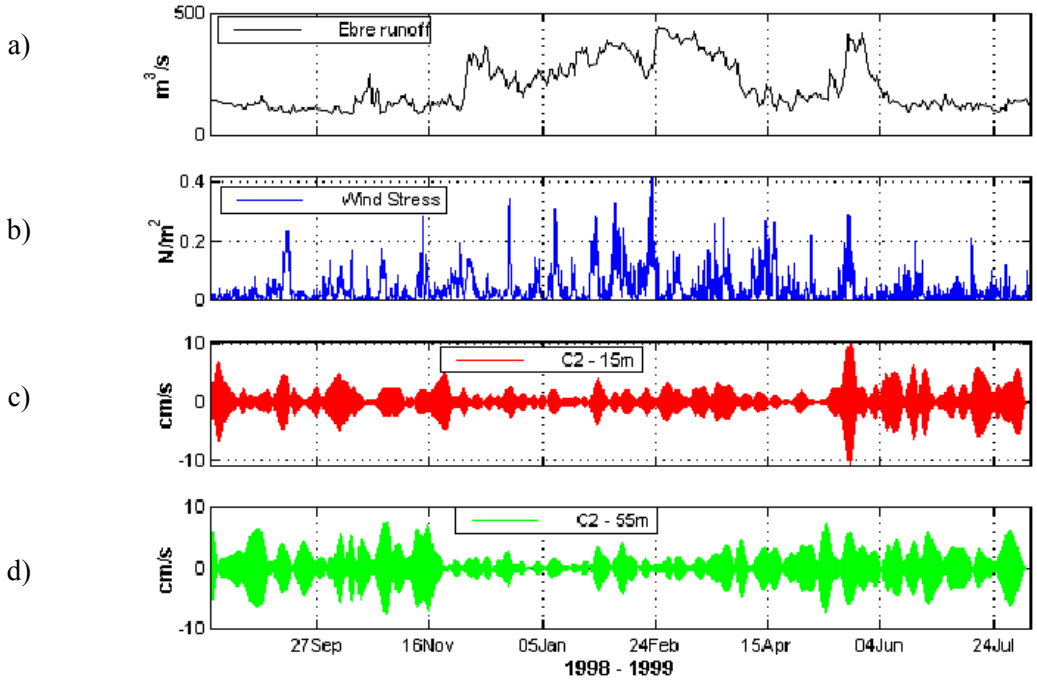

Fig 2. 25: Measurements over the shelf of (a) River runoff, (b) Wind stress and the currents in the near-inertial band at (c) 15m and (d) 55m.

Another important energy peak can be found at the 24 hours periods. This variability of the current is generated by the sea breeze which is a wind generated by the thermal gradients between the air over the sea and over the land having a period of 24 hours and velocities around 5m/s. The currents induced by this wind are more important near the coast and can dominate the inertial oscillations altough their energy is rapidly dissipated in depth, as it was shown by Rippeth et al. (2002).

Finally, we can do the harmonic analysis to see the tide effects. As it happened with the currents over the slope, the velocities induced by the tides are quite low (see Table 2. 3). Its relative importance respect to the complete currents is also negligible during all the year (see Fig 2. 24).

2.7 Study of the low frequency current variability using dynamical balances

To deepen in the mechanisms that contribute to the low frequency variability, we can compute the importance of the different terms in the momentum equation as it was done by Vitorino et al. (2002) in the Portuguese shelf. For simplicity we assume the Boussinesq hypothesis and, in a first moment, we consider that we are in the ocean interior region where the surface and bottom friction effects are not important. With these simplifications, the momentum equations are:

$$\begin{aligned} u_x + v_y + w_z &= 0 \\ u_t + \vec{u}\cdot\nabla u - fv &= -p_x \\ v_t + \vec{u}\cdot\nabla v + fu &= -p_y \\ 0 &= -p_z - g\rho/\rho_0 \end{aligned} \qquad \textbf{(2.5)}$$

where $\vec{u} = (u, v, w)$ represents the current velocity, ρ the density, p the pressure, g the gravity and subindexes t, x, y, z represent partial derivatives respect to time and x, y, z directions. As it has been done in previous sections, we consider u as the alongslope (or alongcoast) current component and v is the across-slope (across-shelf) component.

An additional assumption can be done if we assume that the non-linear terms are of second order of importance. This is justified by the fact that the Rossby number is small (R=V/fL ~ 0.05-0.1) computed with the typical values for the velocity (V~30 cm/s), the Coriolis parameter (f= 10^{-4} s^{-1}) and the horizontal length scale (L~30km over the slope and 80km over the shelf). The equations (2.5) take the following form:

$$\begin{aligned} u_t - fv &= -p_x \\ v_t + fu &= -p_y \end{aligned} \qquad \textbf{(2.6)}$$

From this expression we can evaluate until which limits the geostrophic equilibrium dominates in the movements over the shelf and slope. This will help us to have a clearer idea about the kind of processes that control the current variability. All the terms in the left hand side of equation (2.6) can be directly computed from the current data obtained over the slope and shelf filtered for periods T > 28 hours. The temporal derivatives have been done with a centered finite differences scheme while for the Coriolis parameter we use the typical value of the region.

The time evolution of these terms can be seen in Fig 2. 26 for the measurements obtained at 100m depth over the slope. The results at different depths and over the shelf have a quite similar aspect.

It can be seen how, in the alongslope direction, the Coriolis term is much bigger than the tendency and that the correlation between both is quite low. In consequence, to have a balance in (2.6), the pressure gradient term p_x must equilibrate the Coriolis term, so a geostrophic equilibrium must be established.

In the across slope direction, it seems that both terms have a contrary behaviour, existing a tendency between them to compensate. In this case, the magnitude of fv is much bigger than u_t but this one can't be neglected as it has been done with the along-slope component.

a)

b)

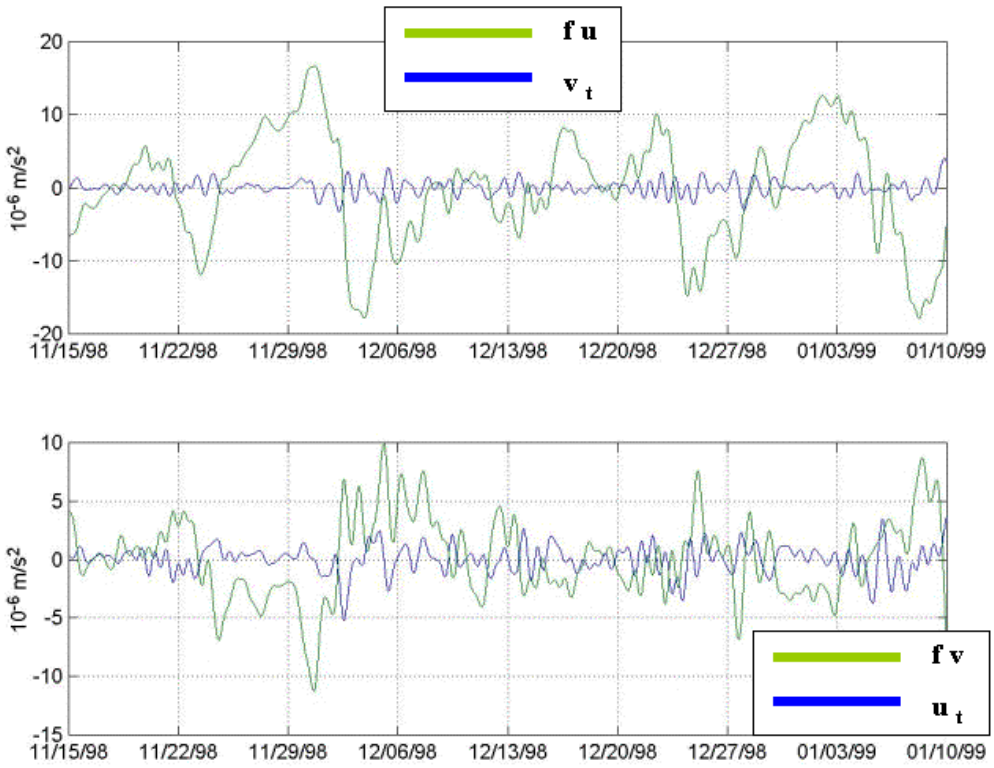

Fig 2. 26 : Time evolution of the Coriolis term and the tendency term for (a) the alongslope and (b) the across-slope components of the slope current at 100m. For the sake of clearity we have done a zoom over 50 days

It can be said that the current over the slope is in a semi-geostrophic equilibrium where the along-slope movements are clearly dominated by the geostrophic equilibrium while in the across-slope direction, the ageostrophic terms as the inertia have a significative role. Therefore,

if we look to the low frequency variability sources, we should think first in perturbations that fulfill the semigeostrophic equlibrium. As an example, it can be said that this kind of balance is fullfilled by the internal Kelvin waves, both the free and the forced ones.

A more complete study can be done if we use the momentum equation integered in the vertical where we also consider both the surface and the bottom stresses. If we do again the aproximation of linear regime, the momentum equation for the along-slope component is:

$$\underset{(1)}{\frac{\partial U}{\partial t}} + \underset{(2)}{fV} = \underset{(3)}{-g\frac{\partial \eta}{\partial y}} \underset{(4)}{-\frac{1}{H}\int_{-H}^{0}\int_{z}^{0}\frac{g}{\rho_0}\frac{\partial \rho}{\partial y}dz'dz} + \underset{(5)}{\frac{\tau_w^y}{\rho_0 H}} + \underset{(6)}{\frac{\tau_B^y}{\rho_0 H}} \qquad \textbf{(2.7)}$$

where U and V are the along and across the slope components of the velocity averaged over the whole water column. η is the free surface elevation, ρ is the density, H the water column height, τ_w the wind stress and $\tau_{B\ the}$ bottom stress.

The interest of working with this equation is that, except the terms (3) and (4) of the barotropic and baroclinic pressure gradients, all the other terms can be computed from the available information.

To obtain proper estimations of the averaged velocity a good distribution of measurements over the whole water column is desirable. For this reason we will focus in the periods when we have ADCP data because this instrument provides a vertical resolution of 4 meters between surface and bottom. Over the shelf there are Doppler measurements in the positions A1 (inner shelf) and A2 (outer shelf), see Fig 2. 1, during March-April 1997. Over the slope, we only have data between July-November 1997 in the position A4, in the shelfbreak over the 90m isobath. In this position, it can be considered that all the measurement points are in the coastal edge of the slope current. In consequence, we expect to measure lower velocities than if they were placed in the core of the jet but we still can consider than the variability captured is representative of the Northern current. In all cases, we have equispaced measurements between bottom and surface so we can compute the averaged velocities and then filter them for frequencies lower than 28 hours. The acceleration term (1) has been computed using a centered finite-difference scheme while the Coriolis term (2) has been obtained with the typical parameter of the region. The wind stress term (5) has been computed with data from coastal meteorological stations altough the use of the atmospheric model results don't change significatively the results. The bottom stress (6) has been estimated with $\tau_B^y = \rho C_D (u_B^2 + v_B^2)^{1/2} v_B$ where u_B and v_B are the measurements obtained in the deeper layer. For the drag coefficient C_D we have used a value of 0.0015, which

is representative of a gentle slope in weak wave conditions. The pressure gradient terms (3) and (4) can't be computed as we do not have information about the density structure or the surface elevation.

It must not be forgotten than there is an inherent error in the method as we do not include the non-linear terms and the computation of stresses are maybe not accurately enough. In any case we do not expect these errors to have a significative impact over the conclusions.

As it has been shown before with the simplified equations, in all cases it can be observed that the Coriolis term is the dominant term with similar values (see Fig 2. 27) except over the slope in autumn where it increases significatively due to the seasonal intensification. The other remarkable point is that, except in some punctual moments, this term is not compensated by the others, denoting that the terms not included in the computation are important (i.e. the pressure gradients). In other words, in the dynamical balance over the slope and the shelf, the pressure gradients (barotropic and baroclinic) dominate and are responsible in a great extent of the low frequency variability, which is near the geostrophic balance.

Over the slope, the tendency term is more or less correlated with the Coriolis term (see Table 2. 4) and in certain moments it increases its importance so it can compensate the Coriolis term completely. The wind has a much less influence and it just is slightly correlated with the Coriolis term. During autumn, its correlation with the tendency increases altough it is still far from equilibrate it. Finally the bottom friction is low correlated with the other terms playing always a secondary role.

The results for the across slope component don't give new information. The tendency term has a greater importance, especially in the surface levels, while the wind and the bottom friction play a secondary role.

Over the shelf, the explanation is slightly different. The relative importance of the tendency is greater and comparable to the Coriolis term during most of time, so indicating that the pressure terms have a minor importance and the geostrophic equilibrium is less dominant than over the slope. The wind also acquires important values and in the outer shelf its correlation with the Coriolis and tendency is quite high (see Table 2. 4). The bottom friction continues to have low values but now it is much more correlated with the wind.

a)

b)

c)

d)

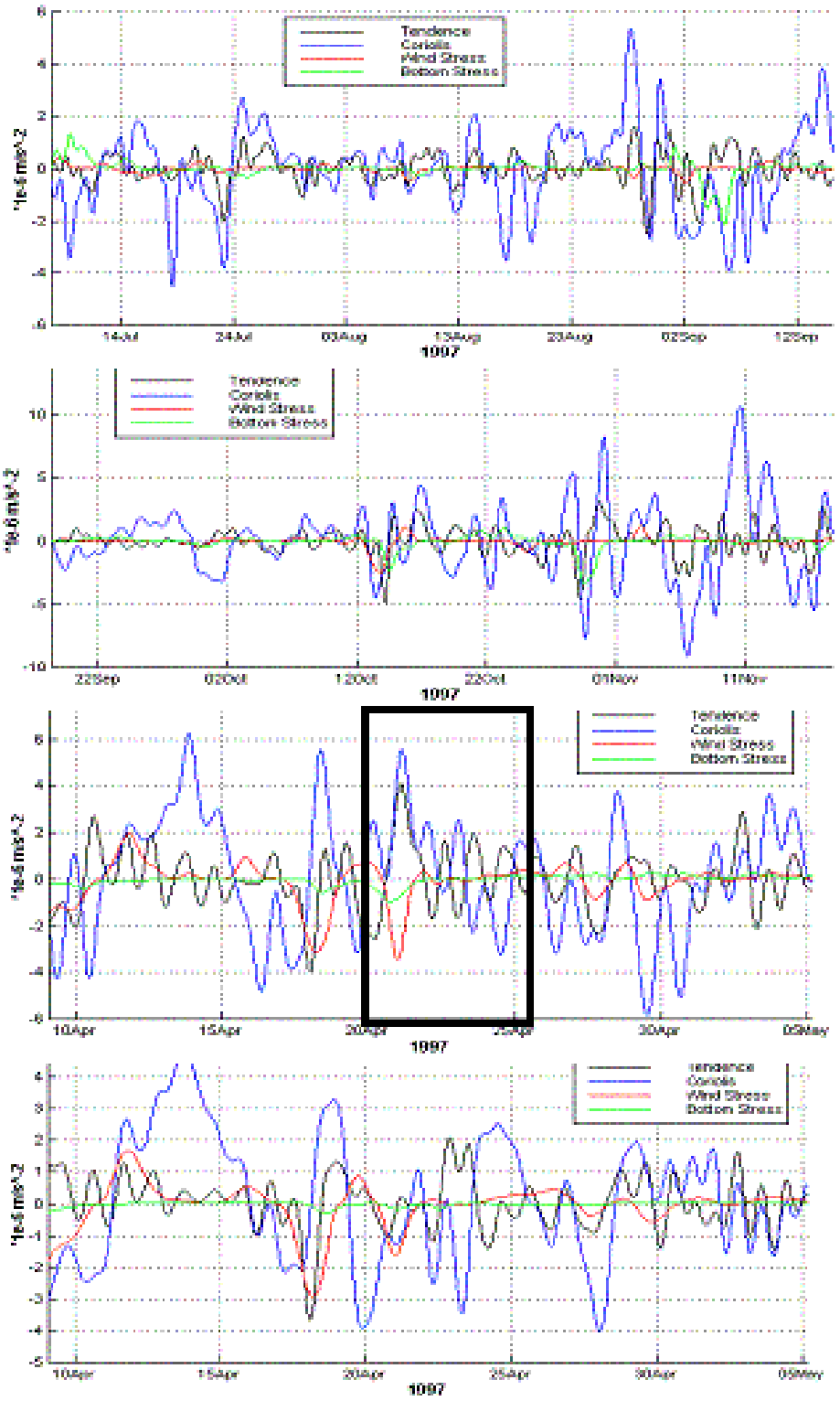

Fig 2. 27: Terms in the momentum equation integrated in the vertical (a) over the slope in summer (b) over the slope in autumn (c) over the inner shelf in spring and (d) over the outer shelf in spring. The frame in (c) indicates the period explained in the text.

This behaviour can be explained looking to a typical example of the wind response to the shelf (Fig 2. 27c). On April 21st there is a wind burst and it can be seen how the Coriolis term and the tendency have the same sign. The equilibrium is reached with the increase of the bottom friction and it seems than the pressure terms are not important. The following days (22-25 April) the wind and the bottom stress stop and a near-perfect equilibrium between the tendency term and the Coriolis term is established, as it happens when the inertial oscillations are triggered.

Slope - Summer 1997			
	Coriolis	Wind	Bottom friction
Tendency	*0.36*	*0.06*	*-0.12*
Coriolis	-	*-0.11*	*0.04*
Wind	-	-	*0.02*
Slope - Autumn 1997			
	Coriolis	Wind	Bottom friction
Tendency	*0.26*	*0.29*	*0.11*
Coriolis	-	*0.13*	*0.09*
Wind	-	-	*0.06*
Inner shelf - Spring 1997			
	Coriolis	Wind	Bottom friction
Tendency	*0.14*	*0.07*	*-0.14*
Coriolis	-	*-0.03*	*-0.29*
Wind	-	-	*-0.48*
Outer shelf - Spring 1997			
	Coriolis	Wind	Bottom friction
Tendency	*0.22*	*0.41*	*-0.01*
Coriolis	-	*0.30*	*0.15*
Wind	-	-	*0.53*

Table 2. 4: Correlation between the different terms of the momentum equation integrated in the vertical for different positions and seasons.

In conclusion, the computations of the terms in the averaged momentum equation for measurements taken between surface and 90m in the Northern current confirms the results obtained for the deeper levels: The low frequency variability over the slope is highly dominated by the geostrophic equilibrium between the pressure gradients and the Coriolis force. The

bottom friction is only significative in certain episodes while the wind has not a significative role. This confirms the typical assumptions assumed for the Northern current in the region (Millot, 1999, García-Ladona et al., 1994).

Over the shelf, the interpretation that we propose is that the control of the variability is shared between the pressure gradients and the wind. This is more correlated in the outer shelf while in the inner shelf the correlations are more complex, probably due to the effects of the coast and the Ebre river plume.

2.8 Influence of wind and atmospheric pressure over the low frequency current variability

In this section we study in which situations there is a relationship between the atmospheric forcing (wind and pressure) and the low frequency variability (periods greater than 28 hours). This is a key point to understand the region dynamics and as a base for the future modelling works. We try to do this study both from a quantitative and qualitative point of view using statistical and numerical tools.

2.8.1 Slope

Previous studies in the region (Font, 1995) show than the wind has no clear influence over the slope current. Contrary to what happens in other regions of the Northwestern Mediterranean (i.e. Gulf of Lions), the wind doesn't blow enough time and strong enough to significatively alter the current. The only observed effect is the modification of the superficial current (<50m) but when wind stops the initial situation is restablished.

The Font's work was based in data in the first 100m of the water column while in our case the first measurement is already at 100m depth. So, as it was expected, the results obtained from visual and statistical comparison (EOFs) don't provide anything new reinforcing the idea that the slope current is not affected by the wind in the deep layers.

The other point of interest we wanted to deal with in this section is the effect of the pressure over the low frequency variability. In the study of the Foix submarine canyon, Puig et al. (2000) identified the passage of pressure cells as the origin of some oscillations with a period of 6-10 days in the circulation in the edge of the canyon. The explanation proposed by them was that variations of water level provoke, by continuity, movements in the water column which are channeled by the canyon.Besides the Puig et al. work, which seems us a quite particular sitution, we do not know any other study in the Balear sea where a direct comparison between pressure and circulation have been carried on.

To see if the pressure can be related with the currents, we compute the energy spectrum of the pressure time series to try to indentify the common peaks (see Fig 2. 28). Comparing with the current spectrum it can be seen that an important peak around 14 days is present, as well as a series of peaks between 2 and 10 days.

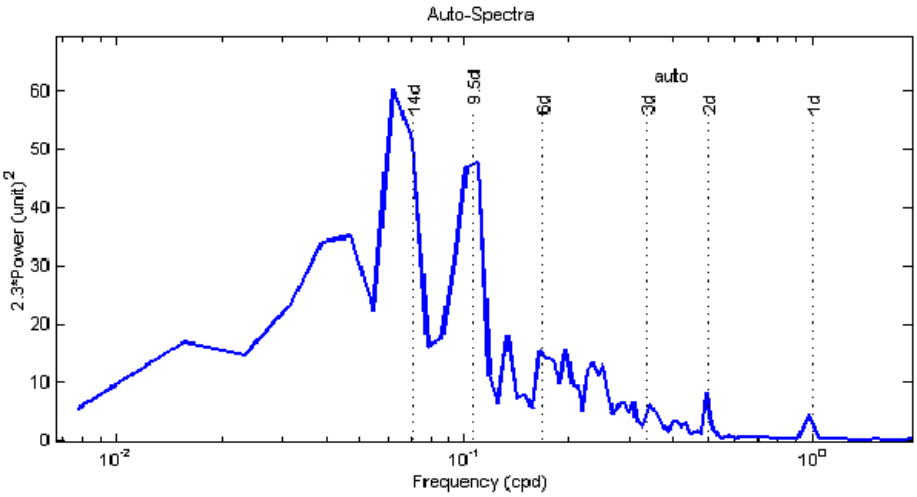

Fig 2. 28 : Variance preserving energy spectrum of the atmospheric pressure over the slope in the position C1.

If we comparre the pressure and currents at 100m filtered with a band-pass filtered center at 14 days (see Fig 2. 29), we can see that there is a strikingly good correlation between the pressure maximum and the along-slope current minimums (south-westward currents). At 300 and 500 meters there is a phase lag related to 100m which is constant during all the period. The amplitude at 300m is comparable with 100m amplitude while in deeper layers (500m) it is reduced to a fourth. After that period, the currents in all depths in the 14-days band is simultaneous but the correlation with the pressure is not so clear.

Concerning to the correlation at other frequencies, it must be said that, visually, there are several moments where it seems that there is a strong relation but there is nothing systematic. In consequence, we will use again the EOFs decomposition to look for pressure-velocity correlations. Nevertheless, as the magnitude of the different variables and their variability is quite different, we decided to use the correlation matrix instead of the covariance matrix in the EOFs computation (Noble and Ramp, 2000). In other words, we have normalized the variances dividing each variable for its standard deviation, so the variability of each variable has the same magnitude Formally, this option doesn't present any problem and it has the advantage than we will be able to find some relations than will stay masked due to the magnitude differences

between variables. With this consideration we have computed the mixed EOFs of pressure and velocity for several frequency bands.

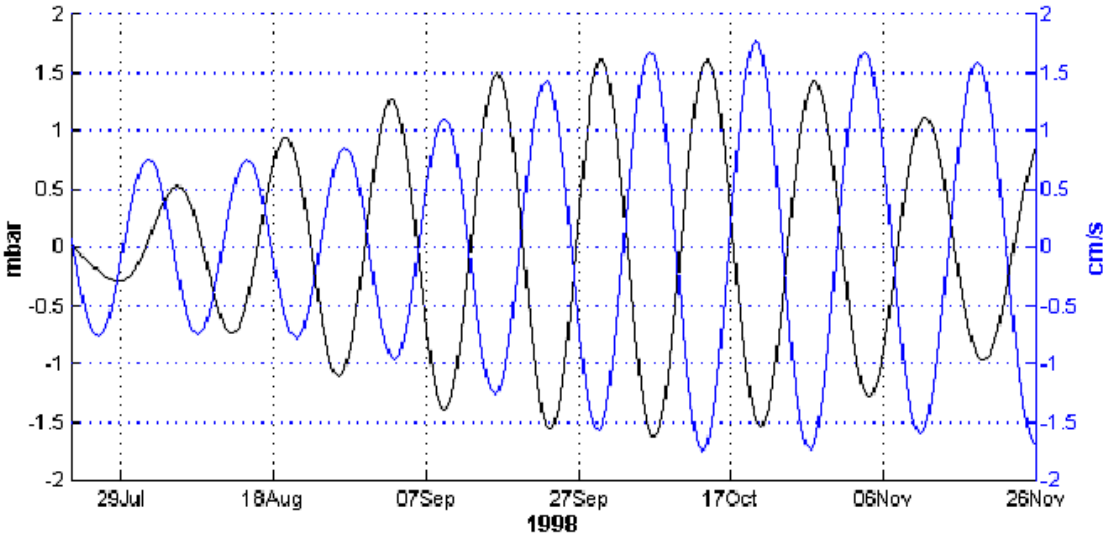

Fig 2. 29 :Comparison of the filtered series at 14 days of pressure(black) and along-slope currents at 100m depth (blue).

In Table 2. 5 there are the results for the across-slope component of the velocity because for the along-slope component there was no significative relationship, except in the 1-6 days band where the results are quite similar between the two velocity components.

What this analysis show is that there is a strong relation between pressure and across-slope movements at 500m depth. In fact, the variability of these movements is associated in a small part (near 15-25%) to what happens at 100 and 300m while the rest is almost all linked to the atmospheric pressure variability in phase (mode 2) or out of phase (mode 3). On the other hand neither at 100m nor at 300m a clear correlation with the pressure variations is observed but maybe this is due to the fact that other more energetic processes mask the correlations.

The explanation of this relation it is not easy to find. Usually, it is considered that the atmospheric pressure does not generate any movement except in cases where the pressure cells move fast enough to generate, through the inverse barometer phenomena, surface elevation gradients which induce a significative movement in the sea. On the other hand, it must be noted that the EOF analysis just tell us that between certain processes there is a statistical correlation but from there it is not possible to establish a direct cause-effect relation.

a) Mixed EOFs in the 1-6 days band > P - Across-slope current				
%	***Mode 1***	***Mode 2***	***Mode 3***	***Mode 4***
P	***8.9***	***60.7***	***30.1***	***0.24***
V 100m	***60.1***	***0.3***	***7.4***	***32.2***
V 300m	***60.2***	***0.4***	***7.1***	***32.3***
V 500m	***13.3***	***38.3***	***48.2***	***0.2***
b) Mixed EOFs in the 4-11 days band > P - Across-slope current				
%	***Mode 1***	***Mode 2***	***Mode 3***	***Mode 4***
P	***8.9***	***60.7***	***30.1***	***0.24***
V 100m	***60.1***	***0.3***	***7.4***	***32.2***
V 300m	***60.2***	***0.4***	***7.1***	***32.3***
V 500m	***13.3***	***38.3***	***48.2***	***0.2***
c) Mixed EOFs in the 9-31 days band > P - Across-slope current				
%	Mode 1	Mode 2	Mode 3	Mode 4
P	6.13	65.42	28.42	0.04
V 100m	67.49	7.53	2.34	22.65
V 300m	67.46	8.37	1.23	22.93
V 500m	25.67	26.88	47.43	0.02

Table 2. 5: Percentage of explained variance for the mixed pressure-current EOFs over the slope for different frequency bands (a) 1-6 days, (b) 4-11 days and (c) 9-31 days.

In a first moment we explore the possibility of a direct effect between pressure and current and to have an idea of how this effect could work we look at the characteristics of the S1 tides. The gravitatory effects of the moon and the sun provokes a direct response both in the atmosphere and the sea, so the sea also receives the effect of the perturbations generated over the atmosphere as variations of the atmospheric pressure. Usually, what is observed in the ocean for the different tidal constituents is a combined effect of both but for the S1 component it is found that the direct effect over the sea is almost negligible (F. Lyard, pers. comm.). The signal found at 24.0h is only responsalbility of the meteorological tide through the atmospheric pressure. So, if we look to the characteristics of the S1 tide we would see the aspect of the direct effect of pressure over the sea.

In the section 2.6.1 we did an harmonic analysis of the YOYO current data and thanks to the time series length (1 year), we could precisely separate the different tidal components which are present around 24 hours. In Table 2. 3 it can be seen that the amplitude of the S1 tide decreases in depth in a similar way than the structure of the first EOF (see Fig 2. 10). This denotes that vertical adjustment to the free surface perturbation is done following this structure, which could be assimilated to the first Kelvin mode. On the other hand, if we compare with the behaviour of the filtered series at 14 days, we find that the amplitude and phase distribution don't coincide with what has been observed for the S1 tides, suggesting that the 14 days oscillations are not a direct effect of pressure.

To finish the exploration of this hypothesis we can use the results of the numerical model MOG2D developed at LEGOS (Toulouse) by Florent Lyard. It is a finite element model which solves the shallow-water equations and that has been successfully implemented in different regions of the world and largely validated with field measurements and altimetry (Carrère et al., 2003). The results that it provides for the tides and the 2D response of an ocean forced by the wind and pressure are quite good and can provide a valuable information to understand and interpret the measurements we have.

In Fig 2. 30, there are the model results for the barotropic velocities generated only with the atmospheric pressure where the forcing has been obtained from the ALADIN (Météo France) results for the year 1999. As it can be seen the velocity results are really small never exceding 2-3 mm/s.

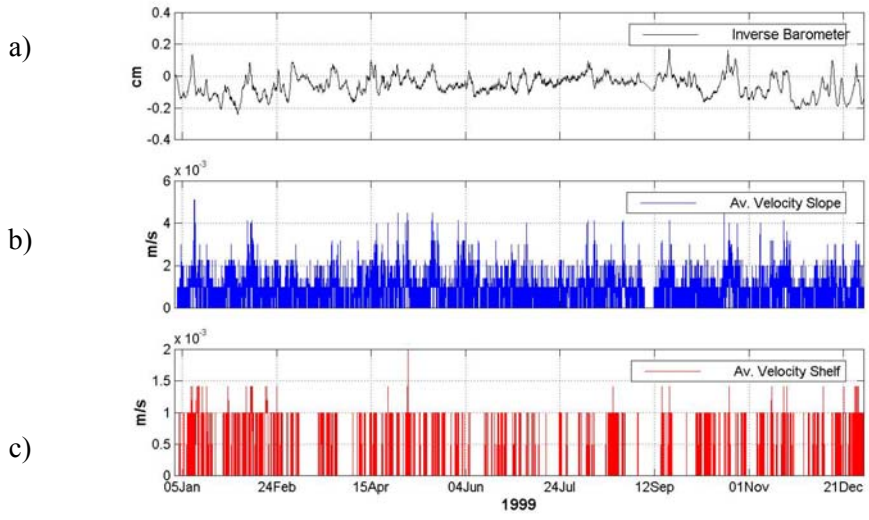

Fig 2. 30 :Results of model MOG2D forced only with the pressure during 1999 (a) Surface elevation generated by the inverse barometer (b) Barotropic current in the slope at C1 (c) Barotropic current over the shelf at C2.

The following hypothesis that we can study to explain the 14 days peak is that it can be due to an astronomical tide where the period coincides with a meteorological tide. This could explain that the pressure and current series were highly correlated (see Fig 2. 29) and it would not imply a direct effect of the pressure over the sea.

The harmonic analysis carried on in section 2.6 is not valid to distinguish the low frequency bands because in the low frequencies the analysis losses resolution in frequencies and can capture a part of the spectra which is not generated by tides. The alternative to study this is to use again the results of the model MOG2D forced by the tides. Fig 2. 31, displays a map of the principal semi-axe of the currents associated to the tide component Mf (period of 13.6 days). As it can be seen the velocities are again really small being around 0.5-1 mm/s. The results for other tidal constituents are analogous, so we can conclude that the low-frequency tides are not the responsible of the currents observed at 14 days.

Finally, we can comment a last hypothesis which is that the currents would be a consequence of a resonance phenomena. Any enclosed or semi-enclosed area (as it is the Western Mediterranean), has a resonance frequency so if it is periodically perturbed with the correct frequency the effects over the fluid are superimposed and can be much more important than a simply response. In order to see which could be this frequency, we consider than a stratified ocean would have a response to external perturbations according to the normal (or Kelvin) modes. In Table 2. 6 there are the phase velocities and the deformation radius associated to the first five normal modes obtained with a winter density profile. The results with the autumn profiles are quite similar.

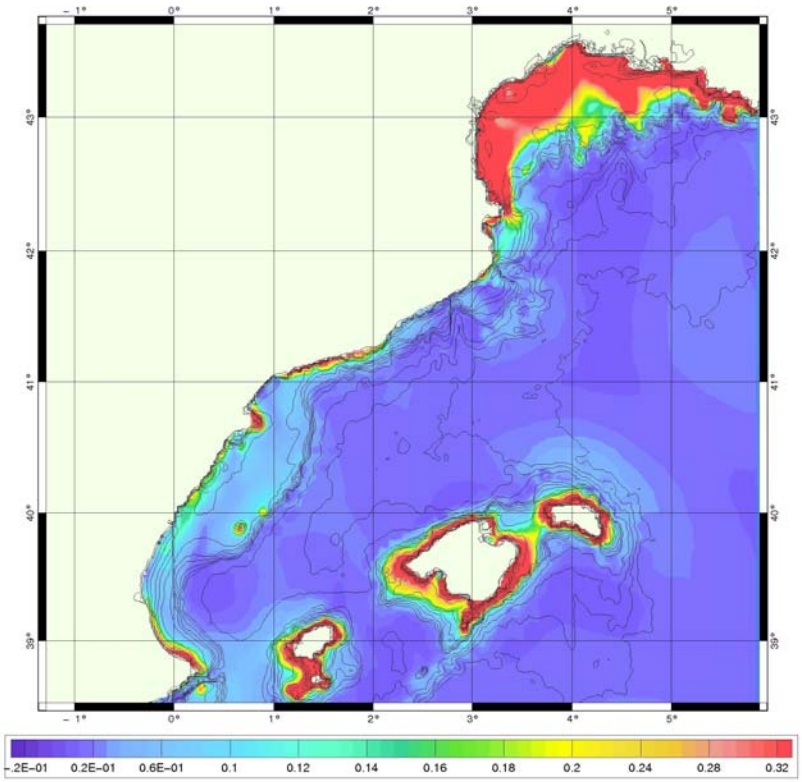

Fig 2. 31 : Results of theMOG2D model for the currents associated to the tide component Mf. Results are in cm/s.

Mode	*Phase velocity (m/s)*	*Deformation radius(km)*
1	***1.53***	***15.30***
2	***0.77***	***7.79***
3	***0.52***	***5.18***
4	***0.39***	***3.92***
5	***0.31***	***3.17***

Table 2. 6: Phase velocity and deformation radius associated to the first five normal modes obtained from a typical winter density profile.

The high order modes tend to loss energy fast so we focus in the low modes because they seem more appropiate to the phenomena we study. In order to a ressonance phenomena appears, the wavelength associated to one of this modes for a period of 14 days, shoud be similar to two times the dimension of the Western Mediterranean basin.

Doing a simple computation we find that a perturbation with a period of 14 days which has a structure as the first baroclinic mode should has a wavelength of $\lambda_{1st} = c_{1st} T \sim 1850\ \mathrm{km}$. On the other hand the east-west dimension of the basin has an average length of around 900 km, so there is a ressonant frequency around 14 days.

Finally, to produce a ressonant phenomena it is needed a forcing with a period near this frequency. In our case it could be the tidal waves Mf or Msf with periods of 13.7 and 14.7 days which also affect the atmosphere, so generating the necessary pulse to the ressonance appears and producing the 14 days peak found in the pressure time series.

2.8.2 Shelf

Over the shelf the wind effect is much more noticeable than over the slope, as it has been shown in previous sections. The fact that the depths are much lower (bottom at 60m depth in the measurement point), implies that it is easier to find the relation between wind and currents at 15 and 55m. Certain relation is clear with simple visual inspection but in order to quantify it we decided to do the same multivariate EOF analysis than in the previous section. This time we have used the wind because we expect it to have a more important effect than the pressure over shallow waters.

The results for the along and across shelf components are not too different and they are summarized in Table 2. 7.

The results of this analysis is that the wind has a direct relation with the barotropic mode, on one hand, and to what is happening in the shallower layer, on the other hand. If we look at the explained variance at each depth and mode, it seems that the variability can be separated in the barotropic and barotropic processes induced by the wind (modes 1 and 2), and other processes generated by other reasons (mode 3). The proportion of each process depends on the frequency band observed. "Grosso modo", it could be said than around 40-60% of the variability is coherent in all the water column and it is associated to the wind, while at 15m, a 30% of the remaining variability is also associated to the wind and unliked to what happens in depth. Finally a 20-30 % of the variability is indepent of the wind.

a) Mixed EOFs in the 1-6 days band > Wind - currents						
%		Mode 1		Mode 2		Mode 3
Wind	10.6	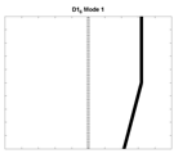	88.3	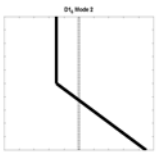	0.01	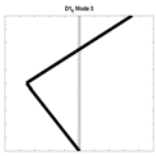
V 15m	54.1		8.5		37.5	
V 55m	53.2		8.7		37.3	

b) Mixed EOFs in the 4-11 days band > Wind - currents						
%		Mode 1		Mode 2		Mode 3
Wind	28.6	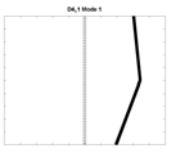	60.3	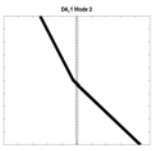	***11.01***	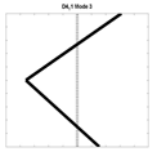
V 15m	40.1		39.2		21.5	
V 55m	68.2		0.1		32.3	

c) Mixed EOFs in the 9-31 days band > Wind - currents						
%		Mode 1		Mode 2		Mode 3
Wind	47.4	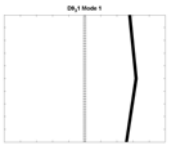	46.6	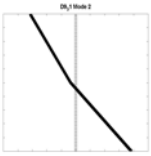	5.9	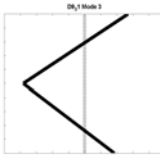
V 15m	56.4		30.7		12.8	
V 55m	73.8		0.4		25.8	

Table 2. 7: Variance explained by the mixed EOFs wind-currents over the shelf.
The results for both velocity components are quite similar so we use the mean values.

2.9 Evidences of the importation of dynamical variability

In previous sections we have shown the importance of the variability in the shelf and slope dynamics, and it has been suggested that, in a great extent, this variability has not been locally generated but it was due to wave propagation or the advection of structures. In this section we try to highlight some of those processes combining the information of the currentmeters over the slope (C1) and shelf (C2) and the measurements obtained with the ADCP over a bottom of 90m in position A4 between March and October 1997. As it has been seen in section 2.4, the currents in the A4 position are representative of the inner part of the Northern current. All the ADCP measurements between bottom and surface are inside the slope current and its vertical structure corresponds to a combination of the barotropic and the first baroclinic modes with a small contribution of the higher order modes (cf. section 2.4.1).

2.9.1 Waves

A first visual inspection of currents in the north and the south (A4 and C1, respectively), show a superimposition of different processes with different frequencies and duration which difficult the direct comparison. Also, the behaviour of each process is different, so we can not expect to find a precise and unique description of the relation between different positions. After carrying on several tests, we concluded that the clearest way to do the comparison would be to use the EOFs amplitude of the along-slope current in A4 (see Fig 2. 11b). These time series can be compared to the slope currents at 100m in position C1 which are in the core of the Northern current. In other words, we want to see the wave propagation along the slope, so we use the first EOF for currents in A4, which is representative of the slope current in the north, and the current measurements at 100m in C1, which are representative of the slope current in the center part of the domain.

If we look to the series filtered at 1-2 days, we find a good relation between the barotropic component of the current (represented by the first A4 EOF) with the currents at C1 (see Fig 2. 32). At the beginning of September, there is an event which propagates with an approximate velocity of 10cm/s and which is probably advected by the current. On the other hand, at mid-October, there are some current pulses which propagate with a velocity of 60-80 cm/s. It is interesting to note that it is also the propagation speed of the first Kelvin mode over the slope.

In the frequency band between 6-10 days we find a variable phase lag of 3-5 days. This is clearer for the 6 days oscillations, implying a wavelength of 60-100km. The 60km wavelength is in good agreement with the dimension of the Northern current meandering commented in section 2.4.1.

Comparing with the measurements obtained over the shelf, we also find a good correlation in the 6-10 days, specially between the barotropic mode in A4 and the bottom velocities over the shelf (see Fig 2. 33). The concordance is quite good with a phase lag of 1 day, leading again to a phase velocity of 60-80 cm/s. Nevertheless it must be noted that over the shelf the theoretical prediction for the Kelvin wave propagation is of 20-30 cm/s. On the other hand, at the end of August, it seems that the propagation is from south to north with a phase velocity of ~30cm/s.

a)

b)

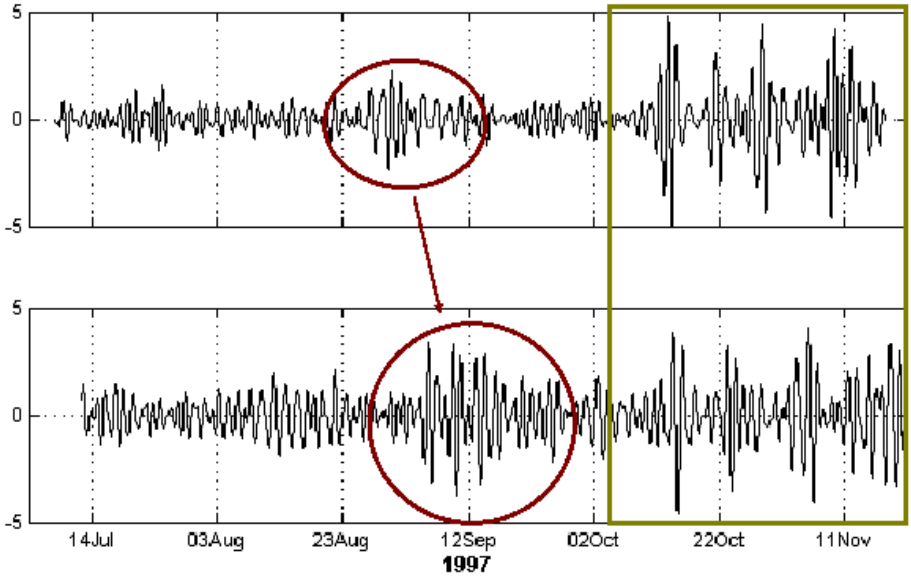

Fig 2. 32 : Comparison of the processes at the north and the south over the slope in the 1-2days band (a) Amplitude of the barotropic mode in A4, (b) along-slope velocity over the slope at 100m in C1.

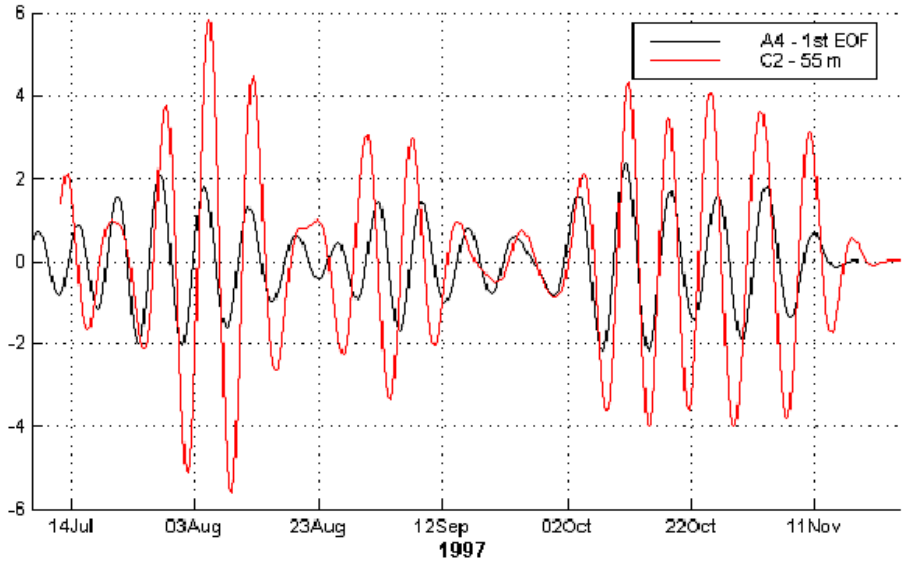

Fig 2. 33 : Comparison of the processes at the north and the south over the shelf in the 1-2days. (a) Amplitude of the barotropic mode in A4, (b)near bottom along-coast velocity over the shelf.

Finally, a cross-correlation computation between the amplitude of the barotropic mode and the velocites over the shelf at 15m depth (not shown), we find that there is a significative peak in the few-hours lag and another at 15 days. The first one can be explained if we think in some

kind of wave similar to what have been shown above, which have a phase velocity of 1m/s. On the other hand, the second peak suggests that there is another process of energy transfer propagating at 3-4 cm/s, much more slowly than what has been observed previously. The origin of this process is still unknown but in chapter 3, with the help of a numerical model, we explore the possibility that it was the signal of a topographic Rossby wave.

2.9.2 Eddies

To complement the observations of wave propagation we want to show the evidence of the propagation of an anticyclonic eddy advected by the current. This kind of eddies in the Balear sea have been previously reported by several authors. Arnau del Amo (2000), from an extensive analysis of SST images showed the frequent existence of anticyclones propagating alongslope from the Gulf of Lions towards the southwest, specially during the summer period. Rubio et al. (2004) tracked one of these eddies and characterized its 3D structure from CTD and ADCP measurements. Usually, this kind of eddies have a diameter around 40-80 km, can have a vertical extent greater than 200-300 meters with associated velocities around 60-70 cm/s. The effect of its passage over the local dynamics is quite important because it generates current inversions that can last several days and subductions of several tens of meters. The mechanism of generation of these structures is unknown and probably different processes as the wind effect or the current instability can originte them. In addition to that, the generation place is probably not unique and it is not still clear if the are all generated in the Gulf of Lions or the can be locally created.

One of the main problems to track the eddies is that the only tool with enough spatial and temporal resolution available is the sea surface temperature satellite images. The quality of this data depends on the cloud covering and what usually happens is that there are lacks of information of several days. On the other hand, the eddies advection is quite variable and they can stay bloked several days in the same place after being fastly advected by the current for a long period. Moreover, the interpretation of the images has an important component of subjectivity, so, finally, the tracking of the eddies evolution is not easy at all. So, we would like to take profit of the current measurements available to study one of this structures observed between July and August 1997 with special emphasis into highlight the above commented difficulties.

In the SST images collected during summer 1997 (see Fig 2. 34), it can be seen how, since 8 July, a clear anticyclonic structure with a diameter of 50km is visible at the north of Barcelona. During several weeks this structure slowly displaces southwestwards close to the coast with a

velocity of around 5cm/s until the 13 of August when it is placed in the south of Barcelona. It is important to note that during this period we haven't found in the region any other structure which last for more than few days.

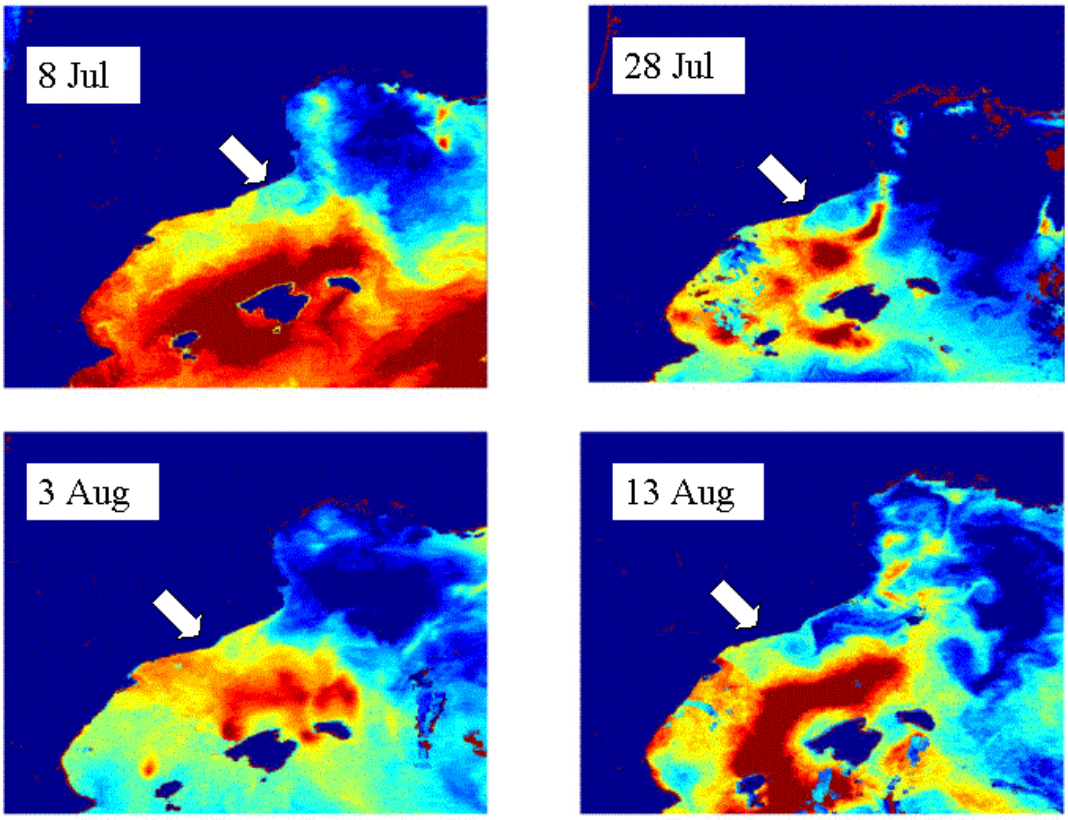

Fig 2. 34 : SST images during summer 1997. The white arrow indicates the position of the anticyclonic eddy commented in the text.

On the other hand, if we look to the current meter measurements in A4 and C1 we observe the passage of an anticyclonic structure with a difference of 6-7 days (see Fig 2. 35). Between the 24-31 of July, an anticyclonic rotation of about 10cm/s is measured in the northern part (A4) in the whole water column. As the current meters are near the coast the most logical is to think that it is a structure that is placed seawards respect to the measurement point, so the measured process is an anticyclonic structure. Between 1-12 August, an analogous inversion it is measured in the southern part (C1) but more energetic reaching the 15cm/s at 100m and 10cm/s at 300m. In deeper levels the inversion is also measured but with much smaller values. On the other hand it can be thought than in shallower levels the associated velocities would be more important.

It is important to notice than the structure measured with the current meters does not coincide with the eddy observed in the satellite images because this one reaches the region around the 13 August, which is the moment where the signal in the south is already lost. So, from here an interesting point can be highlighted because an energetic structure which reaches the 300m depth with velocities greater than the slope current could not be tracked with SST images.

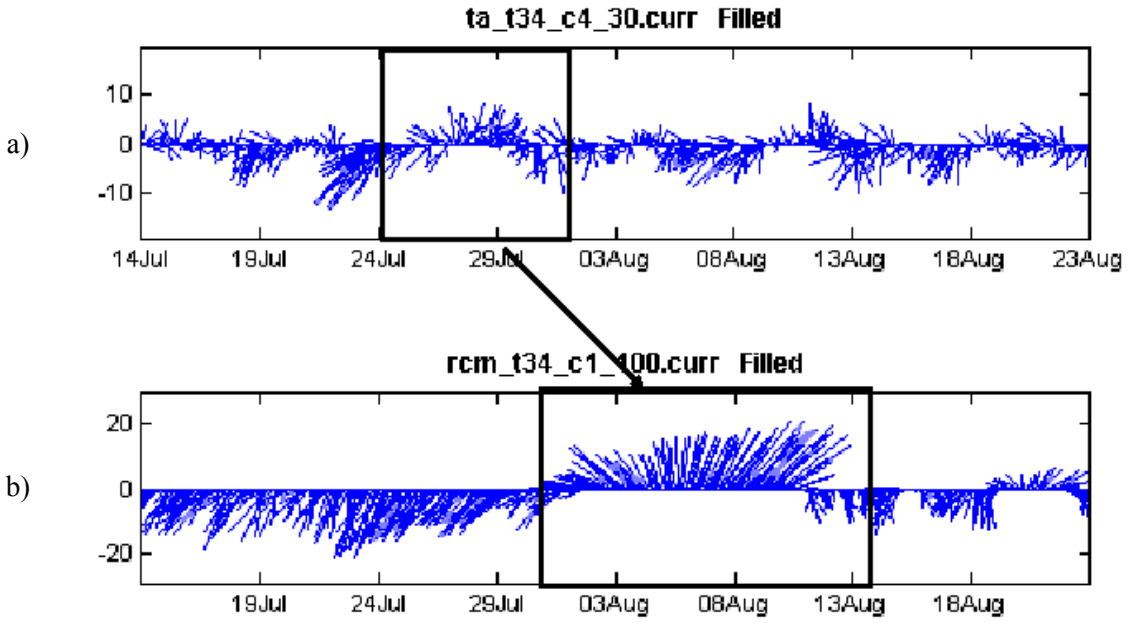

Fig 2. 35: Stick diagrams in the position (a) A4 at 30m depth and (b) C1 at 100m depth.

These measurements seem to indicate that it is an anticyclonic structure which is displaced over the slope with a velocity of around 10cm/s, so probably advected by the slope current. The external part of the eddy is captured by the current meters placed over the shelf break in the northern part while the measurements got in the slope over the 600m isobath are probably near the core of the structure. The eddy extent in the vertical is quite large, occupying until 300m depth, and being deeper than the eddy measured by Rubio et al. (2002) which just reached the 150m depth.

The temperature measurements show a slight increase of 0.2ºC at 100m depth and a decrease of 0.05ºC at 300m associated to the structure passage. These small variations suggest that, in the eddy's core, there is not a clearly different water mass and the temperature varies due to the advection of waters from the same region. Nevertheless, it must be noted that maybe the different water mass was placed over the 100m depth and the velocities measured are the fruit of a barotropic effect.

On the other hand, the origin and path of this eddy is not clear because if it was advected over the slope from the Gulf of Lions, some interaction with the eddy observed in the SST images should have been noticed. The possibility that the measured eddy passed below the other eddy is quite strange as far as it seems not too logical than an eddy which stays for so long time stationary and unaltered has a shallow structure. Another option could be than the eddy has been locally generated at the south of Barcelona but it is also hardly to believe as far as no significant process as current oscillations or strong storms which could generate a similar structure have been observed.

To finish the section, we wanted to comment the observation during March 1999 of a current inversion that lasted for more than one month and which affected the water column until depths greater than 300m. The progressive vector of velocities over the slope at 100m (see Fig 2. 36a) shows how, between 19 February and 15 March, there was a complet inversion of the slope current. The associated velocities reach a maximum of 40cm/s at 100m and 10cm/s at 300m, while at 500m there is no significative effect. It must be noted that at 300m there is no inversion as clear as at 100m but instead there is a marked modification of the current towards the slope during 10 days, with the consequent implications for the open sea-shelf exchanges. The temperature measurements just show small variations which are not significatively enough to give more information.

A first hypothesis about the origin of this inversion is that it could be the effect of the anticyclonic eddy observed by Pascual et al. (2002) and commented in section 2.5 but the depth of the perturbation, the no evidence in the SST images of the eddy displacement and the period where the inversion has been observed, suggest that it is not linked to the big anticyclonic eddy.

In the satellite images (see Fig 2. 36c) it can be clearly seen the Pascual et al. eddy in the northeast but also the entrance of warmer Atlantic waters from the south. The associated front presents a meandering with important amplitudes which reaches the measurement point. So, it could be that the inversion was the consequence of this meandering and not of an advected structure from the north. To complement this idea, we look at the altimeter measurements of the track 248 (see Fig 2. 1 for the track position). It can be seen that days before the inversion is measured, there is a positive anomaly of surface elevation (see Fig 2. 36b). This anomaly is associated to the front meandering, so it is logical to think that it is an intense feature because it has a clear signal in the surface elevation, contrary to what happens with the thermal front oscillations observed during summer which correspond to shallow processes and has no trace in the altimetry data. The fact that this southern meander reach the measurement point is quite atypical and it is probably influenced by the bloking commented by Pascual et al. (2002) and which is not present in other years.

a)

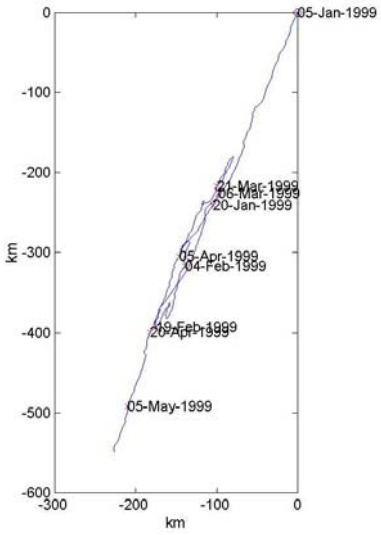

b)

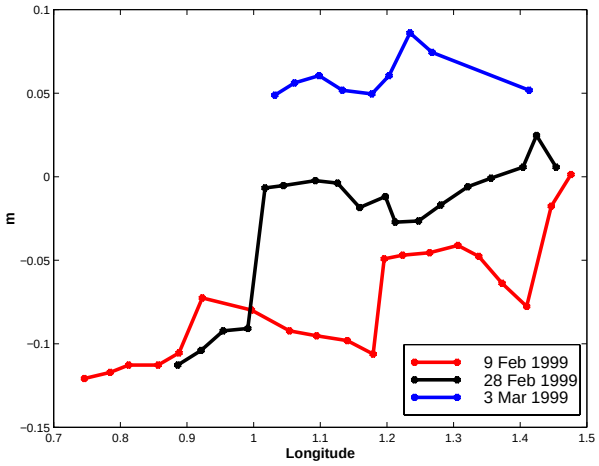

c)

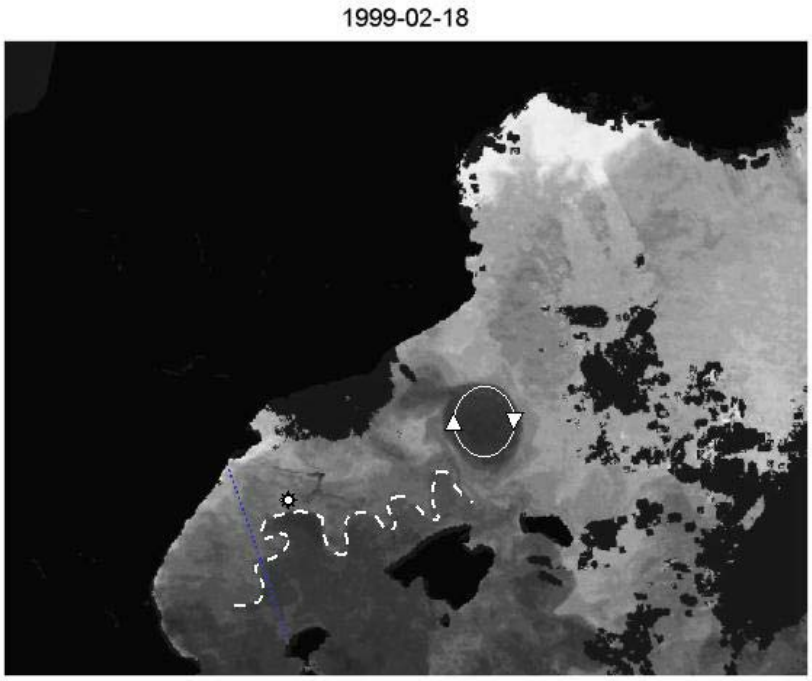

Fig 2. 36 : (a)Progressive vector of slope current measurements at 100m between January and May 1999. (b) Altimetry measurements at track 248 at different moments before and after the current inversion mentioned in the text. (c) SST image of 18 February showing the strong anticyclonic eddy in the northeastern part of the Balearic Sea and the front meandering in the south. Star indicates the measurement point and the blue line the altimeter track.

2.10 Conclusions

From in situ measurements (currents and temperature) and remote data (SST, chlorophyll and altimetry) we have studied the dynamics of the Catalan continental shelf and slope region, confirming and complementing previous works carried on previously in the region.

Over the slope, there is a quasi-permanent current in geostrophic equilibrium (the Northern current), which flows southwestward over the slope with a clear seasonal cycle. Its variability is controlled by the topography and, inside the current, it has a character mainly barotropic. In second order, its vertical structure coincides quite well with the first Kelvin mode.

The high frequency variability over the slope is controlled by processes which have a frequency around the inertial period (18.4h). For depths greater than 100m, only in certain moments where there are strong and isolated wind bursts, it can be seen a clear effect of wind over the inertial oscillations. On the other hand, we have also seen than these oscillations in the near-inertial band are not always the reflex of internal gravitatory waves but there are also gyroscopic waves in periods where the water column is homogenized, or at least part of it. Finally we have confirmed than tides have not a significative importance at any depth.

For the low frequency variability it has been shown that it is basically in semi-geostrophic equilibrium and neither the wind nor the atmospheric pressure have a remarkable effect over it. We have also shown that a possible explanation for the current oscillations with 14 day period could be a ressonance phenomena of the Western Mediterranean basin. On the other hand, a significative part of the variability in the region is not locally generated but it is imported. Several processes measured in the northern part of the region, in the shelfbreak, propagate over the slope and shelf. Some of these processes can be current meanders, eddies or topographic waves as it has been commented in section 2.4.1, but also some information is transferred to the shelf as Kelvin waves or a some kind of low wave still not identified. Finally, we have shown how, in certain periods, the propagation is not from North to South, as it is traditionally assumed, but it can be in the inverse sense due to a propagating wave or due to the structure advection from the south.

For the water masses we couldn't capture the seasonal cycle and we have just found the deepening of the surface waters. The current oscillations have an important effect over the interfaces between water masses as far as they induce significative modifications of the temperature. Finally, we have also observed the effect of an intense anticyclonic eddy reported by Pascual et al. (2002) over the evolution of the winter intermediate waters inducing an accumulation and the posterior sudden advection of a great amount of these waters.

Over the shelf, there is no clear permanent pattern of the circulation and the vertical structure of the current is also well represented by the barotropic mode and the first Kelvin

mode. The apparition of the thermocline in summer unlinks the processes between surface and bottom. The variability is dominated by the oscillations in the inertial-diurnal band induced by the wind, altough it has also been observed the effect of the slope circulation over the shelf. The Ebre river plume doesn't seem to be the responsible of the movements in the measurement points but it has an influence in modifying the interaction between the surface processes and what happens in deeper levels.

For what concerns to the future modelling works, it seems important than the chosen model must be three-dimensional, non linear and it must include a configuration and forcing realistic enough. It must not be forgotten that the dynamics in the region is highly influenced by the general dynamics of the Western Mediterranean, so this must be reflected in the numerical models.

NUMERICAL MODELLING OF THE EBRE REGION DYNAMICS

"Science doesn't try to explain, it built models, principally. By model, I mean a mathematical construction which, with the addition of some verbal interpretations, describe the observed phenomena. The justification of that mathematical construction is just we hope it works".
(*John von Neumann, 1903-1957)*

3 NUMERICAL MODELLING OF THE EBRE REGION DYNAMICS

3.1 INTRODUCTION

One of the main problems in oceanographic research is the difficulty to get real data. It is usually expensive and tough to work in the sea, and the available data sets are limited in temporal and/or spatial resolution. Satellite data is partially solving this problem but it is still not possible to have good 3D pictures of sea state with enough high frequency. One alternative is the use of numerical models to represent the nature in a realistic way. This approach will allow to have a complete description of the sea state and its temporal evolution and a quite good control of the cause-effect relations. The disadvantage is that their results are just mathematical descriptions of nature and they must be validated with real data before being confident on them.

If the numerical modelling approach is chosen, an important point is the choice of the model among all the possibilities present in the oceanographic community. This choice will depend on the dynamical processes that have to be reproduced and the simplifying hypothesis that can be assumed. For coastal applications, a 3D primitive equations model with free surface is desirable, and, for the spatial and temporal range of interest, the hydrostatic and Boussinesq approximations can be accepted.

The numerical resolution of the equations also plays an important role in the choice as the model performance is highly influenced by the way the equations are solved. For shelf-slope implementations a finite-difference scheme solved in an horizontal Arakawa-C grid is preferred[1]. Also, to have a good representation of the bottom processes, the sigma or hybrid coordinates in the vertical are the best possible choice (Kantha and Clayson, 2000).

Once the model is chosen, the initial state and the open boundary will determine the quality of the results. In coastal-shelf implementations, the complex dynamical processes and the fact of having one or more open boundaries, introduces lot of difficulties in the model setup. It is not easy at all to have an initial state perfectly controlled and in equilibrium with the model constraints. Also, the open boundary conditions must be able to realistically reproduce the desired processes and to not introduce numerical noise or unphysical situations.

Finally, the temporal evolution of the model results will be determined also by the forcings applied. The spatial and temporal resolution and the quality of the meteorological forcing fields

[1] It must be noted that, at this moment, 3D finite elements models are still not well established in the oceanographic community. This is the reason why we focus on finite difference models.

and river runoffs have a strong impact into the numerical solutions and should receive a careful treatment.

Another point that must be addressed is the fact that the numerical model will also be used for data assimilation purposes. It is essential to have realistic model to be confident on the error estimations (cf chapter 4) or the data assimilation exercises (cf chapter 5). In consequence the model validation is a basic point that should be treated carefully.

In this chapter, we will set up a numerical model that is specially well suited for coastal applications with the goal of use it in data assimilation exercises and to complement the characterization of the Catalan shelf dynamics began in chapter 2. In section 3.2 a description of the SYMPHONIE model implementation is done: Model characteristics, the initialization technique, the forcing fields description and the data used for model validation are presented. Then, in section 3.3, the model validation is performed with special emphasis in the identification of model errors and limitations. This is essential for assimilation which consists in finding the best estimate given the model errors and the observational errors.

Once we are satisfied with the model configuration and confident on its results, we can use it to study several dynamical features. The complete 3D picture of the hydrodynamics and its temporal evolution provided by the model is a valuable information that will help to characterize several processes that are difficult to measure. In following sections, several idealized model configurations are used to study the non linear adjustment of the slope current (3.4), the role of the wind in the region (3.5) and the shelf-slope exchanges (3.6).

Finally the model configuration for the data assimilation experiments are presented in section 3.7 and several conclusions are pointed out in section 3.7.

3.2 MODEL IMPLEMENTATION

3.2.1 SYMPHONIE model description

Our choice of the model has been to use the SYMPHONIE model developed in the POC (Pôle d'Oceanographie Cotière, Toulouse) by Patrick Marsaleix. This model is a finite difference, free surface, 3D primitive equations model which includes complete thermodynamics. At this moment it can be said that it is a "state of the art" model, and it is basically comparable to other well established models as POM (Blumberg and Mellor, 1987) or GHER (Becker, 1991). The SYMPHONIE model has been extensively used and tested in different configurations for shelf-slope problems as the wind induced circulation on the shelf (Estournel et al., 2003), river plume dynamics (Marsaleix et al., 1998) or slope current

behaviour (Auclair et al., 2003). In addition to that, it has several improvements as the hybrid vertical coordinates or the initialization method that make it really suitable for our needs.

The primitive equations

The model assumes, as basic hypothesis, the non-compressibility, hydrostaticity and Boussinesq approximation, so the equations solved for the movement, in a Cartesian coordinate system (x,y,z) , are:

$$\begin{aligned}
&\frac{\partial u}{\partial t}+\vec{v}\nabla u=-\frac{1}{\rho_0}\frac{\partial p}{\partial x}+fv+\upsilon_h\nabla_H^2 u+\frac{\partial\overline{(-u'w')}}{\partial z}\\
&\frac{\partial v}{\partial t}+\vec{v}\nabla v=-\frac{1}{\rho_0}\frac{\partial p}{\partial y}-fu+\upsilon_h\nabla_H^2 v+\frac{\partial\overline{(-v'w')}}{\partial z}\\
&\frac{\partial u}{\partial x}+\frac{\partial v}{\partial y}+\frac{\partial w}{\partial z}=0
\end{aligned} \qquad \textit{(3.1)}$$

where, $\vec{v}=(u,v,w)$ is the averaged (in the sense of turbulence) 3D velocity field and (u',v',w') are their turbulent counterparts. ρ_0 is reference density, p the pressure field and ν_H is the coefficient of horizontal viscosity. In SYMPHONIE ν_H is a constant value proportional to the grid size and set to 5 m^2/s for a 1km resolution. The two first equations in (3.1) are solved prognostically while the third is the diagnostic equation that allows us to compute vertical movements.

The horizontal pressure gradient is separated into a barotropic, a baroclinic and atmospheric contribution. That is, respectively:

$$\begin{aligned}
&-\frac{1}{\rho_0}\frac{\partial p}{\partial x}=-g\frac{\partial\eta}{\partial x}-\frac{g}{\rho_0}\int_z^\eta\frac{\partial\rho}{\partial x}dz-\frac{1}{\rho_0}\frac{\partial p_a}{\partial x}\\
&-\frac{1}{\rho_0}\frac{\partial p}{\partial y}=-g\frac{\partial\eta}{\partial y}-\frac{g}{\rho_0}\int_z^\eta\frac{\partial\rho}{\partial y}dz-\frac{1}{\rho_0}\frac{\partial p_a}{\partial y}
\end{aligned} \qquad \textit{(3.2)}$$

where p_a indicates atmospheric pressure. It must be noted that in the actual configuration of the model, the atmospheric contribution to the pressure gradient is not included but as it was shown in chapter 2 we do not expect a significative contribution from it.

In addition to the Navier-Stokes equations showed above, the model solves two prognostic conservation equations for the temperature (T) and salinity (S):

$$\frac{\partial T}{\partial t}+\vec{v}\nabla T=-\frac{\partial\overline{(-T'w')}}{\partial z}+\frac{Q_c}{\rho_0 C_p}\frac{\partial I}{\partial z}$$
$$\frac{\partial S}{\partial t}+\vec{v}\nabla S=-\frac{\partial\overline{(-S'w')}}{\partial z} \qquad \textit{(3.3)}$$

where the primes denote turbulent quantities, Q_c is the incident solar flux, I(z) is the short wave radiation that penetrates into the sea and C_p is the heat coefficient for the sea water.

Density is obtained from the temperature and salinity using the linearized form of the state equation:

$$\rho=\rho_0\left[1-\alpha(T-T_0)+\beta(S-S_0)\right] \qquad \textit{(3.4)}$$

where α and β are the thermal and haline expansion coefficients and the subindex 0 denotes reference value. The use of the linear form is to be consistent with the linearized version of the model used in the initialization. In any case, the differences with the complete form are negligible in the configuration we work.

Turbulence submodel

The last terms in the right hand side of the horizontal movement equations (3.1) are the turbulent fluxes. The turbulence scale is lower than the model grid resolution, so they are computed with a turbulence closure. Briefly, we can consider that the turbulent fluxes are related to the vertical gradients:

$$-\left(\overline{u'w'},\overline{v'w'}\right)=\nu_t\frac{\partial}{\partial z}(u,v)$$
$$-\left(\overline{T'w'},\overline{S'w'}\right)=P_t\nu_t\frac{\partial}{\partial z}(T,S) \qquad \textit{(3.5)}$$

where ν_t is the turbulent viscosity that is a function of the dynamics and P_t is the Prandtl number, which is set equal to 1. The turbulent viscosity can be estimated from a relation between the mixing length (L) and the turbulent kinetic energy (K):

$$\nu_t=C_k\,L\,K^{1/2} \qquad \textit{(3.6)}$$

where C_k is an empirical constant.

For the turbulent kinetic energy we use a prognostic equation:

$$\frac{\partial K}{\partial t}+\vec{v}.\nabla K=\nu_t\left[\left(\frac{\partial u}{\partial z}\right)^2+\left(\frac{\partial v}{\partial z}\right)^2\right]+$$
$$+\frac{g}{\rho_0}\nu_t\frac{\partial\rho}{\partial z}+\frac{\partial}{\partial z}\left(\nu_t\frac{K}{\partial z}\right)-\varepsilon+\frac{\partial}{\partial x}\left(\nu_h\frac{K}{\partial x}\right)+\frac{\partial}{\partial y}\left(\nu_h\frac{K}{\partial y}\right) \qquad \textit{(3.7)}$$

where ε represents a dissipation and is computed as a function of the dissipation length L_ε:

$$\varepsilon = \frac{C_\varepsilon K^{3/2}}{L_\varepsilon} \qquad \textbf{(3.8)}$$

where C_ε is an empirical constant.

The mixing and dissipation lengths are computed following Bougeault and Lacarrère (1989) while we define C_ε=0.7 and C_κ=0.1 following Gaspar et al. (1990)

Finally it is worth the comment that the choice of the turbulence submodel is critical for a good modelling of several key issues in the coastal dynamics as the mixed layer depth or river plume dynamics. About the suitability of the turbulence closure used in front of other possibilities, it must be noted that several studies comparing the most popular turbulence schemes can be found in the literature (i.e. Luyten et al., 1996 , and the work done by the GOTM group- www.gotm.net). One of their main conclusions is that there is no universal choice and that all the turbulence models must be "tuned" depending on the implementation. Comparison with data performed in section 3.3.1 shows the good behaviour of this turbulence closure model and the parameters chosen altough it doesn't mean that another scheme wouldn't work fine also.

Spatial and temporal discretization

The equations are discretized using an Arakawa C finite difference scheme (Arakawa and Suárez, 1983). The choice of the most suitable staggered grid among all the possibilities depends on which are the most relevant terms terms of the equations (3.1). Different problems are more sensible to some terms than others (advection, coriolis, pressure gradient,…). An interesting overview of the differences between the staggered grids can be found in Kantha and Clayson (2000) but in general it can be said that in coarse resolution models a B-type grid is preferred while for the high resolution ones for regional applications, C-type grids are best suited.

In the vertical direction, several possibilities are offered in the ocean models. Namely those are z-levels, isopycnal, σ-levels and hybrid combinations of those systems. The choice depends again on the kind of processes that are considered to be the most important. Usually, in climate or large scale modelling isopycnal or level models are preferred, while for coastal and shelf areas terrain following models (σ) are the best suited. Nevertheless there is not a universal choice and all the systems have their limitations. In particular, the main handicap of the σ−models, which are usually chosen for coastal applications, is the so called truncation error associated to the representation of the baroclinic pressure gradient (Haney, 1991). The SYMPHONIE model was originally developed in sigma generalized system but it has recently evolved to a z-σ hybrid system. Schematically it can be said that in shallow areas the levels are

a function of the bathymetry but in the places where the slope of the levels reaches the hydrostatic inconsistency (Haney, 1991) a new z-level is introduced. As a result the number of levels increases in the open sea. This solution allows to have good resolution of the mixed layer, a good representation of the bottom processes over the shelf and reduces drastically the truncation error (see Jordà et al., 2004 for an example in the Catalan sea).

Another key issue of the ocean models is the horizontal advection scheme. The centred schemes (as the one used in the POM) are less diffusive while the upstream ones (as the Smolarckiewicz) are more stable numerically. To preserve sharp gradients as in fronts, diffusivity is not desirable, but if strong discontinuities are present a centred scheme can blow up. The model uses a combination of both as proposed by Beckers (1994) where depending on some stability parameters a linear mix of the two solutions is used.

The temporal discretization used is the classical "leap-frog" scheme in combination with the Asselin filter (Asselin, 1972) to avoid numerical instabilities. It is an explicit scheme more diffusive but cheaper in terms of computer charge that other semi-implicit schemes as the one used in ROMS (Schepetkin and McWilliams, 2005) Also, a mode separation technique between the external (barotropic) and the internal (baroclinic) parts of the equations is used in order to reduce the computer time (Blumberg and Mellor, 1987). This technique is based in the fact that the external mode needs higher temporal resolution in order to represent correctly the fast gravity waves. Consequently the barotropic part is solved more frequently than the baroclinic one, which is more expensive, with a significative gain in computational time.

Boundary conditions

The numerical resolution of the equations presented above requires boundary conditions (BC) in order to give a unique solution. In addition to that, it is there where several physical processes as the atmospheric forcing or the large scale circulation are represented in the model.

In the free surface (z = η) the BC for the horizontal velocity, temperature, salinity and the turbulent kinetic energy are:

$$\begin{aligned}
&\rho_0 \nu_t \left(\frac{\partial u}{\partial z}, \frac{\partial v}{\partial z} \right)_s = \left(\tau_{sx}, \tau_{sy} \right) \\
&\nu_t \frac{\partial T}{\partial z} = Q_e + Q_s + Q_l + (1 - T_r) Q_c \\
&\nu_t \frac{\partial S}{\partial z} = \left(E - P_r \right) S \\
&K = \frac{\left| \vec{\tau}_s \right|}{\rho_0 \sqrt{C_\varepsilon C_k}}
\end{aligned} \qquad \textbf{(3.9)}$$

where τ_s is the wind stress, Q_e is the latent heat flux, Q_s is the sensible heat flux, Q_l is the long wave radiative flux, Q_c is the short wave radiative flux and T_r is the transmission coefficient. E

and P_r respectively represent evaporation and precipitation while C_ε and C_k are turbulent parameters computed in the turbulence submodel.

In the same way boundary conditions must be prescribed in the bottom. Those are:

$$\rho_0 \nu_t \left(\frac{\partial u}{\partial z}, \frac{\partial v}{\partial z} \right)_b = \left(\tau_{bx}, \tau_{by} \right)$$
$$\left(\frac{\partial T}{\partial z}, \frac{\partial S}{\partial z} \right)_b = 0 \qquad \textit{(3.10)}$$
$$K = \frac{\left| \vec{\tau}_b \right|}{\rho_0 \sqrt{C_\varepsilon C_k}}$$

where it is assumed that there is no thermal sources in the bottom. τ_b represents the bottom stress and is computed using a quadratic law:

$$\vec{\tau}_b = \rho_0 C_d \left| \vec{v}_b \right| \vec{v}_b$$
$$C_d = \left(\frac{\kappa}{\log(z / z_0)} \right)^2 \qquad \textit{(3.11)}$$

C_d is the drag coefficient and is computed as a function of the van Karman constant (κ) and the roughness parameter z_0.

Last but not least, there are the lateral boundary conditions. In the closed boundaries (namely the coast) we use free slip conditions but in high resolution models is common to have several lateral open boundaries. The definition of the OBC is critical for the stability and representativity of the model. It has been shown by several authors that interior solutions are highly dependent on the chosen OBC (Palma and Matano, 1998; Marcheisello et al., 2000) and so the choice is not a trivial issue. In our case we get the most satisfactory results using a characteristic equation for the external mode (Flather, 1976):

$$U = U_0 \pm \sqrt{gH} \left(\eta - \eta_0 \right) \qquad \textit{(3.12)}$$

where U represents the component normal to the boundary of the averaged velocity and subindex 0 represents the reference value. The quality of this OBC is closely related to the quality of the reference values used. In our case this is achieved thanks to the initialization method explained below which provides the reference values in the boundaries. For the tangential component and the baroclinic velocities a constant gradient condition is applied $\nabla_n \varphi = \nabla_n \varphi_0$ (where φ is any 3D variable) so the differences across the boundary are set constant all the run. Finally, for the temperature and salinity several choices have been tested but finally the typical advection equation is used for outflows while constant gradient is used for inflow regimes.

In addition to these OBCs, a flow relaxation layer is used to avoid unrealistical gradients between boundaries and model interior. This has been proven to be really useful, specially for

the temperature and salinity, in variable inflow-outflow regimes. It must alse be noted that in any of the cases we tested the use of the relaxation layer damped the variability across the boundaries.

3.2.2 Model domain and forcings used

The model has been implemented in the southern Catalan shelf-slope region (see Fig 3. 1a) in order to complement the data coverage used in chapter 2. The extension of the domain has been defined such that the area of interest, which is around the Ebre delta, is far from the boundaries in order to avoid contamination of the solution due to the boundary conditions. The narrow and wide shelf areas are both included as well as the slope region, so a good comparison of the dynamical regimes in those areas can be done.

The horizontal resolution is 2km, quite below the internal deformation radius (~10km), and the model grid has 141x75 nodes covering an area of 42300 km^2. The grid has been rotated 45º to reduce the number of land points. The x component of the velocity (U) represents across-slope movements while the y-component (V) represents along-slope movements.

In the vertical, the hybrid coordinate system uses a minimum of 21 levels in the shallower areas and a maximum of 41 levels in the deeper parts. The special characteristics of the vertical discretization ensure a good resolution of the mixed layer in the whole domain as well as the bottom boundary layer in shelf areas. A schematic view of the vertical levels distribution can be seen in Fig 3. 1b.

The bathymetry used in the model has been constructed merging data from Canals (1982) and the DBDBV data base with 1' resolution (U.S. Navy's Digital Bathymetric Data Base). Data has been bilinearly interpolated into the model grid and no additional smoothing has been applied. The hybrid vertical coordinate system greatly reduces the truncation errors. Some sensitivity experiments showed that the use of this coordinates, instead of simply using a 21-level sigma coordinate system, reduces the truncation error from 10-20cm/s to 0.3-1cm/s. In consequence, smoothing is not needed. This is important as the bathymetry slope plays a crucial role into the stability of the slope current and its smoothing can degrade the model solution.

The atmospheric forcing of the model is done through a one-way coupling of the atmospheric variables provided by a meteorological model with the sea surface temperature from the oceanic model. The chosen method is based on the well known bulk formulae which were developed in the seventies in the frame of the study of the atmospheric surface layer. The relations are based on bulk weather, SST information from the ocean model and experimentally determined coefficients. The complete formulation can be found in Estournel et al. (2003) and it has successfully been tested in the Gulf of Lions by Dufau-Julliand et al. (2004).

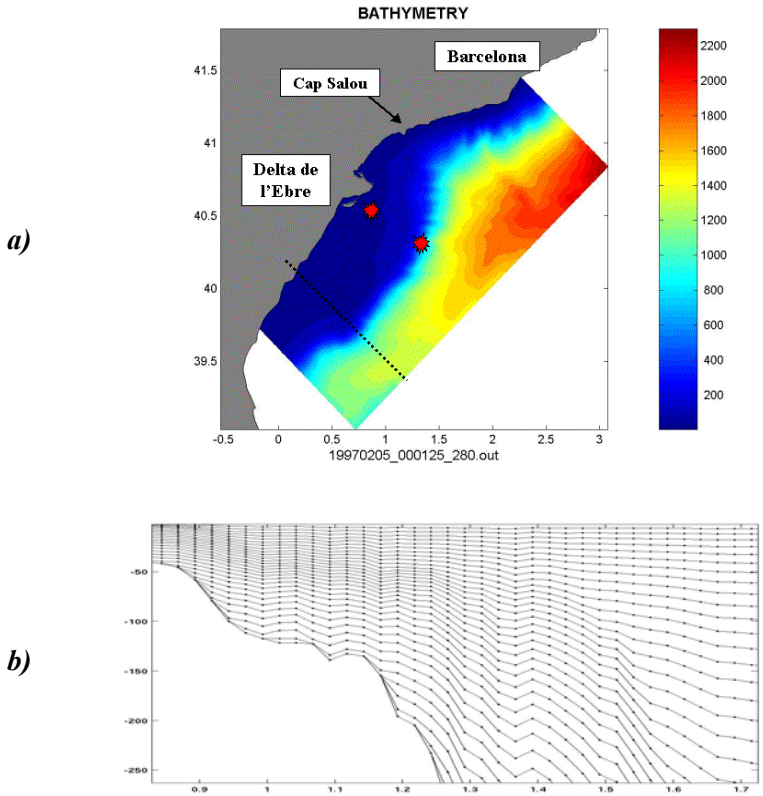

Fig 3. 1: (a) Model domain with bathymetry and (b) vertical grid used in the runs. Dashed line in (a) represents the position of the sections used in the graphs. Stars indicate the current meter positions.

The atmospheric fields are obtained from Arpege atmospheric model (Météo France www.meteofrance.fr). It provides 6-hours analysis for winds and heat fluxes with a spatial resolution of 25km. In appendix 1 , a comparison of ARPEGE wind fields with data shows that its quality is quite satisfactory and very suitable for our needs both in terms of the values and the spatial structures.

Daily averages of the Ebre river runoff are obtained from the "Confederación hidrográfica del Ebro" (www.chebro.es) . Information about river temperature is not available, so we impose an arbitrary and constant value of 11º in winter and 18º in summer. Several tests showed that this doesn't affect the plume results as salinity largely controls the plume evolution.

Finally, the open sea circulation is represented in the model through the open boundary conditions. The modal potential vorticity initialization method (MPV) presented in the next section will provide a solution for the slope circulation in equilibrium with the linearized model equations. We will keep this solution constant in the open boundaries trough the whole simulation, so the variability found in the model results will be generated exclusively in the interior. On the other hand the internal perturbations can freely leave the model through the boundaries.

3.2.3 Model initialization technique

As it was mentioned before, the initialization of numerical models is a critical point for the quality of the results. In basin or global models, it is typical to use a rest state of the ocean and to establish the circulation applying a realistic forcing during several years. In high resolution models this is not possible due to the computational burden and the open boundary conditions. Other alternatives are, for instance, to start the run from climatological data and geostrophic approximations (e.g.: Zavatarelli et al. 2002) or to impose the flux through the boundary conditions. All those methods have several shortcomings. The most critical of them is that there is not a total control on the final state reached after the spin up period. The model adjustment can lead to a final state that significantly differs from what was wished if the initial state is not in equilibrium with the model equations (i.e.: geostrophy is a crude simplification in coastal flows where topography controls the dynamics).

The solution adopted to overcome those problems has been to use the modal potential vorticity method (MPV) first presented by Estournel et al. (2003). This method is based in the resolution of a linearized version of the model transport equations. Afterwards, from the transport, the other 3D variables can be extracted using several approximations. This leads to a quasi-geostrophic equilibrium state that can be tuned with several parameters. The fact that the Northern current is assumed to be in geostrophic equilibrium justifies this assumption. In addition to that, the method has been successfully implemented in several situations in the Gulf of Lions (Auclair et al., 2003, Dufau-Julliand et al., 2004).

Formulation

The MPV formulation is completely developed in Estournel et al. (2003), so, here, I'll just highlight the basic points. Instead of using the whole set of equations, the problem is reduced using several approximations. First of all, the rigid lid approximation is used, so the transport components (U,V) can be deduced from the barotropic stream function ψ:

$$U = -\frac{\partial \psi}{\partial y},\ V = \frac{\partial \psi}{\partial x} \qquad \textbf{(3.13)}$$

After this, the horizontal pressure gradient is decomposed into a vertical and a horizontal term:

$$\nabla_h p(z) = R(z)\nabla p_s = R(z) g \rho(z=0) \nabla \eta \qquad \textbf{(3.14)}$$

where p_s is the pressure in the surface and R(z) can be considered as a nondimensional form of the vertical shear of the geostrophic current.

Using this, the linearized equations of transport, neglecting the advective terms, are:

$$
\begin{aligned}
-f\frac{\partial \psi}{\partial x} &= -g\overline{R}\frac{\partial \eta}{\partial x}+\frac{\tau_{sx}-\tau_{bx}}{\rho_0} \\
&\quad -H\left[\frac{\partial}{\partial x}K_h\frac{\partial}{\partial x}\left(\frac{1}{H}\frac{\partial \psi}{\partial y}\right)+\frac{\partial}{\partial y}K_h\frac{\partial}{\partial y}\left(\frac{1}{H}\frac{\partial \psi}{\partial y}\right)\right] \\
-f\frac{\partial \psi}{\partial y} &= -g\overline{R}\frac{\partial \eta}{\partial y}+\frac{\tau_{sy}-\tau_{by}}{\rho_0} \\
&\quad -H\left[\frac{\partial}{\partial x}K_h\frac{\partial}{\partial x}\left(\frac{1}{H}\frac{\partial \psi}{\partial x}\right)+\frac{\partial}{\partial y}K_h\frac{\partial}{\partial y}\left(\frac{1}{H}\frac{\partial \psi}{\partial x}\right)\right]
\end{aligned}
\qquad \textbf{(3.15)}
$$

where $\overline{R}(x,y)$ is the integral of R in the whole water column and depends on the local bathymetry (h).

$$\overline{R}=\int_{-h}^{z}R(z)dz \qquad \textbf{(3.16)}$$

Solving this system provides a solution for the barotropic stream function in quasi-geostrophic equilibrium. It must be noted that the most important terms of the complete set of equations are kept.

Using (3.13) and (3.14) the 3D velocity field can be obtained from ψ:

$$(u,v)=\frac{R(z)}{\overline{R}}\left(U,V\right) \qquad \textbf{(3.17)}$$

Once (u,v) is found, the surface elevation can be obtained from (3.15) and using the hydrostatic approximation in (3.14) an expression for the perturbation of the density field appears as:

$$\rho'=\rho(0)\frac{\partial R}{\partial z}\eta \qquad \textbf{(3.18)}$$

and the total density field is constructed from:

$$\rho=\rho(z)+\rho' \qquad \textbf{(3.19)}$$

where ρ(z) is a typical density profile obtained from data (for example).

An interesting point is that, in equation (3.15), a relaxation term can be included as $\frac{\psi-\psi_r}{T_r}$

where ψ_r is a reference solution and T_r the relaxation time. Altough we haven't use it here, this could be useful to have a solution that doesn't differ too much from climatology or a large scale model solution.

The implementation of this method implies that the values of ψ in the boundaries and R(z) must be prescribed a priori. A realistic estimation of those parameters can be obtained from previous knowledge of the area, from field data or decomposing the velocity fields obtained

from another model. The fact that R(z) is constant in all the domain could be a shortcoming but no information is available to judge it.

The linearity of the method allows the combination of different solutions. For instance one could compute the solution for an open sea eddy, a slope current and a wind induced circulation and meld all the solutions into an unique field. Dufau-Julliand et al. (2004) combined the solutions from several velocity profiles in order to obtain a good adjustment to a large scale model solution.

As it will be shown latter, this method has proven to be really effective for the coastal model initialization and quite powerful for process-oriented studies. Several tests not presented here, show that its skills are comparable to those of the feature models developed by Gangopadhyay and Robinson (2001) but it is superior in terms of model stability and reduction of the spin up phase.

Ebre model initialization

The barotropic stream function has been deduced from what is usually assumed for the Northern current in our region (Pinot et al., 2002). The slope current has been represented as a transport of 0.7Sv prescribed in the northern boundary and restricted to the slope. This value is an average of the estimations done by Pinot et al.(1995) from field data in the area.

The reference profiles for temperature and salinity are directly obtained from averaging of the FANS-II and FANS-III CTD data. The vertical profile R(z) has been estimated from geostrophic velocities computed from the same data sets (see Fig 3. 2)

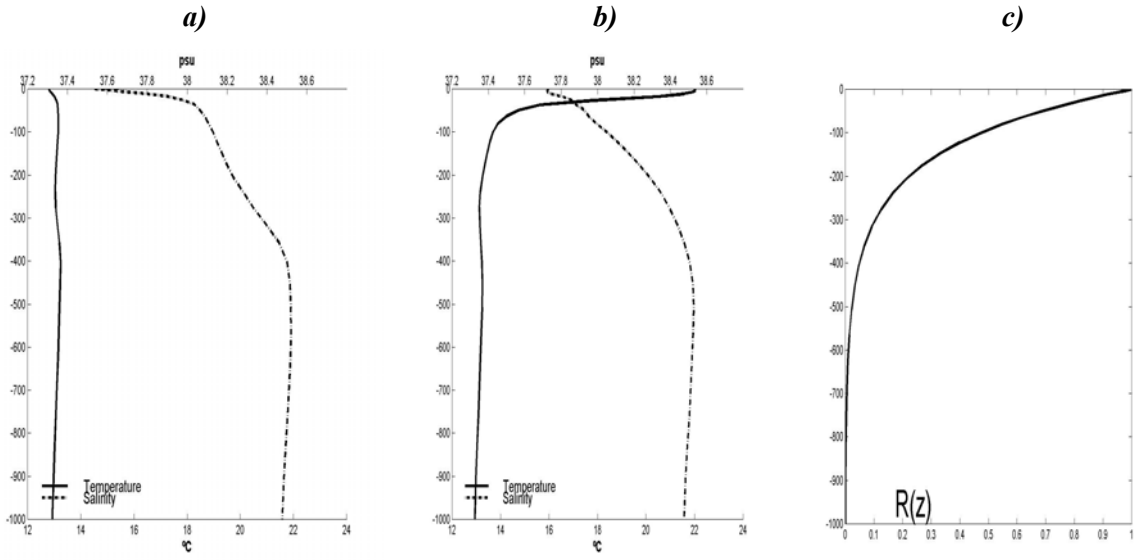

Fig 3. 2: Reference profiles used in the initialization method in (a) winter θ / S, (b)summer θ / S and (c) velocity adimensional profile used in both periods.

As the initialization method is robust and non oversimplified, it is interesting to take a look into the results provided by it. It must be noted that we just prescribed the transport in the northern boundary and the vertical profile of velocities R(z). All the other variables are directly obtained from the linearized equations.

The initial fields for the winter runs obtained from the MPV are presented in Fig 3. 3. The surface elevation, temperature and salinity fields and 3D velocities are in quasi-geostrophic equilibrium. This guarantees that spin up period will be greatly reduced as well as the numerical stability problems. It can also be seen how, in the absence of wind, the current field is controlled by topography. The linear solutions suggest that the equilibrium position for the slope current is such that the base of the current leans against the bathymetry. Wherever we place the inflow position, the MPV displace it to that equilibrium position.

The interaction with the topography is determined by the function R(z). A deeper current tends to flow over the open sea part of the slope, while a shallower one tends to place itself over the shelf break. In this case, the current can easily get on the shelf and may trigger the generation of topographic waves.

Another interesting feature is that south of the shelf widening, the isobaths convergence induces a current intensification. The flow is restricted to flow over the slope, so if its width is reduced (as in the isobaths convergence case just after the shelf widening), by continuity, the current must be narrowed and intensified.

Finally, the weak north eastward current in the open sea is a numerical artefact but sensitivity tests show that it doesn't affect the main results that we will show later on.

A last comment must be done about the suitability of the method for force the coastal model. The set up chosen could be viewed as an overstabilizing solution. In other words, the stability characteristics of the MPV method could avoid to have significant variability in the model interior. This is true, but it is also true that no information at all is available about the exterior of the domain. On the other hand the method has been proven to be transparent enough to export the perturbations generated in the model interior.

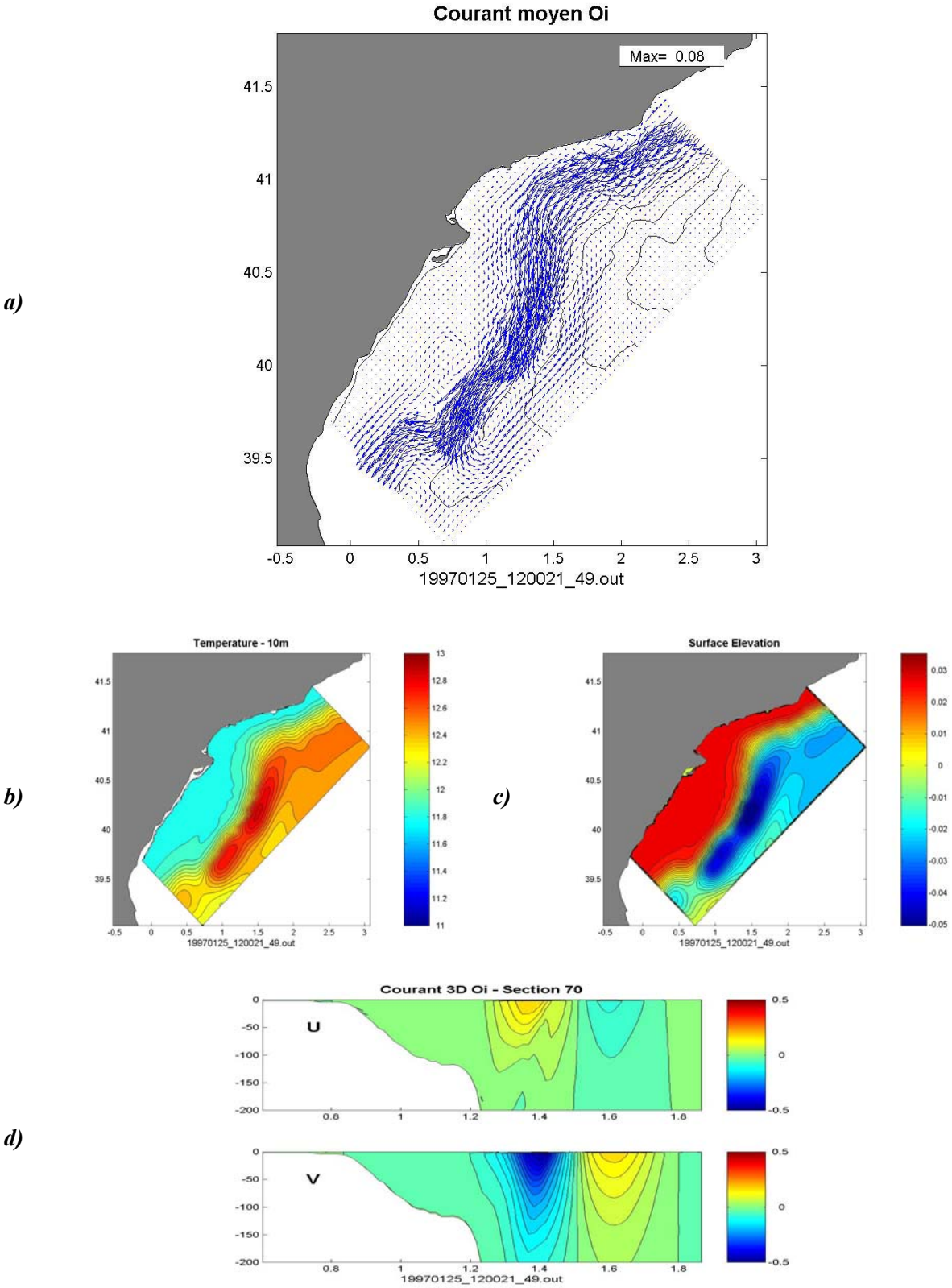

Fig 3. 3: Initial state from the MPV method.(a) Averaged velocity, (b)free surface, (c)10 m temperature and (d)vertical section of the velocity field.

3.2.4 Description of data used to validate the model.

Data used to validate the model results comes from the FANS project (see chapter 2 for an overview of the project). In the frame of that research program, several CTD/ADCP surveys were carried on in the region covering the shelf-slope area around the Ebre delta. In our case, we will use the winter (FANS-II, February 1997) and summer (FANS-III, July 1997) surveys. Around 170 casts were obtained in each campaign with measurements of temperature, salinity, and velocity. It must be noted that velocities obtained from the ADCP have a significant error when bottom depths are greater than 300m (instrument range limit), due to a lack of reference for the ship velocity. In that period, the GPS positioning system was not accurate enough, so velocities over the slope are quite noisy. A visual inspection of the data has been done as well as simple quality controls in order to "clean" from spurious spikes the velocity field. Nevertheless one must keep in mind the observational error associated to ADCP velocities in deep areas when comparison with model will be done. A complete description of the FANS campaigns results can be found in Salat et al. (2002).

Several moorings were also deployed during the FANS project in the shelf and slope area measuring velocity and temperature at several depths. A complete description of the moorings positions and measurements done can be found in chapter 2. Although its temporal covering during the modelling period was irregular, they will be quite useful to complement the validation in terms of statistical properties of the fields.

Sea surface temperature images from AVHRR sensors as well as chlorophyll images from SeaWifs will be used to qualitative validations. The images sources are the same presented in chapter 2. It must be noted that absolute temperature values from SST images are not reliable enough, so we use them just to identify structures. On the other hand SeaWifs images were not yet available for the 1997 period.

3.2.5 Summary and justification of runs

Here we describe the different runs that will be used along this chapter. A summary can be found in

The first step is to validate the model comparing its results with real data. In order to do a useful validation it is necessary to have the most realistic configuration of the model in order to produce results comparable with the available data.

We run two validation simulations to be compared with the data obtained during the FANS-II (winter) and FANS-III (summer) campaings. These runs are initialized via the MPV method with the configuration commented above (section 3.2.3) and the background density profile is

obtained from measured data. For the Ebre river runoff we use real data and for the atmospheric forcing we use the ARPEGE re-analysis for the right period.

The simulations begin one week before the first data is available in order to leave a spin up period to generate a correct river plume and to allow the waves generated by the non-linear adjustments to leave the domain. As the boundary conditions are fixed it is useless to begin the run a longer time before. The simulations last for 20 days until the end of the CTD campaigns.

The REAL1 and REAL3 runs are set up to explore the behaviour of the model in long periods. Here, we run for two months using measured values for the river runoff and the ARPEGE atmospheric forcing.

The BETA1 and BETA3 runs are used to explore the stability of the initial and open boundary conditions. In this case no external forcing is used. The river runoff is set to 0 as well as the wind forcing. Both runs lasts for four months. The first one uses a typical winter density profile while the second one uses a stratified density profile.

Finally, to study the wind driven circulation we use an extensive set of runs (ACA). To cover the most typical situations we run the model in different scenarios defined by the wind forcing, the river runoff and the density profile.

The wind forcings are academic representations of the most typical wind regimes in the region. These regimes have been identified from the ARPEGE results and are represented in Fig 3. 4. We use the Migjorn winds (upwelling favorable), the Llevant and Gregal winds (downwelling favorable) and the Mestral winds. The first three wind blow from the sea and have a wide horizontal structure. In our case we have impose the same wind over all the domain with a maximum velocity of 8m/s. On the other hand, the Mestral wind blows from land channelled by the Ebre valley. In consequence, this wind can be defined as narrow as far as its horizontal structure induce a significative curl. It is also stronger than the open sea winds and we have set it to 10m/s in the standard configuration.

In all cases the wind has temporal evolution described by Fig 3. 4a. During the first two days there is no wind to allow the river plume to freely develop. Then, the wind increases its strength during one day until reach its maximum value. Afterwards, it is set constant during two days which corresponds to the typical duration of the wind bursts in the region. Finally the wind vanishes and the simulation continues without wind for 5 days to investigate if the wind generates permanent structures.

All these simulations have been run using high and low river runoff and in stratified and homogeneous conditions.

RUN	Configuration	Period	Section
Winter - FANS II	Realistic	25 Jan '97 - 15 Feb '97	3.3
Summer - FANS III	Realistic	1 Jul '97 - 20 Jul '97	3.3
REAL 1	Realistic	1 Jan '97 - 28 Feb '97	3.3
REAL3	Realistic	1 Jun '97 - 31 Jul '97	3.3
BETA1 - Homogeneous	No external forcing	4 months	3.4 and 3.6
BETA3 - Stratified	No external forcing	4 months	3.4 and 3.6
ACA-0	Academic - no wind	10 days	3.5 and 3.6
ACA-Mi	Academic - Migjorn	10 days	3.5 and 3.6
ACA-G	Academic - Gregal	10 days	3.5 and 3.6
ACA-L	Academic - Llevant	10 days	3.5 and 3.6
ACA-Me	Academic - Mestral	10 days	3.5 and 3.6

Table 3. 1: Summary of the basic simulations performed
(the sensitivity experiments are not described for clearity)

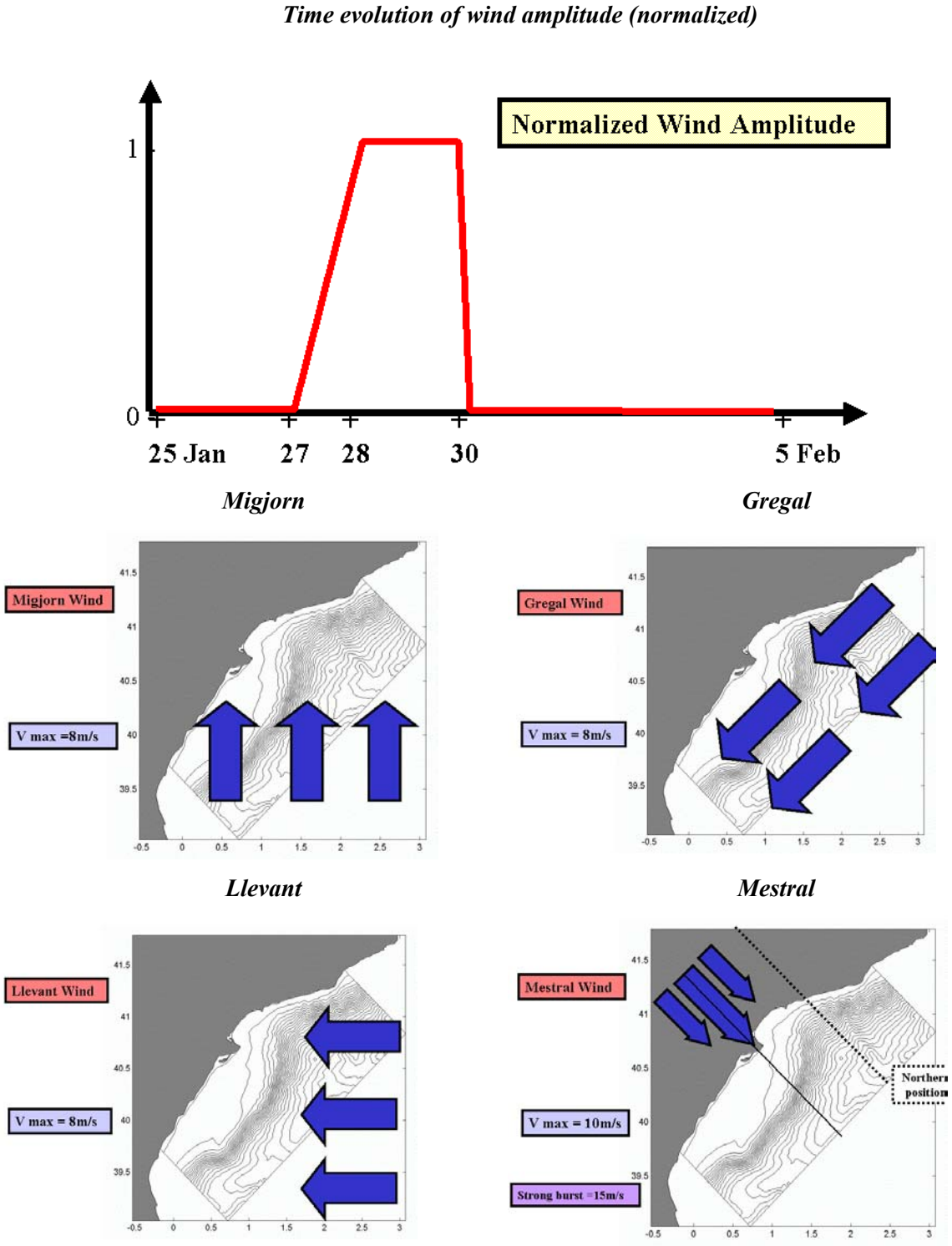

Fig 3. 4: Description of wind fields used in the academic configurations. The time evolution of the wind amplitude in normalized units is presented in top panel. The complete wind field evolution is recovered multiplying this function by the spatial structure represented in the other panels.

3.3 MODEL VALIDATION

3.3.1 Comparison with real data.

Before describing the physical processes simulated by the model we have to know until which point are they reliable. To validate the model results we compare them with real data.

The first diagnostic that can be done is to compare the water masses present in the validation runs with what is found in data. It is possible that during the spin up phase or due to errors into the air-sea fluxes, the model generates water masses with different characteristics that what was measured.

To test if this happens we compare the T/S diagrams from model results with those obtained from data (see Fig 3. 5). In general, model agrees well with data thanks to the initialization method. The principal characteristics are present and no spurious water masses are generated during the simulation. The Winter Mediterranean Deep Water (WDMW, θ =12.7-12.9 ºC and S=38.42-38.46 psu) and the Levantine Intermediate Water (LIW θ= 13.0-13.4 ºC and S=38.48-38.54 psu) are well reproduced, as it was expected, as far as the model forcing is in the surface and the simulation time is not enough to modify the deep structure. However, in shallower levels the surface waters (θ= 12.0-13.0 ºC, S=37.5-38.0 psu in winter and θ= 14.0-23 ºC, S=37.5-38.0 psu in summer) present a bit more dispersion in the data that what was found in the model. A careful analysis of those water shows that this is due to a problem of the model in the representation of the temperature structure and will be addressed later on. For what is concerned to the salinity, the model captures quite well its distribution. The presence of river influenced waters coincides quite well with data in terms of quantity and properties.

Next step is to look precisely to the temperature and salinity structures. CTD simulated casts are obtained from model runs and mapped in order to be compared with T/S maps obtained from data. The interpolation technique used for both data sets, simulated and real, is a simple cubic interpolation.

In winter (FANS-II survey, Fig 3. 6), there is a great disagreement between model and data in the temperature field. The reason is that the initialization technique deduces the temperature and salinity fields from density assuming that both contribute in the same way to the mass field. This implies that their spatial structure is highly correlated. On the other hand it can be seen that this is not happening in data. Probably due to a local surface warming, the measured temperature field differs from the measured salinity, so it is not possible to reproduce such conditions from the chosen initialization technique. Nevertheless, the density field is highly dominated by salinity (Salat et al. 2002), so this it is not a handicap for the quality of simulations.

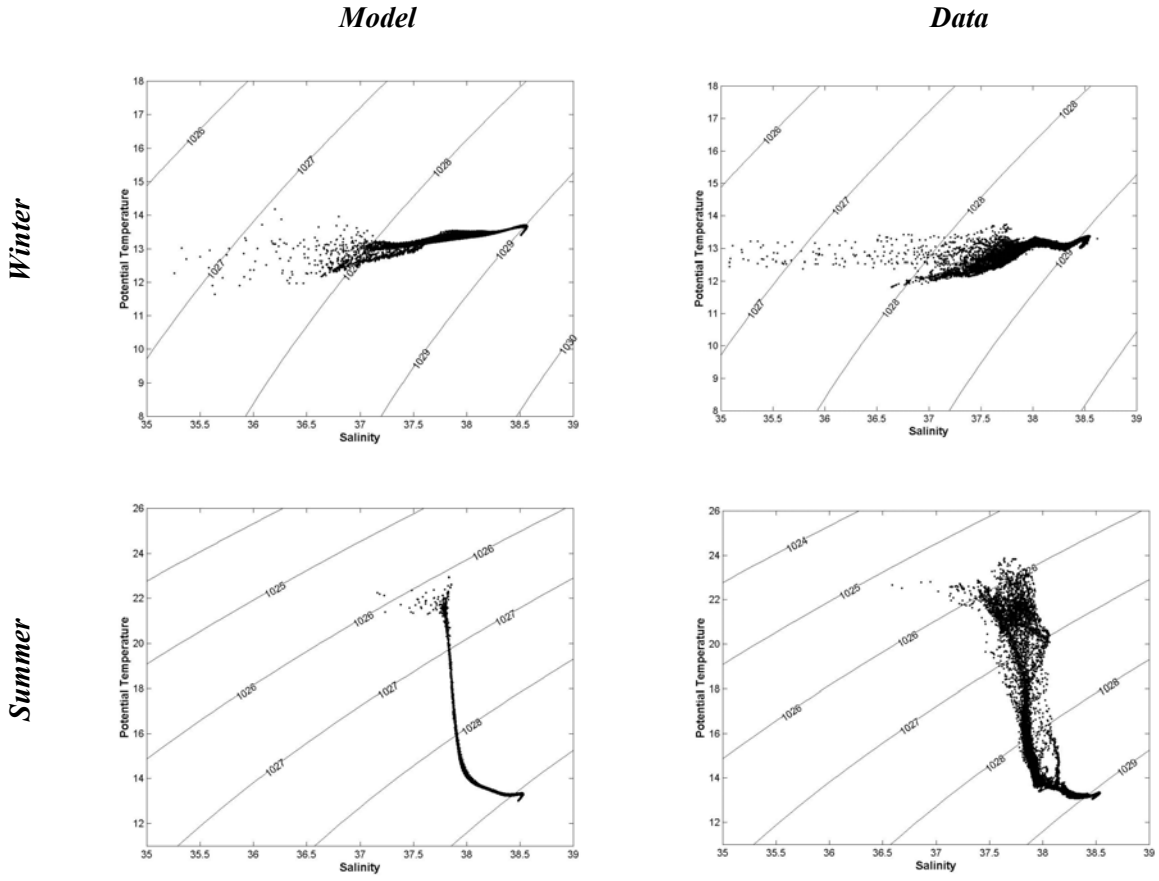

Fig 3. 5: TS diagrams from model validation run and FANS data in summer and winter periods

The salinity fields are more coincident although a slight bias of 0.2 psu is present in the model. The model salinity in the slope and outer shelf regions is quite satisfactory and vertical sections (not shown), show a good agreement with data in the front position and depth. In the inner shelf the plume is well represented in terms of extension, dilution and depth although its position is not correct. Some sensitivity experiments helped us to better understand this. The good structure of the plume is due to the good calibration of the turbulence submodel while its wrong position is caused by errors in the wind direction provided by the ARPEGE model.

In summer conditions (FANS-III, Fig 3. 6) the problem with the temperature field is still present but once more, it is a salinity-driven regime, so this has no great influence onto the quality of results. The salinity field is again slightly biased 0.2 but the vertical structure is well captured and the gradients are correct. The river plume is better placed than in the winter case but its extension is more limited in the model than in data. This is due to the fact that, in summer, river runoff is low (~200m^3/s) and a longer spin up period should be used to allow the plume to mix with shelf waters.

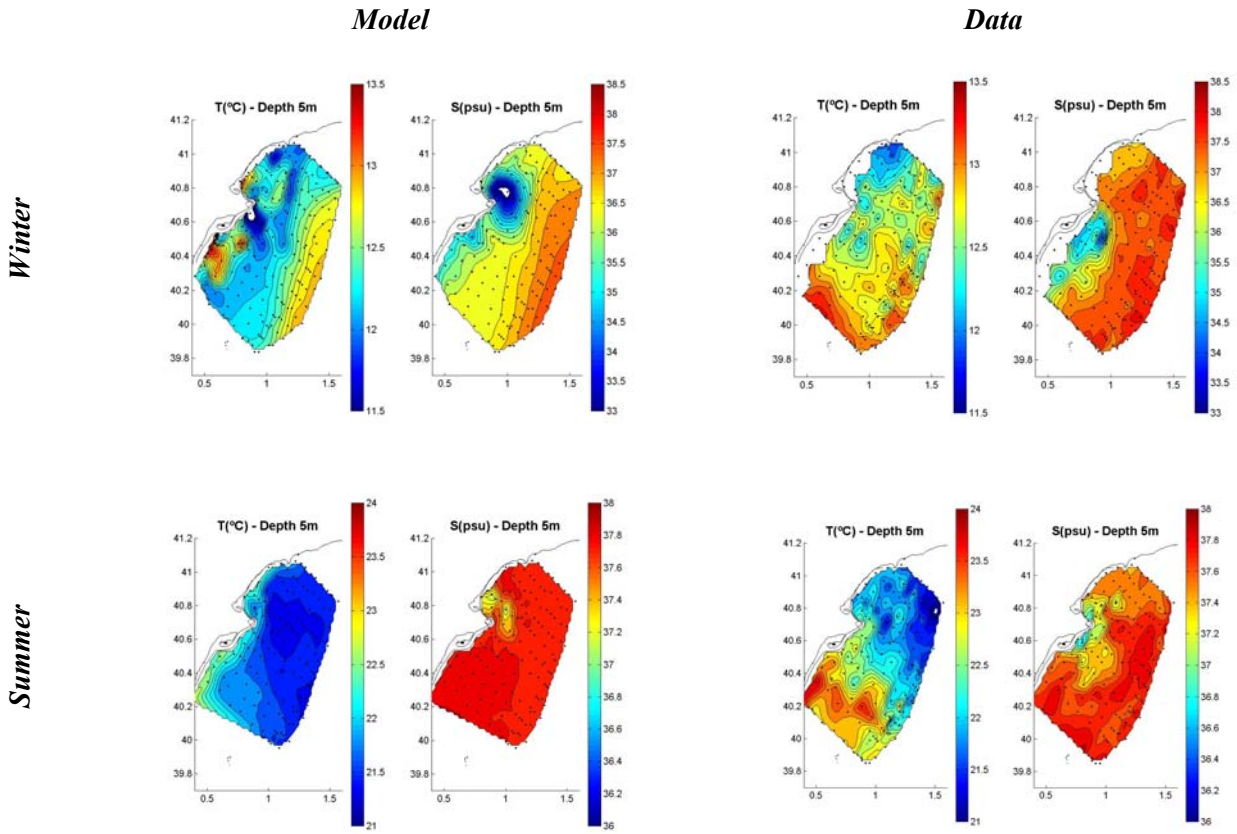

Fig 3. 6: Temperature and salinity obtained from CTD casts for winter (FANS-II) and summer (FANS-III) surveys. CTD casts positions are marked with dots.

The FANS surveys provided ADCP measurements of currents until 300m. We used them to compare with model solutions but keeping on mind that they have an important observational error associated. The winter results (see Fig 3. 7) present a good correlation between model and data. The slope current is well reproduced in terms of intensity, width, position and vertical structure although the weak meander measured is not located in the same place. Over the shelf, data is quite noisy and is difficult to compare with it. Nevertheless it seems that the north-eastward coastal current simulated is also present in the measurements (this current is explained below, in the summer period).

In summer, the model velocity field shows again a good agreement with data in the representation of the slope current both in the surface layers and in its vertical structure. Nevertheless there is a slope current inversion measured in the northern part and interpreted by Salat et al. (2002) as a shelf wave that is not modelled. This enlightens one of the limitations of our configuration: it includes just locally generated variability, so propagating waves or advected structures as eddies cannot be represented.

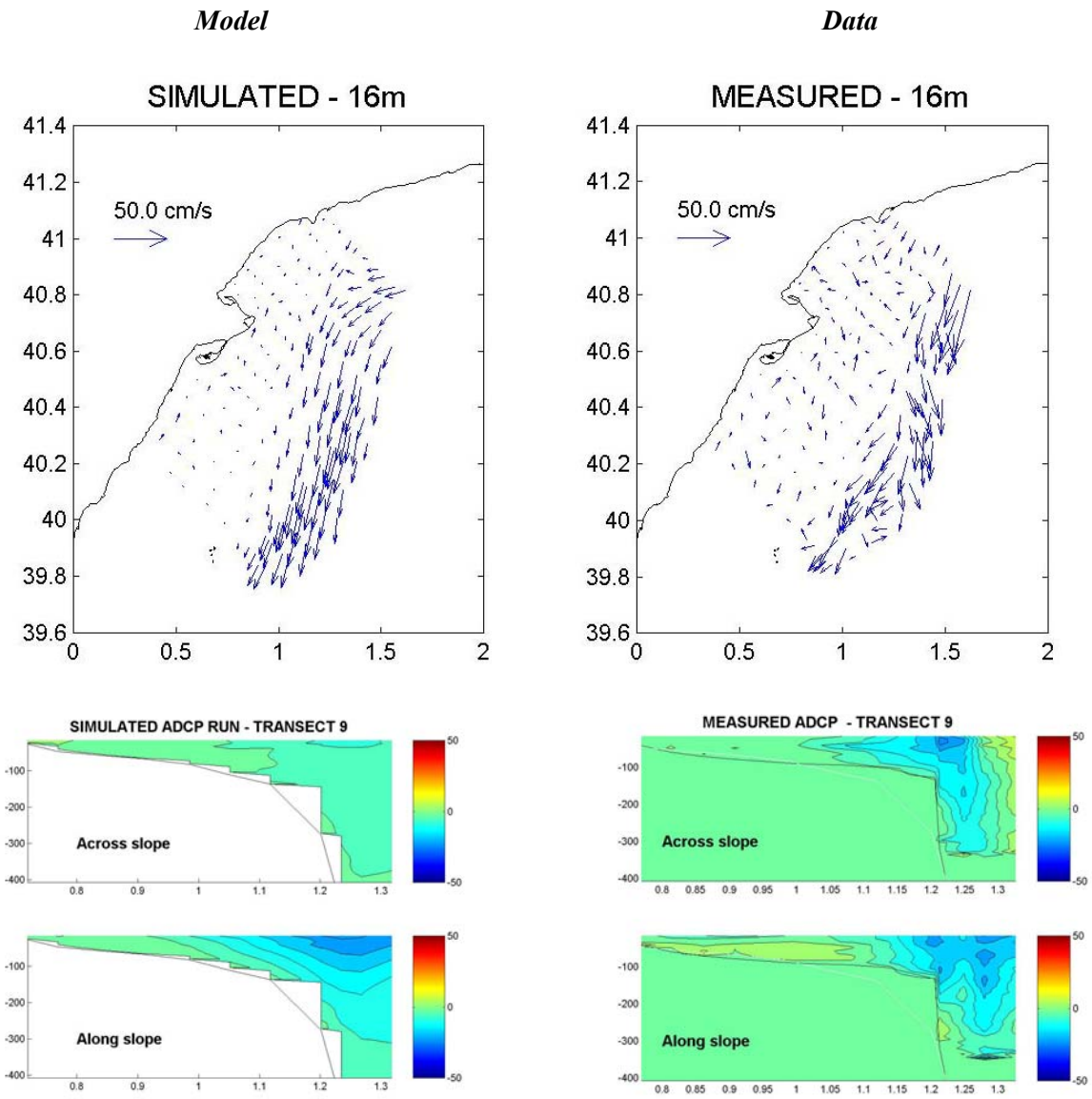

Fig 3. 7: Comparison of current field at 16m depth and in a vertical section along a transect in the winter period.

Over the shelf there is greater correlation between model and data that in the winter case thanks to the fact that currents are more energetic. The north-eastward coastal current around the Ebre delta is well reproduced by the model in terms of intensity and position. The rest of circulation over the shelf is more difficult to compare as it is not a clear pattern neither in the model nor in data.

It is interesting to note that picture of simulated ADCP is also noisy even if there is no observational error that could introduce it. Comparison with instant model outputs show that this noise is due to the inertial oscillations which dominates the shelf and upper layers in open ocean (see Chapter 2) and due to sinopticity errors in the measurements.

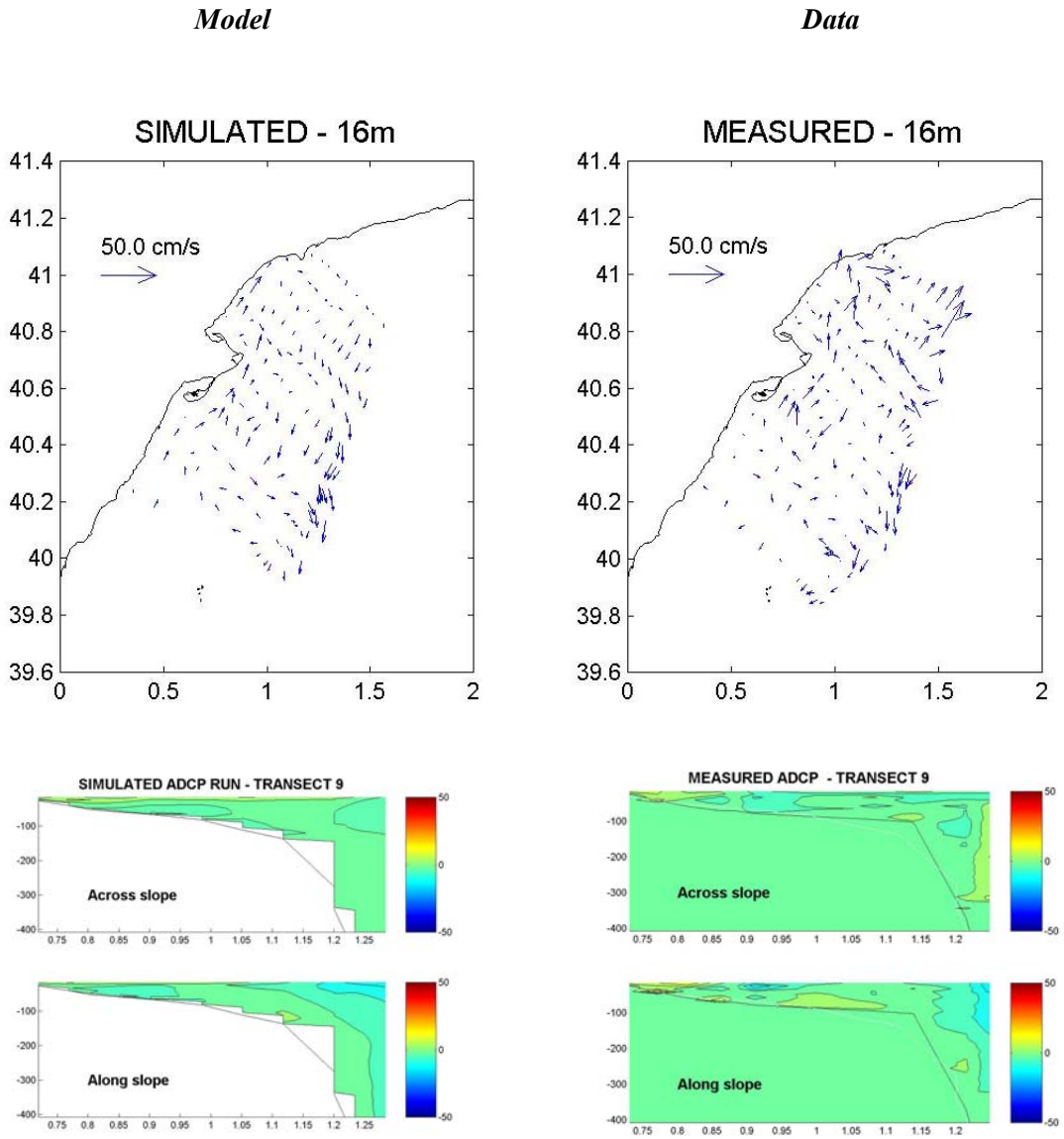

Fig 3. 8: Comparison of current field at 16m depth and in a vertical section along a transect in the winter period.

In order to gain an insight into the kind of processes that our model configuration can capture, we run the model in the same configuration presented before but for a long period (two months) and we look at the frequency content of model variability. In Fig 3. 9 we present the results for currents at 100m depth over the slope and at 15m depth over the shelf and we compare them with current meter data in the same locations and periods (see Fig 3. 1 for location).

The model energetic content in the near-inertial band is in good agreement with data both over the shelf and the slope. On the other hand, in lower frequencies (T > 2 days) the model is much less energetic suggesting that much of the energy content found in data in that frequency

band is due to non-locally generated variability (this hypothesis should be further investigated using a realistic nested model). In higher frequencies (T<12h), it seems that the model lacks the internal wave content. This has several possible explanations. First of all the model is isolated from the open sea (the boundary conditions are fixed), so it can only reproduce locally generated internal wave which reduces a lot the possible contributions. Second, model resolution is 2km so waves with smaller wavelength (probably those with higher frequency) can not be reproduced. Finally, as the model is hydrostatic, the spectra of internal waves that are compatible with equations is limited to those waves with wavelength higher than the water column depth (Gill, 1982).

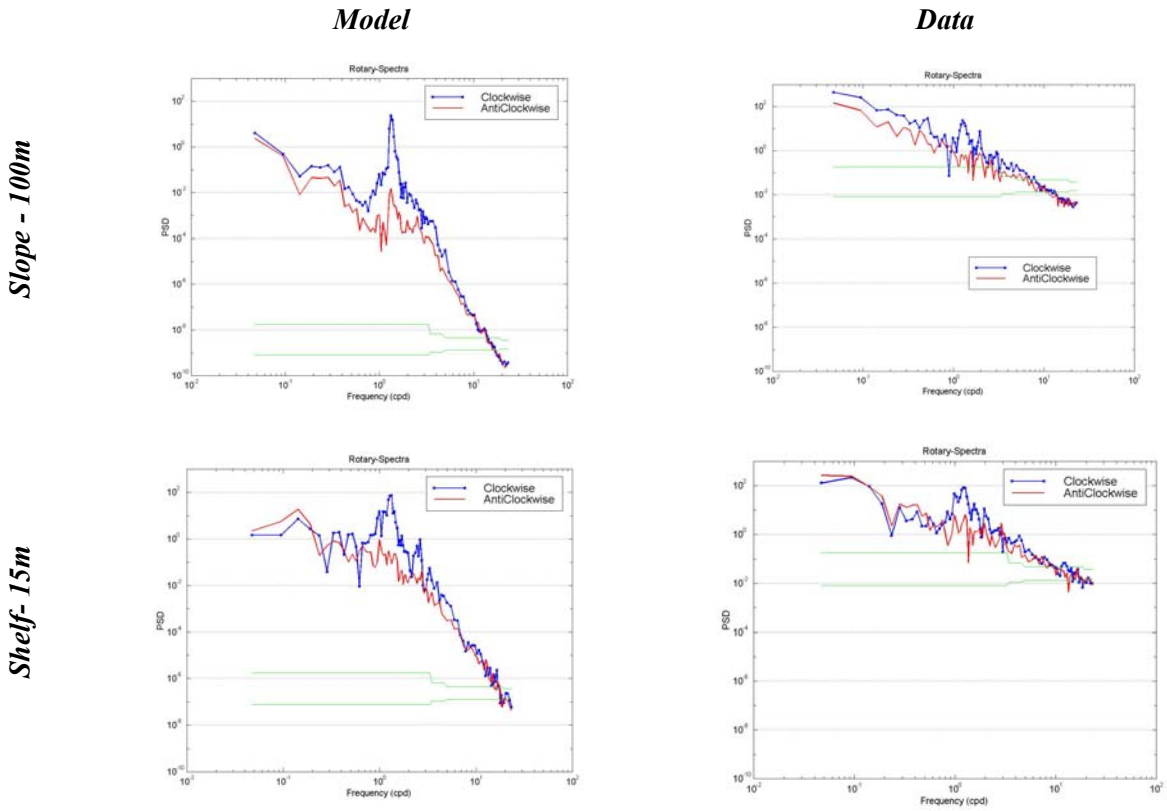

Fig 3. 9: Comparison of the currents rotational spectra in the summer configuration over the slope (top) and the shelf(bottom). Frequency units are cycles per day and the green lines indicate the 95% confidence level.

The conclusion of the model validation is that it reproduces well the main features observed. This is, namely, the slope current, the river plume and shelf response to wind. Water masses are well represented although concordance in the temperature field is limited. However the model configuration presents a major limitation as the open sea variability is not included and no importation of mesoscale is possible. The only way to overcome this problem would be the use of nested models, so the open sea variability will be transmitted from a regional model to our shelf model across the open boundaries. The problem is that, until now, there is no available

model to be nested in which correctly reproduces the dynamics in our area. The results provided by the available models are not satisfactory in terms of the location and characteristics of the Northern current (see Jordà et al., 2004, for an in-depth validation of a nested model). This means that we will restrict our study to the local-generated variability induced by the atmospheric forcing or the current instabilities.

3.3.2 Description of model results

Once the model has been compared with data and some of its limitations illustrated, it is interesting to take a look at the 3D pictures provided by it and at to its time evolution. In this section we will briefly comment the main features present in the model in both simulations (winter and summer).

Winter - FANS II simulation (25 January - 15 February 1997)

In this period, there was no predominance of any wind regime. During the twenty days of simulation there was an alternance of Gregal (NE), Mistral (NW) and Migjorn (S) winds but no one lasted for more than one day. Wind stress associated to those winds was between 0.1-0.2 N/m^2 and after every burst a calm period appeared (see Fig 3. 10a).

The slope current introduced in the initial conditions remains stable along the run with no significative variation of position or depth. Simulated current meters show a decreasing of its intensity from 0.5 to 0.2 m/s (see Fig 3. 10b) but it is due to a slight displacement of the current axis from the mooring position. After 4 days of simulation, a topographic wave is generated in the northern part due to the non-linear adjustment and begins to evolve with a phase velocity of 8 cm/s. This meander reaches the shelf break and a branch of the current enters into the shelf. There, it gains negative vorticity and establishes an eddy type structure that is advected with the same phase velocity.

Over imposed to this, there is the wind-induced circulation occupying an Ekman layer of just 10-15m depth due to the low persistence of winds. No clear velocity pattern is established but inertial oscillations are triggered in all the domain with intensities around 10cm/s. Inertial-internal waves are generated and can be felt in deeper layers (100-500m) with horizontal velocities of 3-5cm/s (see Fig 3. 10b).

Over the shelf there are two different regimes. In the northern part, where the shelf is narrow (see Fig 3. 1), the dynamics is totally controlled by the slope current and its variability (namely the current meandering and the associated anticyclone). In the southern part, where the shelf is wide, the controlling factor is the plume dynamics. The river runoff in this period is high ($>800m^3/s$) and the bulge of the river plume is completely developed after 2-3days. The bulge spreads 25-30km with a thickness of 8-10m. Its horizontal evolution strongly depends on the

wind direction, and, as this is highly variable, the plume position changes quickly. In all the cases the shelf break limits the plume spreading seawards. Another effect of this variable wind is on the vertical mixing of the plume. Fast changes in the forcing enhance turbulence, so vertical mixing of fresh waters is increased.

Linked to the bulge of the river plume, an anticyclonic circulation is created between 6th-13rd of February when wind is weak around the Ebre Delta. This structure remains more or less fixed between the Ebre Delta and the shelf break (see Fig 3. 11a) until a strong S-SW burst breaks it. Velocities associated to the anticyclone are around 20cm/s in surface and it is felt until 20m depth. The special location where it is placed, between the gulf of St. Jordi and the shelf break favours the advection of inner shelf waters to the slope where they are advected by the slope current downstream.

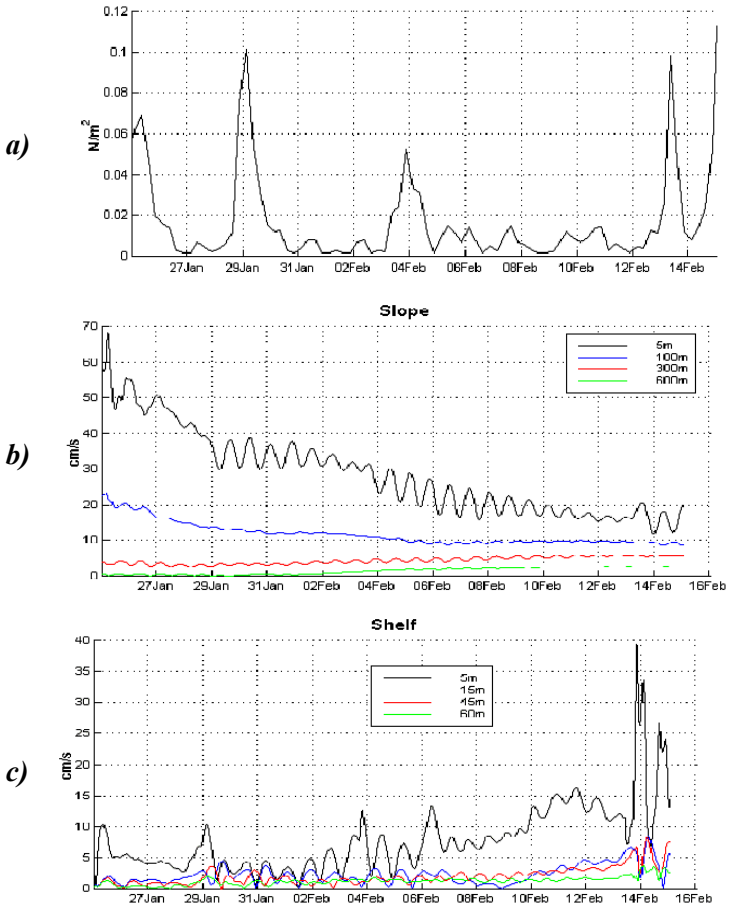

Fig 3. 10: Time series simulated in the winter period of (a) wind and current intensity for (b) slope and (c) shelf.

The high runoff has a secondary effect. The river plume extends south-westwards close to the coast progressing 20km/day and generating a buoyancy driven coastal current in a 10km band from the coast. This current has a thickness of 10 meters and, due to instability processes,

it begins to develop a strong meandering after 5 days. The wavelength of this meandering is about 10km and associated velocities are around 20cm/s in surface. The amplitude of these current oscillations grows until the current reaches a structure similar to a series of cyclone-anticyclone along the coast (see Fig 3. 11a). In the convergence zone of those dipoles, current is directed to the coast, and when water impinges on it, a downwelling is forced by continuity. In the same way, an upwelling is created where current is directed seaward from the coast. Those vertical movements imply an upward (downward) advection of dense (light) water. As a consequence, an alternate pattern of high-low density small structures is set up all along the coast at the south of the Ebre Delta (see Fig 3. 11b). Unfortunately, we have no real data to validate this behaviour.

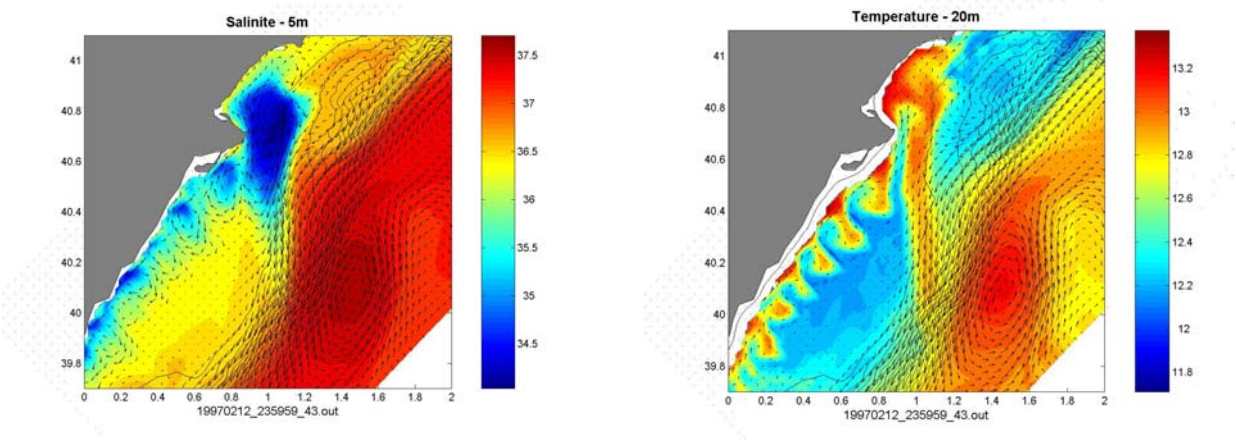

Fig 3. 11: Solutions of the winter validation run at 12th February. (a) Velocity and salinity at 5m depth (b)Velocity and temperature at 20m depth

Summer - FANS III simulation (1-20 July 1997)

In this period, the wind is also variable and the regime changes several times during the simulation. The main bursts are from Gregal (NE), Mestral (NW) and Migjorn(S). The last one last for two days and is followed by 2 days of calm (see Fig 3. 12a).

The circulation over the slope is quite stable without any significative change in its properties and, in this case, no propagating wave is generated. Over imposed to this circulation pattern, there are the wind-induced currents. A fast adjustment of the sea state is reached after each wind burst in the upper 20 meters and inertial oscillations are triggered in the whole water column (see Fig 3. 12b). It is interesting to note that its amplitude over the thermocline (time series at 5 meters in Fig 3. 12) is more important than in the winter case.

Over the shelf the plume extension is quite reduced because of the low river runoff (<200m^3/s), and circulation is just driven by the wind. First the Gregal (NE) burst and after the

Migjorn (S) wind, induces vertical movements all along the coast. There, the situation quickly evolves from a downwelling that lasts for 2 days to an upwelling that is present for 3 days. Vertical displacements are around 15 meters and the effects of the upwelling can be felt until 50m depth.

The Migjorn wind also generates a coastal current directed north-eastward in a 10km band close to the coast. Its intensity in surface is around 15cm/s and has a thickness of 50m. This coastal current is also measured by ADCP in good agreement with simulated ADCP (see Fig 3. 8).

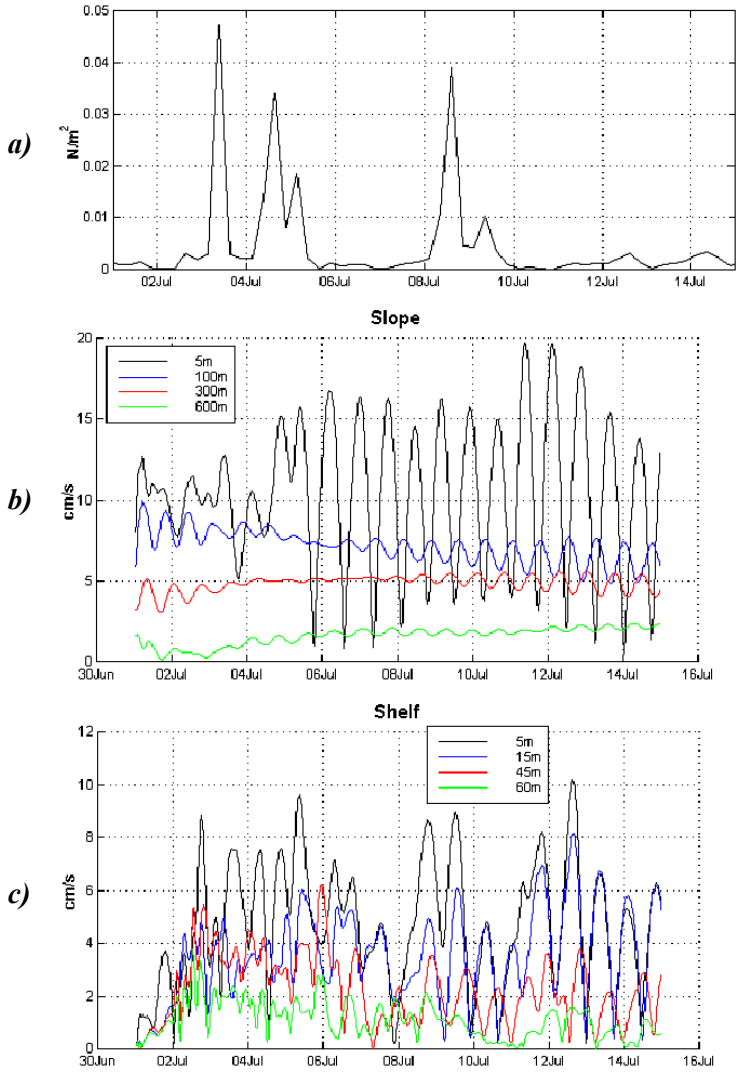

Fig 3. 12: Time series of (a) wind and current intensity simulated in the summer period for (b) slope and (c) shelf.

Finally, the temperature field shows a local warming all along the coast but especially strong in the southern part. The temperature increment is of 1-2ºC in the first 15m depth and occupies a 8km band close to the coast (see Fig 3. 13a). This kind of warming has also been

found in SST images (see Fig 3. 13b). The presence of this feature is due to the combined effect of a strong heat flux (as is usual in summer), with an upwelling favourable wind (namely S-SW winds). In normal conditions, the effects of the heat flux are transferred into the water column through the turbulent mixing. When the upwelling wind is present, it generates upward displacements near the coast which inhibits the vertical turbulent mixing, so the heating is restricted to the upper layers. These vertical displacements are limited to a coastal band with a width of the deformation radius, which is coherent with the 8km band found in the temperature fields.

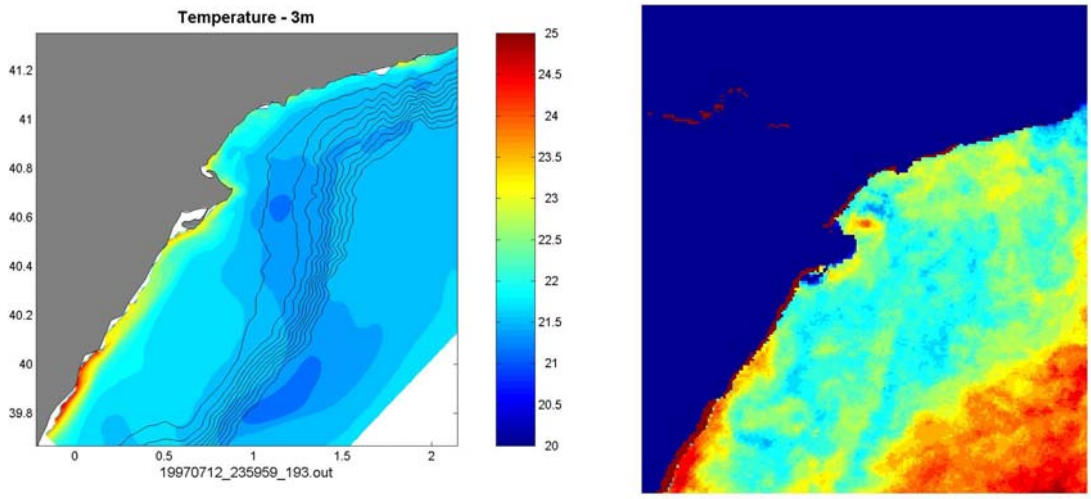

Fig 3. 13:Sea suface temperature for July 12th (a) model and (b) satellite image.

3.3.3 Sensitivity of the model to different parameters

Several sensitivity tests have been performed in order to be more confident in the model configuration and to have an insight into the possible sources of error of our modelling system.

One of the first assumptions that have been done is in the initialization phase. As it was explained before, we defined a current profile R(z) based in the vertical profiles of geostrophic velocity obtained from data collected during the FANS-II and FANS-III cruises. The number of profiles deep enough to be confident in the geostrophic computations is limited and do not cover the entire modelling domain. So, the first sensitivity test carried on is about the influence of the depth of the base of the slope current into the model results. To do this test, several vertical profiles have been used representing different current depths while keeping the same integrated transport. The range of depths is between 150 and 450 meters which have been chosen as extreme cases.

The results (see Fig 3. 14) show that the current position of equilibrium changes from one profile to another: The slope current tends to be placed so the base of the current lies against the bottom. For instance the current with a base at 450m has its core placed over the 1000m isobath while the western limit of the current lies against the slope. For all the range between 450 meters and 200m, which is the depth of the shelf break, and due to the steepness of the slope, all the current solutions are quite similar. Nevertheless, when current depth is less than the shelf break depth, part of the current is placed over the shelf where it is much less constrained by the topography. The stability effect of the slope is lost and the current is much more sensible to the wind forcing and the topographic-type waves generated in the area develop larger meanders.

Current base at 150m ***Current base at 450m***

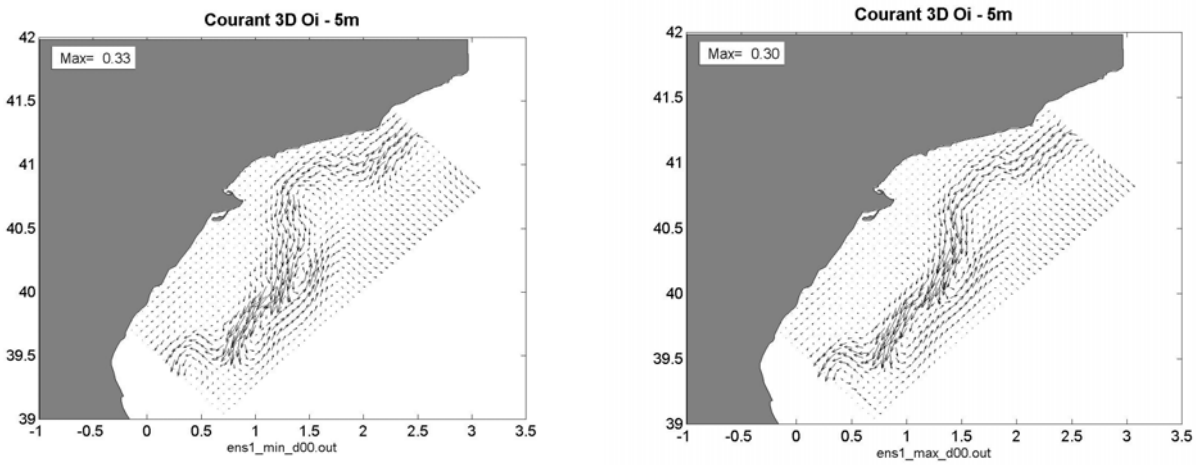

Fig 3. 14:Surface velocity when using a shallow current (right) and a deep current (right)

The comparison with data presented in chapter 2 suggests that it is not quite realistic to consider the slope current thickness shallower than 200m. On the other hand, the model solution seems not too sensitive to variations of the current thickness if it is greater than the shelf break. So, the profile used seems quite appropriate and comparison with data confirmed this choice.

We also took a look at the effect of the stratification over the vertical profile. In other words, how the different conditions for winter or summer can modify the velocity profile. The conclusion was that after 20 days of simulation, which is the typical run time used, no significative modification of the vertical distribution of velocities is found. It seems that, in stratified conditions, a higher order mode could be excited by the mean current over the shelf but after 20 days it has not well established yet. This suggests that for a complete set up of the dynamics in the shelf, a longer run should be used but in this case we should also vary open boundary conditions. That kind of configuration escapes the scope of this study but it would be very interesting to have a realistic set up (namely a nested model) able to run for a long period .

Another parameter that has been chosen a priori is the horizontal position of the current, which in our case was centred over the slope. Several tests carried on changing the horizontal position of the current axe show that the initialization method limits its equilibrium position. For a given vertical profile, all the different initial conditions show the same final solution where the current is placed where its base lies against the slope bottom. In other words, it could be said that the initialization method suggests that a slope current in quasi-geostrophic equilibrium tends to be placed where its base intersects the bottom.

The horizontal distribution of velocities can also have an important impact onto the stability of the slope current. Flexas et al. (2004a) showed that the capacity of the Northern current to generate barotropic instability depends on the shape of the horizontal profile of velocity. Nevertheless, several tests carried on changing this profile showed that, once the width of the current was fixed, the shape of the slope jet was unique. This is due to the combined effect of friction and buoyancy fluxes in the bottom boundary layer for a narrow current in a stratified environment (Chapman and Lentz, 1997). In conclusion, we didn't find a sensitivity of model results to changes on this parameter.

A key point to study for coastal implementations is the turbulence submodel parameters. In our case we tested the choice of the constants C_ε and C_κ. We compared the results obtained using the values proposed by Gaspar et al. (1990) with the results obtained with those proposed by Johns and by Mellor and Yamada (1982), (see Table 3. 2). The model solution showed to be quite sensitive to those parameters especially in the representation of the river plume. In order to chose the best, we used the comparison with the CTD data presented before to validate the model, and the values proposed by Gaspar et al.(1990) lead to the best agreement between model solution and data in terms of plume extension and depth.

	C_ε	C_κ
Gaspar et al. (1990)	***0.1***	***0.7***
Johns	***0.53***	***0.15***
Mellor and Yamada (1982)	***0.47***	***0.17***

Table 3. 2: *Different values for the turbulent parameters C_ε and C_κ used in the sensitivity experiements*

Another "classical" problem in regional and coastal modelling is the choice of the lateral boundary conditions. We took a careful look to their behaviour and the impact of variations of them onto the model evolution. The conclusion is that the formulation presented before behaves

strikingly good. It is very stable and the interior solution is not at all contaminated by them. Boundaries are quite "transparent" to outflows with no significative reflection neither of gravity waves nor of internal waves. The flow relaxation layer also ensures a smooth transition in the fields when fast changes of inflow-outflow regimes appear. Nevertheless, several tests have been carried on for the tracers open boundary conditions and are discussed in Jordà et al. (2004). In summary it can be said that the use of different formulations as the typical advection formulation, radiation conditions or a tendency equation leads to signficatively different results specially for long runs (T>15days). In spite of that it must be said there is no objective criterium to chose one formulation among the others as there is no enough data to compare. In short, we have seen that the choice adopted is well adapted for the implementation done and for the goals of this study.

Finally, we wanted to test a parameter that is usually neglected in small area implementations: The β parameter. In a model domain as the one we use, that is quite perpendicular to the parallels, we expect the β-effect to have a non-negligible influence in the model evolution and the current adjustment. Schematically it could be said that the β-effect tends to align the flow following lines of constant latitude. In our case this means that there will be a small force that "pushes" the current against the slope. We ran the model in the f-plane (β=0) and we found a slight difference into the adjustment of the slope current and the shelf circulation. Nevertheless it must be noted that this differences became masked when a strong perturbation is present as a wind burst or a current meander. It can be said that its effect is of second order of importance in front of the typical forcing considered and that basic features wouldn't be significatively changed by the assumption of f-plane.

3.4 NON LINEAR ADJUSTMENT OF THE SLOPE CURRENT

The first simulation we are going to look at, is a long model run without external forcing (wind or river runoff). This will allow us to test the stability of the initial state and the open boundary conditions and to have an insight into the non linear adjustment of the model state.

We initialize the model using the technique explained above and we leave it to freely evolve without wind or river forcing. The stratification is typical of summer and the values in the open boundary conditions are set equal to the initial field, so the inflow in the northern boundary remains constant during all the simulation time. The run lasts for several weeks to be sure of the stability of the initial conditions.

At first sight it could be said that the initial state is quite stable. After two weeks the velocity field seems really similar to the initial state confirming the quality of the MPV initialization method. The only apparent effect is just a small deceleration of the current

produced by non linear friction and no significative numerical diffusion is observed. Over imposed to the stable flow there are also small oscillations with wavelength ~ 35km and frequency slightly greater than the inertial frequency produced by the non-linear adjustment of the current. Those oscillations propagate away and disappear after some days.

On the other hand, if we look to the results for a longer period in stratified conditions, an interesting process appears. The non linear adjustment of the current due to the advective terms, which were not included in the initialization procedure, induces across slope displacements of the slope jet which generates a wave that propagates downstream with a phase velocity of 2-4cm/s (~1.7-3.5km/day). The point that drew our attention is the behaviour of this wave when it arrives to the shelf widening where the slope direction changes abruptly. Its amplitude grows up and the wave occupies the entire shelf (see Fig 3. 15) in a sort of amplification process.

The wave propagates slowly over the slope in a quasi-geostrophic equilibrium, so a first guess about its origin is that it can be a topographic Rossby wave. In order to confirm this we take a look at the definition of the Rossby wave phase velocity to compare with the model results. If a linear profile is assumed for the topography ($H = H_0(1 - sy)$, where H_0 is the maximum depth, s is the slope and it is considered that H is constant along the x direction), the phase velocity in the along slope direction will be (Pedlosky, 1987) :

$$C_x = -\frac{sf}{L}\frac{1}{k^2 + l^2 + F/L^2} \qquad \textbf{(3.20)}$$

where L is the geometric length scale of the perturbation, (k,l) are the wave numbers in the x and y direction, respectively, and F is the ratio of L to the Rossby deformation radius R for a layer of depth D, so:

$$F = \left(\frac{L}{R}\right)^2 = \left(\frac{f^2 L^2}{gD}\right) \qquad \textbf{(3.21)}$$

It must be noted that C_x is always negative, meaning that the wave propagates leaving the low depths at its right.

Using the typical observed values for the different parameters (Table 3. 3) and considering, for clarity, that waves just propagate in the x-direction (l=0) we obtain a value of C_x=2.13km/day. This matches with the values observed in the model results, so it seems that the simulated wave is a topographic Rossby wave. It is interesting to note that, although this wave was generated due to a numerical adjustment, it is representative of a phenomena that is present in nature and, specially, in the Northwestern Mediterranean (Millot, 1999). Also, Flexas et al. (2004a, 2004b) showed, from laboratory and numerical experiments, how the barotropic instability of the Northern current could generate topographic Rossby waves over the shelf break.

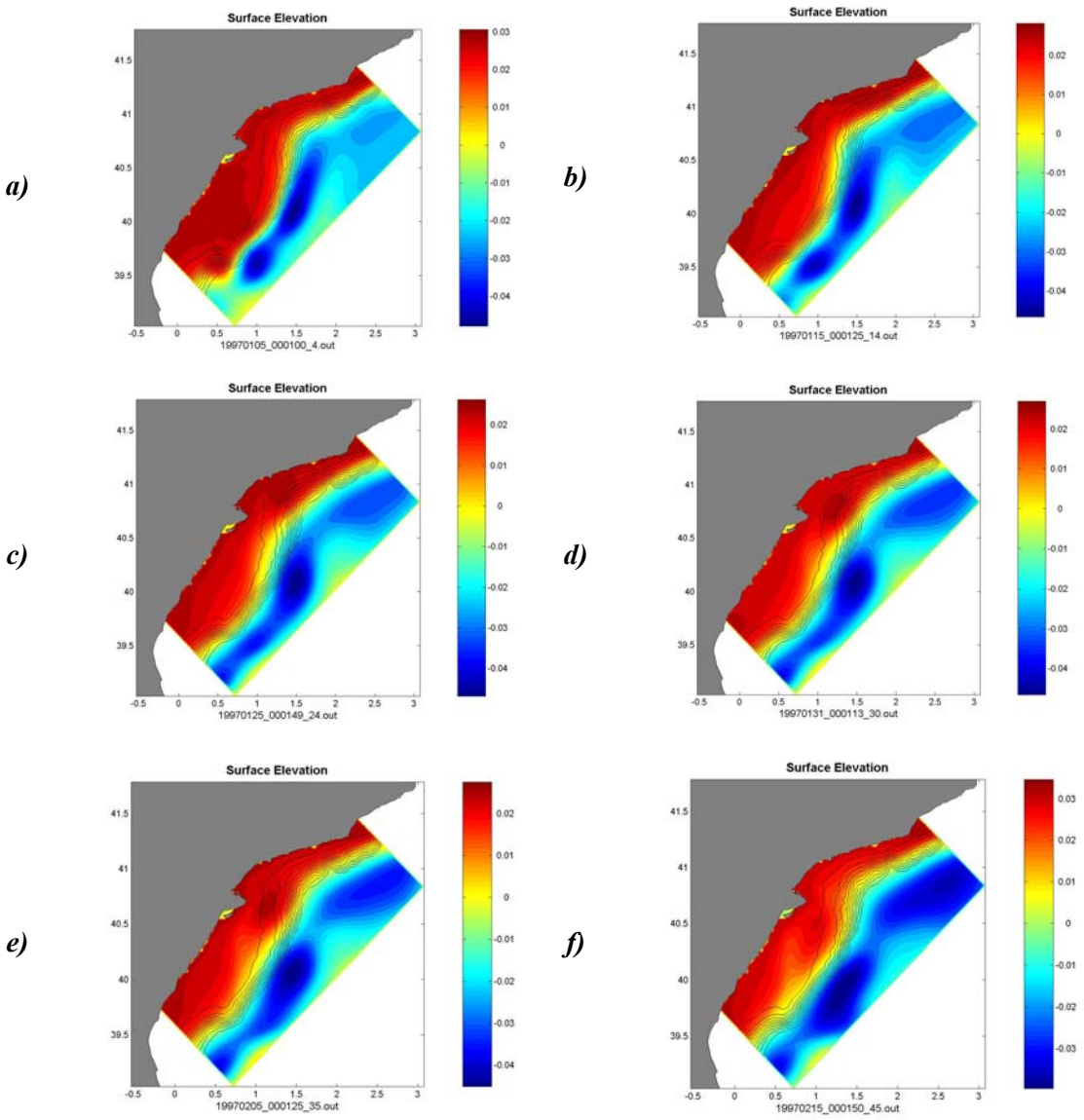

Fig 3. 15: Evolution of surface elevation in the Rossby wave generation propagation. Simulation time (a) 5days, (b) 10 days, (c) 25 days (d) 35 days, (e) 45 days and (f) 55 days.

When the wave reaches the shelf widening it seems that the wave is amplified. In fact, what happens is that the part of the wave that is over the shelf propagates more slowly, with a phase velocity of 0.37 km/day, than the part over the slope. This difference on velocity generates an elongation of the wave shape. To understand this it can be seen in (3.20) that the phase velocity is a function of the bottom slope s. Using a typical value for the shelf slope, the theoretical value for the phase velocity is 0.3 km/day, which matches again with the model value.

Parameter	*Value*
L	*25 km*
s (slope)	*0.037*
s(shelf)	*0.0045*
f	$10^{-4}\ s^{-1}$
λ (wavelength)	*90 km*
D	*40 m*

Table 3. 3: Parameters used to compute the Rossby wave phase velocity

An illustrative picture of what happens can be obtained if we think on the wave as water parcels that keeping their potential vorticity constant moves across the slope. When they goes up (down) the slope, they acquire negative (positive) relative vorticity that forces it to come back to its equilibrium position while forcing adjacent water parcels. A complete and clear description can be found in Gill (1982). In summary, it is an undulatory process where the restoring force is the conservation of potential vorticity. It must be noted that the strength of this restoring force directly depends on the bathymetry gradients. If the topographic gradient is weak, the vorticity gained by the water mass when is displaced is also weak, so it is the force that makes it to come back to its original position. In this case, the velocity of propagation will be consequently reduced in the shallower depths generating the apparent amplification (see Fig 3. 16).

A parameter that can provide a complementary sight to the process is the potential vorticy. Strictly, we should compute it in its complete form (Pedlosky, 1987), but to simplify, and for illustrative purposes, we can use the simple 2D version for the potential vorticity Π:

$$\Pi = \frac{f + \xi}{H} \qquad \textbf{(3.22)}$$

where f is the Coriolis parameter, ξ represents the relative vorticity and H is the water column depth. The problem to map this quantity is that f is much greater than ξ and maps of complete potential vorticity are not clear. On the other hand, as f is near constant, it will be more useful to look at the quantity ξ/H as it is accomplished that $\Delta\Pi = \Delta\left(\frac{\xi}{H}\right)$.

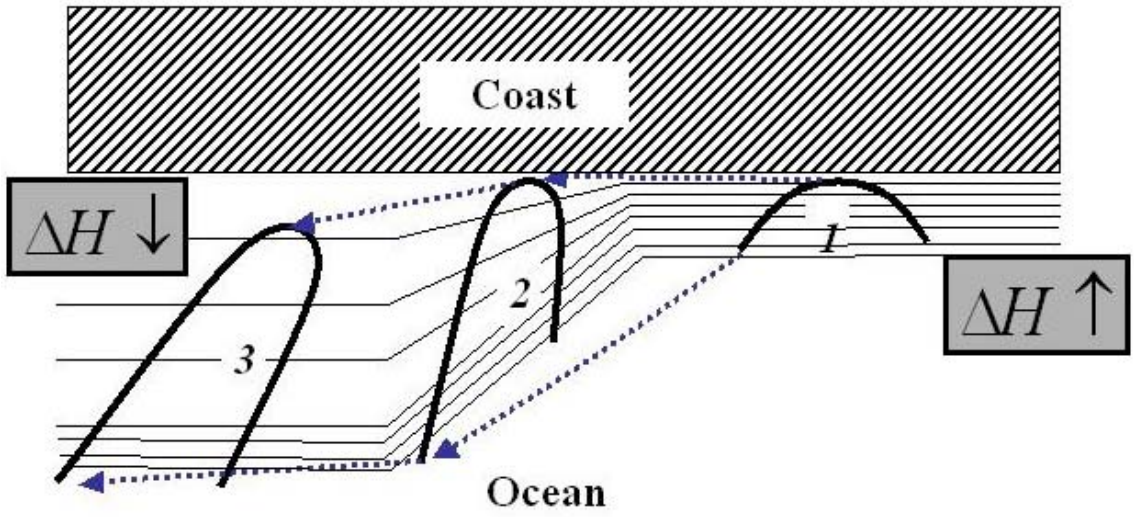

Fig 3. 16: Sketch of the amplification of the topographic Rossby wave in the shelf widening. Bold lines represent different positions of the wave and straight lines represent shelf bathymetry.

In Fig 3. 17, it is represented its time evolution from the moment that wave is generated in the northern part (day 5) with a 10 days interval. During the period that wave is in the northern part (days 5-25), no clear trace of it is found in the vorticity maps. This is coherent with the fact that the topographic waves tends to preserve its original potential vorticity, so although water parcels change its position they do not change its Π. When the wave reaches the Ebre Delta and the shelf widens (days 35-55), a maximum-minimum structure is set up indicating that the wave has lost its initial properties. In fact, the formalism of the Rossby wave is presented on the assumption of small perturbations. When its shape is enlargened, it is breaking with this assumption, so it is not expected to preserve the same theoretical properties.

All what have been presented above is in the frame of stratified conditions. In winter conditions, the wave is also generated and propagates in a similar way than in the summer case but it is no significatively amplified over the shelf (see Fig 3. 18). The reason is that the wave is restricted over the slope and the shelf break without reaching the inner shelf where slope is much gentler. This means that there is no significative difference into the phase velocities and no elongation is created.

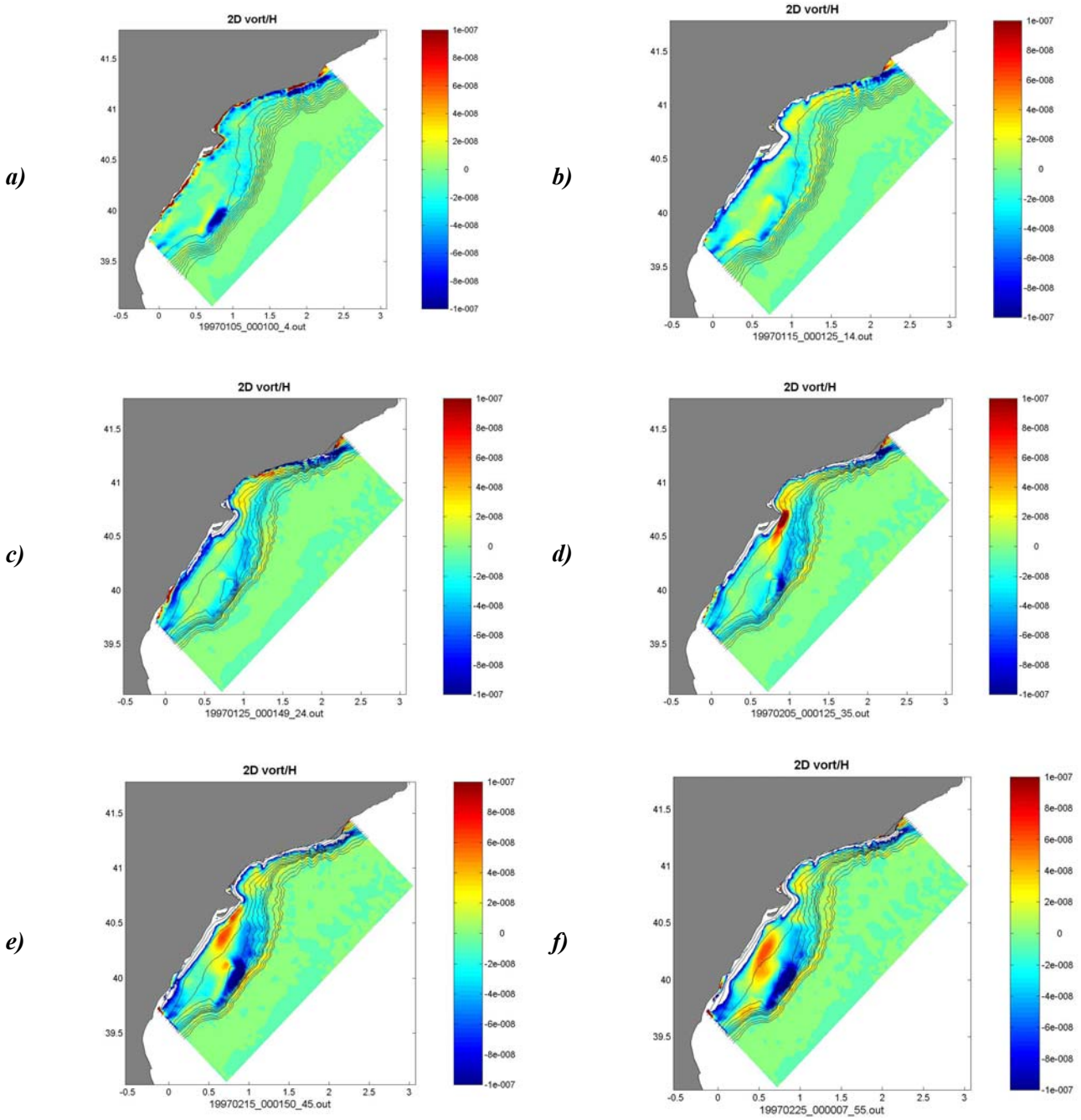

Fig 3. 17: Evolution of ξ/H fields in the Rossby wave propagation. . Simulation time (a) 5days, (b) 10 days, (c) 25 days (d) 35 days, (e) 45 days and (f) 55 days.

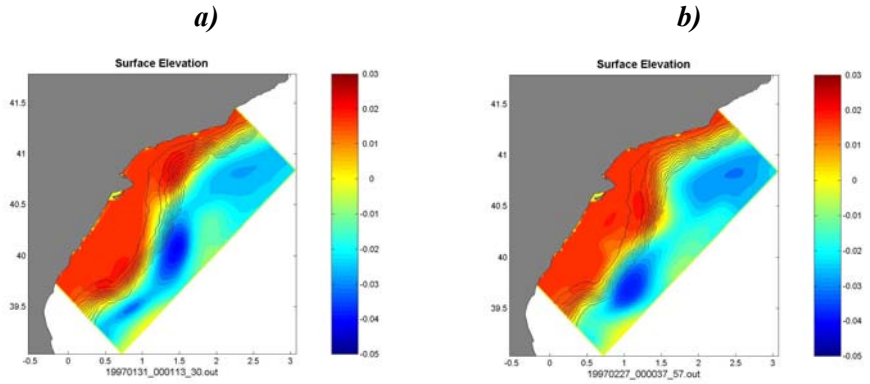

Fig 3. 18: Surface elevation in winter conditions at simulation time (a) 25 days and (b)55 days.

Now it should be clarified why the wave can reach the inner shelf in stratified conditions and not in the homogeneous frame. The explanation is that vertical gradients of density act as decoupling factor between the upper levels and the bottom. Those levels don't feel the topography variations, so the restoring force is reduced and the water parcels can be further displaced. In Fig 3. 19 this process is illustrated in a basic way. In homogeneous conditions, the water column acts as a unique element and, when it is stretched by the changes of bathymetry, all the column acts unified gaining the same relative vorticity at all depths. On the other hand, if stratification is present, we can imagine the water column as a series of coupled layers where the bottom variation will affect, principally, the deepest one. The shallower layer will also be affected but much less. The ratio of compression between the two layers is a function of stratification, $\frac{\Delta H_{deep}}{\Delta H_{shallow}} = f(N^2)$, where N is the Brunt-Väisala frequency. In conclusion, if N is high, $\Delta H_1 << \Delta H_2$, so the upper layer will "feel" a much gentler slope than in the homogeneous case. The relative vorticity gained will also be reduced, and, consequently, the restoring force will be weaker.

In Fig 3. 20, a comparison of vertical structure of the velocity field is presented for the summer and winter cases. It can be seen how the homogeneous frame leads the water column to act as a unique piece, so potential vorticity restrictions prevent the current to go into the shelf. On the other hand, when stratification is present, there is a decoupling between upper and deeper levels. Water parcels in the former do not have any restriction and can go into the shelf until depths comparable to the thermocline depth.

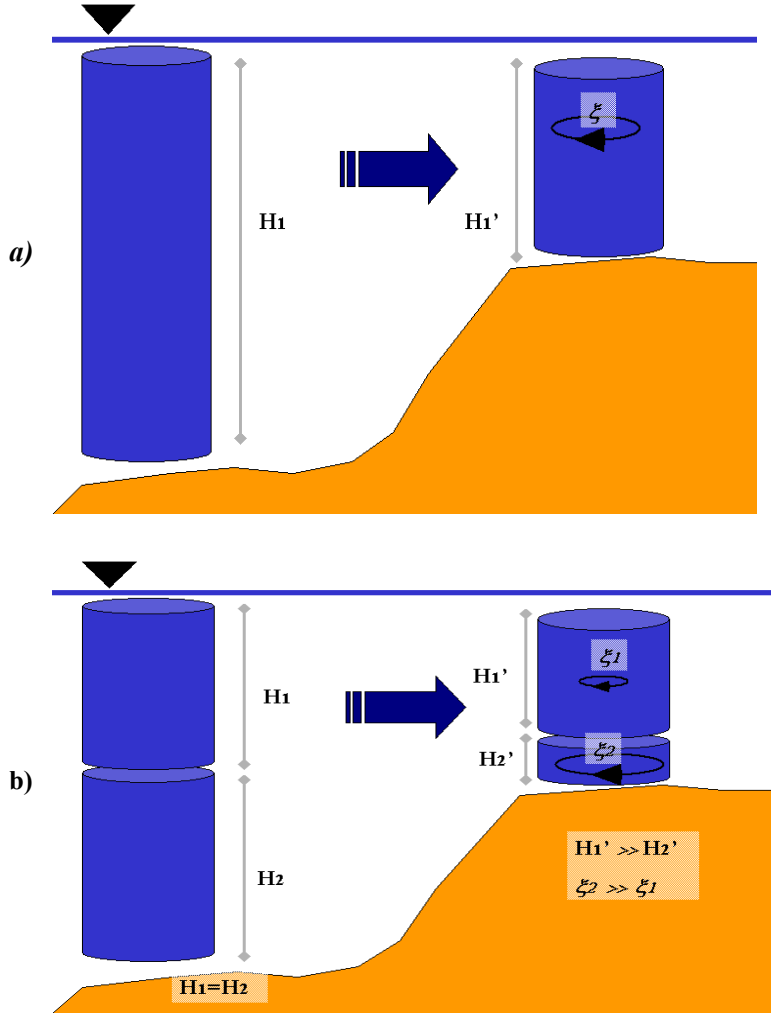

Fig 3. 19: Sketch of water column stretching with (a)homogeneous density profile and with (b) stratification.

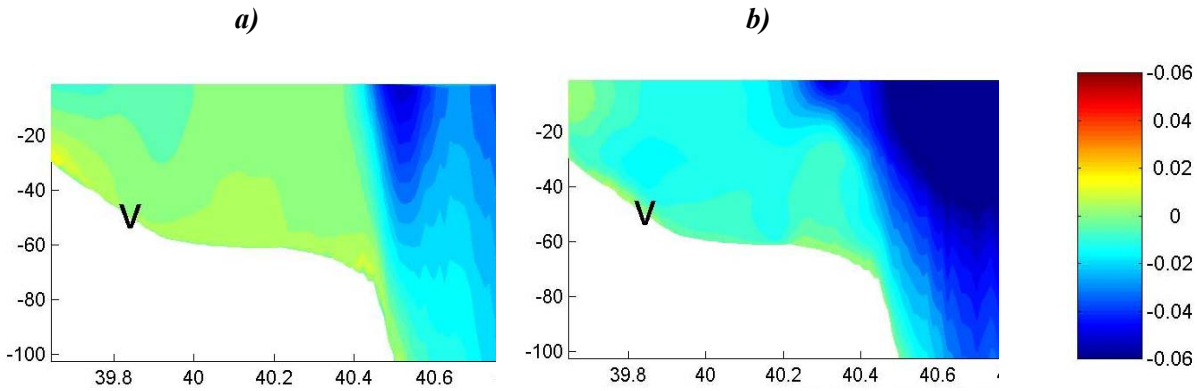

Fig 3. 20: Vertical section of velocity after 30 days of simulation with the (a)homogeneous profile and the (b) stratified profile.

The phase velocity of the wave is small, so that geostrophic adjustment can be reached between sea level anomalies and velocities. Current intensity is around 5cm/s at surface and it decreases with depth vanishing at 50 m approximately (see Fig 3. 21). The vertical structure is highly modified with a vertical displacement of isopycnals of ~40m, which implies the outcropping of subsurface layers. As the wave propagates slowly, this structure will be maintained several days, meaning that the circulation pattern can be viewed as near stationary. The horizontal circulation pattern introduce significant displacments but in the vertical velocities are negligible, contrary to what happens with waves propagatin faster.

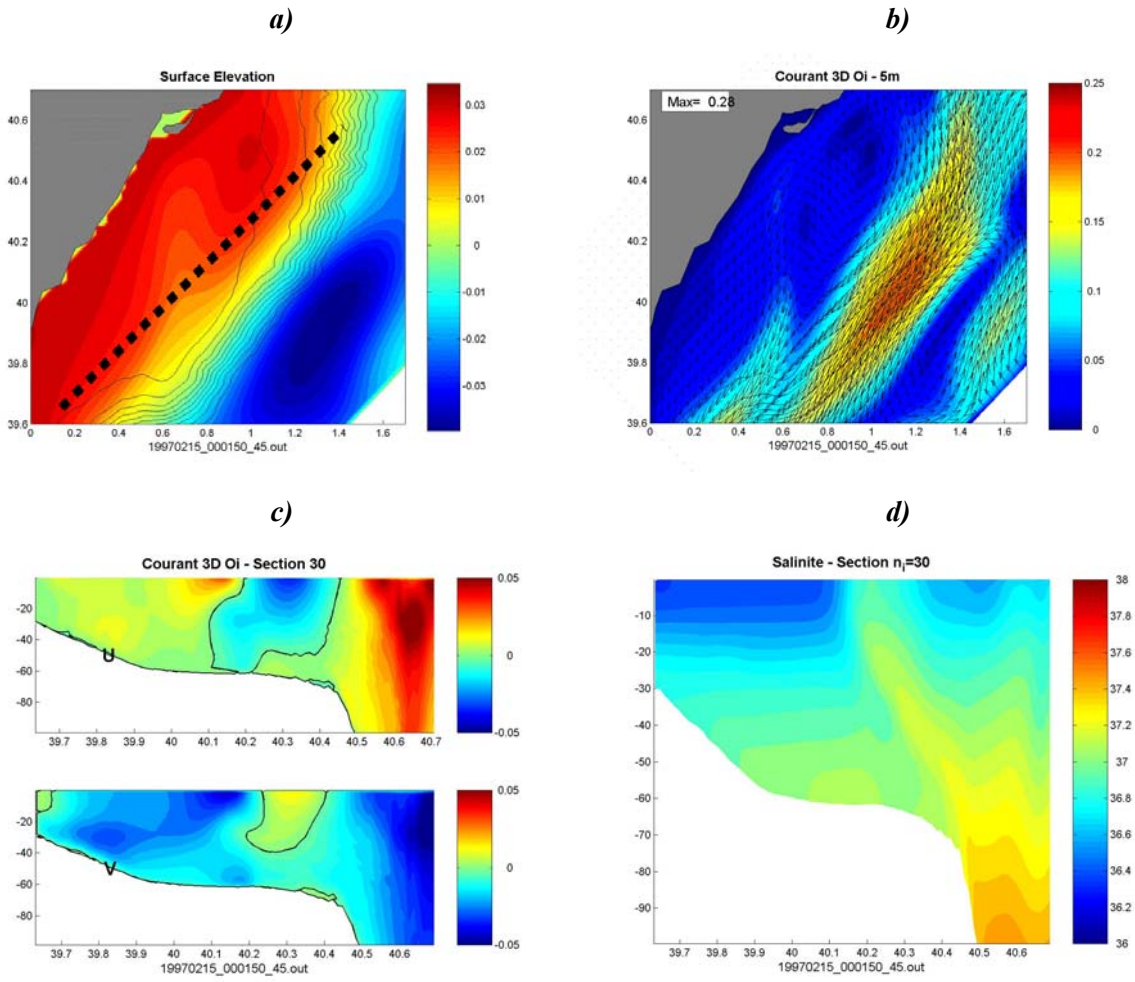

Fig 3. 21: Detail of the topographic wave structure (a) Surface elevation, (b)velocity at 5m depth, (c)vertical section of velocity (U denotes across shelf and Valong shelf components) and (d)vertical section of salinity. The dashed line in (a) shows the location of the vertical sections.

The implications of this process on the shelf dynamics can be quite relevant. Being the phase velocity small, horizontal displacements can be significative, even with small velocities, as the structure lasts for several days in the same location. In order to have a more quantitative

view, we look at the evolution of simulated lagrangian buoys launched at 5m depths in several places of the shelf. The buoys where launched in three different positions over the wide shelf during the simulation in a 15 days interval and they simply evolve advected by the current field. It can be seen that in the summer case (see Fig 3. 22a) the trajectories were really dispersed and almost all the buoys reached the slope both in surface and at 25m. On the other hand, in winter conditions, when the wave amplitude is reduced, the buoys displacement was much more limited and after several weeks they couldn't leave the shelf. So, the amplification of this topographic Rossby wave can be an effective mechanism for the exportation of shelf waters to the open sea.

To deepen on the wave influence on the shelf, in section 3.6, we'll investigate its effect on the renewal of shelf waters.

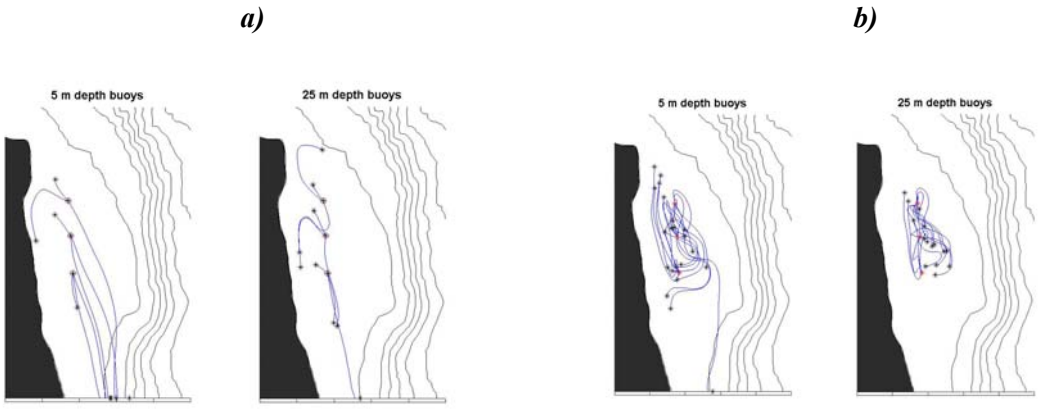

Fig 3. 22: Simulated buoys evolution in the (a) stratified and (b) homogeneous cases.

3.5 ROLE OF THE WIND IN THE SHELF AND SLOPE DYNAMICS

Data analysis performed in chapter 2 has shown the importance of wind into the shelf circulation. Previous works in the region (Salat et al., 1992; Rippeth et al., 2002) also remarked the role of the wind as the basic forcing over the shelf. Also, its influence over the Ebre river plume has also been reported (Mestres et al., 2003 ; Xing and Davies, 2002) while, over the slope, its importance is reduced to the first meters and to the generation of inertial oscillations (Font, 1990).

In this section we will take advantage of the validated numerical model to complement in situ observations presented in chapter 2. We will try to find out which are the 3D circulation

patterns induced by the wind over the shelf and their interactions with the slope current. Results will be based in the ACA family runs explained in section 3.2.5.

3.5.1 No wind

As a benchmark case, we take a look at the no wind runs where the forcing factors are the slope current and the river outflow . The situation over the slope is analogous to what was explained in section 3.4. The initialization method reduces the spin up period and there is just the non-linear adjustment that produces propagating oscillations over imposed to the slope current. Those are small amplitude waves (~6km) with wavelength of 35km, propagating at 8-10 cm/s and being attenuated in 2-3 days. They occupy the first 20 meters of the water column and its importance is of second order when some forcing is applied, so they are not expected to interfere the evolution of model results. Nevertheless, they highlight the fact that the narrow shelf (northern part) circulation is directly controlled by the slope current and its variability.

Over the wide shelf, the topographic Rossby wave reported in the previous section has no time to establish, so all the circulation is induced by the plume dynamics. The Ebre river plume needs 2-3 days to develop from a rest state. In the high runoff case, its influence is mainly restricted to the bulge area with a maximum extension of around 40km and velocities of 10-15 cm/s. A secondary coastal current is established in a 5km band close to the coast until 70km south-westward, occupying the first 5 meters and with associated velocities of 5-7 cm/s.

In the stratified case, the current profile is also stable and keeps its properties with a slight change in its width and depth. The waves produced by the non-linear adjustment have more or less the same characteristics than in the homogeneous case except that their amplitude is greater (~12 km) and that they reach deeper layers (~50m) but after 2 days, they are dissipated.

In the low river runoff runs (summer and winter), there is no circulation over the wide shelf out of the reduced ROFI area (~10km).

3.5.2 Migjorn (S) wind

When the Migjorn wind begins to blow, an Ekman-type circulation is established over the whole domain. The Ekman layer has a thickness of around 20m and circulation therein is controlled by the wind, over imposed to the open sea circulation (namely the slope current). Deeper than the Ekman layer the previous circulation remains unaltered. In surface layers, wind induced currents intensity is around 15cm/s and deflected ~45º to the right. In lower layers, an Ekman spiral is generated by friction until 20m depth, where velocity vanishes. Nevertheless, the slope current and coast line complicates the circulation patterns over the shelf and slope.

In the southern part, over the wide shelf, a general pattern of north-westward currents is established with a vertically averaged velocity of 10cm/s over all the shelf (see Fig 3. 23). Near the shelf break, shelf currents interact with the slope current and are gradually deflected southeastwards. At the coast, an upwelling is generated by continuity. In the two days period where wind blows, the upwards movements imply a vertical displacement of 20-30meters and waters until 80m depth are affected. Velocities near the bottom linked to this process are around 10cm/s.

Associated to the upwelling, a typical coastal current is established. This current follows the coast north-eastward with velocities reaching 50cm/s in surface and being felt until 40m depth. The maximum of intensity is found after the Ebre Delta. This coastal current presents a coastal boundary layer of about 5-7km where velocities are reduced until having null value at the coast. In the northern part (narrow shelf) the coast changes its direction and velocities are weaker than in the southern part (wide shelf) probably due to the interaction with the slope current. Therefore, it can be said that the wide shelf acts as a buffer zone that unlinks the coastal processes from the open sea in good agreement with the definition of wide shelf presented by Sánchez-Arcilla and Simpson (2002).

Vertical section of the velocity field shows a similar behaviour in the northern and southern parts. Vertical extension of this current is 60-70m, and the upwelling cell takes water until that depth. Where bathymetry is shallower, horizontal motion is induced following the bottom. An interesting feature to note is that along coast velocity section (see Fig 3. 23c) shows a wedge form while across slope velocity is homogeneous.

The density field is also strongly modified by the wind. In the Ekman layer, mixing is enhanced and a well mixed layer is established until 20m depth in the entire domain. Wind induced currents advect the density front 20km seawards. Consequently vertical gradients are strengthen there. Near the coast the upwelled waters are clearly seen over the wide shelf while in the narrow shelf the upwelling seems inhibited by the interaction with the slope current.

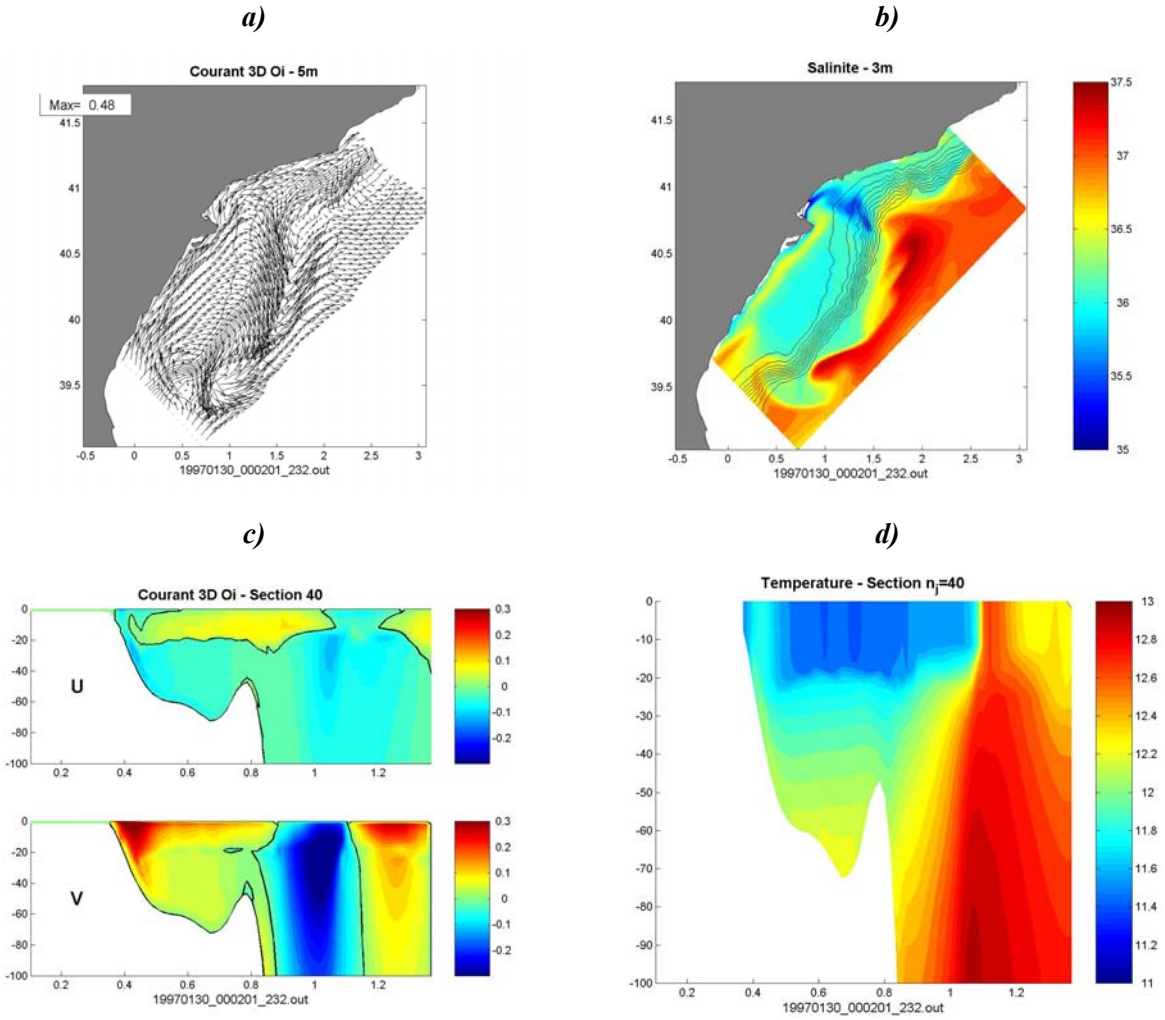

Fig 3. 23: Effects of a 2-day Migjorn wind (S) over the region in winter conditions.(a) Surface velocity, (b)Surface salinity, (c)vertical section of velocity in the wide shelf and (d) vertical section of temperature in the wide shelf. U denotes across shelf component and V along slope velocity.

When the wind stops energetic inertial oscillations are triggered controlling the circulation and enhancing mixing. Associated velocites are around 10cm/s and they can be felt at all depths over the shelf. A 180º phase lag is present at the base of the Ekman layer, around 20m, in good agreement with the study of Rippeth et al. (2002) for the vertical propagation of inertial oscillations in the region. These inertial oscillations last for several days without a significative rate of energy loss.

After 24 hours, the initially displaced slope density front is restored to its initial position. In the open sea, some small scale oscillations appear in the first 20m (baroclinic instability) due to the strong vertical gradients introduced by the front displacement and triggered by the fast

movement of the front. What happens is that, during the wind burst, shelf (lighter) waters are displaced seawards and, when wind stops, inertial oscillations favours its mixing with surrounding (heavier) waters. Afterwards, these modified waters come back to its initial position but with higher density than shelf waters below, so favouring instabilities.

Over the shelf, the water masses remain well mixed, and the coastal current lasts for, at least, 10 days with a small rate of energy loss. In the widening area, the wind pushed the upwelled and plume waters towards the slope current and, when slope circulation is restablished, the current advects them downstream.

The simulations with summer conditions (stratified density profile), show the same circulation patterns. The temperature gradients induced by the upwelling are more important, as the difference between the upwelled waters (originally at 20m depth) and surface waters is enhanced by the stratified situation. On the other hand, the Ekman layer is shallower (~15m) while velocities are stronger. It must be noted that vertically averaged velocity field is more energetic than in the homogeneous conditions. The reason is that the energy transfer from the wind to the sea is more effective that in the homogeneous case. As it can be seen in the formulation of the turbulence submodel (see section 3.2.1), the vertical turbulent coefficient depends on the vertical gradient of density ($\upsilon_v \sim K \; and \; \partial_t K \sim \frac{\partial \rho}{\partial z} < 0$) . Stratification induces a greater loss of turbulent kinetic energy and, consequently, lower values of turbulent vertical mixing. In consequence, with stratified conditions, the energy induced by the wind is less diffussed by the turbulent mixing..

Vertical movements are generated at the beginning of the wind burst and when the stationarity is reached they become null. They are concentrated near the coast over the entire water column and, when the wind stops, strong vertical displacements are found due to the density relaxation all along the coast.

The displacements of the density near the coast and near the slope front generate internal waves that propagate away creating complex patterns over the shelf. In Fig 3. 24 the time evolution of vertical velocity in an across-shelf section at 10 m depth provides evidence of this process. At the beginning of the run (days 0-2), before the wind blows, the non linear adjustment of the slope current generates waves with a period of 16.8 hours and a phase velocity of ~ 40cm/s. These waves are radiated at both sides of the current (dashed line in Fig 3. 24). During days 3-5, the wind blows and induces upward movements near the coast. When it stops the relaxation of the isopycnals generates internal-inertial waves both near the coast and near the current edges which propagates at 70cm/s (solid lines in Fig 3. 25). Over the shelf, the waves coming from the coast interacts with those coming from the slope establishing a complex pattern in the middle of the southern wide shelf.

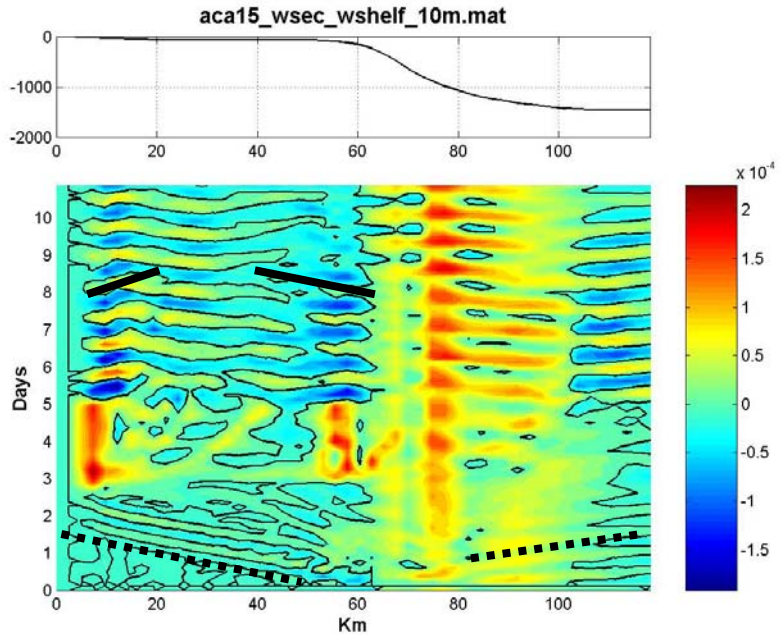

Fig 3. 24: Time evolution of vertical velocity at 10m depth in a across--shelf section over the southern shelf. In top, the bathymetry profile along the same section is presented.

Another place for the generation of internal waves is the edge of the river plume. Associated to the plume, there are strong vertical gradients of density. When wind begins to blow the plume position is altered, so the isopycnals are displaced and a front of internal waves is set up (see Fig 3. 25). These waves have a characteristic wavelength of 13km and propagate at 50cm/s, so its frequency is around 8 hours.

Although the study of the internal wave behaviour in the region is really attractive, time limitations doesn't allow us to deepen on it, so we will limit to the presentation of these evidences.

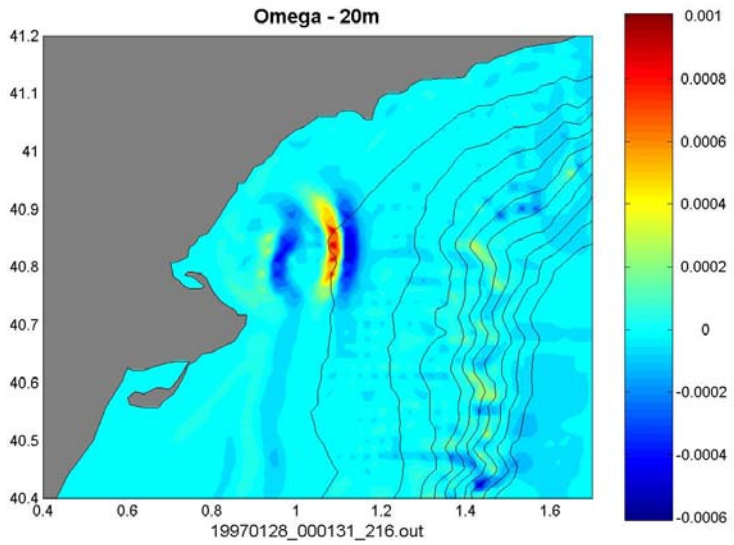

Fig 3. 25: Vertical velocity at 20m depth 12hours after the Migjorn wind began to blow.

3.5.3 Gregal (NE) wind

This case can be considered as the opposite of the previous one and effects are quite analogous. While the wind blows, a 20 meters Ekman-type layer is formed where circulation is controlled by the wind. This layer occupies all the model domain and wind-induced circulation is over imposed to previous velocity field (namely the slope current). In the Ekman layer, waters are deflected to the right impinging on the coast and inducing a downwelling of surface waters to deeper levels. This downwards advection can reach 40-50 meters depth and is restricted into a band of 10-15km from the coast. This band width is in good agreement with theory, which predicts a width equal to the Rossby radius (~10km).

A secondary effect of this impingement of waters on the coast is that a coastal current is set up due to the gradients of the surface elevation (see Fig 3. 26) . This current has averaged velocities of 0.3m/s reaching 0.5m/s in the Ebre delta area due to changes in coastline orientation. The current width is ~12km, which is coherent with the downwelling band width, and can be felt until 50m depth.

The behaviour of the downwelling circulation cells is different depending on the shelf width. In the narrow shelf part, the coastal current and the slope current are adjacent and both directed south-westward. There is transference of kinetic energy between both currents and the result is a unique large current in the first 50meters.

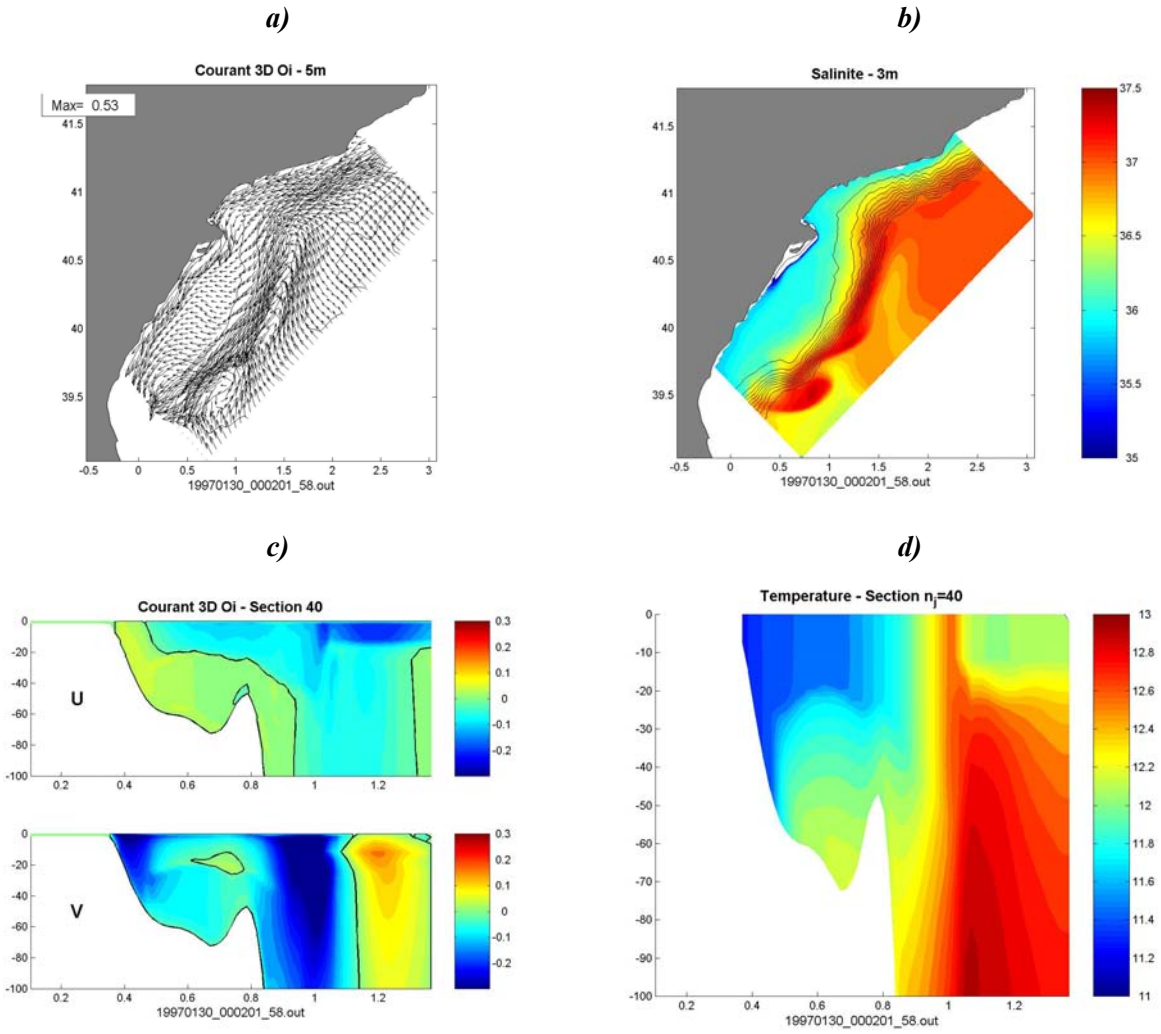

Fig 3. 26: As Fig 3. 23 but for a 2-day Gregal wind (NE) in winter conditions

On the other hand, the wide shelf separates both currents and an across shelf circulation cell is set up (see Fig 3. 26). In the outer part of the shelf, velocities into a 20m surface layer are directed coastward. Near the coast, the across shelf movement vanishes in that layer and water re-circulates below. A seaward movement is present below the Ekman layer with maximum velocities of 5cm/s near the bottom.

Finally, the effects of the wind over the slope current are that it is slightly modified while in the open sea an Ekman spiral is established. In general it seems quite symmetric to the previous case except that the vertical pattern of velocity is different.

For what concerns to the water masses structure, the wind induces a density front displacement toward the coast of about 20km in the whole domain without significative mixing in the open sea. Waters are well mixed over the wide shelf and a typical downwelling profile is

found in the inner shelf and in the northern shelf. The Ebre river plume is also pushed against the coast reducing significatively the ROFI area.

When the wind stops, inertial oscillations are triggered in the whole domain enhancing mixing. The coastal current doesn't last for more than two days, which is quite different from the upwelling case. This could be explained by the fact that upwelling induces a density gradient near the coast than inforces the geostrophic coastal current and that has a long relaxation time. On the other hand, downwelling tends to homogenize waters, so, after the wind burst, there is no mechanism to maintain the coastal current as there is no density gradient. Without the wind, the Ebre river plume tends to establish again and after 3 days its shape is similar to the case without wind.

On the open sea, the displaced density front tends to its initial position in the northern part while, over the wide shelf, the density structure remains well mixed.

When stratification is present no significative differences are found in the general behaviour. The only effect of stratification seems to be that the Ekman layer depth is reduced being around 15m. Also, as it was explained in the previous section, the kinetic energy transference from the wind to the sea is more important, so velocities are greater

3.5.4 Llevant (E) wind

The sea response to the Llevant winds has several coincidences with the other wind regimes as the depth of the Ekman layer (~20 m) and that circulation is dominated by the wind therein. Wind-induced circulation intensity is around 15-20cm/s and deflected 45º in the surface layers (north-westward). The piling of waters against the coast induces a coastal current directed south-westward in a band of 10-15km as in the previous runs (see Fig 3. 27). Its magnitude in surface can reach the 30cm/s and can be felt until 50m. Its maximum of intensity is found in the northern part due to the fact that the coast orientation there is perfectly perpendicular to the wind-induced circulation.

It is interesting to note that the coastal current is partially in opposition to the initial wind-induced currents. This fact induces complex patterns over the wide shelf where, from open sea to coast, it can be found a south-westward circulation reaching 300m (the slope current), a north-westward current occupying the first 20m over the center shelf (wind-induced circulation in the Ekman layer), and a narrow coastal current directed south-westward again and reaching the 50m depth. In the northern part, both coastal and slope current are adjacent until the shelf widening, where the two branches separates.

The wind-induced current in the open sea forces the accumulation of river waters in the Gulf of St. Jordi, at the north of the Ebre Delta, where the river waters dilution is enhanced. The

entrance of slope waters into the shelf in the widening area is directed northwestward, where the slope width is smaller, and reaches more easily the coast than in the Gregal case. Also, the southern part of the Ebre Delta is shelted by the widening and there is no clear apparition of open sea waters there.

The downwelling generated by the impingement of waters against the coast has also similar characteristics than in the Gregal case and the velocity distribution in the vertical is near the same. On the other hand, the density front displacement in the Ekman layer is much lower, mainly because the direction of the averaged transport is opposite to the slope current.

Stratification doesn't seem to play a role as important as in the other wind regimes. Transference of energy from wind is higher and the Ekman layer is shallower than in the homogeneous case but no significative effect is found in the circulation patterns. The downwelling displaced waters around 20m in the vertical and its effects are felt until 40m depth.

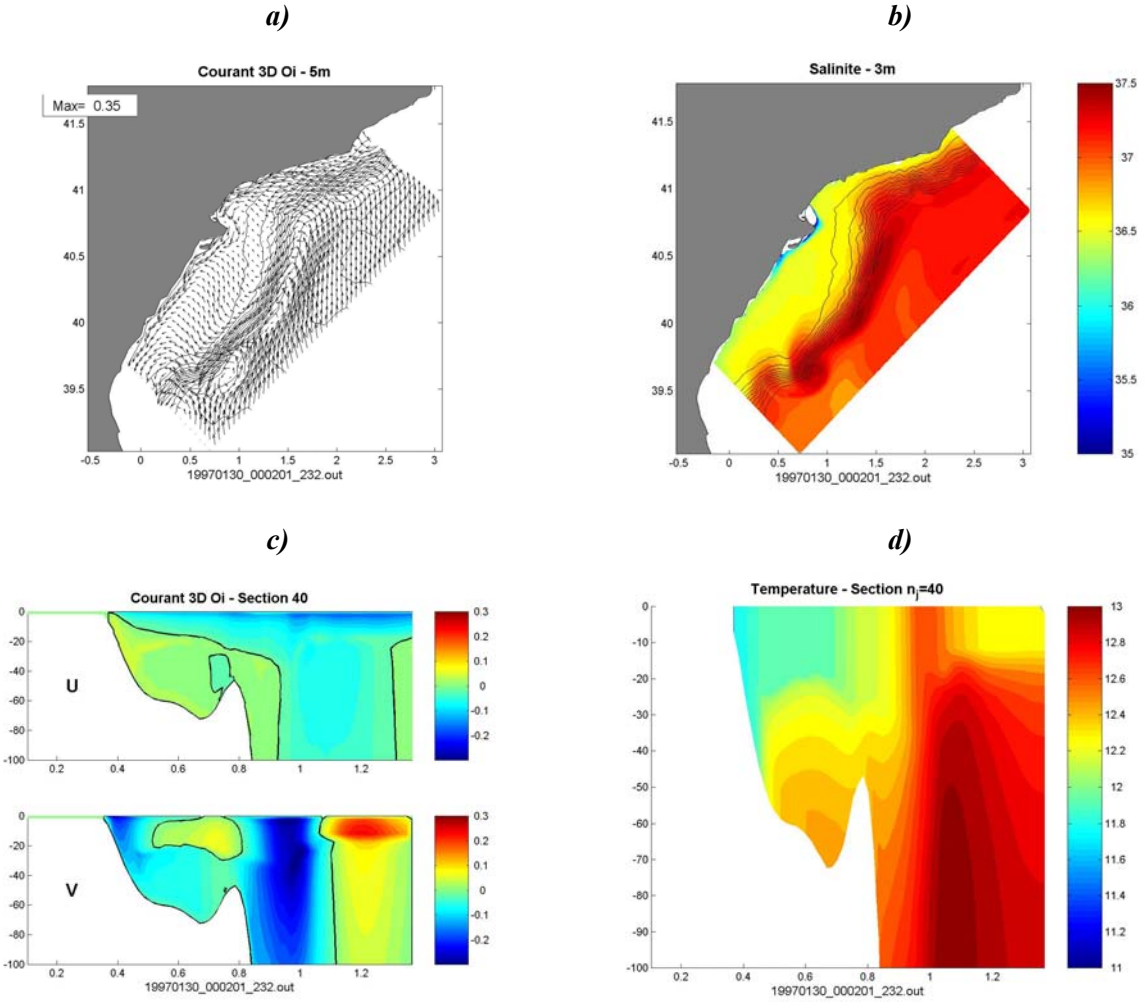

Fig 3. 27: As Fig 3. 23 but for a 2-day Llevant wind (E) in winter conditions

After the wind burst, the inertial oscillations dominate the circulation in the upper layers as in the previous cases. The density front returns to its initial position but no strong instabilities are developed as happened in the Gregal and Migjorn cases. On the other hand, a small eddy (~15km) reaching until 20-30m depth is generated near the Cap Salou and remains stable with associated velocities of 8cm/s in winter and 15cm/s in summer. The mechanism for its generation is summarized in Fig 3. 28. During the wind burst the slope current is displaced towards the shelf in the first 20m. The coastal downwelling enhance the mixing over the shelf and a coastal current associated to the piling of water against the coast is established. When wind stops, the coastal current begins to weaken and the part of the slope jet that was over the shelf recirculates north-eastward in the Gulf of St. Jordi. When this coastal branch reaches the cape Salou it is forced to deflect seawards where it finds the slope current closing the anticyclonic circulation. In its core it has lighter shelf waters that have been well mixed during the wind event and that can also have the eventual contribution of river waters.

This circulation pattern has been already reported by Salat et al. (1978) and by Ballester and Castellví (1981) from field measurements and studied by Espino et al. (1998) with a quasi 3D finite element model. These authors proposed the interaction of the mean flow with the bathymetry as the origin of the anticyclonic circulation. Espino et al. (1998) also suggested that the wind vorticity could strenght or weak the structure. Nevertheless, the results we obtain with a more realistic modelling configuration propose a different mechanism for the generation of the eddy.

3.5.5 Mestral (NW) wind

The Mestral case is one of the most interesting not only because is the most intense and frequent wind but also because it is a narrow (limited) wind jet. The other cases presented before are characterized for being winds blowing from the sea, so there are no restrictions in its horizontal extension and are often homogeneous over the entire domain. However, the Mestral wind blows from the land where it is channelled by the Ebre valley, and it can be idealized as constant in the across-shelf direction but variable in the along-coast direction (see Fig 3. 4). The special characteristic of this shape is that it has a strong rotational that is transferred to the sea creating a complex structure in the ocean response.

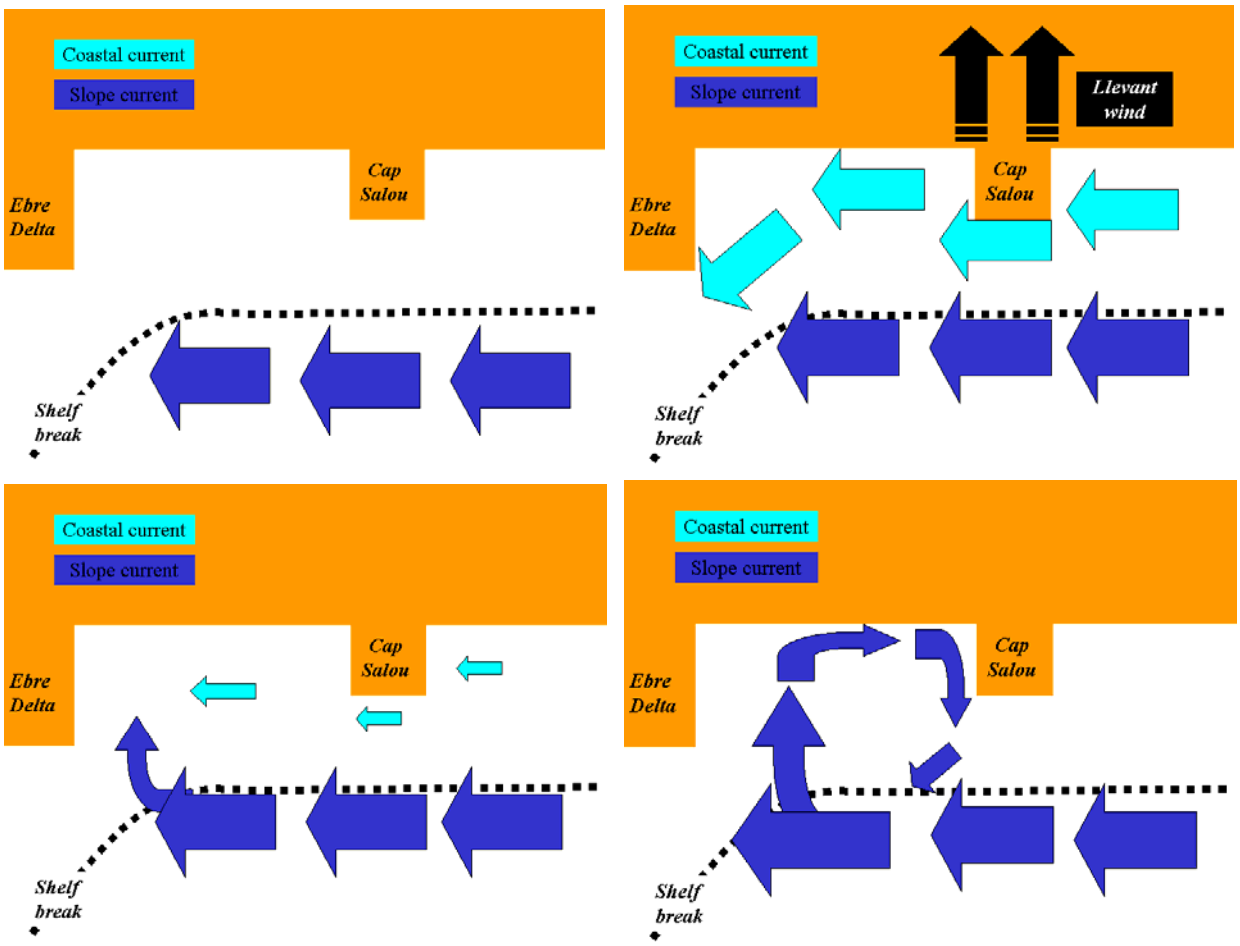

Fig 3. 28: Sketch of generation of cape Salou eddy.

Circulation patterns

The model results for the Mestral case show, as in previous cases, that circulation is controlled by the wind where it blows. There, the averaged transport is more or less directed perpendicular to the wind stress, namely south-westward, parallel to the coast. The key point of the narrow jet is that transport is not constant in the direction perpendicular to the wind (see Fig 3. 29). In the core of the wind jet, velocities are higher than in the edges of the jet, so a more important transport will be induced near its center than in the exterior limits. Those differences in the transport will create a divergence region in the left side of the jet and a convergence region in its right side. The divergence will be associated to a negative increment of surface elevation and to upward movements by continuity. In the same way, a positive increment of surface elevation and a downward movement will be established in its right side.

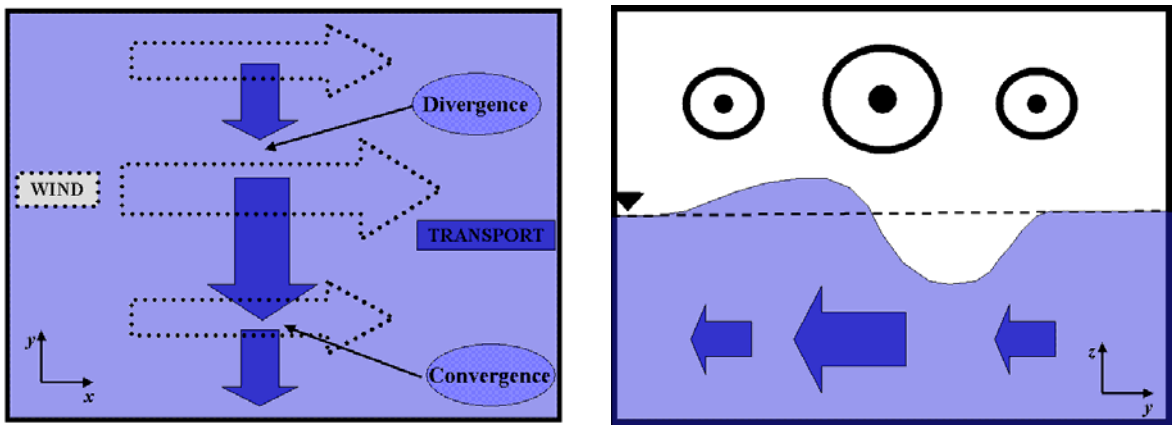

Fig 3. 29: Diagram of the distribution of transport induced by a narrow wind. (a) Horizontal view and (b) vertical section.

The secondary effect of this distribution of free surface anomalies is that the positive (negative) anomaly will induce a geostrophic anticyclonic (cyclonic) motion at the right (left) side of the jet. Those motions are superimposed to the previous circulation, namely the slope current, resulting into a horizontal bending of this current in the upper levels. In the northern part, the positive vorticity cell induces an entrance of the slope current over the narrow shelf, while in the southern part, the negative vorticity tends to create an anticyclonic circulation over the wide shelf (see Fig 3. 30a). The seaward extension of this anticyclonic structure and it shape are fixed by the position of the slope current, which coincides with the shelf break. It must be noted that, in this case, the structure is quite weak but its strength and behaviour strongly depends on wind parameters, as we will show later. In the widening area, the coast line changes its direction inducing a narrowing, so acceleration, of the current close to the coast.

A 10m/s Mestral wind, induces an Ekman layer depth of ~20cm/s just below the core of the jet which is reduced below its edges (see Fig 3. 30b) . Vertical velocities associated are quite significative (20-30m/day) and vertical movements can reach layers deeper than 40-50m. Those movements induce significative displacements of the water masses modifying the vertical structure of density (see Fig 3. 30d). In the upwards region vertical gradients are reinforced, as denser waters are upwelled, while in the downwards area the downwelling of lighter waters generates an unstable situation. Turbulence is increased and mixing of waters over the shelf is enhanced. This modification of the vertical structure is also translated into quite marked horizontal gradients in sub-surface layers (30-50m) reinforcing the vorticity dipole (see Fig 3. 30c).

Finally, the effect of the Ebre plume over this circulation pattern is reduced and do not modify it. The only effect is that in the ROFI area plume-induced circulation is superimposed resulting into an intensification of current close to the coast.

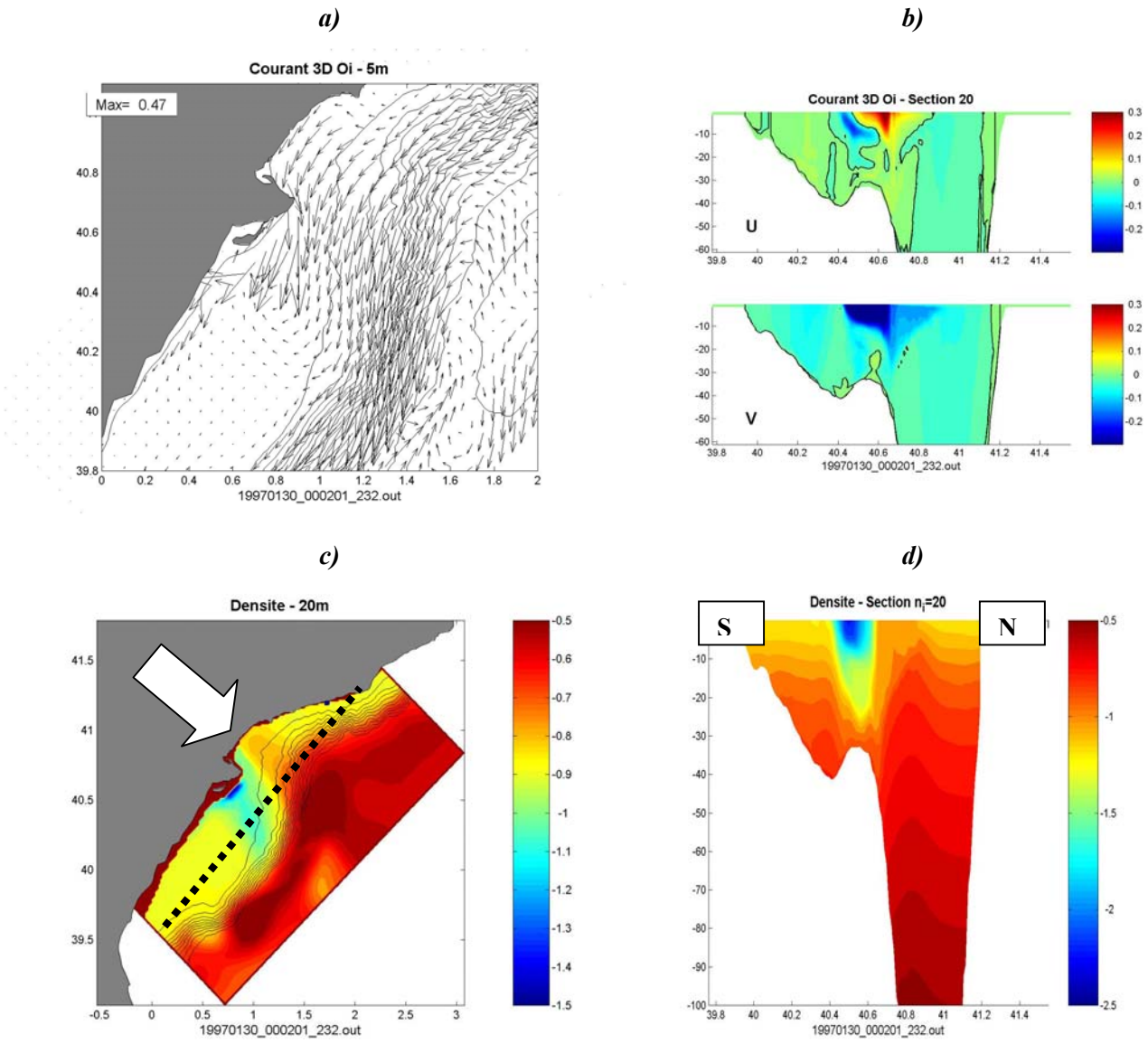

Fig 3. 30: Effects of a 2-day Mestral wind (NW) over the region in winter conditions. (a) 5m velocity, (b) vertical section of velocity, (c)20m density anomaly and (d) vertical section of density anomaly. Dashed line in (c) shows the location of the vertical section and the arrow marks the position of the Mestral wind. U denotes across shelf component and V along slope velocity.

When wind stops, a geostrophic equilibrium is reached and, after 5 days, the dipole pattern is still maintained being the structure identifiable until ~60m depths. This long spin down is caused by the slow relaxation time of the density structure. In other words, it is the time that potential energy stored during the wind event needs to be released and transferred to kinetic energy.

The anticyclone placed in the shelf widening area slightly shifts to the north and expels shelf and plume waters to the slope in the first 20m. It also enhances shelf waters mixing due to the downwards velocities associated to it.

In the wide shelf, the evolution of the positive anomaly of surface evolution can generate complex patterns of circulation but they are highly variable and dependent on the wind configuration.

Superimposed to that, energetic inertial oscillations are set up there were the wind blew lasting for several days. Vertical movements associated to them are about $2\text{-}5\cdot10^{-4}$ m/s, which means that during several days there are vertical displacements of about 15-20m/day.

In the summer case, mean velocities are higher than in the homogeneous case. Stratification is not just inducing a different vertical distribution of velocities but it is also reducing turbulent mixing and thus kinetic energy reduction as it was explained in previous sections. Velocities in the surface layers are higher reaching 60 cm/s and variations of the slope current and rotational structures are also more significative , as it was expected.

The circulation pattern over the shelf is conceptually the same than in the winter case but more intense. Surface anomalies are ~1.5cm greater than with a homogeneous density profile, so the vorticity cells and the current horizontal bending in the north are more intense (see Fig 3. 31a). As a consequence, in the northern part, the slope current reaches the coast producing a piling up of waters which results into an intensification of the coastal current. In the wide shelf, the coastward branch of the anticylonic cell also reaches the coast where it is deflected to the right. When wind stops this evolves to a well defined anticyclonic eddy which is maintained until the end of the run. Once it is formed it interacts with the slope current and is slowly advected downstream by it. Nevertheless it is not strong enough to keep its properties and after ~15 days the structure is no longer present.

The cyclonic bending of the slope current in the northern part also evolves after the wind stops. It does it as a topographic Rossby wave, with the same properties that have been discussed in section 3.4.

Vertical velocity field is similar than in the homogeneous case but horizontal gradients of density induced by vertical displacements of isopycnals are greater due to the stratification. In other words, at a given level, water is upwelled from the same depth but due to the higher vertical gradients of density, its difference with ambient waters is greater (see Fig 3. 31b).

Comparison with satellite images

The processes showed above are of great interest but are provided by a numerical model, so it would be interesting to compare with data to see if the features showed by the model are realistic. Unfortunately there is no available in situ data that could help us to compare, so the best source of information that we can use is satellite images (SST and SeaWifs).

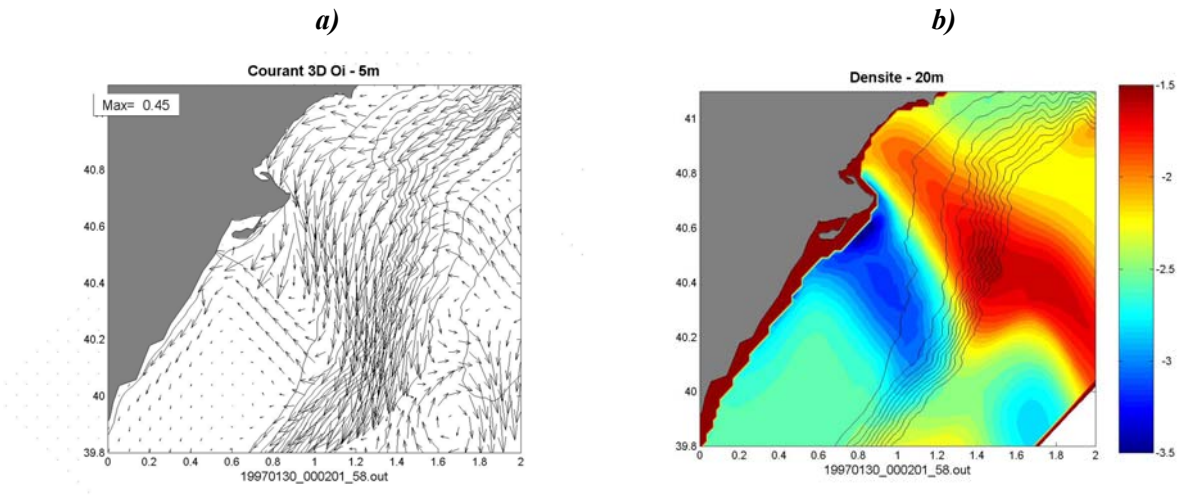

Fig 3. 31: Effects of a 2-day Mestral wind (NW) over the region in summer conditions. (a) 5m velocity, (b) 20m density anomaly.

In year 2001, between January 26th and January 31st, a Mestral event took place reaching intensities of 12m/s. During that period, the Ebre runoff was around 700 m^3/s, so it is expected that the river plume was well developed and could be used as a tracer of the circulation. With SeaWifs images it is possible to trace the plume evolution during that period and to compare with model surface salinities for similar wind conditions.

The model results used to compare have been obtained with a 2-days Mestral event, winter stratification and high river runoff ($1000m^3/s$). It must be noted that we look for a qualitatively comparison since the model configuration is academic and no direct salinity information can be obtained from SeaWifs data.

The comparison shows the same behaviour both in model and data. During the Mestral event, the plume is prevented to expand northward and a clear limit is established for it (see Fig 3. 32a). Then, it is deflected south-westward due to the wind induced circulation. When wind stops (Fig 3. 32b-d), an anticyclonic circulation begins to be set up in the shelf widening and can be easily traced by the plume evolution. The plume expands seawards and northwards with an entrainment of outer shelf waters (high salinity and low signal in SeaWifs) into the plume bulge. This denotes an anticyclonic motion in the wide shelf which advects those outer shelf waters near the Ebre Delta, in good agreement with model results.

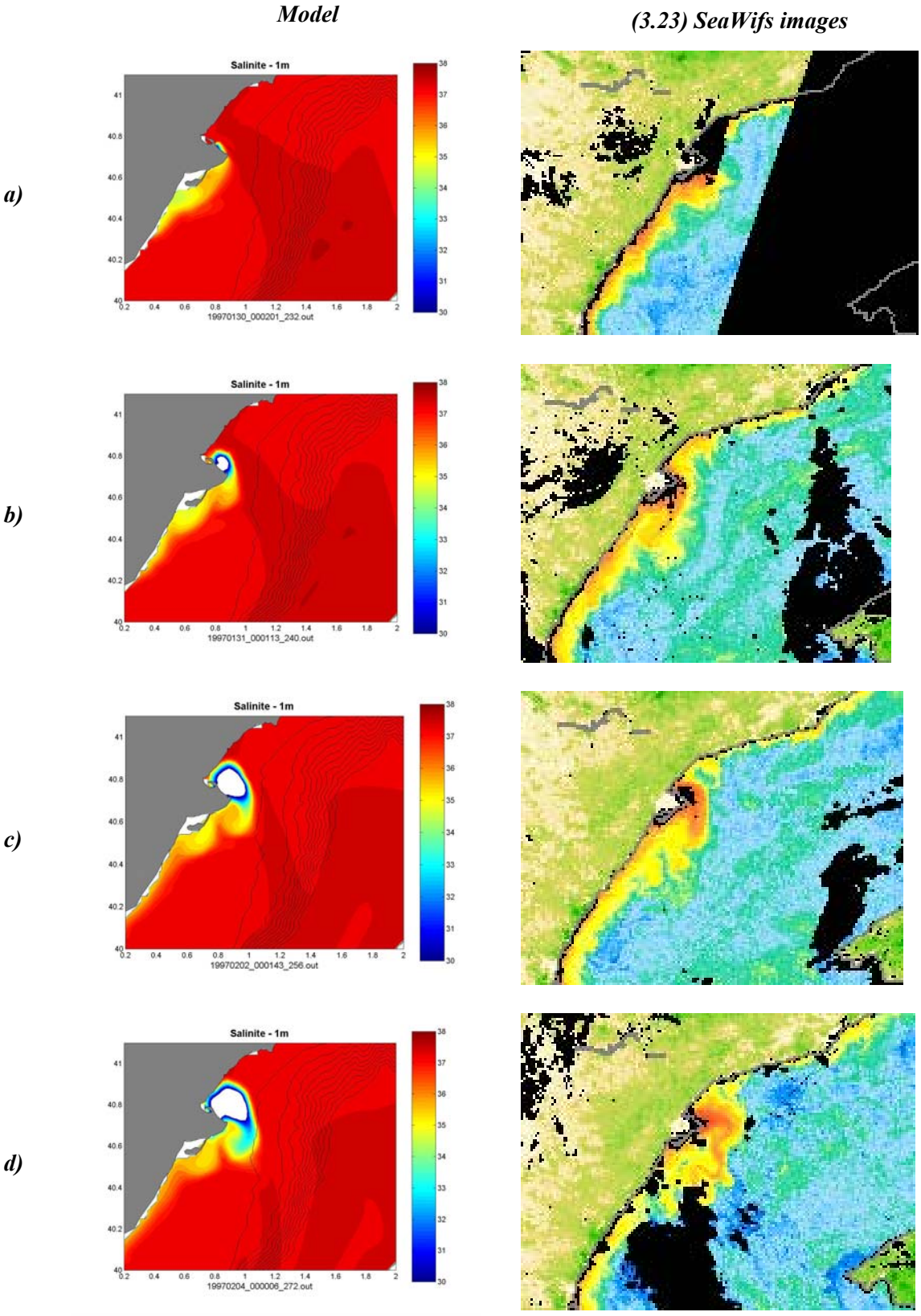

Fig 3. 32: Comparison of model sea surface salinity with chlorophyll SeaWifs images. (a)During the Mestral burst and (b) 1 day, (c) 3days and (d) 5 days after the wind stops.

Role of the slope current

As it was mentioned before, the Mestral events are really frequent in the area (see Fig. 2.2) and model results suggest that dynamics induced by them is quite rich. In addition to that, conclusions find in our area can be easily applied to other coastal regions, so it is worth to deepen a bit more into the effects of a narrow wind.

The first thing that we can clarify is the role of the slope current into the scenario presented above. To do that, we run the model in the same configuration used above but switching off the slope current, so the only forcing is the wind.

After two days with wind blowing, the convergence (divergence) induced by the non-homogeneous wind establish a positive (negative) region of sea surface anomaly. Without the slope current, these regions are perfectly symmetric at both sides of the wind jet (see Fig 3. 33a). The vertical movements associated to those convergences imply a vertical displacement of the density structure that is felt until 100m depth (see Fig 3. 33c) which will be the responsible of the geostrophic circulation set up after the wind burst.

Near the coast, the anomaly of surface elevation is reduced because the wind induced transport there is also reduced by lateral friction. This reduction of the transport implies a reduction of the convergence (divergence) which generates the surface anomaly. The low anomaly values contributes to "close" the cyclonic-anticyclonic circulation as the gradients between the coast and the center of the anomalies are enhanced.

Another process that affects the coastal current is that the circulation branch directed coastward impinges on the coast generating a local piling of water. Then, a geostrophic adjustment is set up and a along coast current is established in a narrow band close to the coast. The band width is similar to the internal deformation radius (~10km) and it is felt in depth until 40m, which is the bottom depth that coincides with the seaward limit of the coastal piling. In the left side of the wind jet (northern part) this secondary current inforces the cyclonic circulation while in the right side (southern part) weakens the anticyclonic cell (see Fig 3. 33b).

The wind influence layer has a thickness of 20m where the wind induced transport takes place. On the other hand, the modification of the surface elevation has a barotropic effect that induces a significative circulation at deeper levels. It can be seen in Fig 3. 33d how the circulation cells are present until 100m depth.

In this entire picture, the bathymetry plays the role of a modifying factor of the barotropic circulation. In addition to that the bottom depth influences the structure of the baroclinic modes and thus the vertical distribution of velocities associated to the surface anomaly. Namely, the zero crossing of the first baroclinic mode over the 1000m isobath (slope) is around 500m while over the 60m isobath (shelf) it is at 30m depth. The consequence is that the vertical profile of velocity will be different depending on the bottom depth. It can be seen in Fig 3. 33d this asymmetry for the coastward branches. The branch over the shelf presents an inversion near the

bottom in good agreement with the structure of the first baroclinic mode while over the slope this inversion is not present.

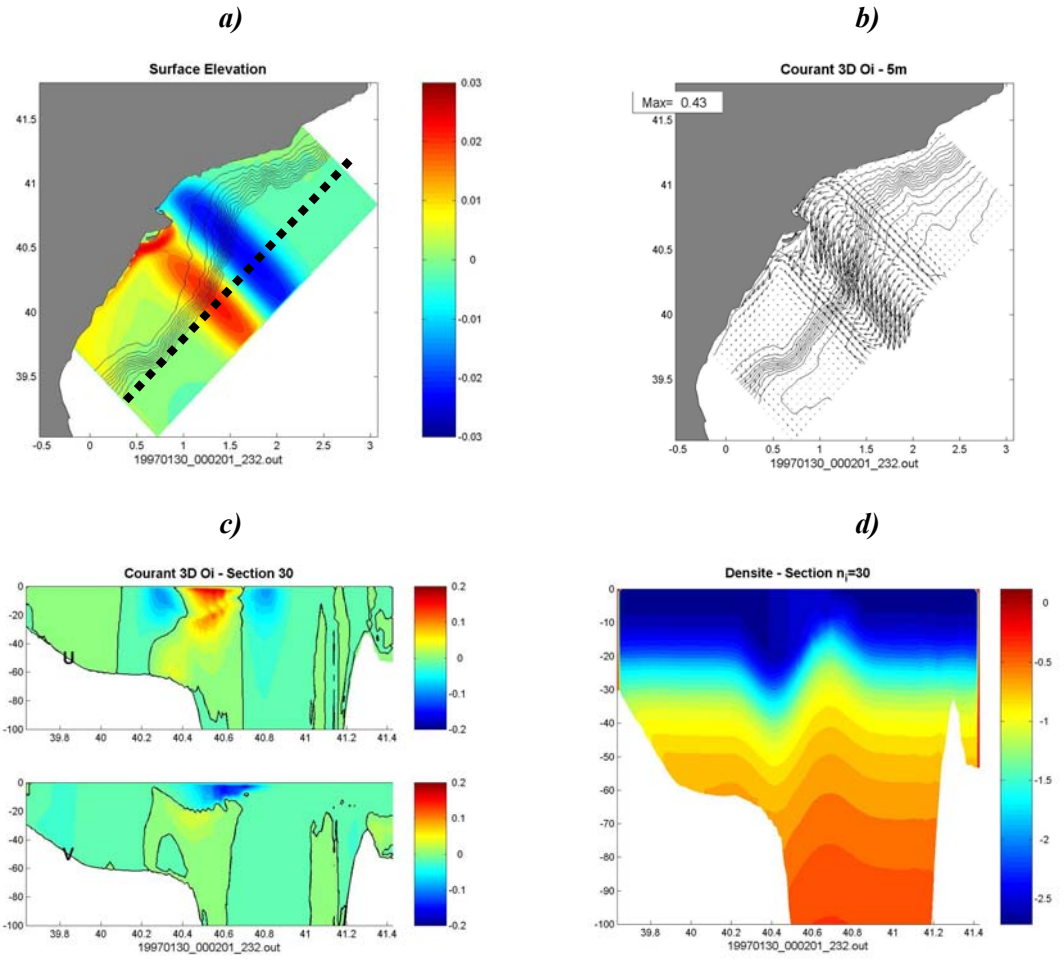

Fig 3. 33: Effects of a 2-day Mestral wind (NW) over the region in summer condition without slope current. (a)Surface elevation, (b)surface velocity, (c)vertical section of velocity and (d) vertical section of density anomaly. Dashed line shows the position of the vertical section.

When wind stops, the Ekman layer dissapears and the circulation becomes strictly dipolar with the positive-negative vorticity cells, where the modification of the density structure induces a geostrophic equilibrium around the surface elevation anomalies. After 5 days, the current intensity is maintained nearly constant thanks to the fact that the geostrophic equilibrium is energetically stable and is just degraded by friction or diffusion with long timescales.

At the same time, the coastward currents are relaxed, as the geostrophic adjustment takes places around the density anomalies, and the pilling of water on the coast is no longer maintained. These coastal currents are weakened and, after two days, they dissapear. In the southern part, the positive anomaly of surface elevation close to the coast propagates away along the coast as a Kelvin wave.

It is worth to comment one process present in this configuration but that is also found in lot of other situations. When coastal current impinges on the Ebre Delta, a local downwelling is set up with a considerable descent of isopycnals. Afterwards, when the wind stops, the current relax and the seaward branch induce a local upwelling in the same place, so the isopycnals go up. This process is analogous to the interaction of tides with the slope and also generates a train of internal waves at the thermocline depth.

Influence of wind jet position

It is not possible to define, from the punctual meteo stations available, the exact position of the Mestral wind jet . The meteorological models are the only source of information we have to define its position but we are not sure about how close to reality are them. On the other hand their parameterization of land topography plays a crucial role into the set up of the narrow jet wind, and Radmila Brozkova (personal communication) suggested that, maybe, ALADIN parameterization of topography in our region is not accurate enough. Also, the atmospheric model resolution is around 10km, so we can expect some level of inaccuracy in the representation of the Mestral wind position and extension. Therefore, it seems interesting to test the effects of a displacement of the Mestral wind position and compare the results with the circulation patterns explained before.

In this case, we run the model with the same wind configuration but displaced 35 km northward. The new position has been chosen from an analysis of ALADIN model results for several Mestral events.

The current structure and its set up is the same than in the previous cases but obviously displaced northward. The main difference is that the anticyclonic cell has a more elongated shape and is parallel to the slope direction. Also there is no southwestward costal current. The reason for both features is that the Ebre Delta coastline forces the coastward branch of the anticyclonic cell to flow to the north, so closing the anticyclone (see Fig 3. 34a).

The new placement of this eddy affects differently the plume evolution. In this new position the river waters are confined and mixed into the Gulf of St. Jordi without seaward extension. The anticyclone will also take inner shelf waters and expels them seawards.

The new wind position also implies some differences in the thermal structure. Now, the wind doesn't blow perpendicular to the coast. There is a significative wind component in the along coast direction that induces a local upwelling around the cape Salou. Once upwelled, the cold waters are advected by the dipole structure seawards (see Fig 3. 34a) where the slope current will advect them downstream (see Fig 3. 34b).

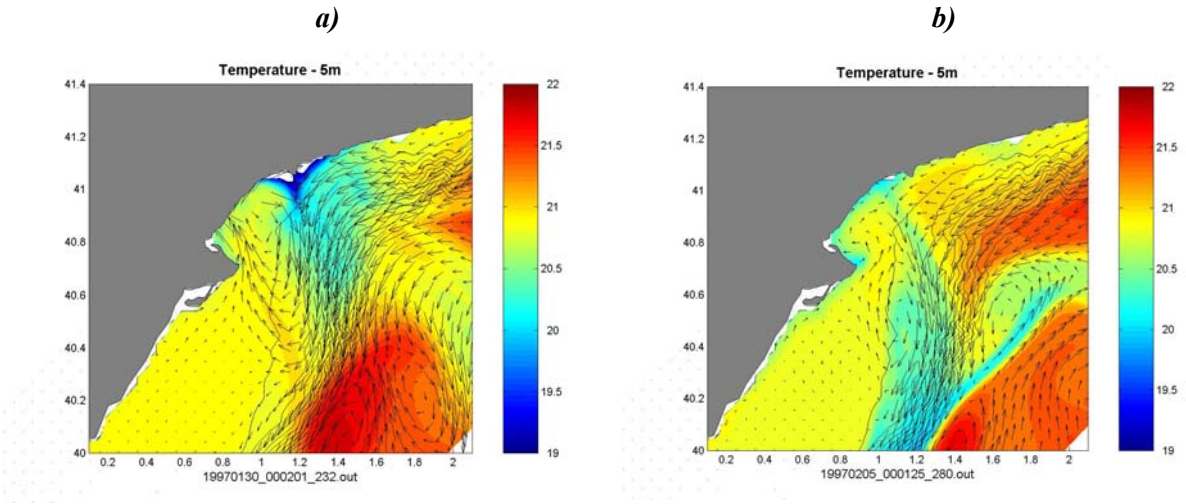

Fig 3. 34: Temperature and velocity at 5m depth after a Mestral wind (NW) displaced 35km northward in summer conditions. (a) Just after the wind burst. (b) 6 days after the wind stops.

In summer conditions, after the wind stops, the anticyclonic eddy begins to displace advected by the slope current. In comparison with the previous case, its displacement is a little faster due to the fact that its elongated shape allows more contact with the slope current, but after 15 days, it is no longer maintained neither.

Influence of wind intensity

The following parameter that we can look at is the influence of wind intensity. Both data collected in meteo stations and results from atmospheric models show that Mestral event intensity is highly variable. In our previous simulations we have used a typical wind intensity of 10m/s but is not strange to find Mestral bursts of until 15m/s. Using this value for the wind intensity the model response is again the same, qualitatively, with the increasing of surface elevation at the right of the jet and the decreasing at the left. The main difference is that values of those anomalies are much greater. In stratified conditions, with wind intensity of 10m/s, the positive increase of surface elevation was 2cm, while with an intensity of 15m/s the increase is of 4cm. This is consequence of the fact that wind stress is not a linear function of wind velocity ($\tau = \rho C_D W|W|$, where ρ is the air density, C_D the drag coefficient and W the wind velocity).

The new wind-induced structure is comparable in intensity with the slope current. It can modify it and the seaward edge of the anticyclonic circulation is place further than in the moderate wind case (see Fig 3. 35a). Vertical movements are also enhanced.

When the wind stops, the anticyclonic eddy is formed with surface velocities of 50cm/s and a vertical structure that can exceed the 100m depth. It is placed over the shelf break. where the

slope current advects it with a velocity of 10km/day (see Fig 3. 35b). In winter, the eddy intensity is reduced, its core is placed over the shelf and the advection velocity is slower.

About the anticyclonic eddy behaviour and after comparison of the different wind cases, it could be said that the key point is the modification of the vertical structure of density. After the wind stops, it is this structure that will define the geostrophic circulation that will be established. Its strength will determine the position of the anticyclonic cell and its vertical extension. It also seems that the eddy will be detached and advected by the current. Its advection velocity will depend on its position with reference to the slope current and on its depth. Deeper is the eddy, more surface of contact with the slope current will it have. Finally, it must be reminded that stratified conditions reduce the turbulent energy losses, so the effect of the wind will be enhanced having similar effects that a stronger wind in winter.

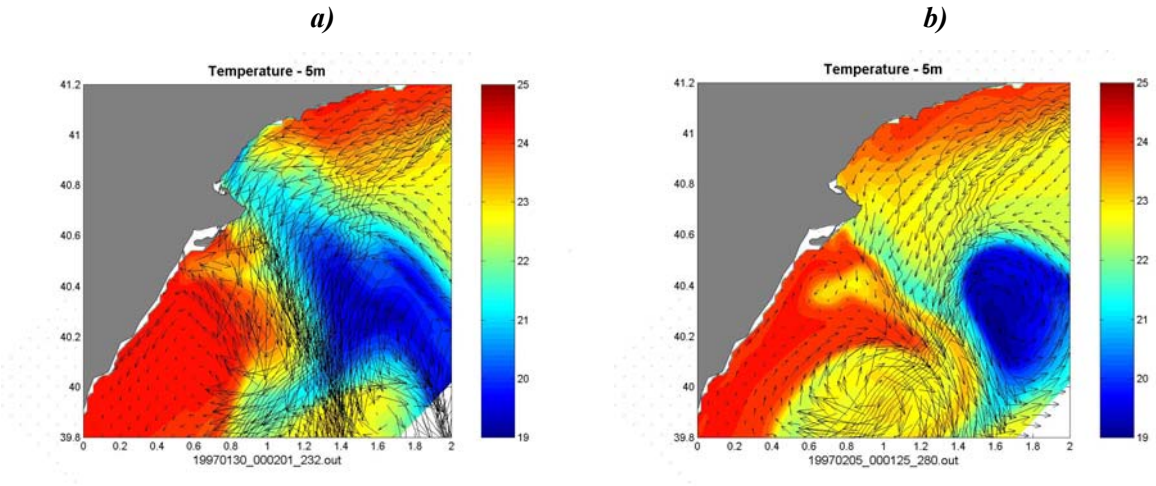

Fig 3. 35: Effects of a 2-day strong (15m/s) Mestral wind (NW) in summer conditions. (a) Just after the wind burst. (b) 6 days after the wind stops.

Influence of wind jet width

To complete the sensitivity of ocean to narrow wind parameters, we have test the effect of wind jet width as it has a direct influence into the rotational transferred to the sea. The width used in previous runs was chosen from ALADIN model results, but because of the same reasons why we can not be sure about the exact position of the jet, we can not be sure about its width. Using a wind jet 1.5 times wider, the structures generated are qualitatively the same but larger (see Fig 3. 36). The maximum velocities are comparable but the vertical displacements are reduced by a factor near 1.5. Consequently the horizontal gradients are smaller, so it is the geostrophic circulation established after the wind. In those conditions the anticyclonic eddy is not well formed and no indices of detachment are present.

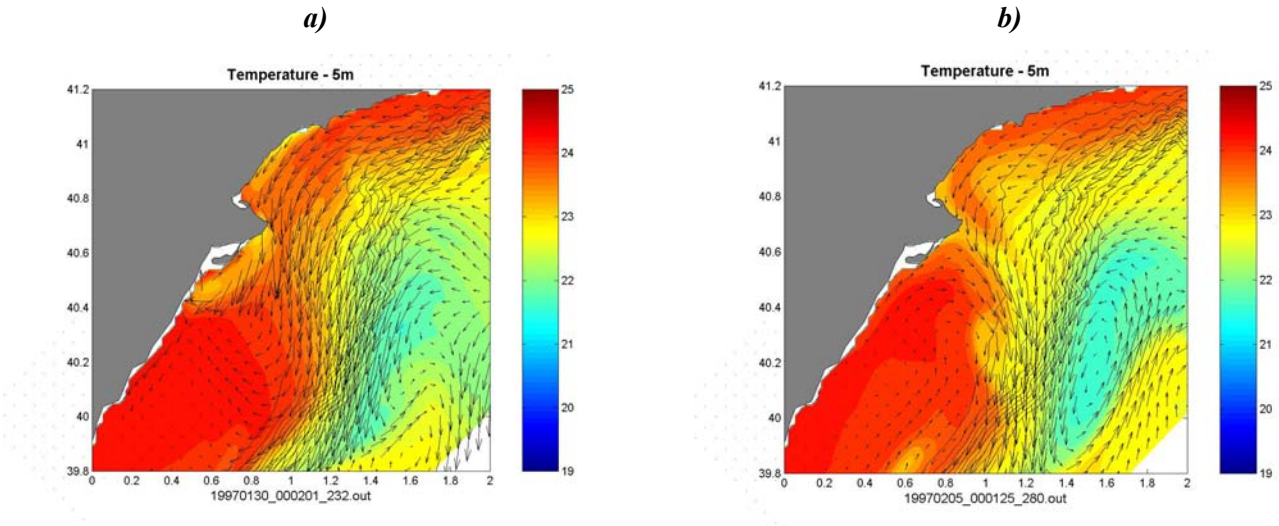

Fig 3. 36: Effects of a 2-day wide Mestral wind (NW) in summer conditions. (a) Just after the wind burst. (b) 6 days after the wind stops.

3.6 SHELF-SLOPE EXCHANGES

The shelf-slope exchanges are one of the main items where physical processes interact with biology. The shelf and the slope have very different characteristics in terms of nutrients content and their interaction has a strong impact into the biological processes.

The exchange mechanisms between shelf and slope depends on the dynamics, in particular it depends on the circulation patterns. In the base of the numerical experiments done, we can distinguish the exchange processes due to the *slope current inherent variability* and those due to the *wind-induced circulation*. Obviously, these are not the only processes present in the real ocean, but their study can give us a good overview of the problem.

To characterize and understand some of the exchanges between the shelf and the slope, we introduce passive tracers in the numerical simulations. The evolution of these tracers is determined by the advection-diffusion model equations, and they are called "passive" as they do not interact with dynamics. Depending on where they are initially placed, they will be representative of different water masses.

In our case, we will focus on a *shelf tracer* (tracer 1) introduced at the initial time over the shelf (depths < 200m, see Fig 3. 37a) and on an *open-sea tracer* (tracer 2) introduced where depths >200m. For the shelf one the lateral boundary conditions do not add more tracer along the run, so the maximum concentration will be found at initial time and will decrease along the simulation. This allows us to quantify the residence time of shelf waters. On the other hand, the

values of the open-sea tracer are set constant along all the run. This will allow us to see how much open waters come into the shelf.

3.6.1 Exchanges induced by the slope current variability

First, we will comment the mechanism processes linked to the slope current inherent variability. With this term, we mean the current variability that is not induced by external forcing mechanisms (wind, open sea variability). If the slope current remained confined to the slope without coming into the shelf, the only exchange mechanism will be the diffusion, which is not quite efficient. Nevertheless, we have shown previously (chapter 2) that the Northern current has a strong variability that dominates the mean circulation and that this is mainly due to the imported processes (waves, eddies). These are not included in our numerical configuration, but the non-linear adjustment to the initial conditions (section 3.4) generates current oscillations that can be assimilated to some kind of imported variability. The velocities (~25cm/s) and wavelengths (~ 40 km) associated to the first oscillations are comparable to the Northern Current meandering characteristics, while the topographic Rossby wave would represent a more permanent structure as the typical anticyclonic eddies advecting along the slope (Rubio et al. 2005, and also chapter 2).

Looking at that simulations we clearly identify a different behaviour depending on shelf width.

In the **northern part**, where the shelf is narrow, current oscillations have an important impact over the shelf waters. A small amplitude meandering is enough to the interaction between slope and shelf waters. Slope current easily comes into the shelf and advects downstream the shelf waters replacing them by slope waters. It must be noted that in this case there is a replacement of waters but without significative mixing.

On the other hand, there is another process that is induced by oscillations with smaller wavelength. When the current meander enters over the shelf, the waters therein are advected not downstream over the shelf but directly over the slope (see tracer concentration in the northern part in Fig 3. 37b-c). Once there, they are advected by current over the slope region and the enhanced turbulent mixing into the current favours the mix between the shelf and slope waters. It must be noted that this mixing is restricted to the slope, and waters doesn't reach the open sea, the slope current acting as a barrier. However, it is clear that if they are placed in the outer part of the slope they could interact with open sea structures more easily.

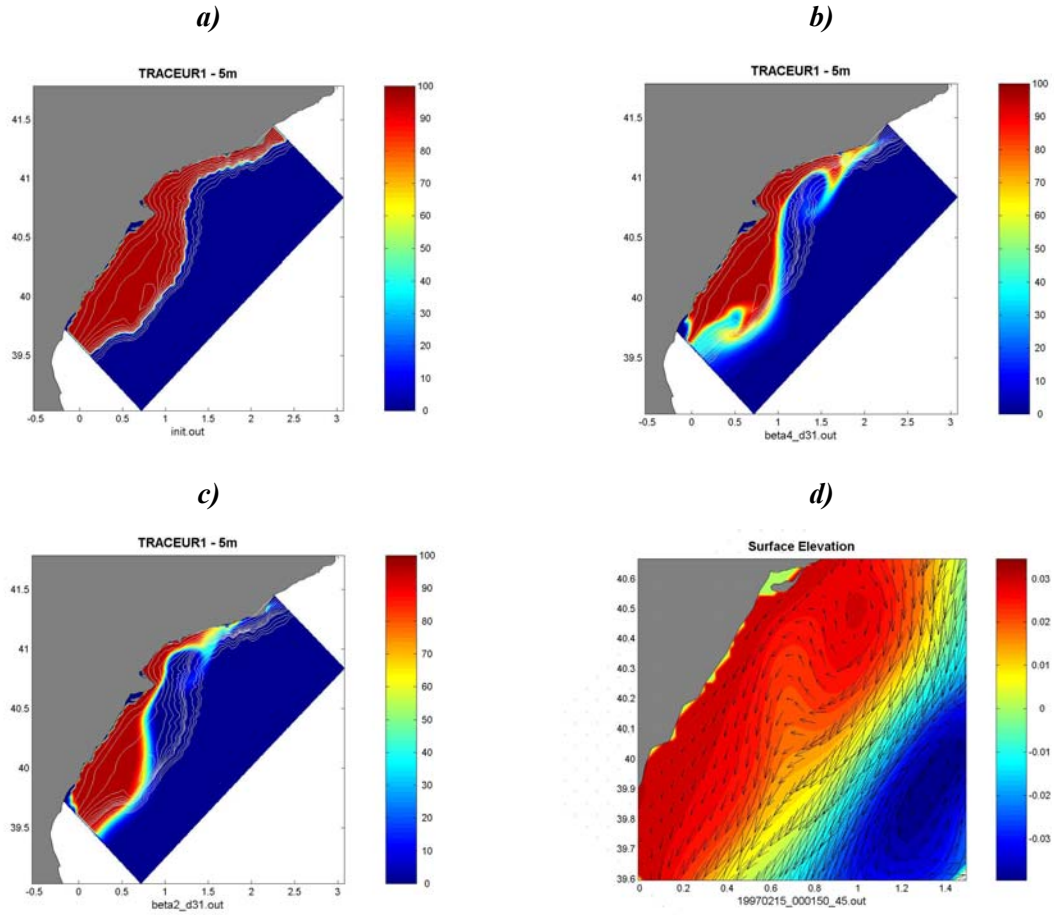

Fig 3. 37: Fraction of shelf tracer in the no-wind runs. (a) Initial conditions and results after 30 days of simulation at 5m depth for (b) homogeneous case and (c) stratified case. A zoom of circulation associated to the wave(d)

To sum up, one interesting thing that appears from the simulations is that we can distinguish the exchange mechanism as a function of the wave-length of the current oscillations (see Fig 3. 38). For the same amplitude, large wavelength oscillations will have smaller across-shelf velocities than meanders with small wavelength. In that case, the dominating process will be the advection over the shelf with small mixing. On the other hand, small wavelengths imply greater across-shelf velocities, which advects shelf waters to the slope, where mixing is much more important due to the enhanced turbulent mixing associated to the slope current.

The first mechanism is more effective for the renewal of shelf waters while the second one is more important in terms of shelf-slope exchange.

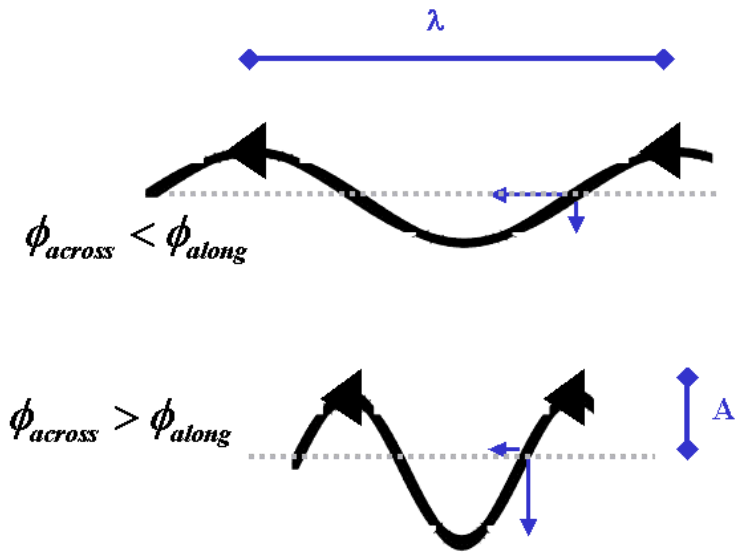

Fig 3. 38: Sketch of the exchange mechanism between shelf-slope waters,depending on the meander wavelength.

To quantify the across shelf transport as function of wave parameters (see Fig 3. 39) we consider a stationary wave defined as $y = A\sin\left(\frac{2\pi x}{\lambda}\right)$ where A is the meander amplitude and λ is the wavelength.

The ratio between across and along shelf transport is simply the tangent of the curve:

$$r = \frac{\phi_{across}}{\phi_{along}} = \frac{2\pi A}{\lambda}\cos\left(\frac{2\pi x}{\lambda}\right) \qquad \textbf{(3.24)}$$

and each transport can be expressed in terms of r as:

$$\phi_{across} = \frac{\mathbf{U}}{\sqrt{1+r^2}}$$
$$\phi_{along} = \frac{r\,\mathbf{U}}{\sqrt{1+r^2}} \qquad \textbf{(3.25)}$$

where **U** is the total transport associated to the slope current.

If the meander has the form of a "long wave", λ>>A, r ~ 0, the transport is exclusively along the shelf. On the other hand, if the oscillation has a small wavelength such that A>> λ, the total transport is across the shelf.

Although *r* could have values between 0 and 2Aπ/λ, the effective transport to induce exchange is the transport across the shelf break. Using the parameters of Fig 3. 39, the maximum value for *r*, which corresponds to the effective exchange shelf-slope, is:

$$r_{effective} = \frac{2\pi A}{\lambda}\sqrt{1-\left(\frac{d}{A}\right)^2} \qquad \textbf{(3.26)}$$

where *d* represents the distance between the shelf break and the wave center position and has values bounded by (-A,A). So, in formula (3.25), *r* must be replaced by this $r_{effective}$.

If *d*=0, the wave is centred in the shelf break and the effective ratio is equal to $2A\pi/\lambda$. On the other hand if the wave is completely restricted to the shelf or to the slope, ($d \leq -A$ or $d \geq A$, respectively) there is no exchange shelf-slope.

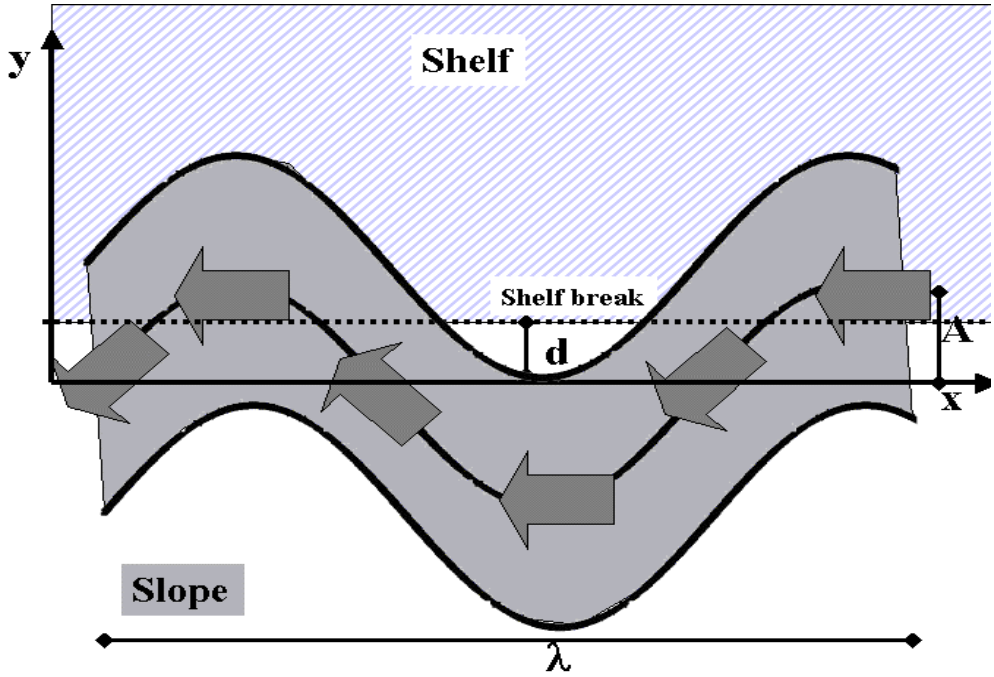

Fig 3. 39: Sketch of a current meander and parameters used to characterize it. λ is the wavelength, A the wave amplitude and d the distance between the equilibrium position of the jet and the shelf break

In the **widening region** (center of the study area) the mechanisms present are the same that we mentioned before, but meanders size needs to reach a treshold value to cover all the area. If the amplitude is not large enough, the current will not be able to reach the inner shelf, where river plume influenced waters (richer in nutrients) are located. In stratified conditions, the meanders amplitude is greater than the threshold value, so this condition is accomplished, and current oscillations easily reach the Ebre Delta advecting shelf and river-influenced waters away. With smaller amplitude meanders, as in homogeneous conditions, this doesn't occur and the plume waters are not able to interact with the slope jet.

In the **wide shelf area**, there is no direct interaction between current oscillations and inner shelf waters and, in the homogeneous case, the inner shelf remain unaffected (see Fig 3. 37b).

On the other hand, in the stratified case, we can expect larger amplitude current oscillations as showed in previous sections. As an example, there is the amplification of the topographic Rossby wave presented in section 3.4. In stratified conditions the amplitude of the wave is amplified in the widening region covering the entire shelf. As it propagates slowly, the cyclonic circulation associated to the wave over the shelf (see Fig 3. 37d) has enough time to advect shelf waters to the slope and, vice versa, slope waters into the shelf. This process is effective enough to "clean" the entire shelf displacing the waters therein to the slope and replacing them by slope waters (see Fig 3. 37c).

About the vertical structure of those processes, it must be noted that they are all set up where dynamics is enhanced, that is in shallower levels where velocity intensity is more important. Near the bottom, friction hampers the slope current entrance into the shelf, so bottom shelf waters are not affected as much as in surface. An effective mechanism to transfer slope waters to the shelf bottom is the downwards movement induced by the current when it approaches the coast. If meanders size is greater than the shelf width, current-advected slope waters impinges on the coast and are downwelled to the bottom. This mechanism is enhanced again if the across shelf velocities are important (small wavelength meandering).

3.6.2 Exchanges induced by the wind

In section 3.5 we presented the wind induced circulation for different wind situations. Here, we will take a look to the implications of those circulation patterns into the shelf-slope exchanges.

In the case of **upwelling winds** (S-SW), the wind induced circulation is restricted to the Ekman layer, so it is there where the shelf-slope exchanges will take place. When the wind begins to blow, shelf waters are advected seawards, even far away from the slope, reaching the open sea. At this point no significative mixing is present (see Fig 3. 40a). When wind stops, waters tend to come back to the shelf but the presence of strong inertial oscillations favours the mixing between shelf, slope and open sea waters. Also, once in the open sea, shelf waters can easily interact with open sea structures enhancing mixing between shelf and open sea waters.

This occurs in the first 20m of the water column. In the bottom, the undercurrent generated by the upwelling cells favours bottom mixing just in the northern part, where the wind upwells slope waters onto the shelf. This mixing takes place around the shelf break except near the submarine canyon where it seems that slope water is channelled into the shelf. In the wide shelf, the origin of the upwelled waters is over the shelf so the inner shelf area is not affected by those processes and bottom exchange is limited to the shelf break.

When stratification is present, wind induced circulation is more energetic and, consequently, the seawards transport and mixing induced by inertial oscillations is more important. In stratified conditions, the deep of the surface mixed layer is reduced so all these processes are restricted to a shallower (~15m) layer.

It must be noted that the interaction of the wind-induced circulation with the coast line or the bathymetry can establish small scale (~10km) eddy-like structures over the shelf. Structures like these are quite effective to bring slope waters into the shelf in the surface layers. If those structures stay for several days the slope waters can reach the coast and be downwelled to the bottom. This kind of small scale process can be very efficient for the shelf-slope exchange in limited areas.

With **downwelling winds**, the slope waters are drifted into the shelf within the Ekman layer. When wind stops, the inertial oscillations favor the mixing over the shelf. In the northern part, waters easily reach the coast and are downwelled until the bottom where they mix with the shelf waters. In the widening shelf area, surface waters enter into the shelf following two preferential paths through smooth canyons (see Fig 3. 40b). These paths coincide with the paths suggested by Salat et al. (2002) from CTD data for the entrance of slope waters into the shelf. The bottom is just affected when the open sea waters reach the coast and are downwelled. Finally, in the wide shelf region, slope waters remain in the outer shelf and no mixing is found in the bottom. The stratification accentuates these processes as the kinetic energy transferred by the wind is more important.

In the Mestral case, with the **narrow jet winds**, the cyclone-anticyclone structure created by the wind rotational strongly favours the exchange. The seawards current bring shelf waters to the slope, which are advected by the slope current downstream mixing with surrounding waters. The coastward current associated to the cyclonic cell brings slope and open sea waters into the shelf in the entire Ekman layer. Waters reaching the coast are downwelled and mix with the shelf waters. The coastward current associated to the anticyclonic cell does the same work but as its shapes is restricted to the shelf break, it is less effective for taking slope waters.

The stratification implies stronger currents in the Ekman layer with a stronger displacement of shelf and slope waters. The eddy created and advected by the current (see section 3.5) has shelf waters in its core that do not mix with the surrounding and that can be transported far away from its original place.

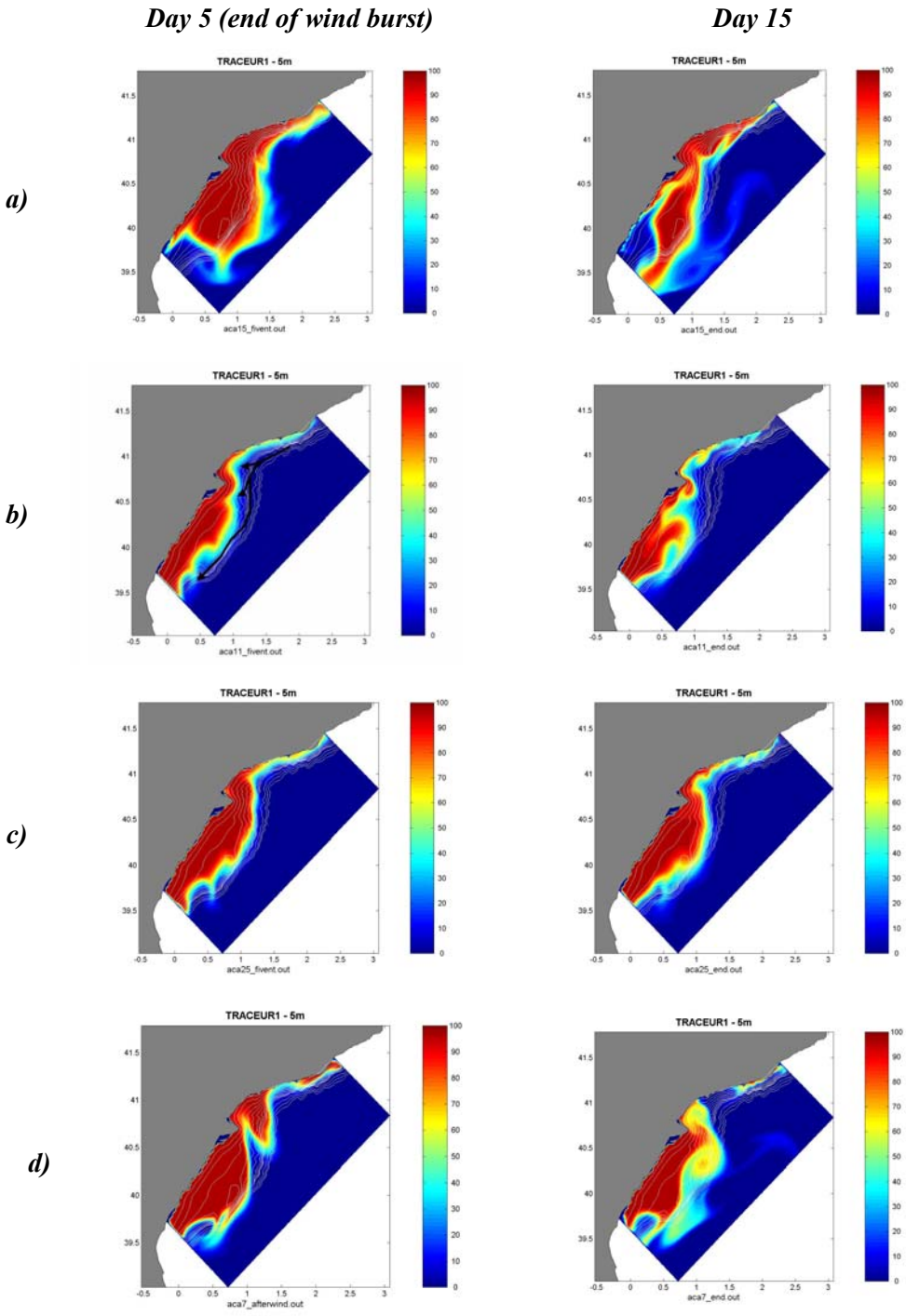

Fig 3. 40: Passive tracer at 5m depth in the different wind regimes: (a)Migjorn (upwelling) (b) Gregal (downwelling) (c) Llevant (SE) and (d) Mestral (narrow jet). In the left column there are the results at the end of the wind burst and in the right column there are the results 10 days after. Red defines shelf waters and blue open sea waters. Isobaths are white lines spaced 20m until 600m depth

3.6.3 Residence time

In order to compare the relative importance of the above mentioned mechanisms into the shelf-slope exchange, we look at the *residence time* of the waters over the shelf. This magnitude will help us to compare quantitatively the effect of different mechanisms.

The reference values will be those obtained for the no-wind runs (dotted lines in figures). To have an insight into the vertical structure of the exchanges we split the quantity of shelf water between those into the upper layers (z<50m; blue in figures) and those into the deeper layers (z >50m; red in figures). Finally we divide the results between the narrow shelf area (northern part), the widening area (center part) and the wide shelf area (southern part).

The no-wind case, where just current variability is present, shows a near constant rate of renewal of 0.7%/day in the stratified case and of 0.4%/day in the homogeneous case (look at dotted lines in Fig 3. 41). If we look into different regions, we find that, in the northern part, almost all waters over the shelf have been renewed after two months. During the first month, those waters where transferred in an 80% to the slope-open sea, especially in deep layers. Afterwards, there were advected downstream by the slope current. In the center and southern parts the evolution is similar but delayed. The reason is that the main mechanism to renew the shelf waters is the current meandering, and specially, the topographic Rossby wave. The delay is due to the time needed by the wave to reach each region.

When the water column is homogeneous the amplitude of current meanders is smaller, and so it is its effectiveness to renewal shelf waters. Coherently, the exchange rate is greatly reduced in all areas and two months is not enough time to completely renew shelf waters in the Northern part.

To see the effect of wind we use realistic wind fields during a two months run both for winter and for summer conditions. When wind acts the exchange is more complicated (see solid lines in Fig 3. 41). It seems that wind inhibits the topographic Rossby wave-induced exchange in the shallower layers, and wind-induced exchange dominates. In deeper layers, significative differences with the no wind run in the northern part. It is interesting to note that, in summer conditions, in the narrow shelf area, wave-induced exchange can be much more effective than winds. Although winds capacity to renew shelf waters is important, no all wind conditions are favourable to do it as it was seen previously and as it happens in summer.

To gain an insight into the effect of the wind into the shelf-slope exchange, we look at the time evolution of shelf tracer for each wind conditions separately (see Fig 3. 42).

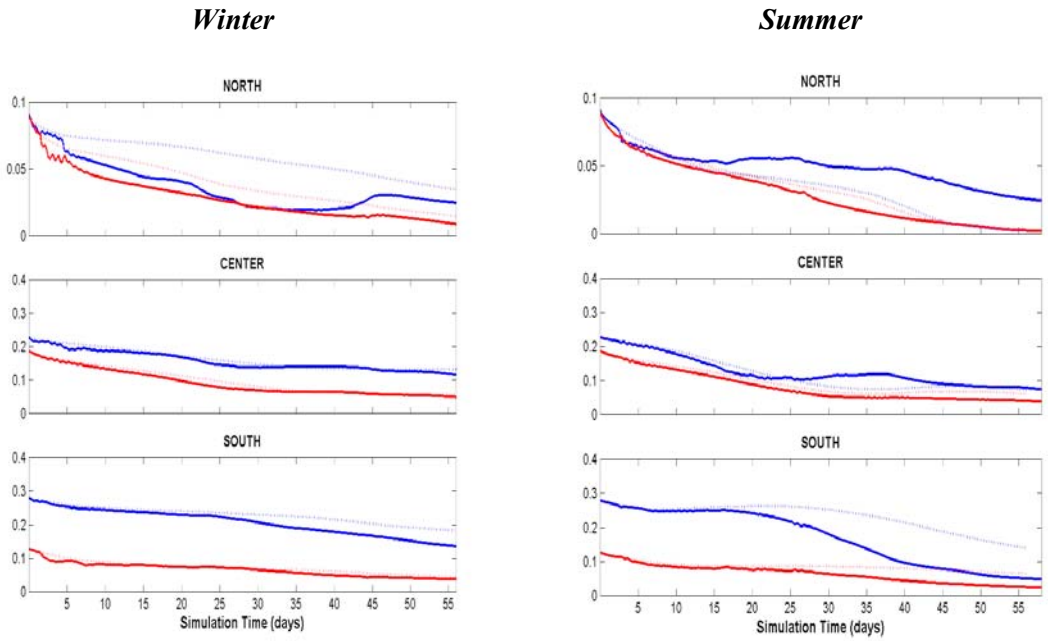

Fig 3. 41: Time evolution of the fraction of shelf tracer for depths shallower than 50m(blue) and greater than 50m (red). Dotted line is the time evolution without wind. In the left column there are the experiments with homogeneous density profile and in the right the experiments with stratification.

In the upwelling case (red line), near the half of the shelf waters in the southern region is taken out in the two days wind burst period. One part is advected northwards to the center shelf while another is advected seawards. In the center and northern region the decreasing rate is much smoother and the shelf waters expelled to the open sea are compensated by waters from deep layers and by those advected from the south.

When dominant winds are the downwelling winds the situation is the inverse than before. The shelf waters in the northern part are advected to the center region being replaced by slope waters. The rate is around 15%/day for surface waters (z<50m) while in deeper layers a small part of the bottom shelf waters is expelled to the slope. In the center region the renewal rate is reduced to 6%/day while in the wide shelf area in the south there is no significative renewal.

Finally, when the narrow Mestral winds acts, the exchange is significative where the wind blows, the northern and center parts. The renewal rate is similar to the downwelling case but in this case it is completely due to shelf-slope exchanges and near no advection between shelf regions is present. It must also be noted that after the wind burst, the wind-induced circulation established remains for more than 10 days allowing a continuous exchange. Also, in the summer case, the drifting eddy induces a significative exchange rate in the southern part.

To sum up the differences among the wind regimes, it could be said that upwelling and downwelling winds are characterized by the advection of shelf waters to other shelf areas and, in a second order of importance, seawards, while the Mestral winds induces exclusively shelf-slope exchanges. The wide shelf is affected significatively just for the upwelling winds and the drifting eddy generated by the Mestral wind. In the widening shelf area and in the narrow shelf, both downwelling and Mestral winds can reduce to the half the shelf waters in few days but for different mechanisms. The former is mainly due to the advection to the southern regions while the last induces shelf-slope exchange.

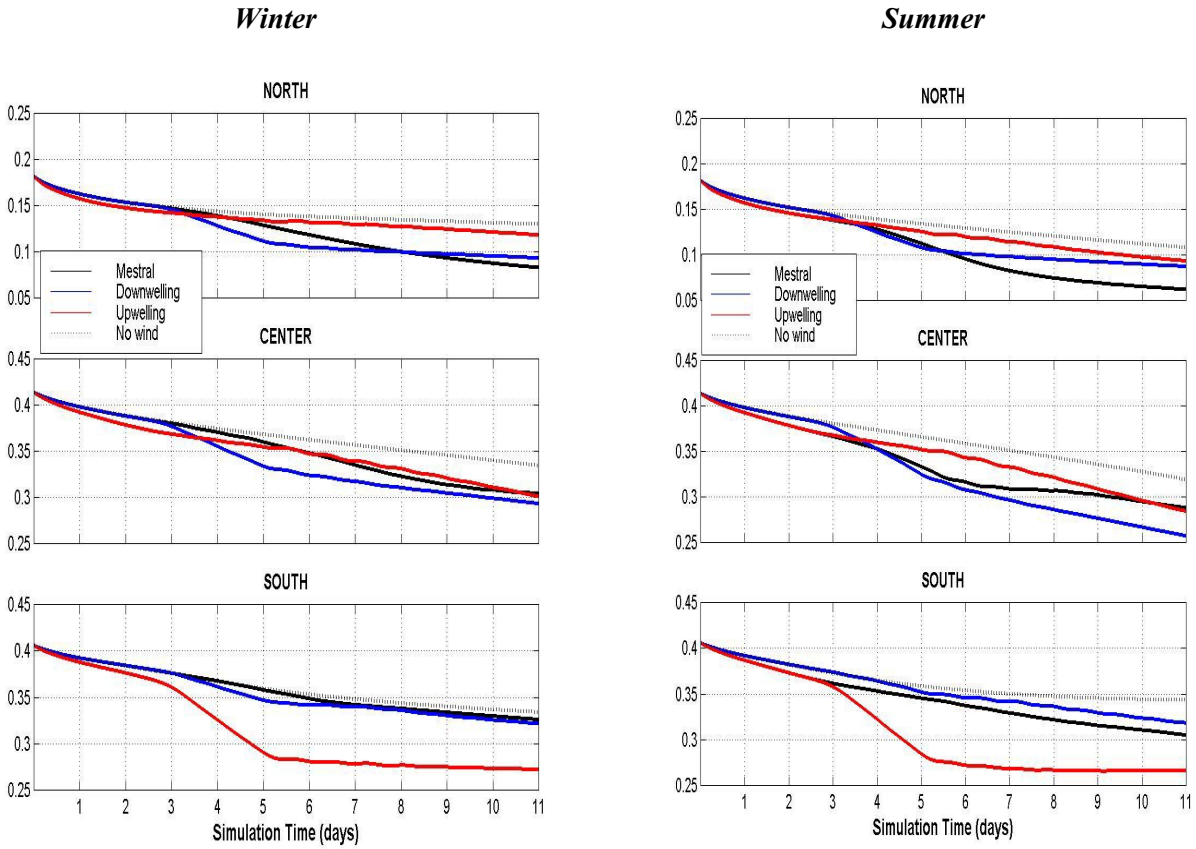

Fig 3. 42: Time evolution of the fraction of shelf tracer in the whole water column in the different regions and for the different wind regimes: Mestral (black), upwelling (red), downwelling (blue) and no wind(dotted).

3.7 CONCLUSIONS

In this chapter we have shown the work done to implement the SYMPHONIE model into the southern Catalan continental shelf, the validation procedure followed and the application of the model to several process-oriented studies.

The model is specially suited for coastal applications and it includes a hybrid vertical coordinate system. This system reduces the truncation errors avoiding the over-smoothing of bathymetry while proper solving the bottom processes.

Another interesting feature is the MPV initialization method. This method solves most of the problems of limited area models, namely the initialization and the open boundary conditions, providing a stabel and well controlled set up.

The model implementation has been validated with real data. The water masses are well reproduced as well as the density structure. The temperature field is not adequate but it doesn't affect the model results. The Ebre river plume is well described in terms of extension and vertical mixing but its position is not adequate due to errors in the wind field. The slope current is well determined and the shelf circulation reproduce some of the main patterns observed in data. On the other hand there is no import of variability, which limits the configuration for long runs.

Once the model has been successfully implemented and validated we have applied it to several process-oriented studies of the shelf-slope dynamics.

First we have described the evolution of a topographic Rossby wave and its interaction with the shelf widening. In stratified conditions the wave is amplified covering all the shelf extension. This phenomena is produced by the different propagation speed in shallower areas.

The stratification acts as a decoupling factor between the shallower and the deeper levels favoring the amplitude growing of the wave in the upper levels. In homogeneous conditions there is no such decoupling and the interaction with the bathymetry prevents the amplification.

The phase velocity is small, so the circulation pattern associated to the wave is near-stationary. In consequence it is very efficient in enhancing the shelf waters renewal and the shelf-slope exchanges although it has a low impact in the vertical transports.

The second process studied has been the dynamical patterns induced by the most typical wind regimes. When the wind blows from the open sea, a wind-driven circulation is established in the first 20m overimposed to the previous circulation pattern.

The upwelling type winds induce a complex pattern over the wide shelf and strong north-eastwards coastal current which lasts for some days even after the wind stops. Internal waves are produced due to the displacements of the density front near the coast and at both sides of the slope current. When the burst is finished, inertial oscillations are triggered controlling the circulation in the upper layers and baroclinic instabilities are triggered on the slope current due to the displacement of the densitiy front.

The downwelling winds are analogous. A SW coastal current is generated and the circulation over the shelf is again complex. When wind stops the inertial oscillations dominates again the circulation, the coastal current is quickly damped and no significative modifications of the slope current are found.

From the simulations with the Llevant wind, we have also proposed a mechanism for the formation of an anticyclonic structure in the gulf of St Jordi due to the effects of a transeint variable wind.

A different case has been the study of the effects of a Mestral wind, which can be defined as a narrow jet wind. Its limited extension in the horizontal provokes a barotropic dipole structure at both sides of the jet. In the northern part, a bending of the slope current is induced while an anticyclonic structure is established in the southern part due to the interaction with the slope current. When wind stops this structure remains for several days placed in the widening area.

The location of the Mestral jet affects the shape of the structures. We have also found that strong winds can provide the anticyclone with a density structure strong enough to allow it to act as an isolated structure and displace advected by the slope current.

The last process studied has been the shelf-slope exchanges. We have seen the effects of the current variability and the wind-induced circulation over them.

Depending on the characteristics of the current meandering, the effects will be differents. A long wavelenght meandering induce an advection of the shelf waters over the shelf, with few exchange rate with the slope. On the other hand small wavelength meandering is much more effective for the shelf-slope exchanges.

The wind-induced exchanges are restricted to the Ekman layer except when the current impinges the coast inducing a downwelling. In that case the open sea waters are advected to the bottom in a narrow band along the coast. On the other hand, the wind-induced eddy structures can be very effective to exchange processes at local scales as in the Mestral case.

Finally, the residence time of the shelf waters has been explored as a function of the forcing factor.

DATA ASSIMILATION METHODOLOGY

"La science est faite d'erreurs
qui sont les pas vers la vérité"
(Jules Verne)

4 DATA ASSIMILATION METHODOLOGY

Once the region dynamics has been properly characterized (chapters 2 and 3) and a realistic modelling system has been set up (chapter 3), the data assimilation methodology can be defined.

In this chapter we present the SEQUOIA data assimilation system justifying its choice among other possibilities (section 4.1). In particular, a key point of our approach is the way the error covariances are defined. Instead of using analytical relations (as is frequently done in operational meteorology), or defining them from the model variability, we use stochastic modelling to explore the error dynamics.

The ensemble modelling approach allows us to characterize the characteristics of the errors in the system, and to define the error subspace that will be used in the reduced order assimilation scheme.

In a first stage we describe the ensemble modelling approach (sections 4.2 and 4.3) and analize the information it provides about the spatial structure of the errors, their time evolution and the linearity of the errors dynamics (section 4.4). Afterwards, we can also use the ensemble results to study the influence of observations in different error regimes through the representers (section 4.5).

The second stage is to explore the use of the ensemble modelling to define the error subspace where assimilation will be done. To do that we use the multivariate EOFs decomposition which allow us to describe statistically the principal modes of error of the system (section 4.6). Once the EOFs have been computed and interpreted we can define the EOF base that will be used in the assimilation for defining the error subspace (section 4.7). Finally, some technical experiments are carried on to explore the performance of the chosen modes in the assimilation.

4.1 FORMULATION OF THE DATA ASSIMILATION PROBLEM

Why are we interested in Data Assimilation?

The main objective of data assimilation is to find the best estimate of reality that can be done combining model results with observations. It can be said that it is the approach that allows to merge the information from a numerical model with the information obtained from observations in order to produce a complete and accurate picture of the sea state. This tool can be used in process-oriented studies to dynamically interpolate measured data (i.e. Morrow and De Mey, 1995), in monitoring and forecasting systems where it is used to correct the model

predictions (i.e. Demirov et al., 2003), to design observational arrays or to explore the predictability of the systems, among others. In our case, we are interested into set up a suitable data assimilation scheme for coastal areas which would be useful for both applications. Once implemented, we use it to evaluate the performance of different observing systems to correct model trajectories.

Basic concepts

A data assimilation scheme is, essentially, a method that allows to incorporate observed information into a background estimate (in our case the model state) considering several information constraints and some laws of temporal evolution and physical properties. In particular, the consistency constraints are related to consider the quality of data and model when correct the model state and the physical laws are those which describes the problem to solve (i.e. from geostrophic approximations to complete non-linear dynamics).

If the temporal dimension is introduced into the scheme, two different approaches are possible, the sequential and the variational methods. The *sequential* methods are those which only considers observations made in the past until the time of analysis (i.e. Kalman filter) while the *variational* methods use all the available information in a given period to estimate the optimal model state (i.e. 4D-var methods). See Bouttier and Courtier (1999) for a clear review about the different methods

The mathematical problem of merging background information with data is solved using a statistical approach where it is intended to minimize the distance between the analysed field and the reality. There are several existing techniques which differ in terms of simplicity, optimality or numerical burden but all of them consider the optimization problem in a least squares sense (several exceptions are presented in Talagrand,1997).

On the other hand, the representation of uncertainties in the background field, in the observations and in the analysis, is done through the probability density functions (pdf). In other words, we assume that we do not know the actual errors but we can characterize their statistical properties. A common way to define them is the Gaussian function where the first and second order statistical moments (mean and standar deviation) allow to define the *pdf*.

Before presenting the mathematical formalism, some definitions are needed. The **model state** is represented as a vector where all the model variables are included in all locations: $\mathbf{x}^T = \left(x_1^1,...,x_{N_1}^1,x_1^2,...,x_{N_2}^2,...,x_1^k,...,x_{N_k}^k\right)$, where $x^1,..x^k$ represent the different model variables (η,T,S,velocity) and $N_1,..,N_k$ is the number of values (usually grid points) for each variable. The dimension of the state vector is $n = \sum_k N_k$.

The model provides a forecast $\mathbf{x}^f$ (also call background in optimal interpolation and variational methods) that is intended to be corrected. The **true state** vector is $\mathbf{x}^t$ which is the best model representation of reality ($\{\mathbf{x}\}$). It is important to note that $\mathbf{x}^t$ is not the real solution but the best approximation we can do with the model.

Similarly the observations can be expressed as an **observation vector** $\mathbf{y}^0 = \left(y_1, ..., y_p\right)$ where p is the number of measurements. The observations do not need to be in the same locations that model grid points and even they do not need to be the same variables that are in the model state vector (i.e. it is possible to measure derived quantities). To compare the model state and the observations it is necessary to use a function that links both spaces : the **observation operator** H.

The errors associated to the forecast are modeled as $\varepsilon_f = \mathbf{x}^f - \mathbf{x}^t$, with $\mathbf{P}^f$ being the **forecast error** covariance matrix. Here, the errors due to the discretization are not included. The **observational errors** are $\varepsilon_o = \mathbf{y}^o - H(\mathbf{x}^t)$, with **R** its covariance matrix. In **R** it is included the instrumental errors, the errors in the observation operator and also the representativity errors. Finally $\mathbf{P}^a$ is the covariance matrix of the **analysis error**. To clarify the meaning of each kind of error, a sketch is presented in Fig 4. 1. The instrumental errors are represented by **E** while the representativity errors (distance between the model true and the reality) are represented by **F.**

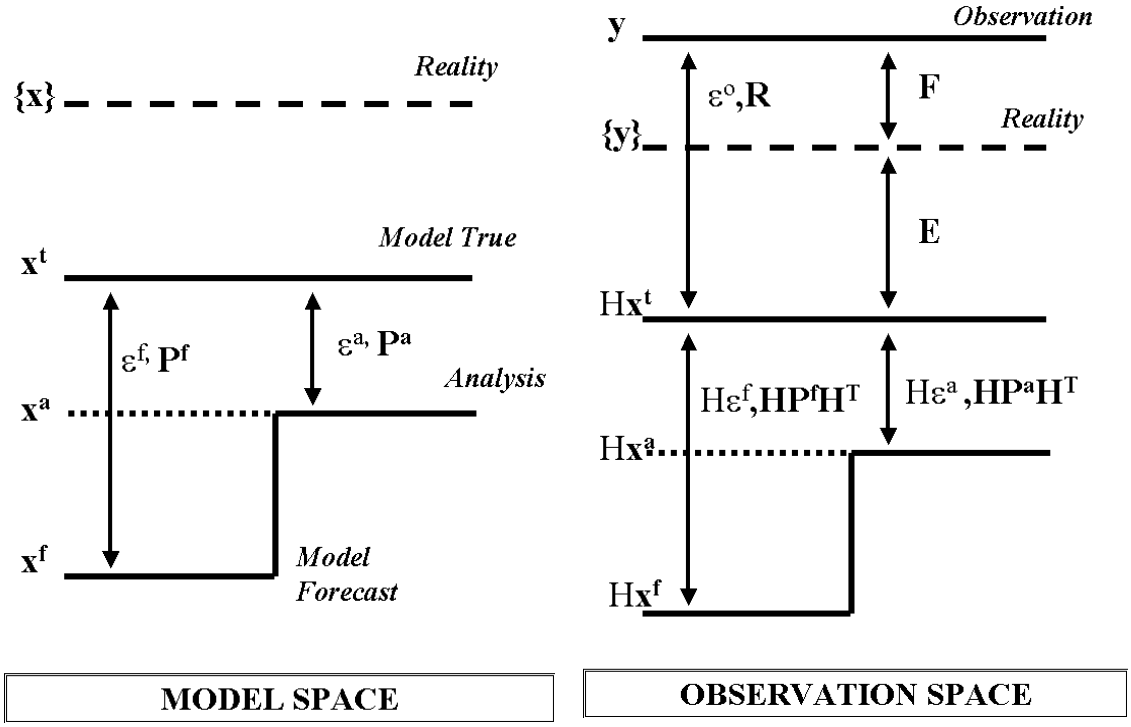

Fig 4. 1: Sketch of the errors and their covariances in the analysis phase(Reprinted from Testut, 2000)

The sequential data assimilation systems are structured with two stages that are successively repeated: the analysis and the forecast phases. The **analysis stage** provides an estimation of the system correcting a "first guess" with the available data. At the same time the analysis error covariance matrix is computed. Then, in the **forecast stage**, a model is used to provide a forecast of the system state and an estimation of the forecast error covariances. The model state prediction is done integrating the model equations from the last analysed state while the forecast error is obtained from the propagation through the model dynamics of the analysis error and adding an estimation of the model error.

In the Kalman Filter (Gelb, 1972), the analysis stage corresponds to an optimal estimation in the least square sense which is also called BLUE (Best Linear Unbiased Estimation). The basic hypothesis assumed in the development of BLUE must be kept in mind to understand the main limitations of the data assimilation schemes. Those assumptions are:

-The observation operator is linear (or linearized): **H**.

-The errors are unbiased: $\overline{\varepsilon}_f = \overline{\varepsilon}_o = 0$

-The analysis is linear: we look for a correction that linearly depends on background observation departures.

-The analysis must be optimal: We look for an analysis state which is as close as possible to the true state in a rms sense.

With this hypothesis the optimal linear analysis is defined with the following equations:

$$\mathbf{x}^a = \mathbf{x}^f + \mathbf{K}\left(\mathbf{y} - \mathbf{H}\mathbf{x}^f\right) \qquad \textit{(4.1)}$$

where **K** is the Kalman gain and it is defined following:

$$\mathbf{K} = \mathbf{P}^f\mathbf{H}^{\mathbf{T}}\left[\mathbf{H}\mathbf{P}^f\mathbf{H}^{\mathbf{T}} + \mathbf{R}\right]^{-1} \qquad \textit{(4.2)}$$

From this, and assuming that the gain matrix **K** is optimal, the analysis error covariance matrix can be expressed as:

$$\mathbf{P}^a = \left[\mathbf{I} - \mathbf{K}\mathbf{H}\right]\mathbf{P}^f \qquad \textit{(4.3)}$$

where it is accomplished that:

$$\left\|\mathbf{I} - \mathbf{K}\mathbf{H}\right\| < 1 \qquad \textit{(4.4)}$$

and, in consequence:

$$\left\|\mathbf{P}^a\right\| \le \left\|\mathbf{P}^f\right\| \qquad \textit{(4.5)}$$

the analysis stage ensures that the norm of the error covariance matrix is reduced.

The hypothesis of the linear analysis assumed is a strong assumption but, for strongly non-linear error processes, there is no general and simple way to calculate the optimal analysis. The fact of using the linear analysis in non-linear problems is possible at the expense of optimality.

In the forecast phase of the Kalman Filter, a linear dynamic model, *M*, allows the time evolution (from time n to time n+1) of the model state. This model is such that

$$\mathbf{x}_{n+1}^{t} = M_{n,n+1}\,\mathbf{x}_{n}^{t} + \varepsilon_{n}^{m} \qquad \textit{(4.6)}$$

where $\mathbf{x}^t$ is the true state, n is the time index, and ε^m is the error of the model, which is assumed to have zero mean and covariances represented by matrix **Q**.

This model is applied to the analyzed field to obtain the forecast state at time n+1:

$$\mathbf{x}_{n+1}^{f} = M_{n,n+1}\,\mathbf{x}_{n}^{a} \qquad \textit{(4.7)}$$

and it is also used to obtain the estimation of the forecast error covariance matrix as:

$$\mathbf{P}_{n+1}^{f} = M_{n,n+1}\,\mathbf{P}_{n}^{a} M_{n,n+1}^{T} + \mathbf{Q}_{n} \qquad \textit{(4.8)}$$

The analysis and the estimation of the forecast errors are based on the covariance matrices $\mathbf{P}^f$, **R** and **Q**. The correct definition of these matrices is what determines the properties and quality of the data assimilation scheme.

It must be noted that in ocean, dynamics is non linear, so neither the observation operator *H* nor the model *M* are linear. In that case, the Kalman Filter is generalized to the **Extended Kalman Filter (EKF)** where *H* and *M* are replaced by their linearized versions **H** and **M** in the operations concerning the errors.

The EKF which is at the base of most of the sequential assimilation schemes can be summarized as:

Extended Kalman Filter -EKF

Forecast stage

$$\mathbf{x}_{n+1}^{f} = M_{n,n+1}\,\mathbf{x}_{n}^{a} \qquad \textit{(4.9)}$$

$$\mathbf{P}_{n+1}^{f} = \mathbf{M}_{n,n+1}\,\mathbf{P}_{n}^{a}\mathbf{M}_{n,n+1}^{T} + \mathbf{Q}_{n} \qquad \textit{(4.10)}$$

Analysis stage

$$\mathbf{x}_{n+1}^{a} = \mathbf{x}_{n+1}^{a} + \mathbf{K}_{n+1}\left(\mathbf{y}_{n+1} - \mathbf{H}_{n+1}\mathbf{x}_{n+1}^{f}\right) \qquad \textit{(4.11)}$$

$$\mathbf{K}_{n+1} = \mathbf{P}_{n+1}^{f} H_{n+1}^{T}\left[H_{n+1}\mathbf{P}_{n+1}^{f} H_{n+1}^{T} + \mathbf{R}_{n+1}\right]^{-1} \qquad \textit{(4.12)}$$

$$\mathbf{P}_{n+1}^{a} = \left[\mathbf{I} - \mathbf{K}_{n+1} H_{n+1}\right]\mathbf{P}_{n+1}^{f} \qquad \textit{(4.13)}$$

In this work, we focus on the sequential data assimilation schemes mainly for practical reasons but a variational approach could be considered (strictly it is underlying behing the sequential scheme). The variational methods are based in the minimization of a penalty (or cost) function which measures the distance between the model results and the observations:

$$J(\mathbf{x}) = \frac{1}{2}\left(\mathbf{x}-\mathbf{x}^b\right)^T \left(\mathbf{P}^b\right)^{-1} \left(\mathbf{x}-\mathbf{x}^b\right) + \left(\mathbf{Hx}-\mathbf{y}^o\right)^T \mathbf{R}^{-1} \left(\mathbf{Hx}-\mathbf{y}^o\right) \qquad \textit{(4.14)}$$
$$J(\mathbf{x}) = J_b(\mathbf{x}) + J_o(\mathbf{x})$$

This approach lead to an equivalent formulation of the BLUE estimation (Gelb, 1972) but in this case it is not the forecast (f) which is considered but the trajectory of the background (b).

The advantage of this method is that one obtains a global minimization, which can be really attractive for reanalysis purposes. In comparison with EKF it is also much cheaper and its implementation in the complete form is feasible. On the other hand the minimization of this function over a time interval requires an adjoint model which is usually difficult to be obtained. In addition to that, the method assumes that there is no error in the model ($\mathbf{Q}$=0) as it just intends to correct initial and boundary conditions. Finally, it doesn't provide an estimation of the error statistics $\mathbf{P}^f$.

Implementation in oceanographic problems

In oceanic implementations, the dimension of the state vector is very large (n~10^6-10^7) and the computational burden of the complete EKF makes it impracticable. In order to reduce the problem size, some approximations are needed but they must be carefully implemented so that the quality of the results will not be degraded. In addition to that, another problem in the oceanic data assimilation applications is that the linearization of the filter can represent a serious handicap. Also, the model error covariance matrix $\mathbf{Q}$ is difficult to know.

In the EKF, the most expensive part is the computation of the forecast error covariances, so most of the simplification methods focus on that part. The most common are the *asymptotic filters*, where an asymptotically constant Kalman gain matrix is used (it is only possible if the observational network is constant, i.e:Fukumori et al., 1993), and the *reduced-order filters*, where the dimension of the stochastic forcing is explicitly reduced either by using a coarse resolution model for evolve the error statistics, or by reducing the state space to a small set of basis functions (i.e EOFs; De Mey and Benkiran, 2002). In this last group it is included the SEEK filter (Single Evolutive Extended Filter, Pham et al., 1998) where the reduction operator can evolve with time with the model in order to better capture the dynamics of error statistics (altough this approach has almost never been used).

The *Ensemble Kalman Filter* (EnKF; Evensen 1994,2003) is another alternative where an ensemble of model states is used to represent the error statistics instead of using the covariance matrix. Namely, in this probabilistic approach a set of model states (differing among them in some model parameter, the initial conditions or the forcing applied) is evolved with time and the ensemble covariances are interpreted as error covariances. The advantage of this method is that it allows to consider the complete non-linear evolution of error covariances altough the analysis

is linear. Its computational coast is equivalent to N integrations of the model run, where N is the size of the ensemble (~100-300 members). Another problem is the choice of the model perturbations that will characterize the system errors.

Finally, we wanted to mention the *Optimal Interpolation*, a sequential method which do not provide a mechanism to predict the forecast errors, and which do not use the dynamics to calculate the weights to update the state of the system. The basic assumption in the OI scheme is that the error covariance matrix $\mathbf{P}^f$ is replaced by an approximation $\mathbf{B}^f$ (background error covariance matrix) where:

$$\mathbf{B}^f = \mathbf{D}^{f\,1/2}\mathbf{C}\mathbf{D}^{f\,1/2} \qquad \textit{(4.15)}$$

The matrix $\mathbf{D}^f$ is diagonal and contains the forecast error variances while in the matrix $\mathbf{C}$ it is included the error covariances. The time evolution of the state is as in the EKF and in the analysis phase an equivalent gain is formulated as in (4.12) but using $\mathbf{B}^f$ instead of $\mathbf{P}^f$. The time evolution of variances in $\mathbf{D}^f$ can be obtained from a variety of simplified prediction schemes (i.e: Daley,1991). Different versions of this method are used in most operational data assimilation applications (MFS, MERCATOR, FOAM).

Among all the different data assimilation schemes mentioned before (and other possibilities as the variational schemes or the adaptive filters) there is no "best" choice. It depends on the characteristics of the problem that must be solved. Linearity of the dynamics, stationarity of errors or computational cost are some of the criteria that can determine the choice.

Data assimilation in coastal areas

In coastal and shelf areas, the data assimilation problem needs a specific approach as far as the typical hypotheses assumed in the open sea are no longer valid. In oceanic applications it is common to consider homogeneity and stationarity for the model error variances and isotropy for the error covariances. Also, the separability of the covariance functions in the horizontal and the vertical is acceptable. In the coastal ocean, non-linear processes are important and dynamics is more sensible to atmospheric forcing and more controlled by the coastline and bathymetry. These dynamical characteristics make the error statistics non-isotropic, non-stationary,non-homogeneous and non-separable (Echevin et al., 1999; Auclair et al., 2003; Mourre et al., 2004). As a consequence, a detailed study of the error space is necessary to properly characterize the error statistics which are basic for the data assimilation. This will be done through the ensemble modelling approach, as it will be shown later.

The SEQUOIA data assimilation system. The MANTA Kernel.

SEQUOIA is a data assimilation toolbox developed in the Pôle d'Oceanographie Côtière de Toulouse by Pierre de Mey. It is the successor of the SOFA system (De Mey and Benkiran,2002), a code which has been implemented in several operational systems as the Mediterranean Forecasting System (MFS) or the MERCATOR project. SEQUOIA is formed by several modules which drive the model, select data and perform the analysis. Its modular behaviour allows to use different analysis kernels and different dynamical models (just the interface is model-dependent).

In our case we use the **MANTA analysis kernel** which is a reduced order code based on global, four-dimensional best linear estimation where the order reduction is done on a base of 3D multivariate EOFs (Empirical Orthogonal Functions). The dynamical constraints are not explicitly declared, and the coherent physics and statistical relationships between variables are introduced via the EOFs. Another advantage of use these functions is that they provide an external criterion to truncate the assimilation problem. The eigenvalues associated to each mode are a measure of the explained variability associated to them giving an indication of the dominant modes.

To schematically explain the algebra behind the MANTA code, it can be said that it follows the same structure as the Extended Kalman Filter (see eqs. (4.9)-(4.13)) but we will use some simplifications: The forecast error covariance matrix $\mathbf{P}^f$ is replaced by *the background error covariance* matrix $\mathbf{B}^f$ which doesn't evolve in time, and a *Reduction Operator* $\mathbf{S}$ is used to reduce the order of the problem. Therefore, we include an Optimal Interpolation implementation in the MANTA kernel.

We assume that the matrix $\mathbf{B}^f$ can be factorized as:

$$\mathbf{B}^f = \mathbf{V}\boldsymbol{\Delta}\mathbf{V}^{\mathbf{T}} \qquad \textit{(4.16)}$$

where $\mathbf{V}$ is a constant orthogonal matrix whose columns are the eigenvectors (EOFs) of background errors and $\boldsymbol{\Delta}$ is a diagonal matrix whose elements are the eigenvalues. Also note that (4.16) is equivalent to (4.15).

The problem is truncated to the dominant modes using external criteria (i.e. explained variance of selected modes). This can be expressed as:

$$\mathbf{V} = \mathbf{S}\left|\overline{\mathbf{S}}\right. \qquad \textit{(4.17)}$$

where the vertical bar expresses the column-wise juxtaposition of both matrices. The matrices $\mathbf{S}$ and $\overline{\mathbf{S}}$ are respectively the reduced-space and the null-space simplification operators. The null-space errors are not calculated so they won't be included in the following formulation.

The background error covariance matrix writes:

$$\mathbf{B}^f = \mathbf{S}^{\mathbf{T}}\mathbf{B}\mathbf{r}^f\mathbf{S} \qquad \textit{(4.18)}$$

The $\mathbf{Br}^f$ matrix is as a diagonal matrix containing the error variances. Now the OI problem can be expressed in the reduced space with some parameterization of the null-space effects.

The Reduced-Order Optimal Interpolation gain in the full-state space writes:

$$\begin{aligned} \mathbf{K}^{\mathbf{ROOI}} &= \mathbf{S}^{\mathbf{T}}\mathbf{Kr} \\ \mathbf{Kr} &= \mathbf{Br}^f\mathbf{Hr}^{\mathbf{T}}\left(\mathbf{HrBr}^f\mathbf{Hr}^{\mathbf{T}} + \mathbf{Rr}\right)^{-1} \end{aligned} \qquad \textit{(4.19)}$$

In practical, the computation of **Kr** is done using the alternative proposed by Pham et al. (1998) in the context of the SEEK filter, which is usually cheaper:

$$\mathbf{Kr} = \left(\mathbf{Br}^f\right)^{1/2}\left(\mathbf{I} + \boldsymbol{\rho}\mathbf{r}\,\mathbf{Rr}^{-1}\boldsymbol{\rho}\mathbf{r}^{\mathbf{T}}\right)^{-1}\boldsymbol{\rho}\mathbf{r}\,\mathbf{Rr}^{-1} \qquad \textit{(4.20)}$$

where $\boldsymbol{\rho}\mathbf{r} \equiv \left(\mathbf{Br}^f\right)^{1/2}\mathbf{Hr}^{\mathbf{T}}$ is the matrix of reduced-order representers.

At analysis time, the model restarts from its previous fields plus a correction in reduced space which is converted back to full-state space by $\mathbf{S}^{\mathbf{T}}$. Observations are related to the reduced state space by means of the *reduced-order observation operator* **:**

$$\mathbf{Hr} = \mathbf{HS}^{\mathbf{T}} \qquad \textit{(4.21)}$$

The reduced-order observational error covariance matrix Rr includes the representativity errors in the reduced space due to the observability of the null space. In other words, we consider that processes that can not be included in the reduced-order space are akind of an observational error. This leads to:

$$\mathbf{Rr} = \mathbf{R} + \mathbf{E}_{NSREV} \qquad \textit{(4.22)}$$

where $\mathbf{E}_{\mathrm{NSREV}}$ is a diagonal matrix which includes the Null-Space Representativy Error Variances (NSREV). It is important to realize that in many cases this can be more important that values in **R** and that it is not necessarily diagonal (as **R** is).

Finally, the analysis errors now become:

$$\begin{aligned} \mathbf{B}^a &= \mathbf{S}^{\mathbf{T}}\mathbf{Br}^a\mathbf{S} \\ \mathbf{Br}^a &= \mathbf{(I - KrHr)Br}^f\mathbf{(I - KrHr)}^{\mathbf{T}} + \mathbf{KrRrKr}^{\mathbf{T}} \end{aligned} \qquad \textit{(4.23)}$$

In practice, the EOF base can be computed from departures from a climatology either from data or model outputs. If the *natural variability (nv)* EOFs are used, it must be assumed that the forecast error covariances can be efficiently expressed on these nv-EOFs. This is the approach used in the SEEK filter and can be quite effective in some cases. Nevertheless it must be kept on mind that, in some cases, the error subspace is not contained in the nv-EOF base. For instance, if the model doesn't present a variability in the current thickness, as happens in the MFSTEP OGCM (P. Marsaleix, personal communication), the assimilation scheme won't be capable to correct errors in the current depth as it is not included in the nv-EOFs.

Another possibility is to calculate the EOFs from Ensemble (Montecarlo) simulations: *ensemble EOFs.* In this case the methodology is the same than in the Ensemble Kalman Filter (Evensen, 1994). A model error is introduced into an ensemble of simulations as a perturbation of some model parameter (initial conditions, open boundary conditions, atmospheric forcing,…) and the covariances of the ensemble are interpreted as the error covariances. This approach has the advantage that error dynamics is well represented but an extensive work to characterize all the error sources (or at least the dominant) must be done.

Due to the characteristics of the assimilation scheme chosen some questions closely linked to the assumptions done arise:

-Is it possible to define a manifold of stationary error EOFs useful over a given period?

-Can the error be truncated severely in a coastal model? How?

4.2 DEFINITION OF THE ENSEMBLE RUNS

The EOF base which will define the error subspace to reduce the order of the assimilation problem will be calculated from ensemble modelling statistics. This approach consists in generating an ensemble of model states which will evolve with time and which differ among them in some parameters of the modelization (i.e. initial field, lateral boundary conditions, wind forcing, …). The idea behind this approach is that we assume that the introduced perturbations represent an error of the modelling system. The evolution of the dispersion of model trajectories in space and time is then interpreted as the dynamics of the errors. The error covariances in matrix $\mathbf{P}^f$ are calculated from the ensemble of runs. A sketch of the procedure is presented in Fig 4. 2. A center forecast can be perturbed in the initial conditions, so generating an ensemble of model states at t=0, or during the model integration through the atmospheric forcing, the open boundary conditions or any model parameter. At the end, the ensemble present a dispersion of the model states that are interpreted as errors.

The choice of the ensemble EOFs requires a careful definition of the error sources and of the dynamical frameworks of the modelization. We want to include in our base the most important errors, at least in the first order of approximation, and investigate their dynamics in the most common scenarios.

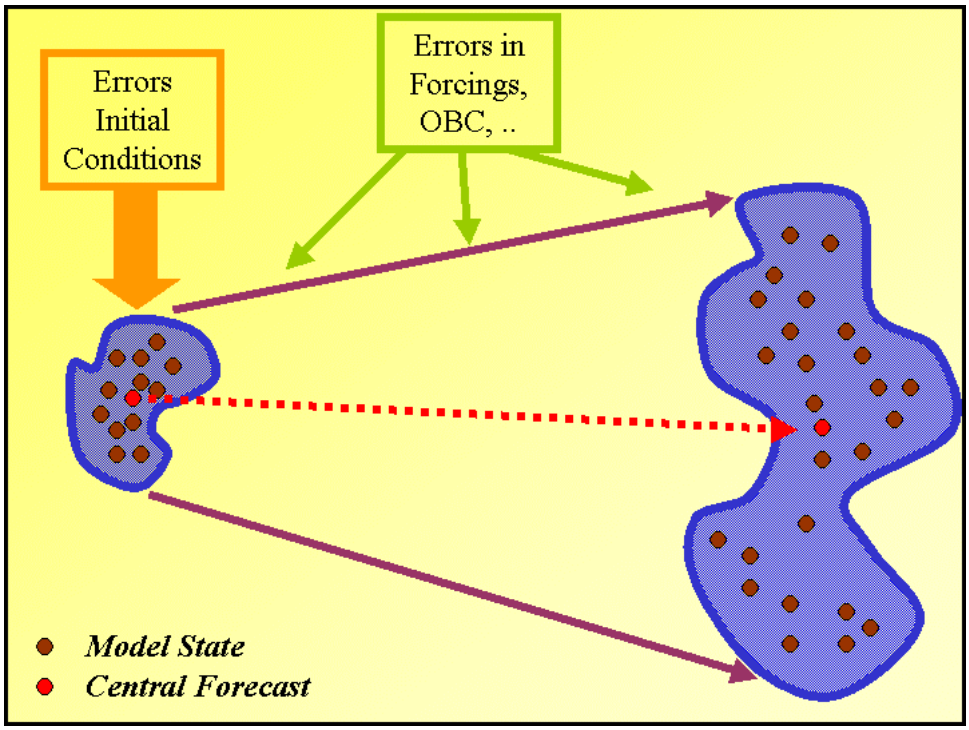

Fig 4. 2: Sketch of the ensemble modelling strategy.

4.2.1 Definition of error sources

A key point into the approach chosen to characterize the error statistics is the selection of the main error sources in our modelling system, as far as the ensemble results will strongly depend on the model parameters that have been perturbed. As it is not possible to include all of them, we have to select the main ones, namely those that will be the most influent into the model results. In fact, the uncertainties about some model parameters (i.e. turbulent coefficients) are greater that over the wind field (for instance), but their impact over the model results are less crucial than the consequences of a small error into the wind field.

After the data analysis performed in chapter 2 and the modelling studies presented in chapter 3, we conclude that **the main sources of error in the region are the characterization of the wind field, the slope current and the density profile**.

We have shown in the previous chapters that **wind** is the main forcing factor over the first 30-50m of the water column. Different wind directions lead to quite different circulation patterns, and the spatial structure and location of the land winds have also a big influence (see Mestral wind examples). The wind intensity is also determining into the evolution of the river plume, the upwelling intensities and, even, the generation of eddies associated to the Mestral winds.

On the other hand, in appendix 1, there is the comparison between ARPEGE wind fields and data in several meteo stations. It could be seen that meteorological model results are quite

good both in terms of wind intensity and direction but they are not perfect. In addition to that, validation is mainly done using land stations as not much information is available over the sea. This can distort the conclusions as far as the meteorological modelling system assimilates data from land stations, so improving its skills over the land but not necessarily over the sea. Finally, the punctual data available doesn't provide a reliable validation about the spatial structure and curl of the wind fields (i.e. we can't be sure about the width or location of the Mestral bursts).

The **slope current** is a well known permanent feature in the region (Millot, 1999; Font et al.,1995), and it is considered to be a part of the Northern current which flows cyclonically around the North-Western Mediterranean. Its strength, thickness and position are key parameters into the region dynamics and vary along the year (see chapter 2). In the model configuration used, those parameters have been "tuned" to data but they are still a source of uncertainties.

Comparison with current meter data (see Fig 4. 3) shows that the model doesn't reproduce correctly the low frequency component of the slope current due to an error into its strength or its horizontal location. It could be said that this is due to the simplified configuration implemented (fixed academic boundary conditions) but at this moment this is the best choice as there is no regional model which can improve the solutions at the boundaries (see Jordà et al., 2004). On the other hand, we also expect that, in the near future, this will be solved, but in any case those current parameters will still be a source of uncertainties as they are difficult to measure and to control.

The parameters that must be "tuned" for the current characterization are depth, width, horizontal position and strength. It has been found that, after the MPV initialization phase (see chapter 3) all those parameters except strength are linked and the equilibrium solution can be defined with a unique parameter. In our case we select current depth for simplicity. Once it is fixed, the initialization method provides the complete 3D description of the slope current. It must be noted that in non-equilibrium configurations several parameters should be used, but at this moment it escapes the scope of this study.

Some preliminary tests show that ensemble of model runs where current strength or the **density** profile have been modified do not show an interesting behaviour in the dispersion of results. The variability found at the end of the runs is practically the same that was introduced in the initial conditions with MPV, so its study won't help us to better characterize the error dynamics.

Other possible sources of error are the bottom stress, river runoff and tides, but they are of second order of importance, when looking at short-term forecasting capabilites, as shown by previous authors and sensitivity experiments carried on in previous chapters. Sensitivity tests to the bottom stress parameterization didn't show significative differences in the main circulation. The dynamics over the shelf has been modified but to a less extent that modifications induced

by the wind. The river runoff is a well measured quantity and the errors in the modelling of the river plume will just affect the ROFI region which is limited. Finally, tides are negligible in the area (see chapter 2) and its non inclusion into the model won't change the quality of the results.

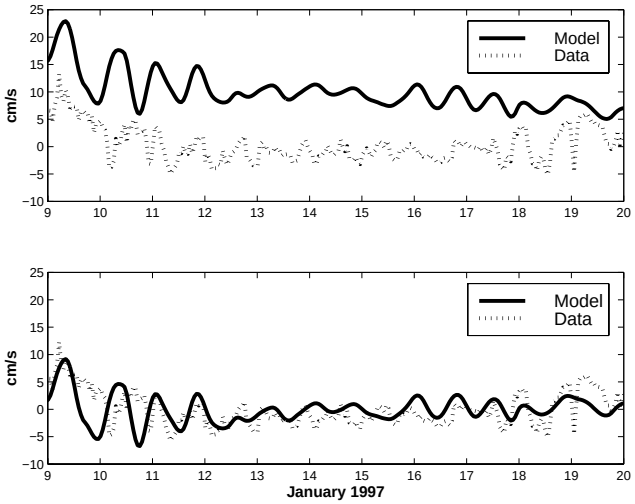

Fig 4. 3:Comparison of model-data along-slope currents at 50m depth for the January 1997 period for total velocity (top) and high frequency part (bottom).

In conclusion, the error sources selected are the current depth (set up in the initial conditions) and the wind field (modified all along the model run). Obviously, in some particular cases the choice taken could be not enough (i.e. low wind regime with high and variable river runoff), but the performance of the data assimilation system should be evaluated from a global point of view keeping on mind its limitations. So, the approach chosen seems to be the most convenient, at least in a first order of importance.

4.2.2 Definition of typical scenarios

The ensemble modelling approach tries to characterize the spatial structure and time evolution of the errors but these characteristics can be dependent on the hydrodynamical conditions. For instance, an error in the wind field could be more important during a Mestral event (narrow winds blowing from land) than during a Llevant burst (large winds blowing from sea), or maybe its effects over the circulation will be less critical in homogeneous conditions than in stratified ones.

In order to not be too specific into our configuration and to be able to generalize our conclusions, we ran the ensemble runs in several scenarios to test if the error dynamics is affected by different hydrodynamical conditions.

Again, it is not possible to cover all the possibilities, so we select the most frequent and most different situations. The principal parameters that define a scenario are the current depth, the wind regime, the river runoff and the averaged density profile.

The depth of the current has been selected due to the known seasonal evolution of the Northern current being shallower in summer (base of the current at ~200m) and deeper in winter (base of the current ~400m) (Garcia-Ladona et al. ,1994; Millot ,1999).

The wind regimes selected are the Mestral(NW) and Llevant (E) cases. These are two of the three principal winds in the region (see chapter 2) and represent the two kinds of wind structures present in the area. The Mestral wind is a narrow wind which generates a dipole structure in a localized place while the Llevant wind is a broad wind blowing from the sea and inducing a downwelling pattern all along the coast (see chapter 3 for a complete description).

The circulation over the shelf is highly influenced by the river plume, at least near the Ebre delta, and it is expected that behaviour of errors will be different in that area depending on the river runoff. A typical winter (summer) time series with an averaged value of 800 m^3/s (200 m^3/s) will be used for the high (low) discharges.

Finally, the ambient density will have an influence into the vertical structure of circulation or into the sea response to the wind. An homogeneous density profile extracted from FANS-II data (see chapter 2) is used to characterized winter conditions while a stratified one obtained from FANS-III data is used for summer scenarios.

Current depth perturbation				
	Current depth	Wind regime	River runoff regime	Density
ENS1	***	Mestral	High	Homog.
ENS15	***	Llevant	High	Homog.
ENS16	***	Mestral	Low	Stratified
ENS17	***	Llevant	Low	Stratified.
Wind perturbation				
	Current depth	Wind regime	River runoff regime	Density
ENS5	Deep	***	High	Homog.
ENS7	Deep	***	Low	Homog.
ENS8	Shallow	***	High	Stratified
ENS9	Shallow	***	Low	Stratified.

Table 4. 1: Summary of the scenarios chosen for both ensembles (current and wind).

No all the possibilities are included as some of them can be redundant or hardly probable in reality (i.e. high runoff in summer conditions). The selected combinations lead to eight different scenarios summarized in Table 4. 1.

One small note about the nomenclature used below in the text. Often we refer to the ensemble of current depth perturbations as the *current ensemble* and about the ensemble of perturbations in the wind fiels as *wind ensemble*.

4.3 EXPERIMENTAL PROTOCOL OF THE ENSEMBLE RUNS

The stochastic approach chosen to define the error statistics is based into a reference model run in some particular regimes (see Table 4. 1) that will be perturbed in some way. In the previous section, we defined the error sources (the model parameters that will be perturbed) and the scenarios where we run the model. Here, we describe the configuration of the reference run and the technique selected to generate the perturbations.

4.3.1 Reference run configuration

The model set up for the assimilation exercises will be quite similar to the one used to validate the model (see section 3.3). The FANS-II configuration will be used for the winter experiments while the FANS-III will be the one used in summer conditions. Lateral boundary conditions are fixed constant during all the run and equal to the initial conditions. Several figures of the domain and principal forcing factors have been presented in previous chapters.

The simulation is initialized using the MPV technique (cf 3.2.3) where just a barotropic streamfunction and a vertical profile of velocity must be prescribed. The former has been defined in order to describe the Northern current (Millot, 1999), a southwestward current limited to the slope with an associated transport of 0.7Sv. The vertical profile of velocity, R(z), is defined analytically as an exponential function:

$$R(z) = e^{-z/zref} \qquad \textbf{(4.24)}$$

where z_{ref} is a parameter that determines the thickness of the current and it is set equal to 250m. These parameters are used into the MPV method to find the 3D initial field which is in equilibrium with a linearized version of the model. The reconstruction of the temperature and salinity fields needs a mean profile of density which in our case has been obtained from FANS-II (winter) and FANS-III (summer) CTD data.

After the model is initialized, a realistic atmospheric forcing provided by ARPEGE atmospheric model is applied with a horizontal resolution of 25km. It provides analysed heat fluxes and wind fields every 6 hours. For the river runoff we use daily data from the

"Confederación Hidrogràfica del Ebro" which is frequently enough to reproduce in a realistic way the Ebre river plume dynamics.

The modellization period is from 10th-18th February 1997 (winter period). In fact this is just relevant to select the wind regimes that we want to include in the simulation as far as heat fluxes do not have a significative contribution and density structure is selected in the initialization phase.

The model simulation will lasts for eight days, which is a compromise between computational burden, the realistic behaviour of the model, and the validity of EOFs. The river plume just needs ~2 days to be set up, and the response of all the domain to the wind is faster than 1day, so eight days seems a reasonable duration (Auclair et al. 2003). During this period there is a three days calm period which will allow the river plume to be developed without external constraints. Afterwards, a strong Mestral event takes place during 2 days with velocities reaching 15m/s. Finally, the simulation finishes with a calm period of 2 more days.

The river outflow is not constant during all the period. Measured time series have been used both for the winter and the summer cases. In the first, a mean value of 800m^3/s is obtained with maximum values at 14th February of about 1200m^3/s. In the summer period the fresh water input doesn't reach more than 200 m^3/s.

4.3.2 Description of the perturbation technique

The principal sources of error have already been characterized as the characterization of the slope current and the wind field. To generate an ensemble of model runs we perturb those parameters to see how this affects the model evolution. The data assimilation formulation is placed in a linear framework considering that error statistics can be defined with statistical moments of first and second orders. In consequence, the model perturbations must also be done in this framework and distribution of parameters should be Gaussian.

We have shown previously (section 3.3.3) that the current position and its horizontal shape are determined by the vertical profile and the bathymetry, so the parameter selected to control the slope current structure is its depth. From definition in (4.24) this can be done through the prescription of z_{ref}. The generation of this value for the different members is done with a simple formulation:

$$\begin{aligned} R_{pert}(z) &= e^{-z/z_{pert}} \\ z_{pert} &= \overline{z}_{ref} + \varepsilon\, dz \end{aligned} \qquad \textbf{(4.25)}$$

where ε is a random number obtained from a Gaussian distribution of zero mean and variance equal to unity. The reference value is the same used in the reference run (z_{ref} = 250 m), while dz has been set equal to 40m. An additional constraint to avoid unrealistic profiles has been added, limiting the maximum and minimum values of z_{pert} to 375m and 125m, respectively.

Reference depth (z_{ref})	250 m
dz	40m
Minimum perturbed depth	125m
Maximum perturbed depth	375m

Table 4. 2:Summary of parameters used in the generation of current depth ensemble

Another constraint is introduced in order to force the different runs to keep similar physical properties. We want the transport to be the same in all the perturbed fields and that maximum surface velocity remains constant. This implies that the horizontal extent of the slope current must be adjusted to ensure those properties.

An example of the different initial fields obtained with three different velocity profiles can be found in Fig 4. 4. It can be seen how the shallower profiles tends to generate larger meanders as currents shallower than the shelf break tends to be placed over the shelf where the stabilizing factor of the slope is lost, so oscillations can reach greater amplitudes.

To generate wind perturbations, the technique we use is similar to the proposal of Auclair et al. (2003) where the perturbation is generated from an EOF decomposition of the wind field. If we have a series of model results long enough, we can decompose it in a EOF base:

$$\varphi = \sum_{i=1}^{I} \alpha_i(t)\,\phi_i \qquad \textbf{(4.26)}$$

In our case φ represents the wind field, ϕ is the spatial EOF and α is its temporal counterpart.

To generate a perturbed field we modify the temporal mode in the following way:

$$\varphi = \sum_{i=1}^{I} (1+\varepsilon_i)\alpha_i(t)\,\phi_i \qquad \textbf{(4.27)}$$

where ε is again a random number which depends on the mode *i* and is obtained from a Gaussian distribution with zero mean and variance equal to 0.2 (so considering errors of 20%). The random value is fixed constant through all the simulation to avoid unrealistic discontinuities.

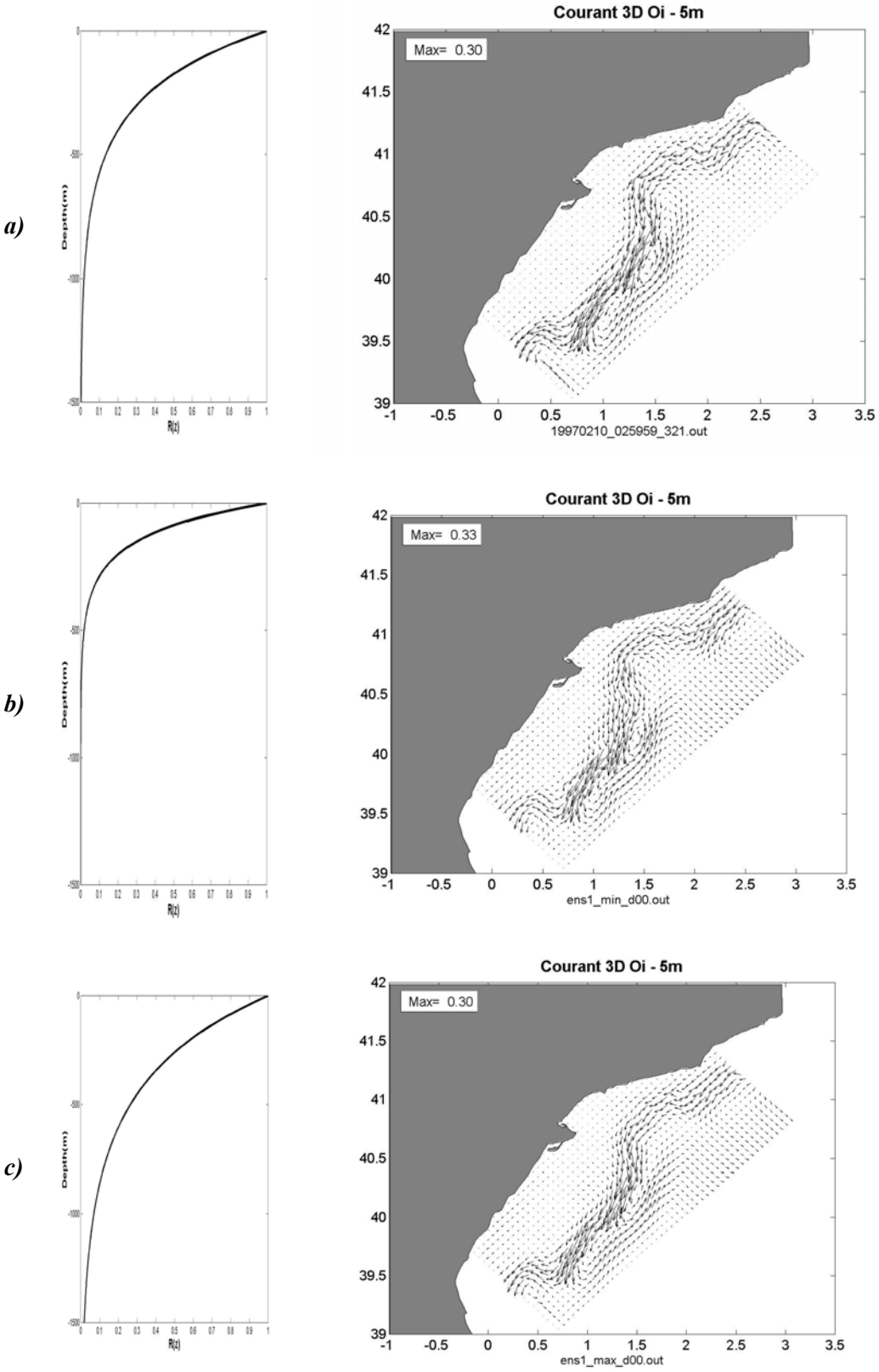

Fig 4. 4: Different velocity fields resulting from the use of a) Reference depth (250m) b)Minimum depth (125m) and c) Maximum depth (375m)

The EOFs have been extracted from 6hours ARPEGE wind fields for the 1997 January-February period to be coherent with the modelling configuration presented in chapter 3. Its spectra of eigenvalues is quite red which means that most of the variance of the wind field is explained with few modes, so just the first 10 modes have been used to generate the wind perturbation. The spatial and temporal shape of the first modes is presented in Fig 4. 5 for illustration. It can be seen how the first mode, which represents a 45 % of the variance, is representative of a typical Llebeig (SW) wind while the second mode (28% of explained variance associated) has the structure of a Mestral (NW) wind. Highest order modes represent a Llevant (E) wind and modifications of the Mestral structure.

A comparison with the ALADIN (higher resolution) EOFs, shows a good agreement between both sets of EOFs in the first modes. Discrepancies are present in small scale structures (higher modes) that won't make a big difference in the generation of perturbed wind fields. In conclusion, the fact that wind fields come from a low resolution (25km) meteorological model is not expected to diminish the quality of the approach as the main wind errors are related to large scale structures with size >> 25km.

This approach has several advantages. First of all, the perturbations do not introduce unrealistic structures neither in space nor in time as far as they are linear combinations of coherent structures (the EOFs). In addition to that, the magnitude of the perturbation is scaled by the amplitude of the EOF so it ensures that no spurious gusts will appear. For instance, if we gave the same weight to all the modes during all the simulation, we could have a southerly wind (correspondent to EOF #1, see Fig 4. 5) in a period where northerlies dominate. This will introduce an exaggerate error into the system, and we would leave the regime of small perturbations which is one the basic hypothesis of the data assimilation formalism.

An example of a perturbed wind field is presented in Fig 4. 6. Comparing it to the original field, it can be seen that its structure is quite realistic and that it is just a small modification of the reference wind both in magnitude and structure. About the time evolution it can be seen that the perturbed field evolution is smooth and coherent. All the wind events are present but slightly modified either in strength or in intensity, so ensuring a realistic atmospheric forcing with a controlled error.

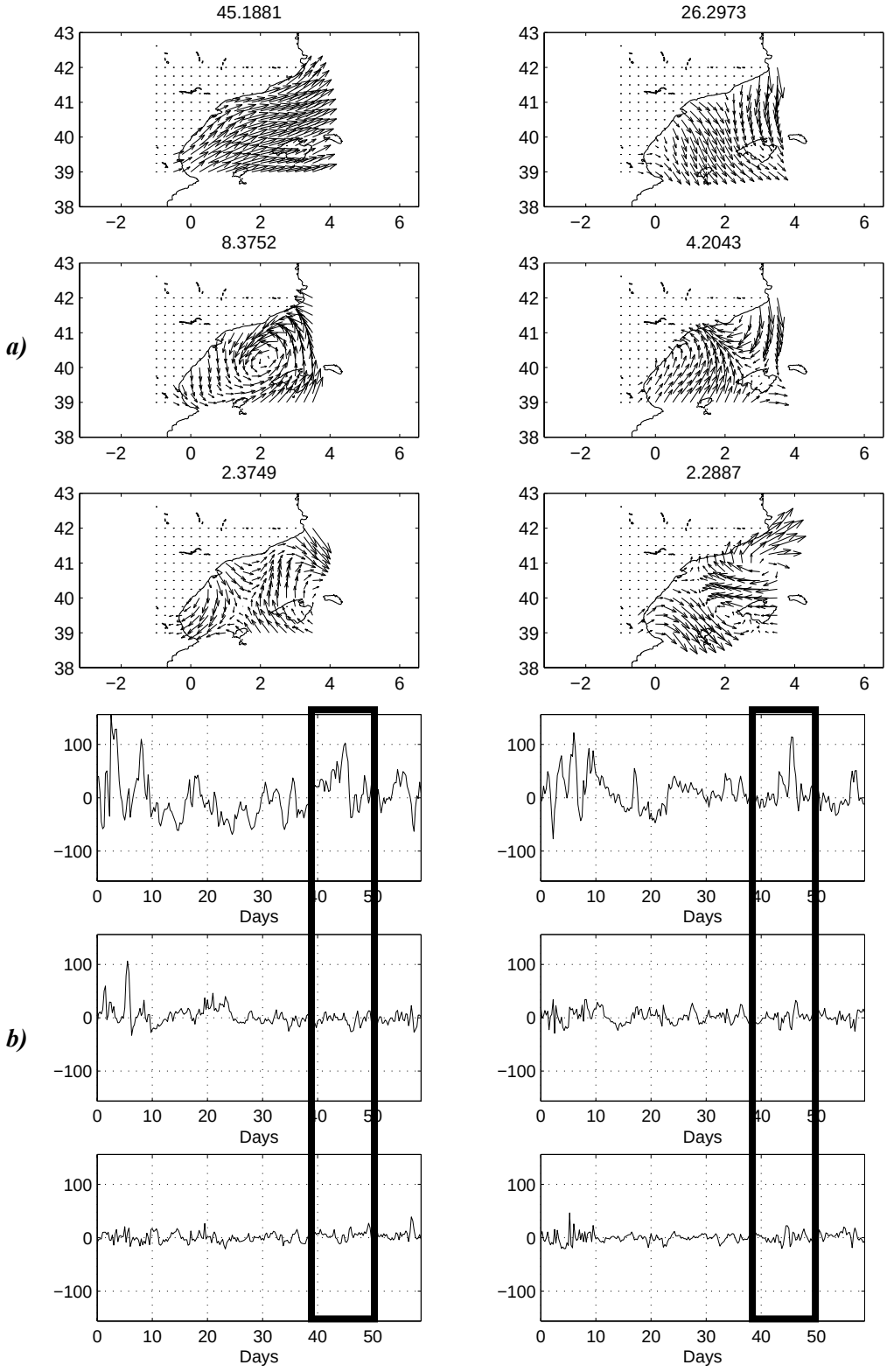

Fig 4. 5: First six ARPEGE wind EOFs (a) Spatial modes (b) Temporal modes. The explained variance associated to each mode is on top of figures. The solid lines indicated the period of simulation

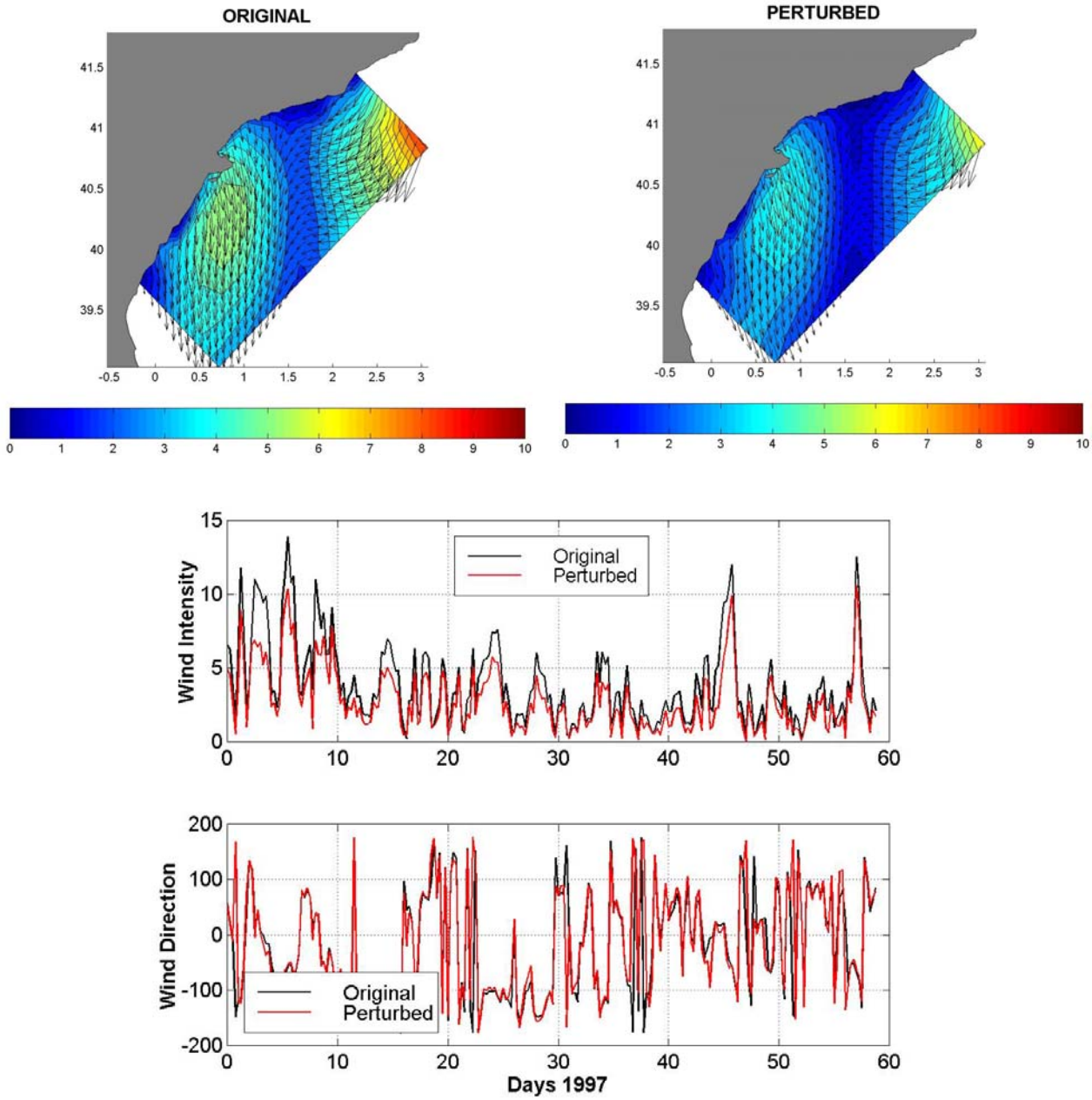

Fig 4. 6: Comparison of a particular perturbed wind field with the original field. (a)-(b) Spatial structure and (c) Temporal evolution

Finally, we wanted to do a brief comment about its practical implementation. An ensemble modelling approach needs significant computational resources to be feasible. In our case the ensemble of simulations is run in the cluster of the Pôle d'Oceanographie Côtière made of 20 PC-Linux. Each node of the cluster has a 2.4GHz processor with 1.5Gb of RAM, and each simulation needs 4 hours of computer time. In the basic configuration, each ensemble is formed by 150 members so, when the 20 nodes are available, an ensemble run is achieved in 30 hours, which is quite affordable.

4.4 ANALYSIS OF THE RESULTS

4.4.1 Physical description of the reference run

Suitability of the model to data assimilation exercises

From all the work presented in chapter 3 and several comparisons done with data, we can say that the model configuration is highly realistic, although having some shortcomings that must be kept in mind. We have shown that its response to wind forcing is quite correct, both in terms of structures and magnitudes. Fast transients as inertial oscillations and internal waves are also included in a realistic way. Plume dynamics is also satisfactory and the slope current, which is the other main forcing in the area, is well represented.

The main limitation of our model configuration is the non-inclusion of imported variability. The fact of using fixed boundary conditions doesn't allow the representation of propagating waves or the advection of structures from other regions (i.e. Gulf of Lions), although it is known that is a key issue in the dynamics of the area. The use of variable boundary conditions is not straightforward as there is no available regional model reliable enough to provide them, and we had no time to explore that possibility. Nevertheless, this limitation is no longer important if we focus on the locally generated variability.

On addition to that, we have also shown how sensitive are the results to errors in the wind field. Position and strength of the Mestral events have a crucial role into the sea response. Also, the river plume position and the strength of the upwelling-downwelling processes are highly sensible to errors into the wind field.

To sum up, we can rely on our model configuration to do data assimilation exercises where the features that are intended to be corrected are of local origin or due to the initial conditions. Errors linked to the wind field should also be taken into account.

Model results

Here we will just describe the basic features of the dynamics found in the reference run because the details of much of those features have already been presented in chapter 3.

The slope current issued from the initialization procedure remains stable during all the simulation with small wavelength oscillations due to non linear adjustments. After the 3rd day, a current meander associated to a topographic wave is triggered propagating downstream with a phase velocity of ~30cm/s. The amplitude of this meander is enhanced when current is shallower than the shelf break as it can easily go into the shelf where slope is gentler and topographic control is weaker.

Over the shelf, the circulation is controlled by the river and the wind. The plume is well developed after 2 days. In the cases with high river runoff, it spreads until near the shelf break,

where it can interact with the slope current meanders. This interaction takes place in the first 5-10m and it seems that it has no great effect below. When river runoff is low, the ROFI area is reduced to ~15km in a near circular bulge.

When wind is present, it modifies the circulation in the upper 50m over all the domain. The vertical profile of wind-induced velocities favours turbulence and plume waters mixing is enhanced. Wind also limits the spreading of the plume modifying its shape in a short time scale.

In the northern part, near cap Salou, an upwelling induced by the Mestral wind is created bringing to the surface waters from 70m depth. In the summer runs, horizontal thermal gradients associated to this upwelling are more important.

In the simulations with the Llevant wind, we find that wind do not modify significatively the circulation. It just induces a different plume spreading and enhances mixing in the inner shelf of the Gulf of St Jordi.

In both wind regimes, strong inertial oscillations are triggered at the end of the wind burst. They occupy all the domain and last for several days until the end of the run.

When stratification is included in the simulations, processes in surface and bottom layers are unlinked. Also, the energy transferred by the wind is greater than in the homogeneous case, due to the reduction of the turbulent mixing. Finally the horizontal gradients created by the upwelling are much more important.

a)

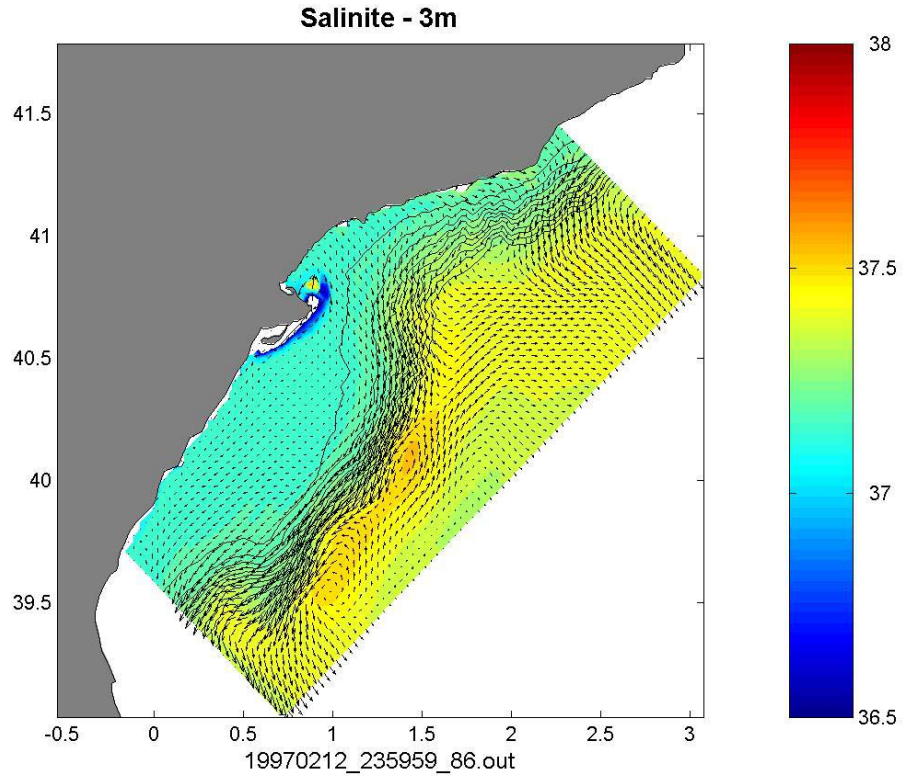

b)

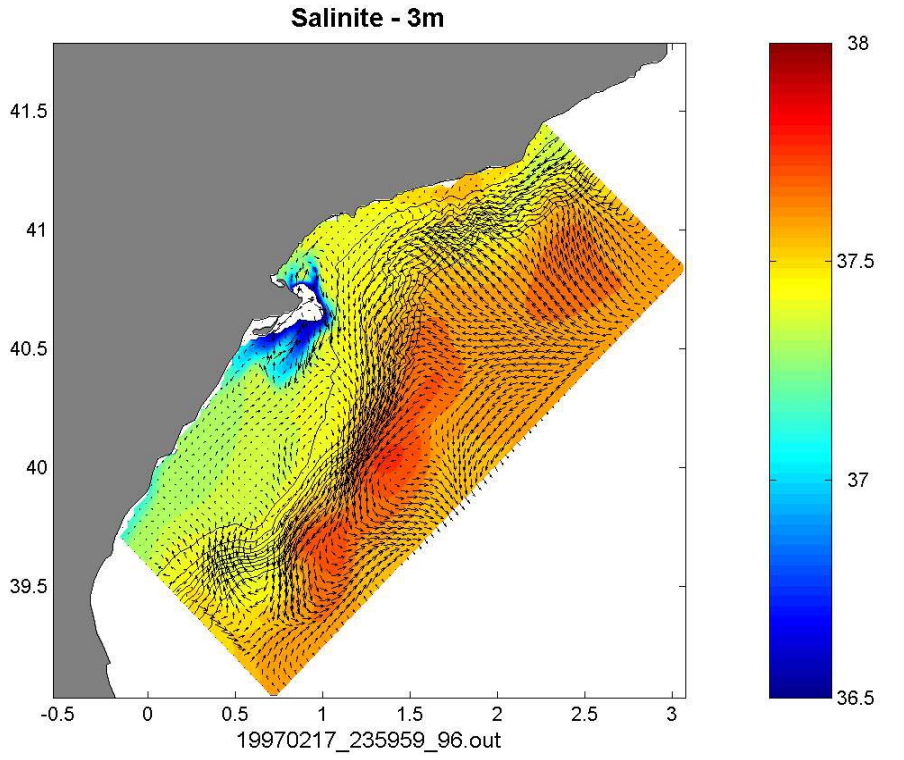

Fig 4. 7: Surface velocity and salinity for the reference run used in data assimilation exercises in the homogeneous conditions (a)before and (b) after the wind burst.

4.4.2 Statistical moments

Mean

One of the main requirements that must be accomplished in the data assimilation framework is that the errors must be unbiased (Gelb, 1972). This can be expressed as:

$$E\left[\mathbf{e}^f\right] = 0$$
$$E\left[\mathbf{x}^f - \mathbf{x}^t\right] = 0 \qquad \textbf{(4.28)}$$
$$E\left[\mathbf{x}^f\right] = E\left[\mathbf{x}^t\right]$$

This means that the mean of the forecast and the mean of the true must be equal. In our ensemble approach this can be translated to the requirement that the mean of the ensemble simulations must be equivalent to the reference run (our truth).

In all the ensembles, the mean value obtained from the ensemble of model runs is highly coincident with the reference simulation at all times. This ensures that the errors, represented by the dispersion of ensemble results, are not biased.

A comparison between the reference value and the mean of two ensembles is presented in Fig 4. 8. At first sight no large difference is appreciable and if we compute rms and correlation this is confirmed (see Table 4. 3). The observed differences are due to nonlinearity in the model response. As the correspondence is fairly acceptable we use the ensemble average as the reference for the EOF calculation (section 4.6).

	Correlation		***RMS (reference-ensemble mean)***	
	η	***T***	***η(cm)***	***T(ºC)***
Current ensemble	0.99	0.92	1.4	0.08
Wind ensemble	0.99	0.91	1.2	0.06

Table 4. 3:Comparison between reference results and mean of the current ensemble (ENS1) and the wind ensemble (ENS5)

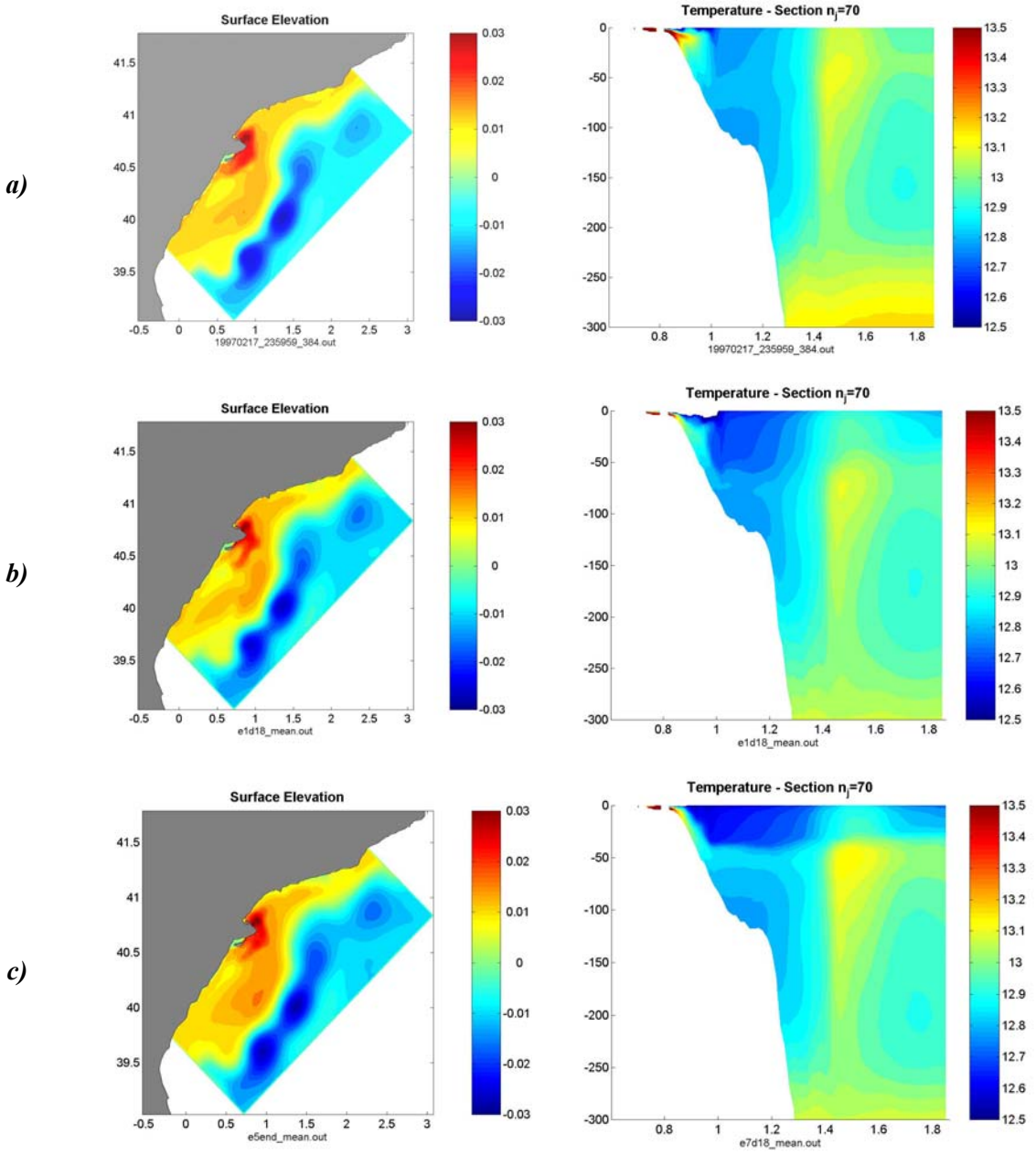

Fig 4. 8: Sea level(left) and vertical section of temperature (right) at the end of the run for (a) Reference (b) Mean of the Current ensemble ENS1 and (c)Mean of the Wind Ensemble ENS 5.

STD of Current ensemble

Standard deviation maps computed from the ensemble results give an idea of the dispersion generated by the introduced perturbations. They can be interpreted as errors maps, so the error dynamics can be tracked by the evolution of the STD fields.

Looking to the STD results for the current ensemble, it can be seen that the variability is mainly associated to the strength of the current meanders (see Fig 4. 9). The maximum are found over the slope in the place where the meandering is located in the reference simulation (compare with Fig 4. 4). In the rest of the domain (i.e. over the wide shelf in the south) values are near zero, as the variability there is generated by wind, which is the same for all the members of the ensemble.

The exception to that is in the salinity field. In ENS1 and ENS15, where the river runoff is important, the plume reaches the shelf break. When the current is shallow, its large meandering favours its interaction with the river plume over the shelf. The position of the bulge is displaced and a significative signal of variability is found. It is important to note that high variability associated to the plume is due to the fact that gradients of salinity (and to a less extent of velocity and temperature) therein are important. A little change of plume position implies a big change in salinity, so the trace in the STD maps is very visible.

The vertical structure of the ensemble variability is mainly determined by the initial perturbations. The initialization technique adjusts the density field to the velocity field obtained from the inversion (see section 3.2.3). This implies that different members of the ensemble, with different structure of the velocity field, have also a different vertical structure of density. In Fig 4. 9c, it can be seen how the variability is due to the isopycnal tilting which generates the different current profiles. Overimposed to this initial dispersion, the current meandering also induces differences in the vertical structure but are less important. Finally, in the first 40m, there are low STD values because the mixed layer, where circulation is mainly induced by the wind, is quite similar in all the members.

The initial dispersion into the vertical structure of the density field also affects the signal of the upwelling in the salinity/temperature maps. The upwelling characteristics are the same in all the members of an ensemble as they have the same wind field and stratification. Namely, the origin of the upwelled waters is at the same depth in all the simulations. The difference in the vertical structure implies that the characteristics of those upwelled waters are different among all the members. Therefore, the trace of the upwelling in surface will be quite variable.

With Llevant wind field (ENS15, see Fig 4. 10a-b) the most significative difference is in the magnitude of the STD in the upwelling region. In fact this wind tends to induce a downwelling in the same region which also generates a signal in the STD maps but much weaker. Also, as the Llevant winds are weaker, the wind-induced mixed layer depth in the ensembles ENS15 and

ENS17 is reduced to 25m. Below that layer the vertical structure is quite similar to the Mestral wind scenario.

When stratification is present (ENS16-ENS17, Fig 4. 10c-f), the processes observed in the STD are the same but less clear. The reason is that stratification induces greater differences among the members into the density structure. This dispersion largely dominates the standard deviation maps masking the other processes as the meandering or the upwelling. In the vertical, the structures are again similar to the homogeneous case but much stronger.

To sum up, processes observed in the four current ensembles are mainly the same and can all be found in the STD maps more or less clearly. The differences induced by different wind regimes, river runoff or stratification, are mainly linked to the magnitude of the variances and not to their structure.

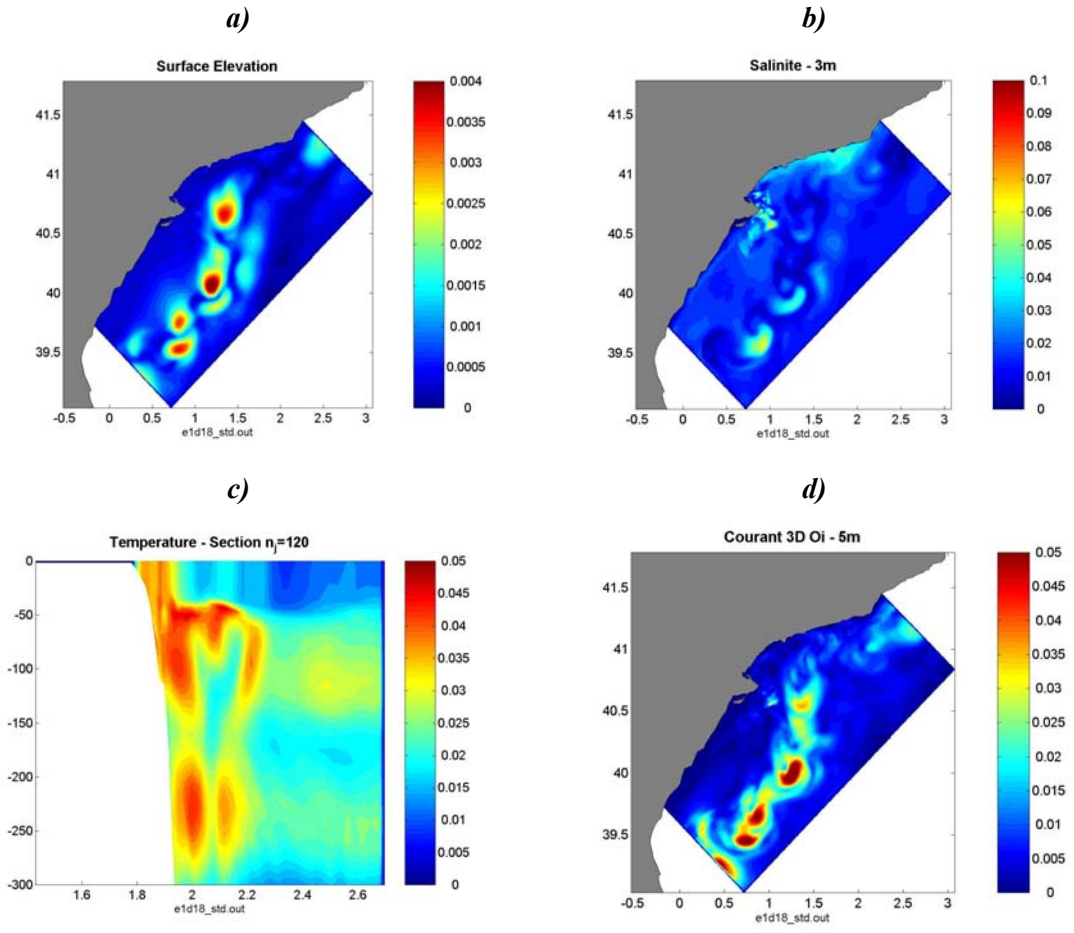

Fig 4. 9: Current ensemble-ENS1 STD for (a) Elevation (b) 3m salinity (c) Vertical section of temperature in the north and (d) Surface velocity

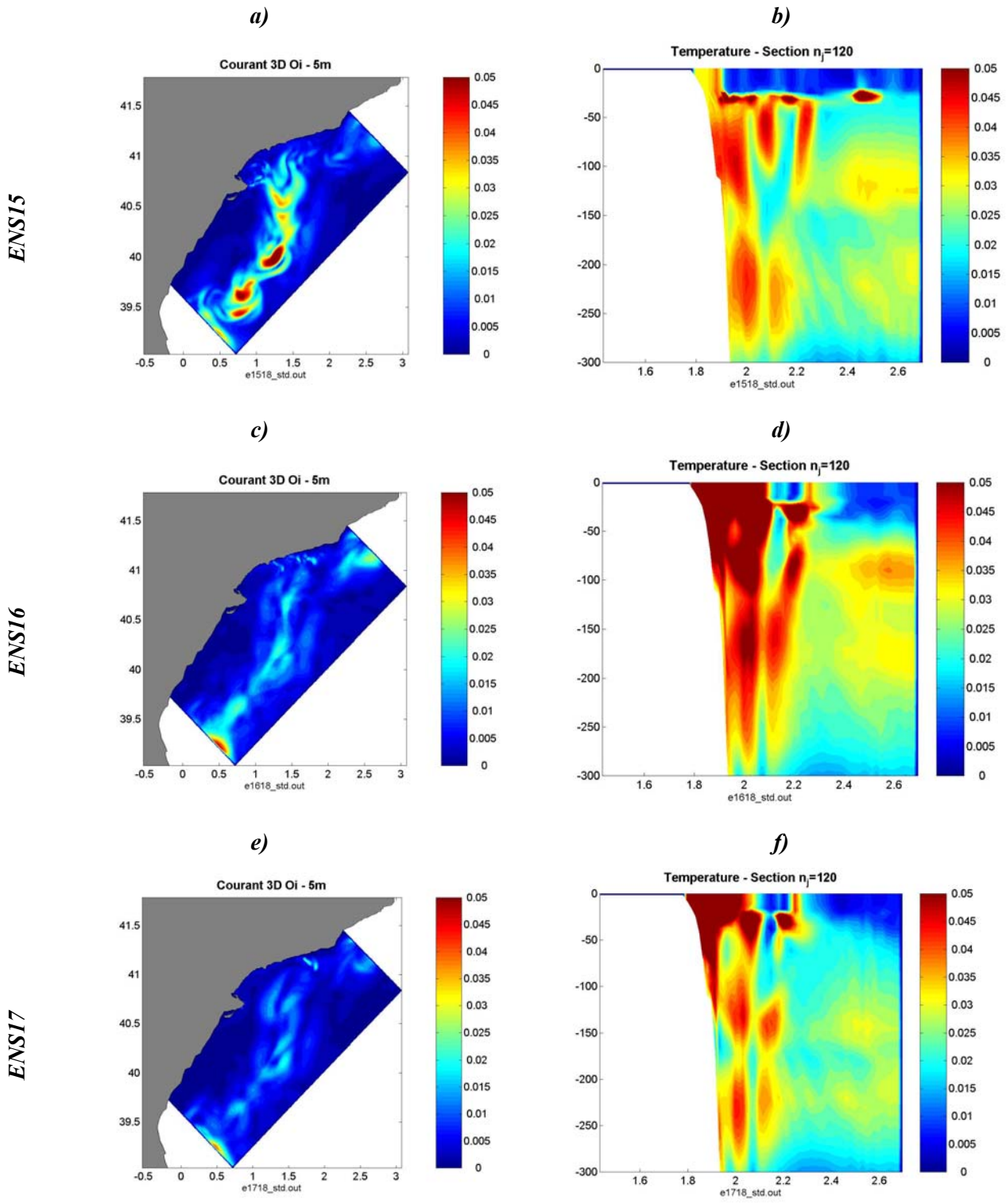

Fig 4. 10: STD for the current ensemble in different scenarios. Surface velocity (left) and vertical section of temperature in the northern part (right).

STD of Wind ensemble

The maximum values of the standard deviation computed from the members of the wind ensemble are found in the mixed layer. For depths greater than 50m, no variability is found. This is coherent with the fact that the wind influence is restricted to that layer (see chapter 3). Secondary processes as the internal waves generation are too weak to be visible in the STD maps.

As it was expected, variability is noticeable in the processes driven by the wind (see Fig 4. 11). The maximum values of STD in density and velocity fields are associated to the plume. Its spreading and vertical mixing depend on the wind intensity and direction, so the ensemble of simulations presents large deviations on the plume characteristics.

The upwelling around cap Salou is also directly affected by the wind field perturbations and presents significative dispersion of results. It is interesting to note that the current ensemble showed important variability associated to the upwelling but for different reasons. In that case it was due to the different density structure of the members of the ensemble while now is due to differences into the forcing that provokes the upwelling.

Finally, the perturbation of the wind also implies a large variability of the mixed layer depth and the velocity field in the first 50m. It is more noticeable around the slope where velocities are more intense because wind-induced currents are overimposed to the slope current.

In subsurface there are high values of STD just near the canyons. This is due to the fact that wind affects the topographic alignment of the current. Its perturbation slightly modifies the current position with reference to the canyon, which affects the characteristics of current-canyon interaction (Klinck, 1996).

With low river runoff (ENS7, see Fig 4. 12a-b), maximum values of STD are still associated to the plume, but as the ROFI area is reduced, the extension of this area of maximal variance is much more limited.

In the stratified scenario (ENS8 and ENS9; see Fig 4. 12c-f) , the STD patterns are similar but magnitudes are quite larger. As it was explained in chapter 3, stratification reduces the vertical turbulence and, consequently, energy transfer from the wind to the sea is more important and also the consequences of wind perturbations.

To sum up, it happens the same than in the current ensemble. Different scenarios lead to different magnitudes of STD, but the structures are quite similar

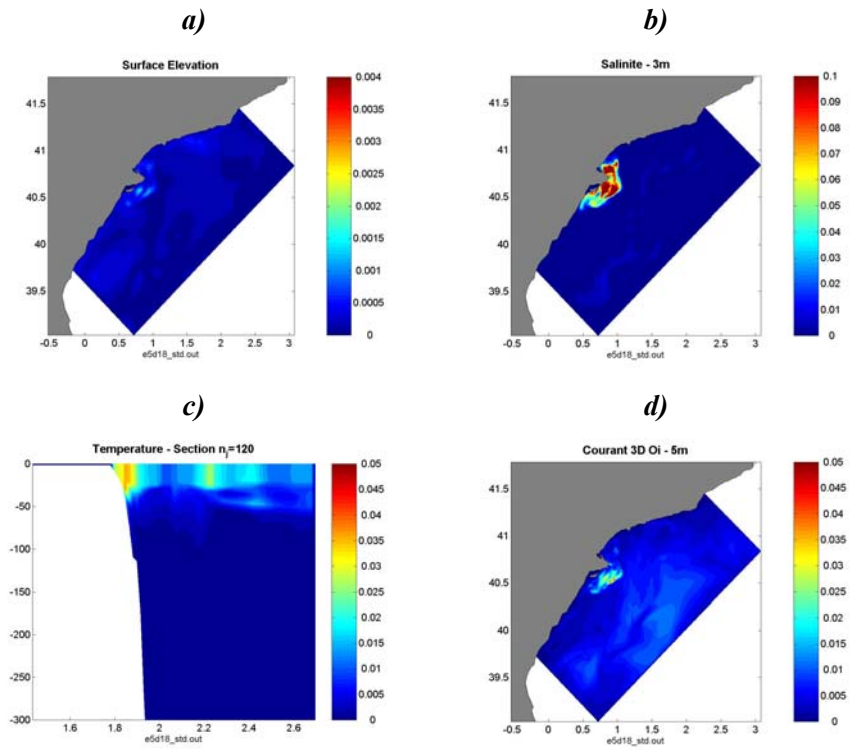

Fig 4. 11: Wind Ensemble STD for (a) elevation (b) 3m salinity (c) Vertical section of temperature in the north and (d) surface velocity

Skewness and Kurtosis

The modelization of error is done through the error expectancy (considered equal to zero) and covariances which is equivalent to assume that error statistics is Gaussian. A way to evaluate this assumption and the "linearity" of the main dynamical error processes during the period studied is to compute higher-order statistical moments. From the ensemble runs we can compute the Skewness (third-order) and Kurtosis (fourth-order) to have an idea about the departure with respect to a Gaussian distribution (Auclair et al. 2003). There are defined as:

$$\overline{S} = \frac{n\overline{M}_3}{(n-1)(n-2)\overline{\sigma}^3} \qquad \textbf{(4.29)}$$

$$\overline{K} = \frac{n(n+1)\overline{M}_4 - 3(n-1)\left(\overline{M}_2\right)^2}{(n-1)(n-2)(n-3)\overline{\sigma}^4} \qquad \textbf{(4.30)}$$

where n is the number of elements of the ensemble and σ is the standard deviation. The jth-statistical moment M_j is defined by:

$$\overline{M}_j = \sum_{i=1}^{n}\left(x_i - \overline{x}\right)^j \qquad \textbf{(4.31)}$$

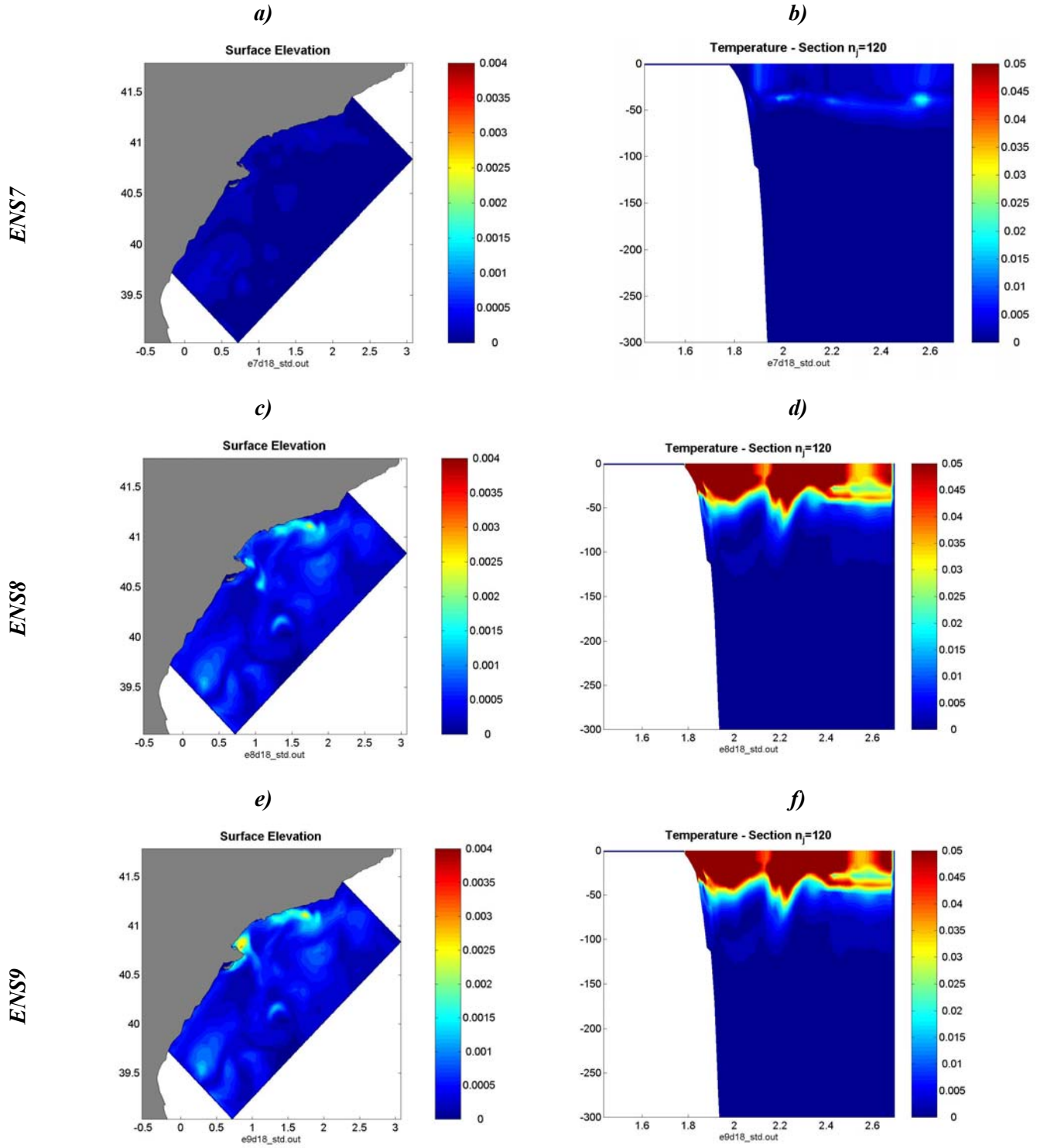

Fig 4. 12: STD for the wind ensemble in different scenarios. Free surface elevation (left) and vertical section of temperature in the northen part (right).

The Skewness gives a measurement of the asymmetry of the distribution. On the other hand large values of Kurtosis indicate a peak distribution while large negative values indicate a larger spread.

The results for the current ensemble (ENS1) and the wind ensemble (ENS5) are presented in Fig 4. 13. Before comment them it must be noted that the size of the ensemble (150 member) maybe is not enough to recover clear structures in the higher-order statistical moments. High values of asymmetry or peakness can be induced by an insufficient sampling and not but the underlying physical process, so noisy patterns of those fields can appear.

When current characteristics are perturbed, the final distribution presents high asymmetry values (skewness) around the slope current, and the maximum and minimum values are distributed at the edges of current meanders. This is explained by the behaviour of the current when it is shallower than the shelf break. In that case the current enters into the shelf and its meander is enhanced by the gentle topographic slope while currents deeper than the shelf break remains stabilized over the slope. This produces a marked asymmetry represented by the maximum and minimum skewness values. On the other hand, most of the ensemble members with current depth deeper than 200m behave really similar, so the distribution is quite peaked as high values of kurtosis indicates.

It is interesting to note that, in the North, where the ensemble variance is low (compare with Fig 4. 9b), skewness and kurtosis values are also small. This suggests that error process linked to the upwelling is quite Gaussian, which is coherent with the fact that STD in the upwelling region is induced by differences in the initial density distribution which is Gaussian by definition.

In the wind ensemble case, asymmetry and peakness are much lower than in the current ensemble. Maximum values are found associated to the river plume but its patchiness structure is difficult to interpret. There are also high values associated to the base of the Ekman layer that can be explained by the non-linear effects of turbulent mixing.

In conclusion it can be said that error processes linked to wind are quite Gaussian while those associated to the current are not due to the interaction with bathymetry. This is in good agreement with the results found by Auclair et al. (2003) in the Gulf of Lions.

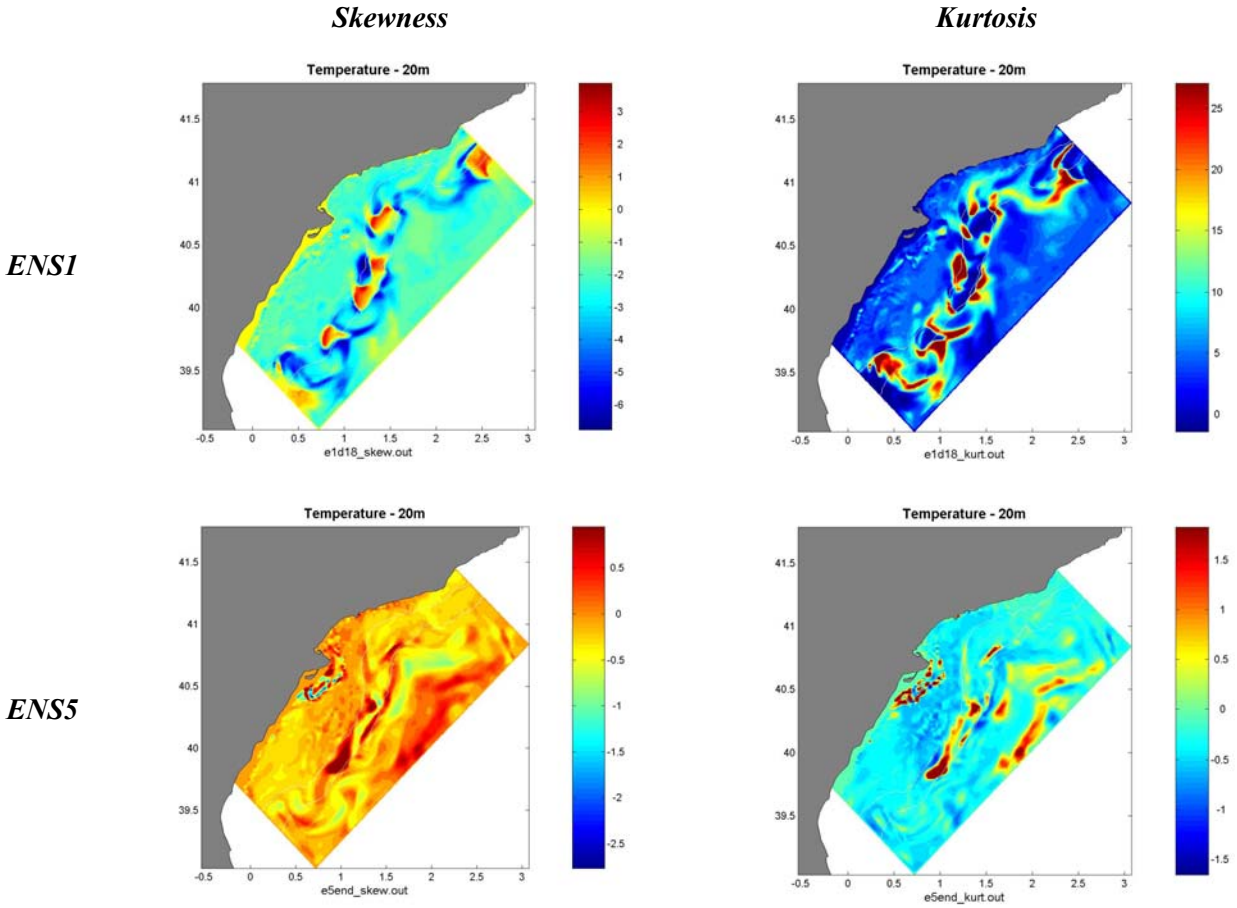

Fig 4. 13: Skewness (left) and Kurtosis (right) for the 20m temperature in the current ensemble (top) and the wind ensemble (bottom)

Time evolution of STD

A key point for the assimilation is whether the error dynamics is stationary or not as it will constrain the data assimilation approach. If the error structures are constant in time, a data assimilation scheme with a constant covariance matrix ($\mathbf{P}^{\mathbf{f}}$) could be acceptable (i.e. Optimal interpolation). On the other hand, for error structures highly variable in time this approach would be highly insufficient and a more complex approach would be necessary (i.e. Ensemble Kalman filter). In order to evaluate the stationarity of the errors, we look at the time evolution of the standard deviation.

When the current depth is perturbed, the standard deviation is quasi-stationary without any significant change between day 15 and 18 (see Fig 4. 14). The structures are quite similar even in amplitude. The trace of the meandering variability is present in the same places and just the shape is a bit distorted. The only that depends on the time is the signal of the upwelling

(difficult to trace in the velocity fields) which is obviously not present before the wind gust at day 15.

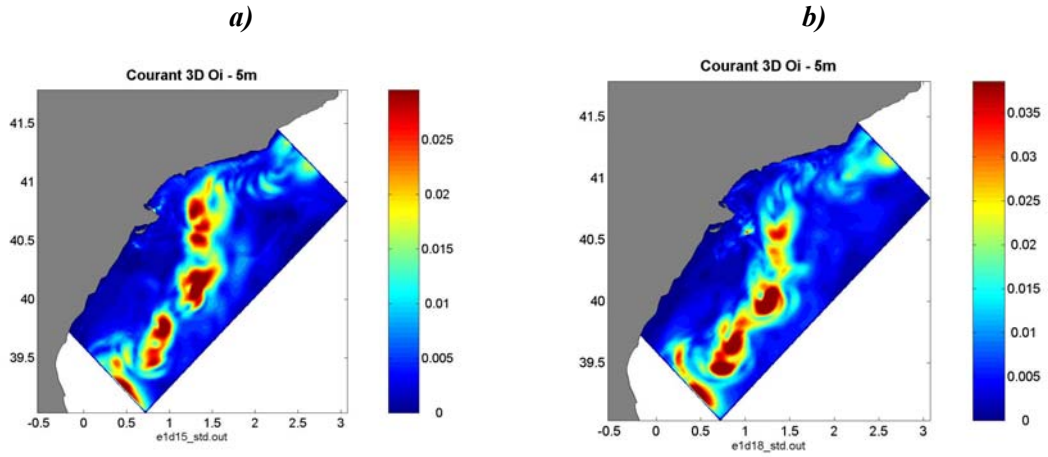

Fig 4. 14: STD of surface velocity for the current ensemble (a)After 2 days of simulation and (b)At the end of the run.

On the other hand, the wind ensemble STD dramatically evolves with time due to the fast adjustment of the sea state to the wind (~f^{-1}=18hours), which is highly variable in the region. This is much more visible in the surface velocity field because its response to the wind is faster than the density which has more "memory". In Fig 4. 15 it is shown the surface velocity STD at two different times. At day 15, the error maximum is located in the northern part, where the Mestral wind is blowing. Three days later, the error structure has evolved and it is then along the entire domain in the open sea. These structures strongly depend on the wind regime, so changing its shape, strength and position.

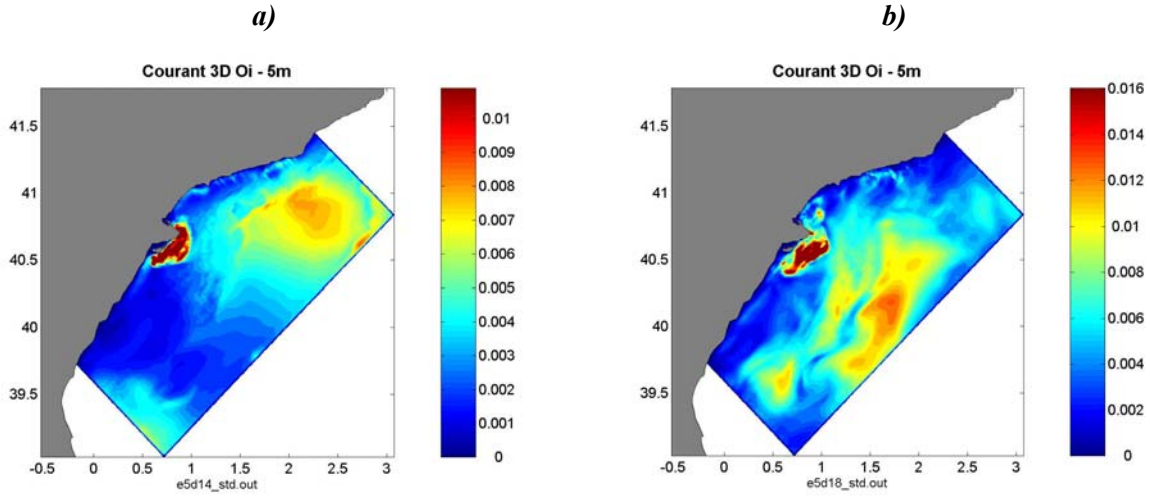

Fig 4. 15: As in Fig 4. 14 but for the wind ensemble.

If we look more carefully at the STD evolution, it is found that the changes strongly depend on the variable and the spatial location (see Fig 4. 16). Before the strong wind burst, no noticeable changes are found but, after the fourth day of simulation, the dispersion is accentuated. Then, it can be seen how changes in salinity are much more significant near the ROFI area (centre shelf), while for the temperature the upwelling zone (northern shelf) is also sensible. Both magnitudes keep the STD values after the wind gust and until the end of the simulation. Dispersion in the surface elevation results is mainly found in the southern shelf and is linked to the pilling of water by the wind. On the other hand, when wind stops, all the ensemble members recovers a similar elevation field. Finally, surface velocity dispersion is more important in the ROFI area but is non negligible in all the other areas, especially in the open sea. This dispersion is also maintained along the runs due to the inertial oscillations triggered at the end of the wind event.

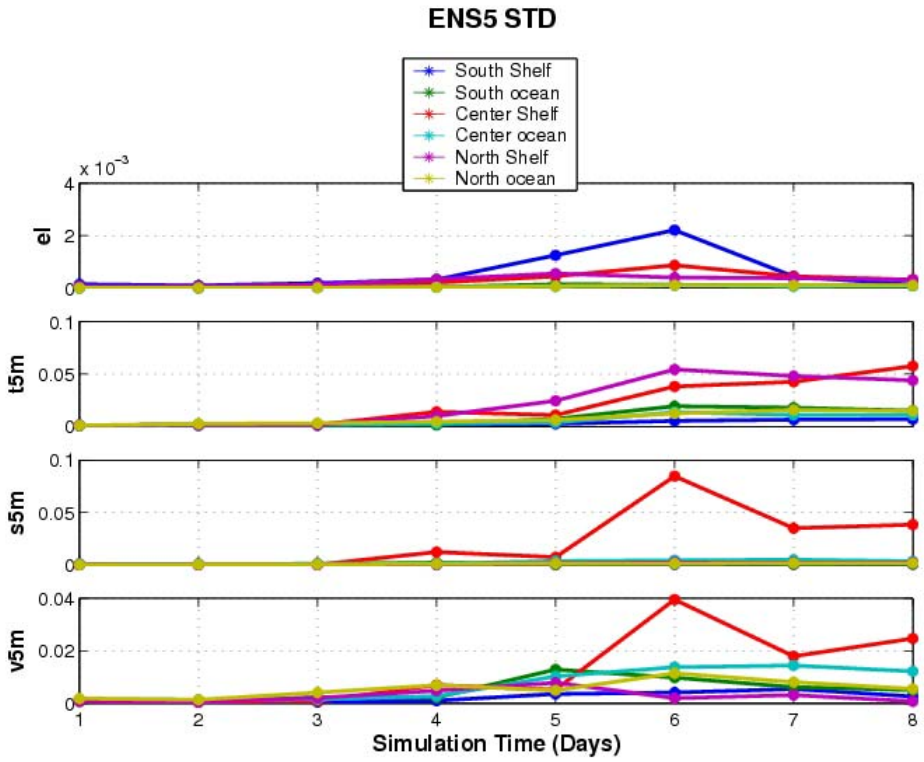

Fig 4. 16: STD time evolution in the wind ensemble for different variables and locations. From top to bottom it is represented elevation,surface temperature, surface salinity and surface velocity. The different colours represent different locations.

In summary it can be concluded that neither the spatial structure nor the magnitude of the variability associated to errors in the wind field is stationary. This issue will be addressed again later on.

4.4.3 Is the system response linear?

The Kalman filter, which is at the base of most of the sequential data assimilation schemes, is optimal when the error dynamics is linear (this doesn't imply that model must be also linear). In consequence, it is basic to know if we are in a linear regime and, if not, how far of it we are in order to know if our data assimilation scheme is expected to be effective or not. If we found that the error evolution is highly non linear our scheme won't be able to properly correct the model evolution and its contribution will be negligible.

One way to check the linearity of the system response is to look at the dispersion of values of a certain variable in a certain place. As the perturbation is Gaussian, we also expect a Gaussian distribution at the end of the run as it will be in a perfect linear response. In Fig 4. 17 and Fig 4. 18 the dispersion of values is presented for a point located over the shelf and in the open sea, respectively. It can be seen that the Gaussian perturbation of the current depth generates a final distribution of errors that is slightly non linear while errors into the wind field induces a quite Gaussian final distribution. Nevertheless it must be noted that this depends on the variable and location.

For the current ensemble, the distribution is not perfectly Gaussian, especially in the open sea. In fact, it is some kind of "semi Gaussian" asymmetrical distribution for all the variables. This can be partially explained because we use 150 members, that can not perfectly describe a Gaussian distribution. Nevertheless the main point is that initial fields, which are already the solution of the initialization method, are not Gaussian neither. Previously we have shown that the MPV method presented a quite different behaviour for currents shallower than the shelf break (~200m). Those currents can come into the shelf evolving quite differently than the currents which remain restricted to the slope. It is important to note that this is not a weakness of the initialization technique. It is the result of the model spin up phase which is physical, and if we had initialized the model using another approach, the expected solution will be the same but after a longer spin-up period. At the end of the run the ensemble dispersion have changed but the overall rate of non-linearity is similar than in the initial ensemble. In some variables as the averaged velocity the distribution have became more linear but in temperature or salinity is the inverse.

a)

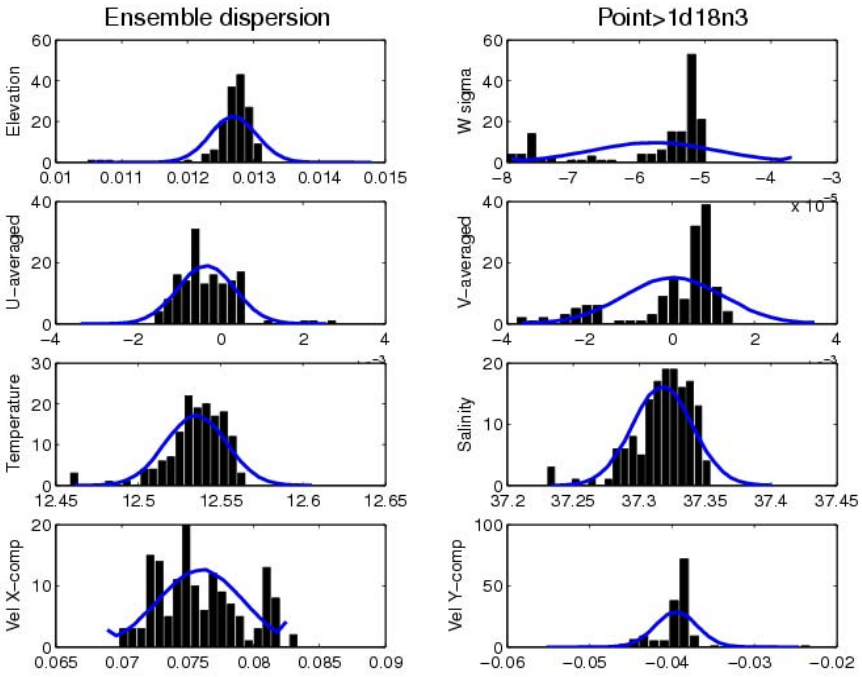

b)

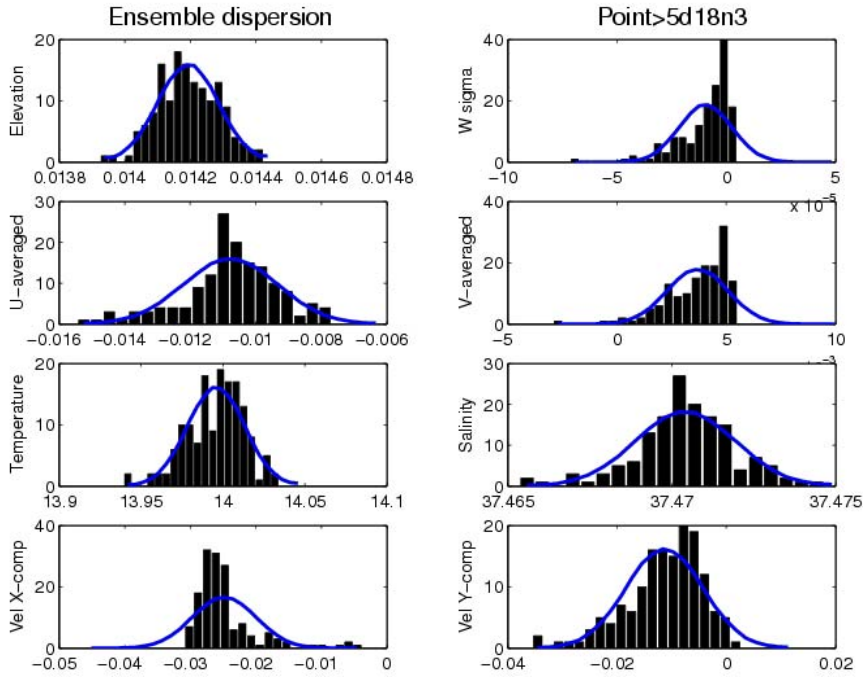

Fig 4. 17: Histograms of the ensemble values dispersion over the shelf for different variables. (a) Current ensemble final state. (b)Wind ensemble final state. Blue line is the analytical Gaussian distribution.

a)

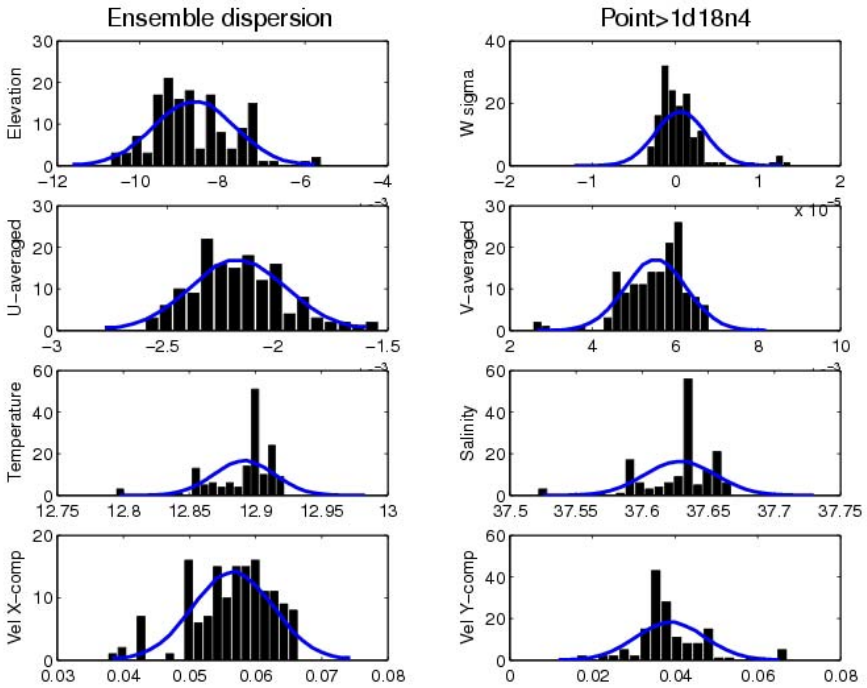

b)

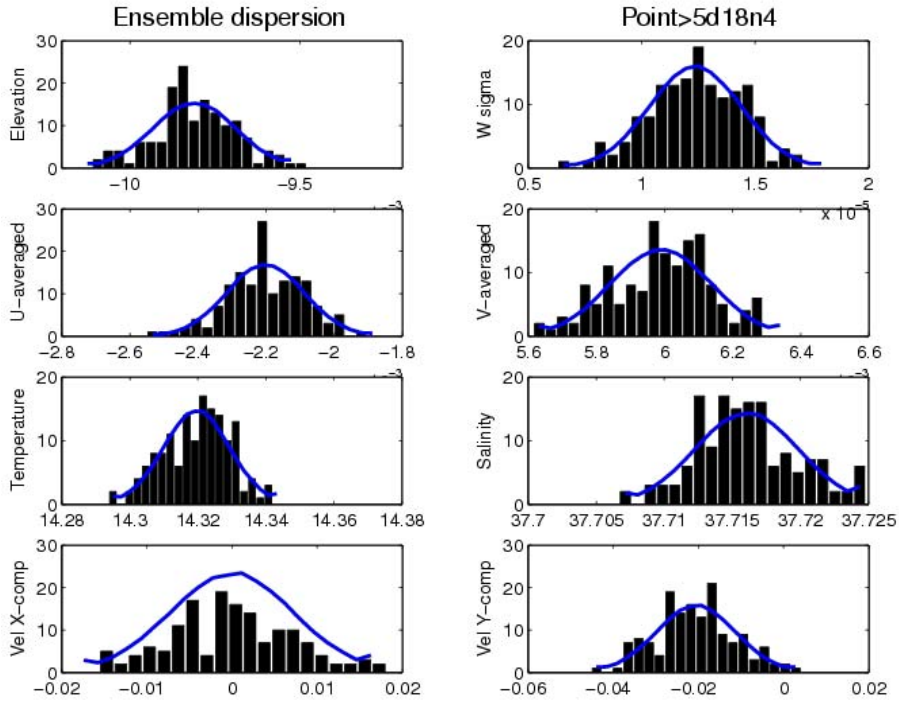

Fig 4. 18: As Fig 4. 17 but for a point located in the open sea

For what concerns to the wind ensemble, its behaviour is much more linear for all the variables and all the locations (except the vertical velocity and the averaged velocity over the shelf which are conditioned by the coast line). This linearity can be due to the fact that wind is highly variable and non-symmetric behaviours have no time to be set up. For instance, the upwelling and downwelling processes are quite symmetric in its initial phases. Afterwards, the coast-line and bathymetry can break this symmetry but in the real configuration this phase is not reached.

As a conclusion of the analysis of the ensemble results we can say that error dynamics follows the dynamics of the region. Maximum values of STD are associated to the main processes simulated (plume evolution, current meandering, wind induce circulation and upwelling). The dispersion of the ensemble results allows us to conclude that errors associated to the slope current initial conditions are quasi-stationary and slightly non-linear while those associated to the wind forcing are highly linear but non-stationary.

4.4.4 Memory time

Another question that arises from this non-stationarity is the memory time of the system. We would like to know how much time the system needs to forget its initial conditions because this information is necessary to define the assimilation cycle. Namely, when we correct the model state bringing it closer to data, we would like to know for how long this correction will be valid before the system errors degrade the model state. This will determine with which frequency we need to do the corrections to avoid large divergences of the model solution.

When considering errors in the initial characterization of the slope current, we found that the memory time is really large. Two members with different velocity profile but the same forcing needs long time to converge to the same solution. This is due to two main reasons. First, the quasi-geostrophic equilibrium of the initial fields is a robust feature difficult to be altered if no strong external forcing is applied. In other words, there is no a priori reason why the two states should converge as both are already in equilibrium. The second point is that, in our configuration, the forcing at the boundaries is fixed and no imported variability is present. Current meandering or the advection of structures could modify the initial velocity structure leading the different member to the same state. To sum up, the wind forcing and the locally generated current variability are not able to modify the main structure of the slope current, so its memory time is large. This has the advantage that, in principle, it would be enough to correct the current structure once. If we consider other processes as the imported variability, the assimilation cycle should have a frequency similar to the frequency of the processes that must be corrected.

The other case to consider is when errors are present in the wind forcing. The system response to the wind is quite fast and the definition of the memory time becomes more interesting. To evaluate it, we compare the evolution of the wind ensemble (ENS5), with another one which is exactly the same but starting four days later (ENS51). This can be interpreted as two ensembles with the same forcing but with different initial conditions.

In Fig 4. 19 is presented the time evolution of the free surface STD and temperature STD for both ensembles. It can be seen that after one day they have the same values for the surface elevation variance and, after the wind gust (15th February), the evolution of both ensembles is quite similar. The temperature field needs more time to reach the same values of STD but once there, the evolution is similar in both ensembles. Obviously, this measure is not enough, so we look to the spatial structure of both STD fields (see Fig 4. 20). It can be seen how after one day both elevation STD fields are quite similar in shape and magnitude and just small differences are present associated to the river plume. This is due to the fact that ENS51 had not the time to complete develop the river plume. Three days later, with calmer wind conditions, both fields are still coincident with the only exception of the plume process.

It must be noted that, in this case, the memory time is so short due to the fact that the wind burst is strong enough to make both systems to converge. In calmer periods, it is probable that the memory time will be longer, but also the associated errors (magnitude of STD) will be less significant.

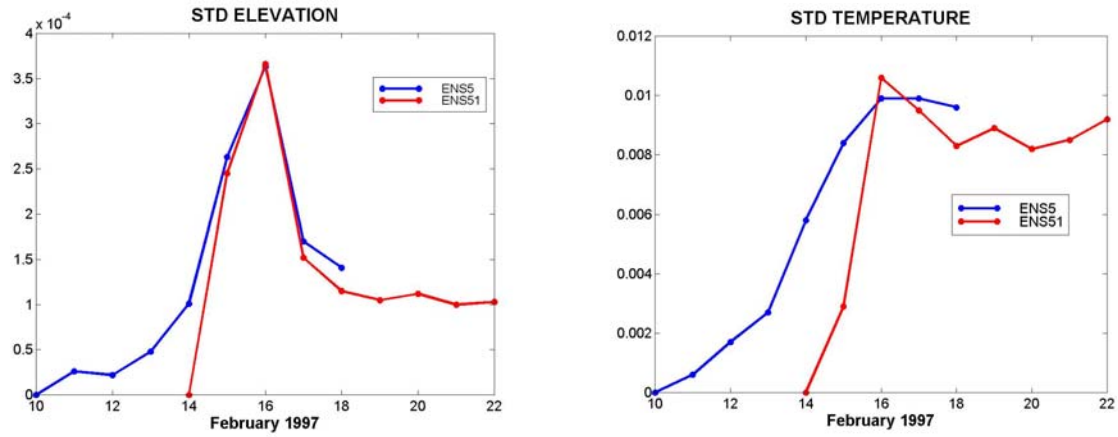

Fig 4. 19: Time evolution of STD for two wind ensembles starting at different times. Results for the free surface elevation (left) and the temperature (right).

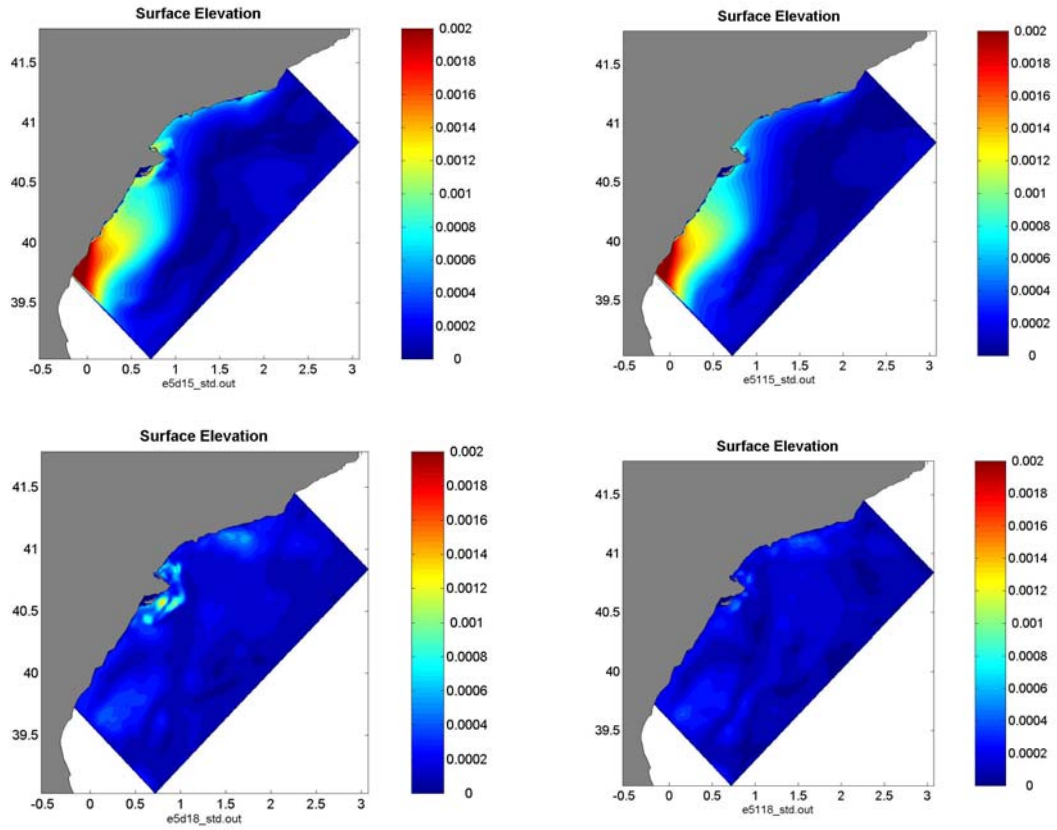

Fig 4. 20: Comparison of elevation STD maps for ensemble ENS5(left) and ENS51 (right) at day 15 (top) and at day 18(bottom).

4.5 INFLUENCE OF OBSERVATIONS

The ensemble modeling allows us to establish correlations between different elements of the state vector. In other words, from the ensemble of model results we can explicitly compute the covariances between different variables and locations. Besides of using them to establish a reduced order space for assimilation purposes, the covariances can give us an insight into the influence of different observations over the state vector. The way to evidence this influence is through the representers, also called influence functions (Echevin et al. ,1999; Bennett 1992).

Formulation

Those influence functions directly arise from a re-formulation of the analysis stage in the Kalman filter. The equation (4.11) can be re-written as (Benneft, 1992):

$$\mathbf{x}^a(t_i) = \mathbf{x}^f(t_i) + \sum_{j=1}^{j=p_i} b_j(t_i)\mathbf{r}_j(t_i) \qquad \textbf{(4.32)}$$

$$\mathbf{x}^a(t_i) = \mathbf{x}^f(t_i) + \mathbf{r}\,\mathbf{b}$$

where $\mathbf{r}_j(t_i)$ is the influence function (representer) of the j^{th} observation at time t_i , $b_j(t_i)$ is the associated scalar coefficient and p_i is the number of observations at time t_i.

The vectors $\mathbf{r}_j$ are the columns of the matrix $\mathbf{r} = \mathbf{P}^f \mathbf{H}^\mathbf{T}$ and have the same dimension that the state vector $\mathbf{x}^\mathbf{f}$. On the other hand, the vector of coefficients $\mathbf{b} = (b_1, ..., b_j, ..., b_p)^T$ verifies that:

$$\left(\mathbf{H}\mathbf{P}^f\mathbf{H}^\mathbf{T} + \mathbf{R}\right)\mathbf{b} = \left(\mathbf{y}^0 - \mathbf{H}\mathbf{x}^f\right) \qquad \textbf{(4.33)}$$

The analysis of the state vector in (4.32) can be interpreted as the addition of two elements: the forecast $\mathbf{x}^\mathbf{f}$ and the combination of corrective terms, the so-called representers. These influence functions directly depend on the error covariance matrix $\mathbf{P}^\mathbf{f}$ and can be viewed as propagators of the information in the observation space into the model space.

In our case, we use the representers to identify the spatial structure of the influence of different observations. They will give also an idea about the weight of the correction provided by a given difference between observation and model forecast. It must be noted that, as far as the model state is multivariate, the influence will be also multivariate, which is coherent with the fact that physics link all the variables.

In practice, the computation of the representers for a single observation is easy, as it just requires to calculate the covariance between the observed variable in the observation point and the complete state vector. Also, the computation of the correction induced by an observation is not complex. For instance, if we consider a punctual measure of temperature in the point x_0, the observation operator H reduces to a vector with a single non-null element, and using equations (4.32) and (4.33), the innovation of the state vector (δx) can be expressed as:

$$\delta\mathbf{x} = \mathbf{x}^a - \mathbf{x}^f = b_0\mathbf{r}_0 \qquad \textbf{(4.34)}$$

where,

$$\mathbf{r}_0 = \mathbf{H}_0\mathbf{P}^f = < T(x_0), \mathbf{x} > = < T_0, \mathbf{x} >$$

$$b_0 = \frac{T_0^{obs} - T_0^f}{< T_0, T_0 > + \varepsilon_{obs}^2} = \frac{\delta T_0}{< T_0, T_0 > + \varepsilon_{obs}^2} \qquad \textbf{(4.35)}$$

$< >$ expresses covariance and ε_{obs} is the observational error associated to the measure.

Combining (4.34) and (4.35) we obtain a compact expression:

$$\delta\mathbf{x}_i = \frac{< T_0, \mathbf{x}_i >}{< T_0, T_0 > + \varepsilon_{obs}^2}\delta T_0 \qquad \textbf{(4.36)}$$

To interpret this, it is more useful to use correlation instead of covariances. Being $correl(x_1, x_2) = \frac{< x_1, x_2 >}{\sqrt{< x_1, x_1 >< x_2, x_2 >}}$, we can transform (4.36) into:

$$\delta \mathbf{x}_i = \frac{correl(T_0, \mathbf{x}_i)}{1 + \frac{\varepsilon^2_{obs}}{<T_0, T_0>}} \sqrt{\frac{< \mathbf{x}_i, \mathbf{x}_i >}{< T_0, T_0 >}}\ \delta T_0 \qquad \textbf{(4.37)}$$

From this expression, it can be seen that the correction of an element *i* of the state vector (x_i) due to an increment δT_0 is proportional to the correlation between the element x_i (which is a given model variable in a specific location) and T_0. If there is no correlation between both, there is no reason to correct anything. Besides that, the magnitude of δx will depend onto the observational error and the variances at each point. Namely, a large measurement error ($\varepsilon_{obs} >> <T_0, T_0>$) will imply no correction at all (i.e. no reliable data won't have any influence). Also, it is important the ratio between the model variance at point *i* and model variance at the observation point. If this is small (i.e. model uncertainties at the observation point are not important), the correction will also be small. On the other hand, if model uncertainties in the correcting point are larger, model state there will be largely corrected.

Description of some influence functions

Here, we show few examples to enlight the existing differences linked to the ensemble used for compute statistics (current/wind), the kind of observation and its location. We did several experiences placing the simulated observation in different points with different dynamical characteristics (shelf widening area, wide shelf and open sea) and using different variables. The comments will be base in two of those experiences where the observing point was located in the widening area over the slope. In one of them the measure was of surface elevation while in the second one we simulated a measure of temperature at 20m depth. Computations are done from the ensemble results (ENS1 and ENS5) at the end of the simulation period.

First, we show the correlations because it is clearer to have an idea about spatial structures (magnitudes will be the same for all cases). The first thing that can be noted in Fig 4. 21 is that the correlation between the surface elevation in the widening area (marked with a black dot in the figure) and the other variables and locations depend on the ensemble used to do the statistics.

If we consider errors in the slope current characteristics (i.e. current ensemble runs), the elevation in the widening area is highly correlated with the shelf and slope. This is coherent

with the idea that the errors in the slope current will propagate through all the domain following the current structure. As these errors imply changes in the whole 3D density structure its effects are felt in the entire domain around the slope (i.e. the isopycnals tilt around the current axis). Over the slope and the outer shelf the correlation is very high while the inner shelf is unaffected (correlations ~0) and the open sea is negatively correlated.

When we face errors in the wind fields (i.e. wind ensemble runs), the correlation structures have a different shape which directly depends on the way the sea reacts to the wind forcing. The widening area is correlated with the surroundings until a distance of 60km seawards while the shelf is not affected. The interaction of wind-induced currents and the coast provokes a complex response over the inner-shelf which is different from what is found over the in the open sea justifying those weak correlations.

It must be noted that wind errors also affect the whole domain due to the fact that size of the domain is comparable with the size of wind structures, so errors on the wind events affect all the area. This feature should be kept on mind in the data assimilation exercises. A punctual measurement ($\Delta\phi_0$) will be able to correct the whole model state, even at long distances. This has a positive and a negative effect. If the assimilation system includes the error process which generates this $\Delta\phi_0$ the whole model state could be corrected in an easy and "cheap" way. However, if that error process is not included in the representation of covariances, the assimilation scheme will definite degrade the model solution.

It also happens that all model variables are correlated in some way. Errors in whatever parameter have an influence over several variables, so correlations among them will be present. For instance, if we look to the correlation of surface elevation variations with temperature, important values are found. In the case where we perturb the slope current, the variations on surface elevation are linked to changes in the whole density structure, so it's logical to find high correlations (positive or negative) with temperature. The structure of those correlations is linked to the current meandering present in the simulation. When errors in the wind field are considered correlation values are lower and the spatial structure more complex due to the different circulation patterns induced by wind.

We also want to stress the point that correlations do not necessarily mean that different variables are linked in a cause-effect relation. It means that the errors which provoke a dispersion of model results have an effect over all of them.

To sum up, it can be seen that relations between different locations and variables are highly dependent on the error processes considered, and, in all cases, their structure is strongly anisotropic. This confirms the results presented by Echevin et al. (1999) and complements them as far as we show that structure also depends on the ensemble used to compute the statistics.

On the other hand, their stationarity must be considered (Mourre et al., 2004). In the case of the current ensemble, the influence functions are near-constant in time as the errors are linked to a robust structure which is mainly stationary. With the wind ensemble, the influence functions are highly variable depending on the wind regime.

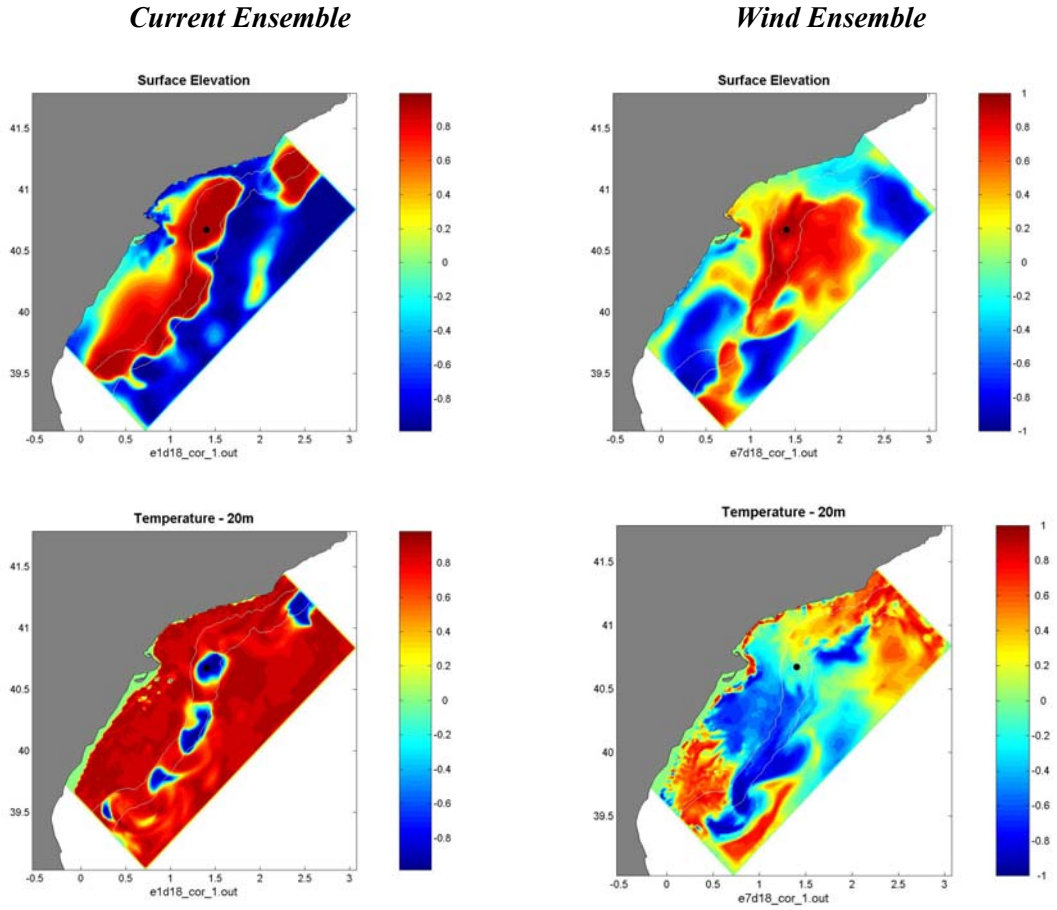

Fig 4. 21: Correlation between surface elevation in the position indicated by the black dot and the surface elevation field (top) and the 20m temperature (bottom). The correlation is computed from the current ensemble (left) and from the wind ensemble (right). 200m and 1000m isobaths are represented in white.

Now, we compute the complete influence functions following (4.37), where other parameters, beside the correlation, appear. The influence of a given measurement over the model state will depend, as it was mentioned before, on the observational error, the model variance at the observation point and the model variance at the "influenced" point. We use two kind of observations, surface elevation, where we consider a $\Delta\eta$=5cm with an observational error of 1cm, and temperature at 20m depth, where we assume ΔT=0.1ºC with an observational error of 0.01ºC.

In Fig 4. 22, the representers for an observation placed in the widening area and computed from the current ensemble results (ENS1) are presented. It can be seen how the correction in the surface elevation and temperature is much greater if the observed variable is the 20m temperature. The reason is that the controlling factor is the ratio between the observational error and the variance in the observation point in (4.37). When measurement is temperature, this ratio is much smaller than when the surface elevation is measured. In the current ensemble the free surface variability is reduced due to the initialization method, so the temperature variances are much greater. Obviously, the observational error has also a great influence. If the mesurement was very reliable (ε_{obs} small), the correction will be more important.

This reasoning is also valid for the situation of the observation. If it is placed in a low variance position (which implicitly means that we trust the model), the correction will be smaller than if it is placed where the model is less reliable.

The variance in the "influenced" point is also determining ($<x_i,x_i>$ in (4.37)). Regions and variables with more variance (i.e. more uncertainties in the model result) will be more corrected than regions where model is reliable (i.e. small variances). This is the reason why the aspect of the correlation between surface elevation and temperature at 20m depth (see Fig 4. 21c) differs significatively from the aspect of the influence function (see Fig 4. 22c). Namely the upwelling region in the northern part is masked in the correlation while it is really visible in the representer due to its high variance.

As it happened with the structure of the correlations, the influence functions also depend on the way the ensemble of model results has been generated. To compare with the results showed above, in Fig 4. 23 it is presented the representers obtained from the wind ensemble results. It can be seen how, beside the different spatial structure, the values of the correction also differs from what was shown in Fig 4. 22. Again this is due to the different variance present in the ensemble results. The errors in the wind field have a reduced effect over the temperature at 20m, so the variance there is smaller and, consequently, the corrections.

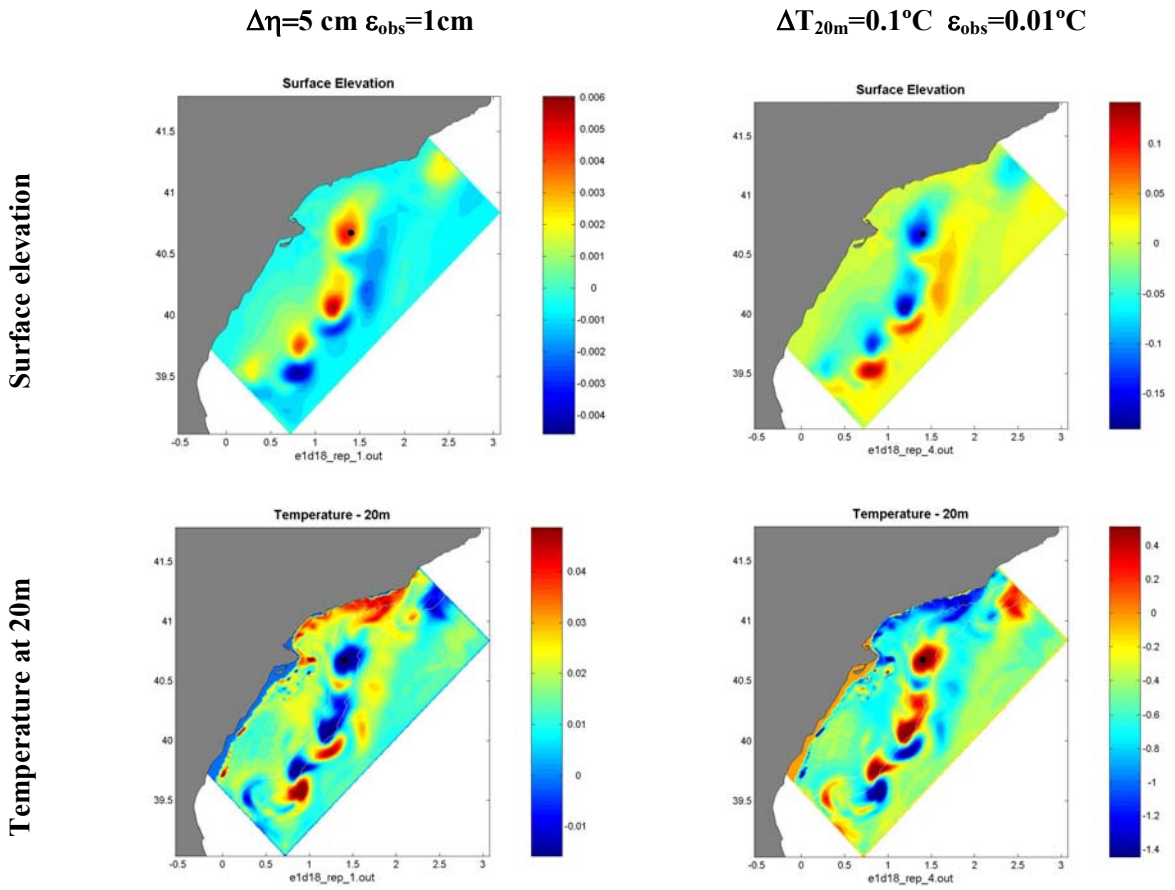

Fig 4. 22: Influence function of a Δη=5cm (left) and a ΔT=0.1ºC(right) computed from the current ensemble (ENS1). The black dot indicates the measurement point(Note that the colorbars are different!!)

To sum up, the representers gave us an insight into the expected behaviour of the data assimilation (altough strictly speaking we should use a reduced order representer to be equivalent to the assimilation scheme). The influence functions are global in the sense that all variables in all locations are linked (i.e. correlations far from 0). This is due to the way the ensembles have been generated. Errors in the slope current definition (depth, width, intensity) will affect the whole 3D density structure of the model state as the current is in a quasi-geostrophic equilibrium. Errors in the wind forcing also have this global behaviour because the spatial scale of the atmospheric structures is comparable to the size of the model domain. Nevertheless, in this case the correlations are significative just until 50m (the base of the surface mixed layer).

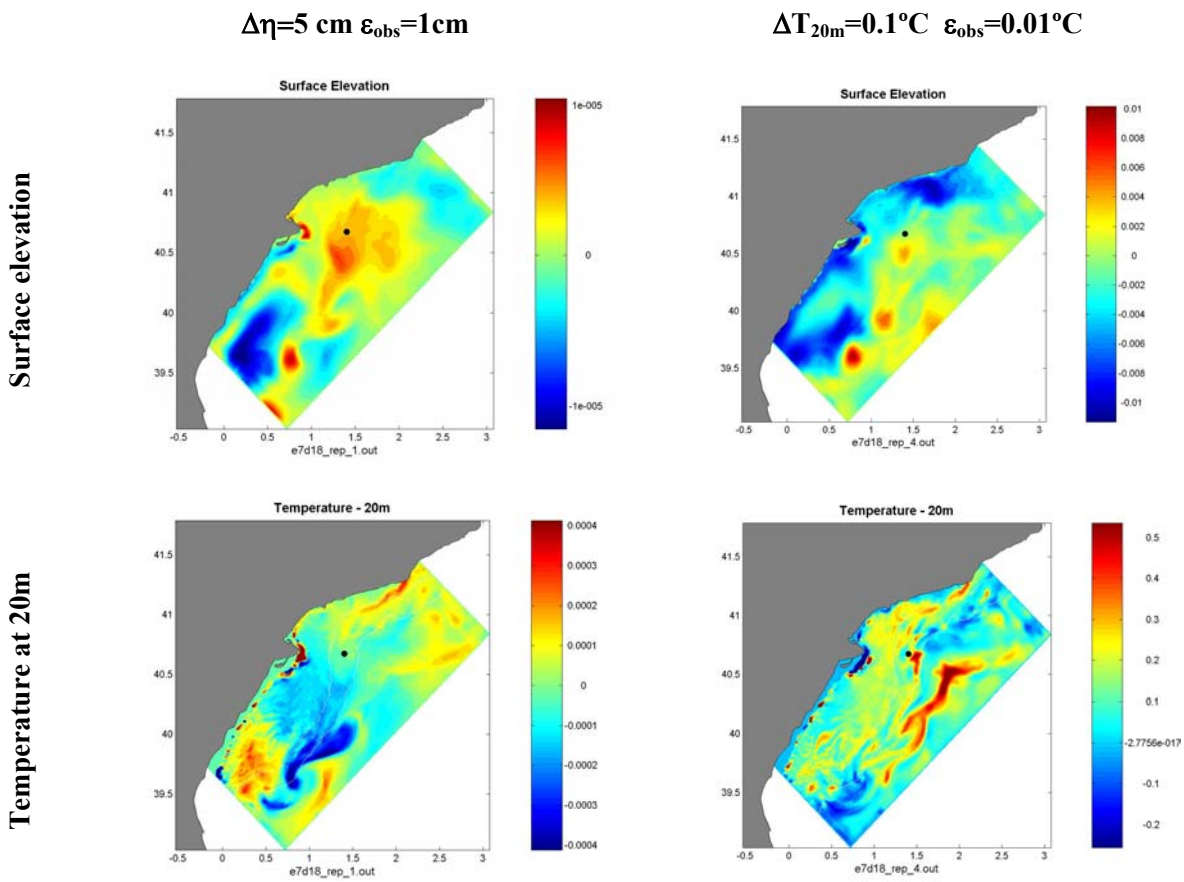

Fig 4. 23: Influence function of a Δη=5cm (left) and a ΔT=0.1ºC(right) computed from the wind ensemble (ENS5). The black dot indicates the measurement point(Note that the colorbars are different!!)

A warning that must be kept on mind is that the small scale structures showed by the influence functions are due to the particular dynamical situation reproduced by the model. A different scenario (i.e. different wind regime), will have associated a different error structure which would induce another shape for the representer.

Finally the model state correction will depend on several factors summarized in equation (4.37). Those are:

-The ratio between the variance at the observation point and the observational error will determine the magnitude of the correction.

-A large observational error (data not reliable) implies a reduction of the model correction.

-Reduced model variance in the observation point or in the "corrected" point implicitly means that model is reliable and do not need to be corrected. Analogously, important model variances will lead to significative corrections.

4.6 ENSEMBLE MULTIVARIATE EOF ANALYSIS

The goal of this work is to use an EOF decomposition to characterize the error dynamics described previously. The dominant modes of this multivariate EOF base obtained from the ensemble runs will be used in the assimilation exercises to reduce the order of the covariance matrix. The analysis performed in section 4.4 suggests that it would not be necessary to compute the EOFs from all the ensembles. Their characteristics are basically the same and structures are equivalent, being different just in their amplitudes. Therefore, we will focus on the computation of the EOFs for a current ensemble (ENS1) and a wind ensemble (ENS5).

For assimilation purposes, we are interested into the most complete base, where different error structures will be represented, in order to be able to correct the widest series of processes. This leads us to the idea of combine the members of both (wind and current) ensembles, to generate a new base where we expect to find most of the features of ENS1 and ENS5 bases. On the other hand, we have also shown that variability is not stationary, so we will complete the mixed ensemble with members at different times, in order to capture all the high frequency error structures. To sum up, we compute a "Mixed" EOF base, from an combination of members coming from the current and wind ensemble at different time steps with the idea of forming the most complete base for assimilation purposes.

In this section, we will first comment several technical details associated to the computation of the EOFs. Afterwards, the results of computations will be presented, and, to finish, some ensemble diagnostics will be performed from the EOFs results.

4.6.1 Technical details of the multivariate EOF computation.

Toumazou's algorithm and practical implementation

For problems with a small state vector, the choice of the technique used to compute the EOFs is not critical and several subroutines in Fortran or MATLAB could be used without worry about the computational time. However, if the computation must be done for a primitive equations 3D model in a realistic configuration, the dimension of the state grows too much, and the efficiency of the usual techniques to compute the EOFs is not enough.

In our case, the model state is of dimension $2 \cdot 10^6$, and a typical size for the ensemble is 150-300 members. To try to solve a problem of this size with a MATLAB subroutine or a typical SVD Fortran code implies strong limitations in terms of computational time and memory and even, in some cases, it would not be applicable. The alternative found to deal with this problem was to implement the algorithm proposed by Toumazou and Cretaux (2001) where a Lanczos eigensolver technique is used to compute only the dominant modes of a smaller symmetric matrix.

In a Singular Value Decomposition, the computation of the eigenvalues of a matrix *D* is done expressing this matrix as

$$\mathbf{D} = \mathbf{U}\Sigma\mathbf{V}^{\mathbf{T}} \qquad (4.38)$$

where **U**(**V**) is the matrix of left (right) singular vectors of **D** and $\mathbf{\Sigma}=\mathrm{diag}(\sigma_1,\sigma_2,...,\sigma_n)$ is a diagonal matrix with the singular values of **D**. It is also accomplished that $\mathbf{U}^{\mathbf{T}}\mathbf{U}=\mathbf{V}^{\mathbf{T}}\mathbf{V}=\mathbf{I}$.

The main difference with a Lanczos method is that, in this strategy, the problem is reformulated as:

$$\mathbf{D}^{\mathbf{T}}\mathbf{D} = (\mathbf{U}\Sigma\mathbf{V}^{\mathbf{T}})^{\mathbf{T}}(\mathbf{U}\Sigma\mathbf{V}^{\mathbf{T}}) = \mathbf{V}\Sigma^{2}\mathbf{V}^{\mathbf{T}} \qquad (4.39)$$

and then just the *k* largest singular values and associated vectors (v_i) are computed by solving:

$$\mathbf{D}^{\mathbf{T}}\mathbf{D}\,v_i = v_i\sigma_i^{\,2} \qquad (4.40)$$

The left singular vector is computed solving the equation

$$\mathbf{U} = \mathbf{D}\mathbf{V}\mathbf{\Sigma}^{-1} \qquad (4.41)$$

which is straightforward as **S** is a diagonal matrix.

For a complete description of the properties of this method, the reader is referred to Toumazou and Cretaux (2001).

Normalization

One problem that have been identified after the first analysis is that if there are some processes with high variance associated, it will control the EOF decomposition. In some cases all the variance of this process will be retained in the first EOF but usually it is shared into several modes, so masking other interesting processes. In our case this is what happens with the river plume. Its variability due to errors in the wind field largely dominates and masks other processes like the current oscillations or the upwelling. On addition to that, the EOFs are multivariate, so its influence is not felt only over the salinity field but over all the variables. As we are interested in having the most complete EOF base where the maximum number of processes will be represented, we need a tool to avoid this. In our case we decided to use a normalization mask.

When computing multivariate EOFs, it is recommendable to normalize the covariance matrix by a factor which depends on the variable in order to not be influenced by the different scales and units of the variables. For instance, a typical std for the free surface elevation can be around 0.05m while for the temperature this value is ~1ºC. If no normalization is done, the EOFs will be dominated by the temperature variability masking all the processes with trace in the elevation field. What is usually done is to divide the covariance matrix by the variance of each variable, so bringing to the same level of importance processes with different units.

For example, if the state vector is defined as

$$\vec{x} = \left(\eta_1,...,\eta_n,T_1,...,T_n,S_1,...,S_n\right) \qquad \textbf{(4.42)}$$

then it is transformed, before the EOF computation, to

$$\vec{x}' = \left(\eta_1/\sigma_\eta,...,\eta_n/\sigma_\eta,\ T_1/\sigma_T,...,T_n/\sigma_T,\ S_1/\sigma_s,...,S_n/\sigma_s\right) \qquad \textbf{(4.43)}$$

The problem arises when a given process has a variance much bigger than the others. In that case, the classical normalization will become insufficient as this process will still be dominant in spite of the normalization.

The proposed normalization mask consists in dividing by a factor that depends on the value of a given field (i.e salinity or bathymetry), so being a function of the variable and the space. The process that must be masked (or attenuated) has to be identified in terms of a variable ϕ and two threshold values (ϕ_1,ϕ_2) must be fixed. Then, two normalization values (σ_1,σ_2) have to be defined, so the normalization parameter σ will be simply defined, for each variable, as:

$$\begin{cases} \sigma(x,y) = \sigma_1 \quad if \quad \phi(x,y) < \phi_1 \\ \sigma(x,y) = \left(\dfrac{\phi - \phi_1}{\phi_2 - \phi_1}\right)(\sigma_2 - \sigma_1) + \sigma_1 \quad if \quad \phi_1 \le \phi(x,y) \le \phi_2 \\ \sigma(x,y) = \sigma_2 \quad if \quad \phi(x,y) > \phi_2 \end{cases} \qquad \textbf{(4.44)}$$

For example, if the shelf processes are weaker that those in the open sea and it is desired to make them more visible in the EOFs computation, the control variable ϕ could be the bathymetry with ϕ_1=100m and ϕ_2=200m . All the points over the shelf will be divided by the normalization parameter σ_1 that will be smaller than the parameter σ_2 , used in the open sea. To avoid discontinuities, a linear transition between both values would be used near the shelf break. This will give more importance to what happens over the shelf, so it will be reflected in the EOF decomposition.

In our case, we want to damp the effects of the river plume variability because they mask all the processes that are not in the plume. Thus, the control variable is salinity and the threshold value is 37 psu. We consider than lower values are into the ROFI area and all model grid points therein will be normalized with stronger values. An example of the impact of the normalization mask is presented in Fig 4. 24. It can be seen how without normalization, almost all the signal in the first EOF is associated to the plume in the salinity but also in the velocity field. If a constant normalization is applied other processes appear in the velocity field but the salinity part is still controlled by the plume variability. Finally, when using the normalization mask based in salinity values the plume is brought to a second plane and the signal of other features as the current variations or the upwelling is found in the first EOF.

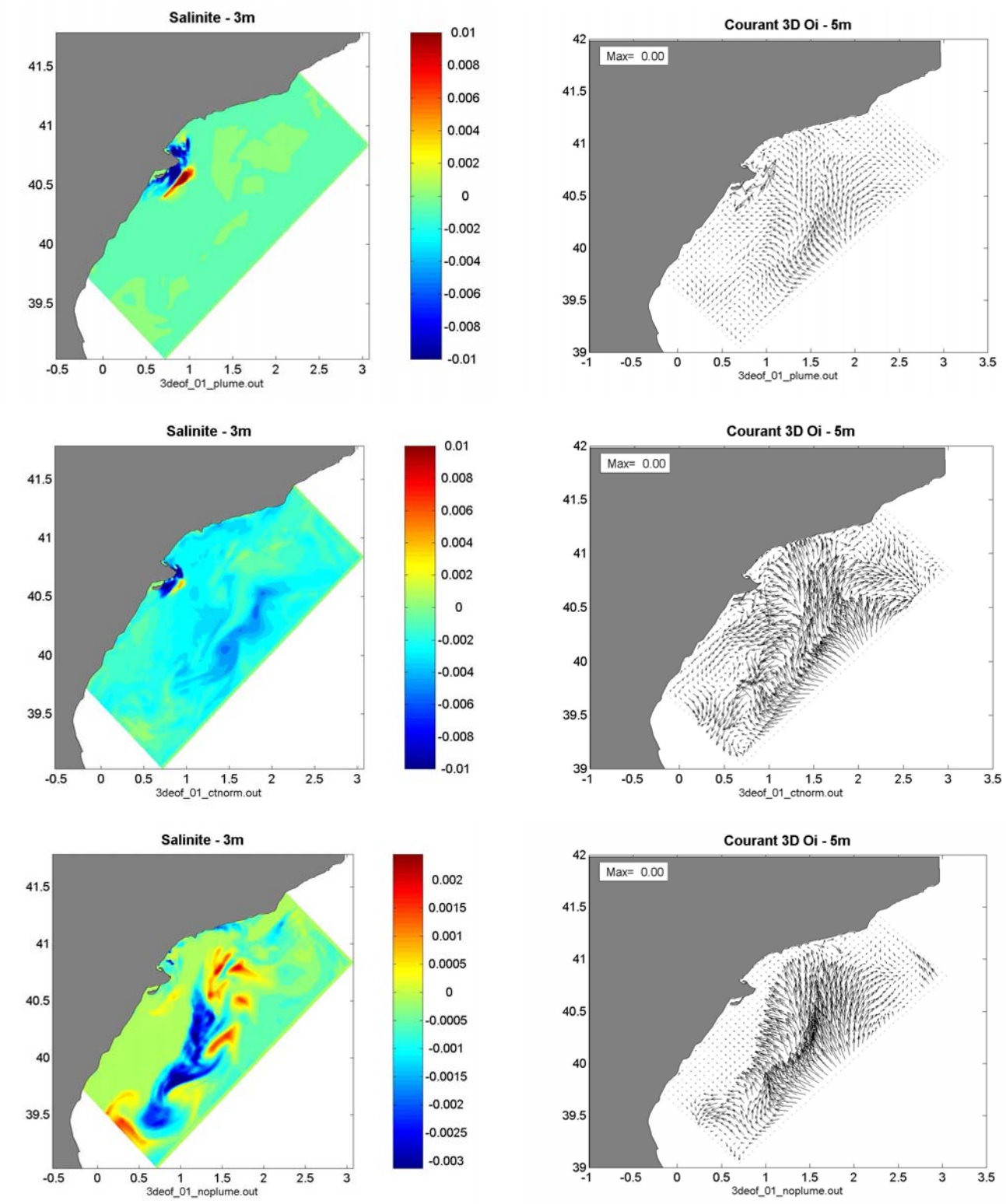

Fig 4. 24: First multivariate EOF from the wind ensemble for surface salinity (left) and surface velocity (right) with no normalization (top), constant normalization (middle) and uisng the normalization mask based on salinity values (bottom).

It must be noted that the choice of the normalization mask is quite subjective and depends on the previous knowledge of the region and, specially, on the priority of processes that have to be enlightened.

Computation of EOFs for Δt =2 days

As it was mentioned in the introduction of the section, we will generate a mixed EOF base from the combination of ensemble members at different times. We do that to enrich the EOF base used in the assimilation with error processes at different times (in the c of the wind ensemble the error samples are indeed quasi-independent from each other). We want to include as much processes as possible in order to provide our "assimilation toolbox" (the EOF base) with the maximum number of tools (processes represented in the base). The underlying idea is that sampling the model ensemble results every two days, we will recover much more error structures than if we compute the EOFs just at the end of the run.

To justify this idea, we look at the wind ensemble EOFs obtained every two days (see Fig 4. 25). It can be seen how the spatial structure and intensity of surface elevation EOF change from one date to other (which is coherent with the memory time of 1 day found previously). Some of the processes can be found in several EOFs at different moments. For instance, the negative anomaly along the coast associated to an upwelling process is present in the first mode of day 14 and the second mode of day 16 but not at day 18. This means that if we compute the EOFs just at the end of the run we won't be able to correct errors associated to the strength of the upwelling process.

To sum up, it can be seen that if we keep just the modes at day 18, we won't be able to reproduce what is present at day 14, for example, and our capabilities to correct model errors will be strongly limited.

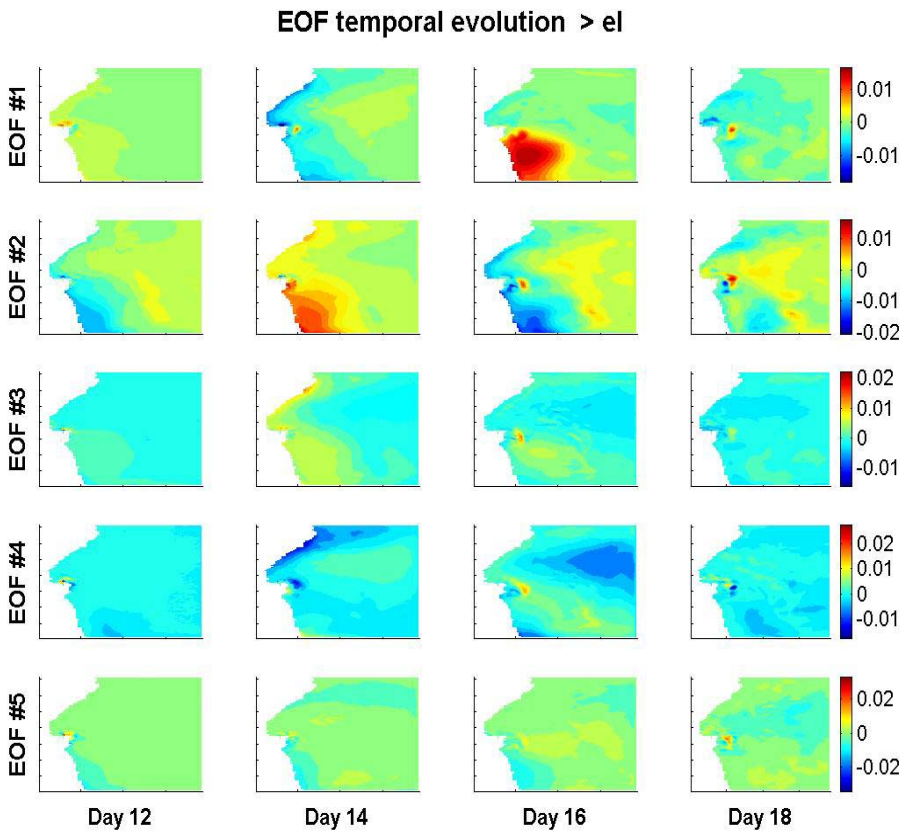

Fig 4. 25: Free surface elevation for the first 5 multivariate EOFs calculated from the wind ensemble every two days

In section 4-1 we have shown that the eigenvalue spectrum has a crucial role in the assimilation. The forecast error is directly obtained from the eigenvalues associated to the eigenvectors that forms the EOF base. The eigenvalue, as a measure of the variance, reflects the enhanced dispersion linked to the wind burst. It is important to keep this feature in mind, because the values of the forecast error have a direct impact in the amplitude of the correction provided by the data assimilation scheme. In the limit, if we have a near negligible value for the forecast error, we are considering that our model is near perfect (variance almost 0), so the assimilation will not correct anything. In the inverse case, big values of the forecast error means that our model is wrong and needs big corrections but this could lead to inconsistencies with model dynamics and the final solution could be degraded.

It is interesting to note that the eigenvalue spectra also changes with time (see Fig 4. 26). Before the wind gust, at day 12, the eigenvalues are really small (~10^{-5}). When wind begins to blow values increase until at day 16, where the wind is the strongest and so the sea variance, when the eigenvalues reach its maximum value (~6 10^{-4}). After, when wind is relaxed, the values are reduced again.

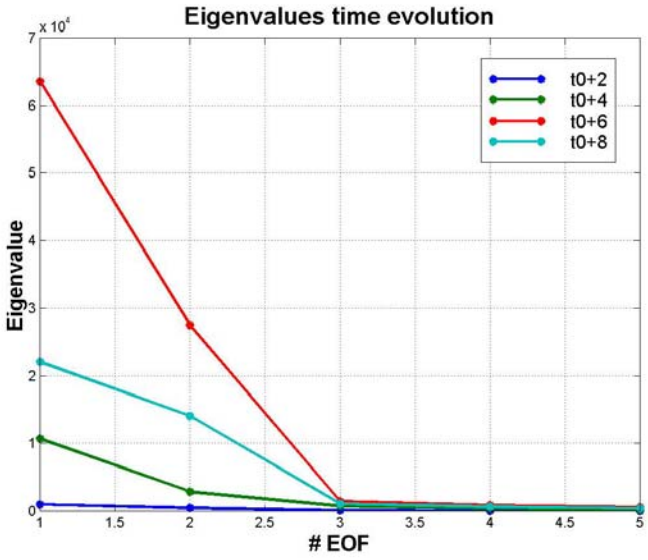

Fig 4. 26: Eigenvalues associated to the multivariate EOFs obtained from the wind ensemble at different times.

Convergence

Another property of the EOF base that must be checked is its convergence. We need to know if the EOF distribution found is representative of the actual variability of the model errors. Namely we would like to know if the number of members used in the ensemble runs is statistically significant to properly generate an EOF base.

First we look at the spatial structure of the obtained modes depending of the number of members used (see Fig 4. 27 and Fig 4. 28). It can be seen how, a small number of members is enough to represent all the structures in both ensembles (ENS1 and ENS5). The difference between using 75 or 150 members is almost negligible. For higher order modes (n>5) more than 100 members is needed but they are rarely used (the fraction of explained variance associated to them are really small <1%) .

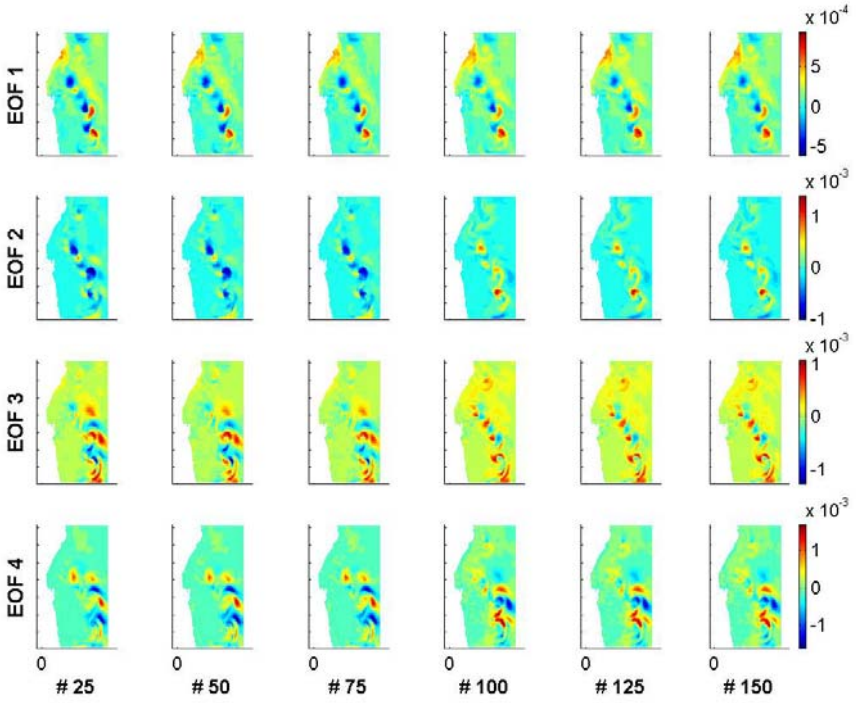

Fig 4. 27: Surface temperature of the multivariate EOF for current ensemble (ENS1) calculated with a different number of members (25 to 150).

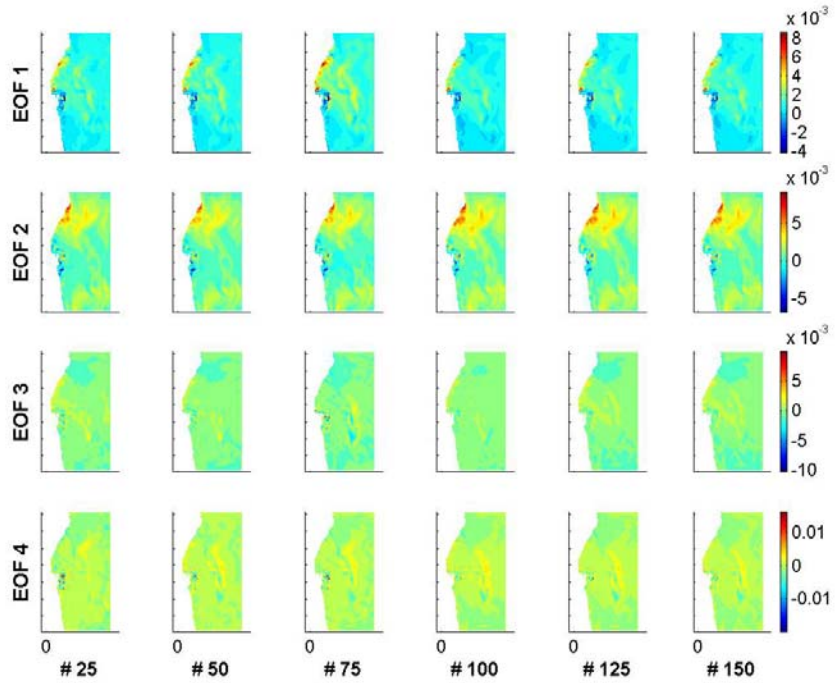

Fig 4. 28: Surface temperature of the multivariate EOF for wind ensemble (ENS5) calculated with a different number of members (25 to 150).

Although the spatial structure of the EOFs reach a convergence with just 75-100 members, it is interesting to look at another parameter that can be used to evaluate the convergence: the eigenvalue associated to each mode. It is possible that same spatial modes change their eigenvalue depending on the number of members used to compute them. As we look for the most robust result we are interested into a stable representation of the variance.

In Fig 4. 29 it is represented the evolution of the eigenvalues as a function of the number of ensemble members used to compute the EOFs. It can be seen how, when more than 100 members are used, the values are quite stationary. The variations are not much significative related to the absolute values and no crossing of modes is found.

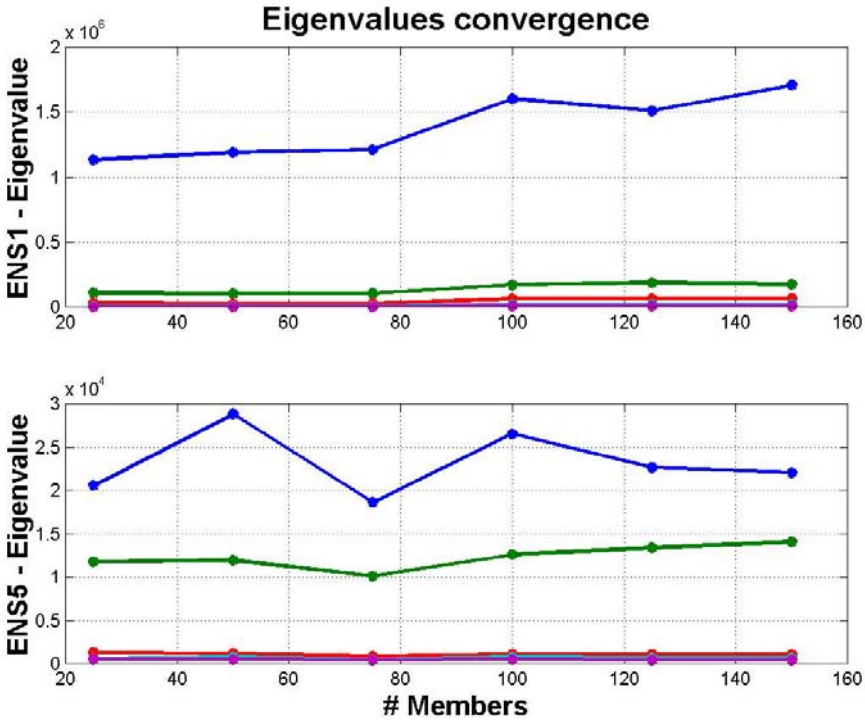

Fig 4. 29: First 5 eigenvalues evolution as a function of members used in the calculation for current ensemble(top) and wind ensemble(bottom)

In conclusion it can be said that 100 members seem enough to reach convergence, so the use of 150, as we do, is quite safe. Nevertheless, it must be noted that this conclusion is valid just for our configuration. Other regions with other error dynamics maybe will be more complex and 150 members will not be enough to reach convergence. In all the cases it must be checked to ensure the suitability of the EOF base.

4.6.2 Results of EOF computation

After the analysis carried on in section 4.4.2 and several preliminary tests, we have found that much of the information contained in all the ensembles is redundant, so, in this section, we focus on the EOF computation of one ensemble where current is perturbed (ENS1) and one ensemble where wind is perturbed (ENS5). The discussion of these two bases includes most of the features present in the EOFs from all the ensembles run.

Current ensemble EOFs (ENS1)

The explained variance of the EOFs obtained from the current ensemble at the end of the run is summarized in Table 4. 4. It can be seen that the eigenvalues spectra is quite red, meaning that most of the variance is contained into the first mode. Also it quickly decreases so more than 99% of the variance can be explained with the first 5 modes.

%	*EOF #1*	*EOF #2*	*EOF #3*	*EOF #4*	*EOF #5*
ENS1	86.13	8.81	3.35	1.05	0.45
ENS5	54.63	34.83	2.64	1.56	0.99

Table 4. 4: Explained variance associated the first 5 EOFs for the current ensemble (ENS1) and the wind ensemble (ENS5)

The structures found in the ENS1- EOFs are directly linked with the slope current features and its oscillations. The variability associated to the meandering found in the STD maps (section 4.4.2) is now shared in different EOFs (see Fig 4. 30 and Fig 4. 31). The first mode, which explains the largest fraction of the variance, presents the basic meandering structure of the error. This structure can be traced in all the variables as it was expected since the current is in quasi-geostrophic equilibrium and its meandering also alters the density and free-surface elevation fields.

The higher order modes complement the representation of the meandering, so different combinations of all modes leads to different strength and location of the meanders. This is clearer looking at the vertical structure of the EOFs (Fig 4. 30c and Fig 4. 31c). It can be seen how the number of negative-positive anomalies increase with the mode number suggesting a kind of harmonic decomposition of the field variability. Using an adequate combination of those structures it is possible to displace the pycnocline wherever is needed, so recovering all the cases present in the ensemble of simulations.

This harmonic decomposition, which will allow to generate all the vertical structures of density, is coherent with what is found in the horizontal. Depending on the vertical gradient of density, the slope current will be more or less deep, and so its meandering more or less marked.

In the upper layers, EOFs values are small, due to the fact that variance therein is also small. The reason is that in the surface mixed layer the circulation is controlled by the wind, which is the same in all the ensemble members. In other words, if the wind forcing has no errors, we do not expect significative errors in the model results in the surface layers, as dynamics therein is wind-controlled.

The variability associated to the upwelling in the northern part presented in the STD maps is included in the first EOF without a significative trace in the higher order modes.

Finally, we wanted to stress the fact that the multivariate 3D EOFs relate all variables and locations. For instance, the positive anomaly of salinity linked to the upwelling in the northern part, means that stratification is stronger (wind strength is the same in all the ensemble members). The stronger stratification is related to a deeper current (because of the MPV initialization technique) which presents a reduced meandering. On the other hand, to reduce the current meandering in the widening area is necessary to add a negative anomaly of density to the mean field (see Fig 4. 8). This is why in the first EOF there is a positive anomaly of salinity in the upwelling region and a negative anomaly in the widening area.

This multivariate and 3D behaviour is a key point for the assimilation. All processes are linked and information about one of them can allow to correct another one. Also locations are related, so, if we have the information to correct the vertical structure of the slope current in one point, we will be able to correct it in all the domain.

Wind ensemble EOFs

The EOFs obtained from the ensemble of simulations where the wind has been perturbed also show a red eigenvalue spectra but not as much as in the current case (see Table 4. 4), being most of the variance shared in the two first modes. In any case, more than 95% of the variance can be explained with the first 5 EOFs.

The main characteristic of this new set of EOFs is that all modes have zero values below 80-100m depth, meaning than the wind errors have an effect restricted to the surface layer (i.e. no secondary effects which could affect deep layers are present).

Another characteristic is that several processes are mixed in each mode. In other words, the EOF decomposition didn't achieve to separate different physical features and the different modes modulate the characteristics of the features captured in the first mode. Although the separation of physical processes would be good for assimilation purposes, it is also logical that it didn't happen since perturbations in the wind field were global, so affecting simultaneously all processes. This mechanism generates high covariances between different processes but it must

be noted that it is not the reflex of physical relations between those processes. The covariances are due to the fact that different processes are generated by the same forcing mechanism. This distinction is important because it could happen that two processes were related in a particular configuration but not in another different one.

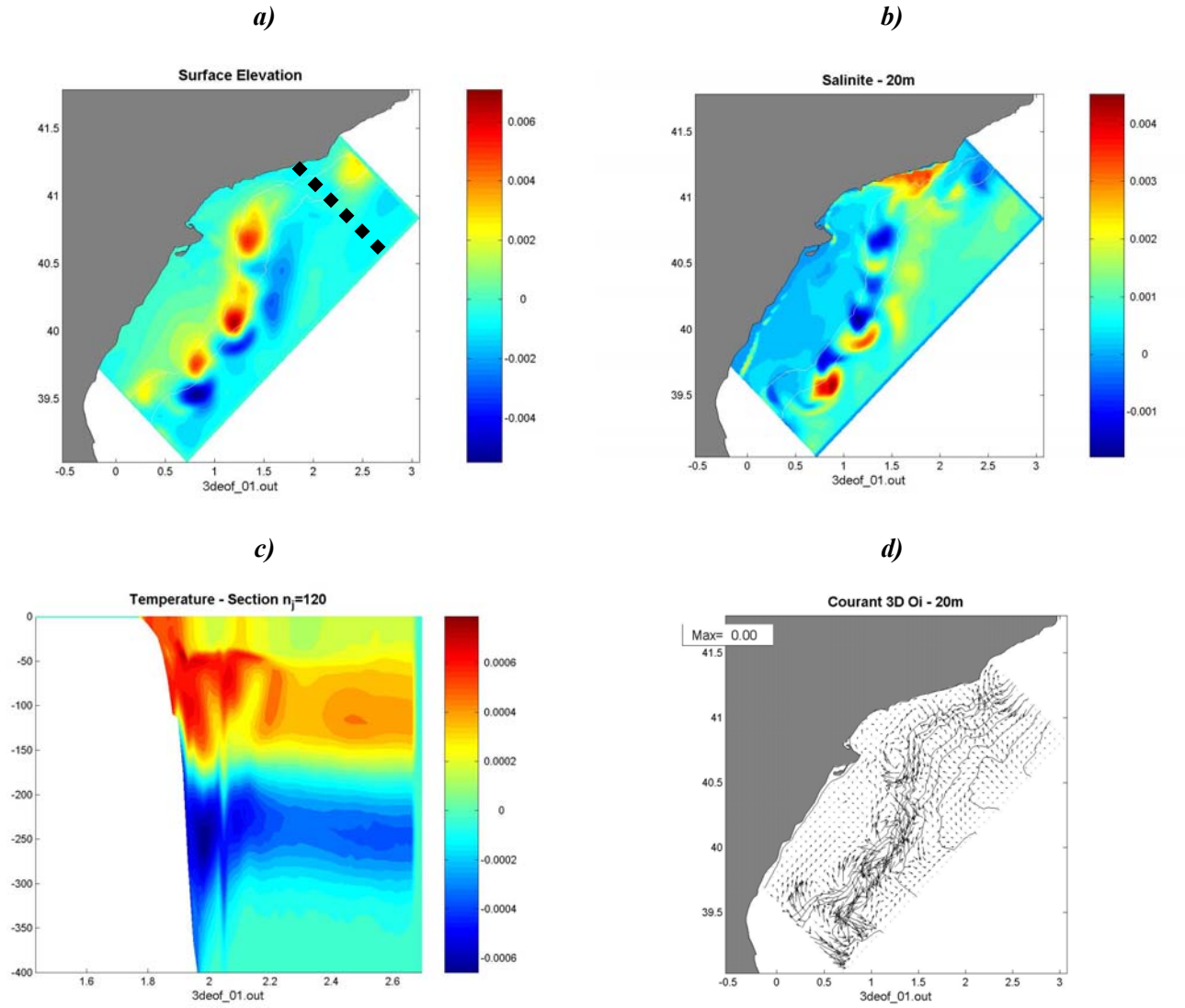

Fig 4. 30: 1st multivariate EOF from current ensemble (ENS1). (a) Surface elevation, (b) 20m salinity, (c)Vertical section of temperature in the North (d) 20m velocity field. The dotted line in (a) indicates the location of the vertical section in (c)

In all the modes, it can be seen the trace of river plume variability (see Fig 4. 32 and Fig 4. 33). Errors in the wind field provoke differences in the position and extension of the plume which are represented as the max-min structure in the EOFs.

The upwelling in the northern part has also a trace in the different modes but, in this case, the reason is different than in the current ensemble case. Now the variability is generated by the perturbations of the wind field and not due to differences in the density structure.

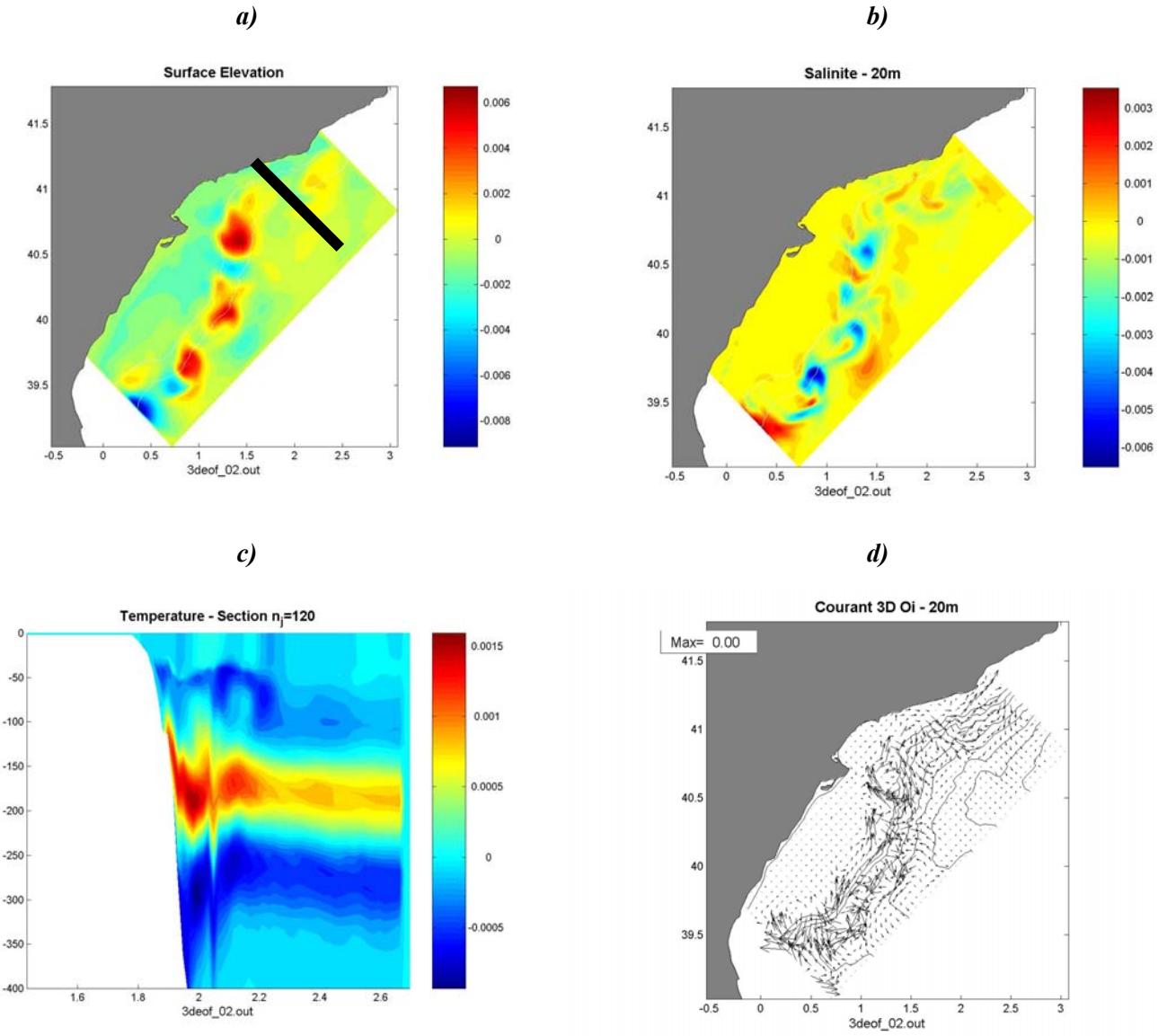

Fig 4. 31: As Fig 4. 30 but for the 2nd multivariate EOF ofcurrent ensemble (ENS1)

The river plume and upwelling variability are represented in the surface elevation, salinity and temperature fields but it is much less visible in the velocities. The reason is that variability of the velocity field is highly controlled by the inertial oscillations whose characteristics (phase, intensity) are highly sensible to errors in the wind field. So, what the EOFs are capturing in the velocity field is the variability induced by different inertial oscillations, which is a high frequency process. This is a interesting issue that should be addressed if velocity observations had to be used. Usually we are interested in the low frequency component of the dynamics, so it should be considered a kind of filtering not only of data but also of the model results before assimilation.

Finally, the vertical structure reflexes the changes in the configuration of the mixed layer due to the different wind fields. If a correction is applied projected in these EOFs it will change the mixed layer features. Namely, it will decrease the temperature in the first meters while increasing it below 30m depth. If we consider than colder waters are in surface, this would lead to a shallower mixed layer where the vertical gradient of temperatures is enhanced. On the other hand, a negative correction will induce a warming of the first 30m while a cooling of the layers below, so homogenizing the upper layers.

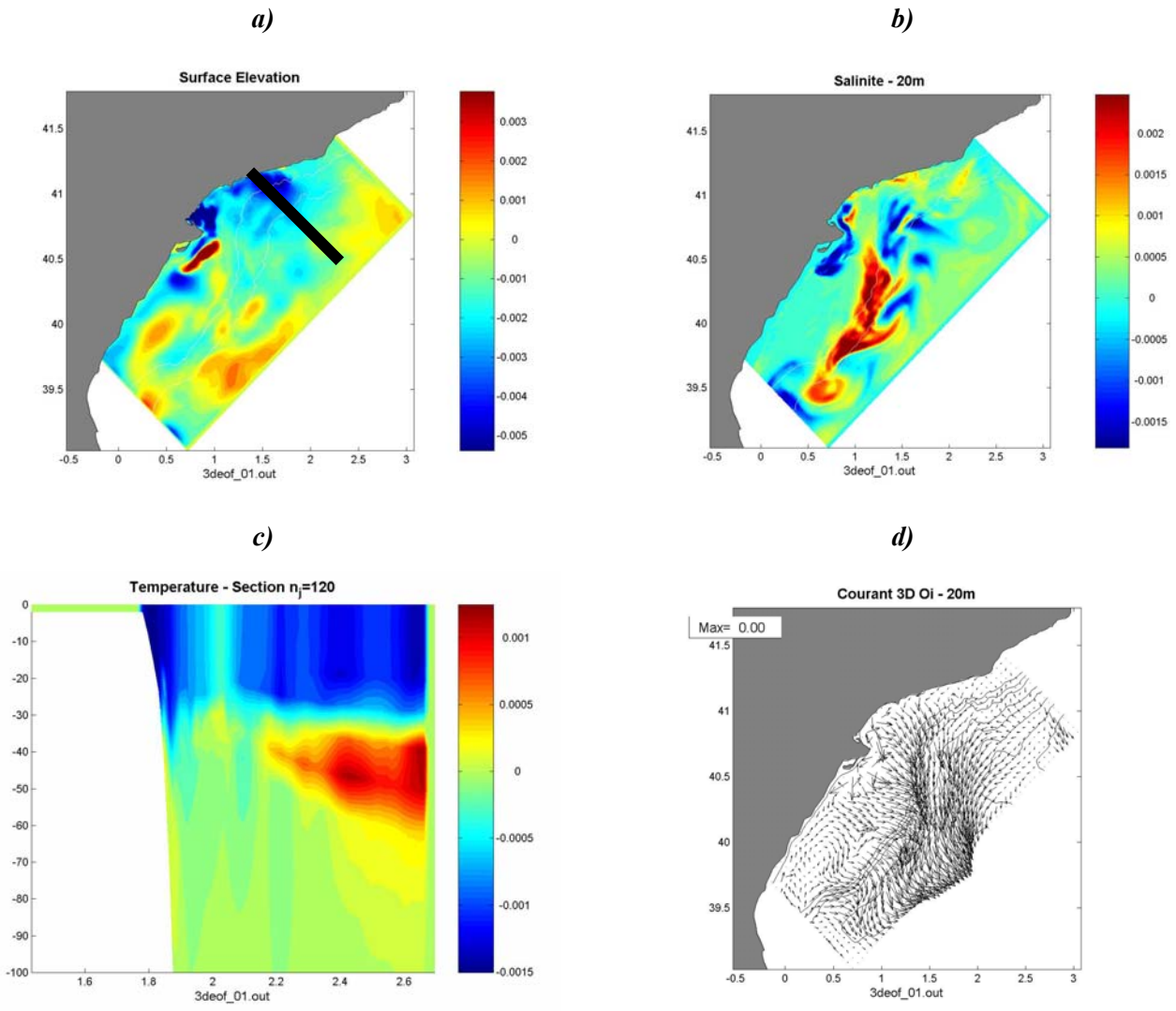

Fig 4. 32: 1st multivariate EOF from wind ensemble (ENS5). (a) Surface elevation, (b) 20m salinity, (c)Vertical section of temperature in the North (d) 20m velocity field.. The dotted line in (a) indicates the location of the vertical section in (c)

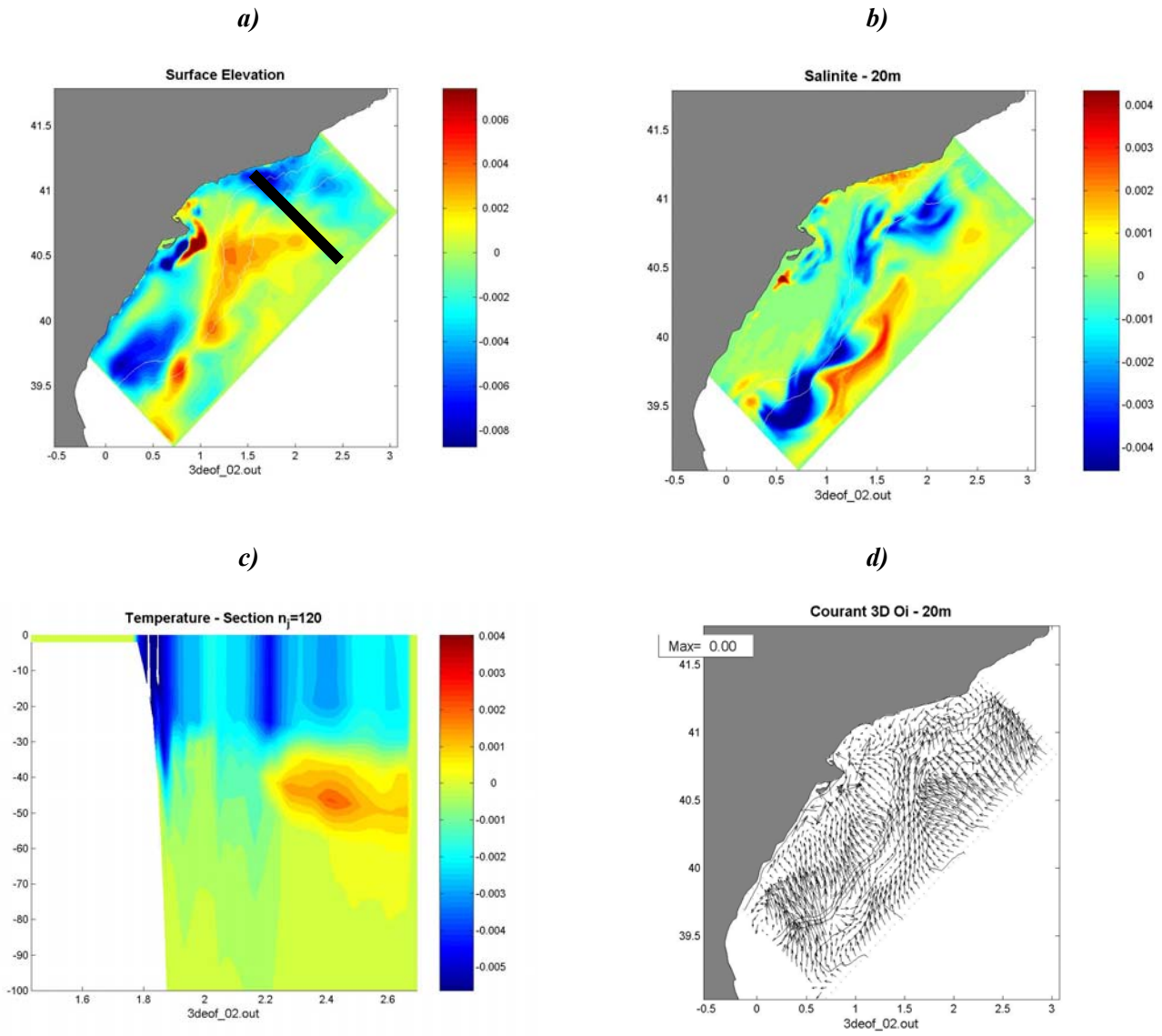

Fig 4. 33: As Fig 4. 33 but for the 2nd multivariate EOF of wind ensemble (ENS5)

4.6.3 Ensemble statistical diagnostics using EOFs

Amplitude of the modes vs. Amplitude of perturbation

An interesting diagnostic that can be done is to compare the amplitude of the EOFs for each member of the ensemble to the weight of the perturbation used to generate it. We want to see how the perturbation we introduced in the initial conditions or the forcing is distributed in the different error modes. In a perfectly linear system, we would expect a straight-line response, meaning that if the perturbation (represented by the random number) is increased, the system error (represented by the amplitude of the EOFs) will be increased in the same way.

For the current ensemble the diagrams reflects the non-linearity of the system response to perturbations of the slope current structure (see Fig 4. 34a). In fact, it seems that the modes behaves as harmonics re-inforcing the idea that they form a kind of harmonic decomposition of the current meandering. As the mode order increases, the number of zero-crossings presents in its response to the perturbation also increases. In other words, the EOF decomposition of current ensemble variability provides an harmonic base which allows to reconstruct the current meandering and its evolution in time. Obviously, the wavelength of the current oscillations that can be reproduced is fixed.

On the other hand, the wind ensemble shows a more linear behavior in good agreement with results presented in section 4.4.3. The noisy aspect of the diagrams is due to the fact that we perturb all at the wind modes at the same time, everyone with different random weight, so it is difficult to define the strength of the perturbation. In any case, it can be seen that the system response to wind errors is quite linear. Recent results in the Gulf of Lions also confirm this conclusion (S. Mangiarotti, *Personnal Communication*). An interesting issue that could be explored is that if a transfer function could be established between the wind modes and the current modes, a reconstruction of the sea state from wind forcing could be done. Obviously the results will far from perfect but maybe they would be a good first guess for assimilation purposes (for instance).

Evolution of the Forecast Error

Once the EOF base defining the error subspace is established, it is possible to estimate the evolution of the Forecast Error as a function of the ensemble members time evolution. The forecast error time evolution is useful to see how the model uncertainties evolve in the error subspace and helps us to identify which processes are stationary or which are related to special dynamical events.

a)

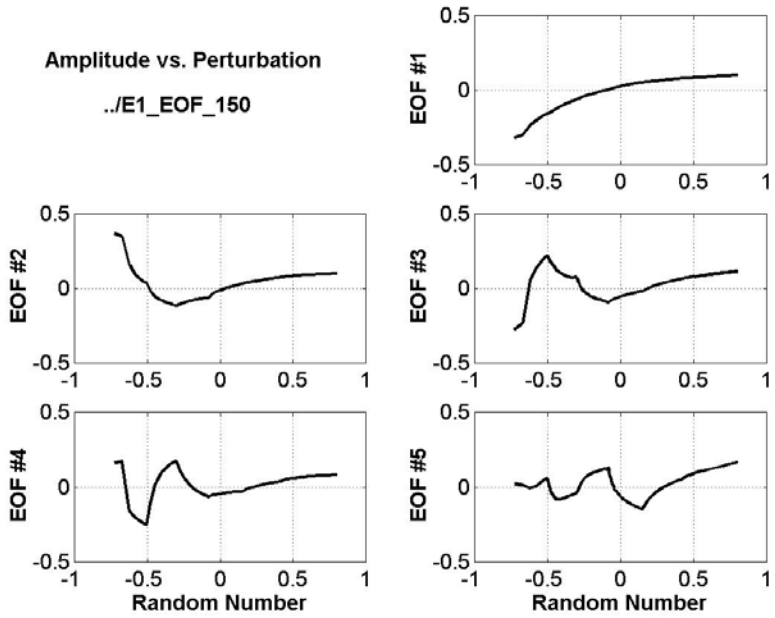

b)

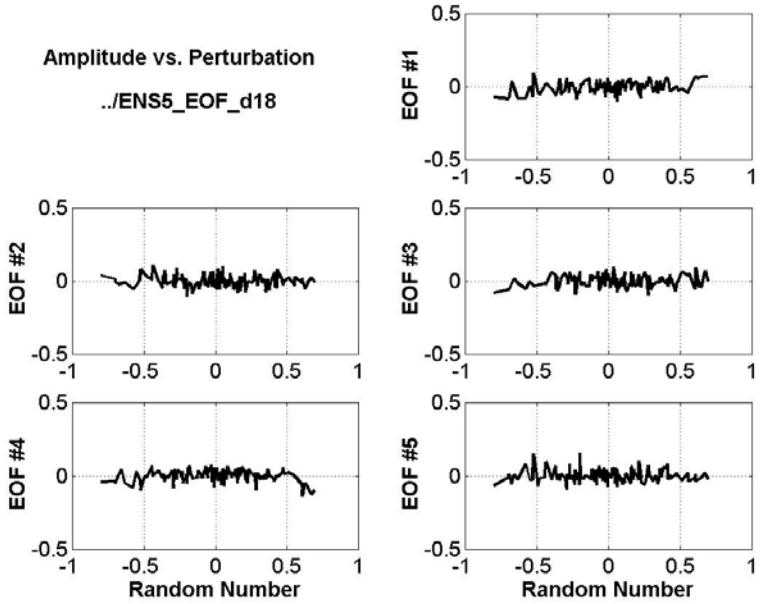

Fig 4. 34: Amplitude of the EOFs as a function of the perturbation in the(a) current ensemble and (b) wind ensemble. The computations are done with the ensemble results at February 18th (end of simulation).

To do that, we project, at different time steps, all the ensemble members over the EOF base and we compute the variance of those projections:

$$\varepsilon_j^f(t) = \frac{1}{N_{ens}} \left[\sum_{i=1}^{Nens} \left\langle \mathbf{x}_i^f(t) - \overline{\mathbf{x}}^f(t), S_j \right\rangle^2 \right]^{1/2} \qquad \textbf{(4.45)}$$

where ε_j is the forecast error associated to the j-th mode, N_{ens} is the ensemble size, <,> indicates scalar product and S_j is the j-th EOF of the base. This is equivalent to compute the eigenvalues of the EOF base at different times, so ε_j can be seen as a measure of the ensemble variance associated to a specific mode.

In the case of the current ensemble, the variance associated to each mode is quite stationary (see Fig 4. 35). The first mode is highly dominant keeping most of the ensemble variance while all the others are in a similar level. What happens is that the first mode is enough to explain the current depth changes, so to characterize the error in the current structure. The other modes, as it was shown in the previous section, are a kind of harmonics which complement the dominant mode describing the small scale features of the slope current meandering. The variance retained in those modes is slightly variable along the time which means that different modes combinations are needed to represent the evolution of the meander.

The wind ensemble case is much richer in the error forecasting time evolution (see Fig 4. 35). During the first three days, the variance levels are low and the only process triggered is almost entirely represented by the 5th mode. When Mestral blows at day 15th the other modes begin to gain importance and the global variance increases. Most of the variance induced by the wind burst is retained in the first mode with a significative contribution of 2-4th modes. When wind stops the first mode losses importance being replaced by the 3rd and 4th.

The important conclusion that must be kept from these results is that model uncertainties due to errors in the wind forcing change their regime through all the simulation. The dominant error mode changes quite fast (~1-2 days) linked to atmospheric situations.

If this variability in the eigenvalues spectra could be take into account in some way, it is probable that data assimilation will be significatively improved. In other words, if the values in the diagonal matrix $\mathbf{Br}^f$ could be linked to the physical process, the forecast error modellization could evolve in time linked to the wind regime. This approach will be explored in chapter 5.

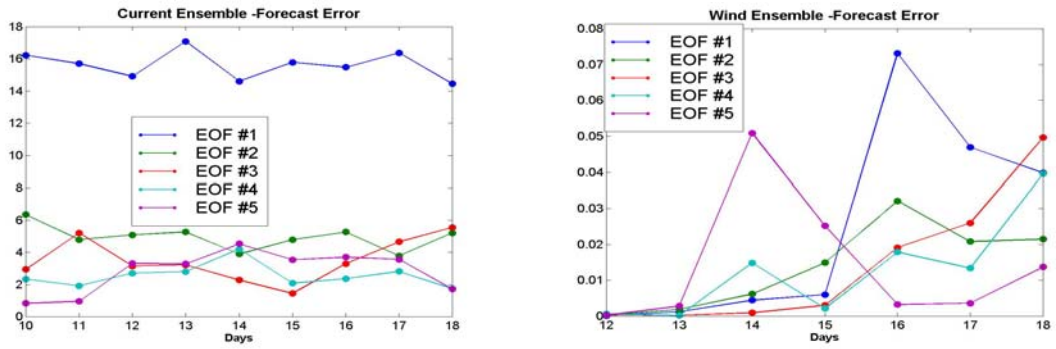

Fig 4. 35: Forecast Error time evolution for the Current Ensemble (left) and the Wind Ensemble (right)

4.7 THE EOF BASE FOR ASSIMILATION

4.7.1 What do we demand from the EOF base?

We want to define a reduced order space where the assimilation procedure will be carried on. Our choice has been to use the model error subspace to do the assimilation therein, and the way to define it is through the Empirical Orthogonal Functions obtained from ensemble simulations. During the assimilation the vector of differences between observations and model will be projected into the subspace base, i.e. the EOF base. In order to improve the data assimilation procedure we are interested into keep in that base the maximum of error processes, so the scheme could "choose" the correct one depending on the observations available.

The generation of the EOF base for assimilation can be considered from two different approaches. The first one is to generate an ensemble simulation which includes as much sources of error as possible and to compute the EOFs from that ensemble. Due to practical reasons, we assume that the error processes associated to the wind and to the current are uncorrelated (which is reasonable as it seems the EOFs of both bases are uncorrelated), so we mix the results obtained from both ensembles to generate a extended ensemble from where we compute the EOFs.

The second possibility would be to simply juxtapose the modes obtained from each ensemble (and even other modes obtained independently) to generate a sort of "toolbox" which will explicitly include the representation of different error processes. This new base $\tilde{\mathbf{S}}$ can be expressed as:

$$\begin{aligned} \tilde{\mathbf{S}} &= \mathbf{S}_{current} \left| \mathbf{S}_{wind} \right| \mathbf{S}_{others} \\ \mathbf{S}\mathbf{S}^{\mathrm{T}} &= \mathbf{I} \\ \tilde{\mathbf{S}}\tilde{\mathbf{S}}^{\mathrm{T}} &\neq \mathbf{I} \end{aligned} \qquad \textit{(4.46)}$$

where $\mathbf{S}$ is the selected EOFs from the current ensemble, the wind ensemble or other sources (i.e. a river plume mode).

The first approach is more consistent from a mathematical point of view as it provides an orthonormal base which is one requirement of the reduced order formulation. On the other hand it has the drawback that a "super-ensemble" where all the error sources are included can make difficult the isolation of error processes into different modes and, even, it can create spurious structures without a clear meaning, forcing to use a larger number of EOFs.

The second approach provides a clear distinction of the error processes as the modes have been selected "by hand". The problem is that they do not constitute an orthonormal base but several preliminary tests suggest that this is not a major problem for the assimilation.

In conclusion we have two possibilities with several advantages and drawbacks that will be explored in chapter 5. On the other hand, the juxtaposed base is straightforward to be generated

and the discussion has already been done in section 4.6.2. Now we will show the EOF base obtained from a mixed ensemble where different members of the ENS1 and ENS5 at different times have been included

4.7.2 Mixed EOFs

These EOFs have been calculated from an ensemble of 250 members where we included 100 members of the current ensemble at the initial and final time and 150 members of the wind ensemble every two days.

The spectrum of eigenvalues is again red with most of the variance (~80%) included in the first mode (see Fig 4. 36 and Fig 4. 37). The reason is that the variability associated to current ensemble members dominates in the covariance computations. This is induced by the fact that variability linked to errors in the current characteristics are present until 300-400m, while the variability associated to errors in the wind field is restricted to the first 50-80m.

In general, the EOFs obtained mixing different ensemble members are quite coincident with some of the modes obtained in the non-mixed ensembles but with different weight. The two first modes are the same than in the ENS1 EOFs (compare Fig 4. 36 with Fig 4. 30) confirming that current ensemble members dominate the variability. These modes allow to generate modifications of the vertical structure of the current and to establish the current meandering. The third mode is coincident with the first wind ensemble EOF while the 4th mode represents the influence of a Llevant (E) wind with the piling of water over the shelf. Also the combination of the third and fourth mode allows to isolate the upwelling processes in the North. The fifth mode is an harmonic of the current meandering while the combination of the 7th and 8th mode allows to represent a typical upwelling-downwelling structure al allong the coast (compare with results presented in chapter 3).

The free-surface component of the EOFs is much clearer and allows to better isolate processes than the temperature or salinity fields. One possible explanation is that the free-surface elevation quickly adjusts to different dynamical regimes without a significative "memory" of past situations. On the other hand, the temperature and salinity fields react more slowly, so they can be considered as "temporal integrators" and the final state reflects all the different processes over imposed. When combining different ensemble members, this generates a noisier covariance structures which can degrade the corrections provided by assimilation.

Finally, we wanted to comment that a red spectrum for the eigenvalues will highly condition the corrections induced by the assimilation. The projection of the distance between model and observations will be weighted over the different modes depending on the forecast error (i.e. the eigenvalues). To have a clear dominant value imply that all the corrections will have the same aspect, namely that of the dominant EOF.

In real cases, where we do not know a priori which are the real errors, maybe it would be recommendable to relax a bit this red spectrum (reducing the differences between the different eigenvalues), so giving more freedom to assimilation to adjust to the most convenient error mode. Nevertheless a warning must be given about the tempting idea of give the same forecast error to all the modes. If we were sure that each EOF represents a well define error structure, it could be attractive to leave the assimilation to choose, but we are not and to give too much weight to higher order modes will introduce noise in the correction (small scale structures).

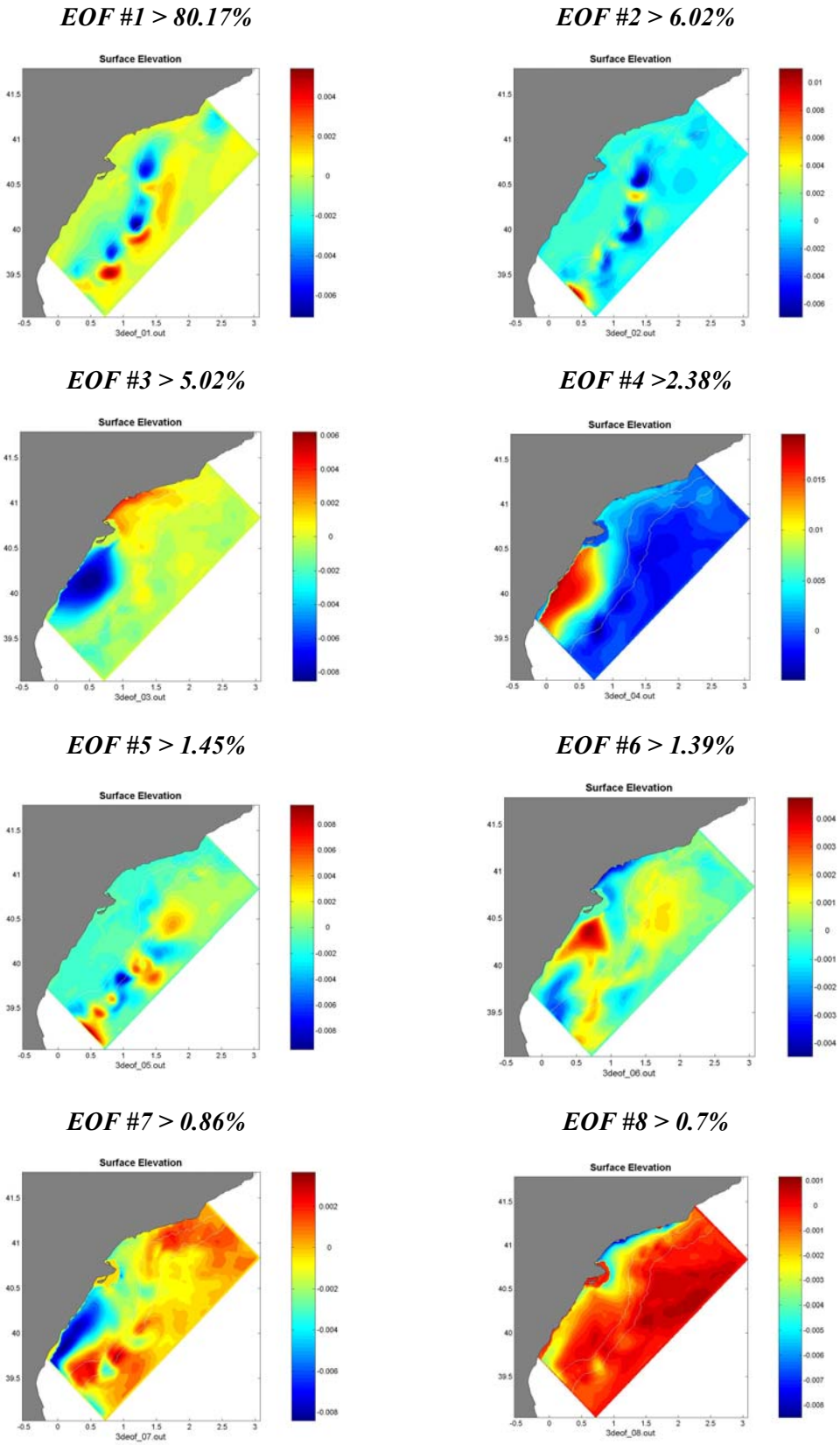

Fig 4. 36: Free surface elevation of the first eight EOFs computed from the mixed ensemble. The percentage of explained variance associated to each mode is indicated on top.

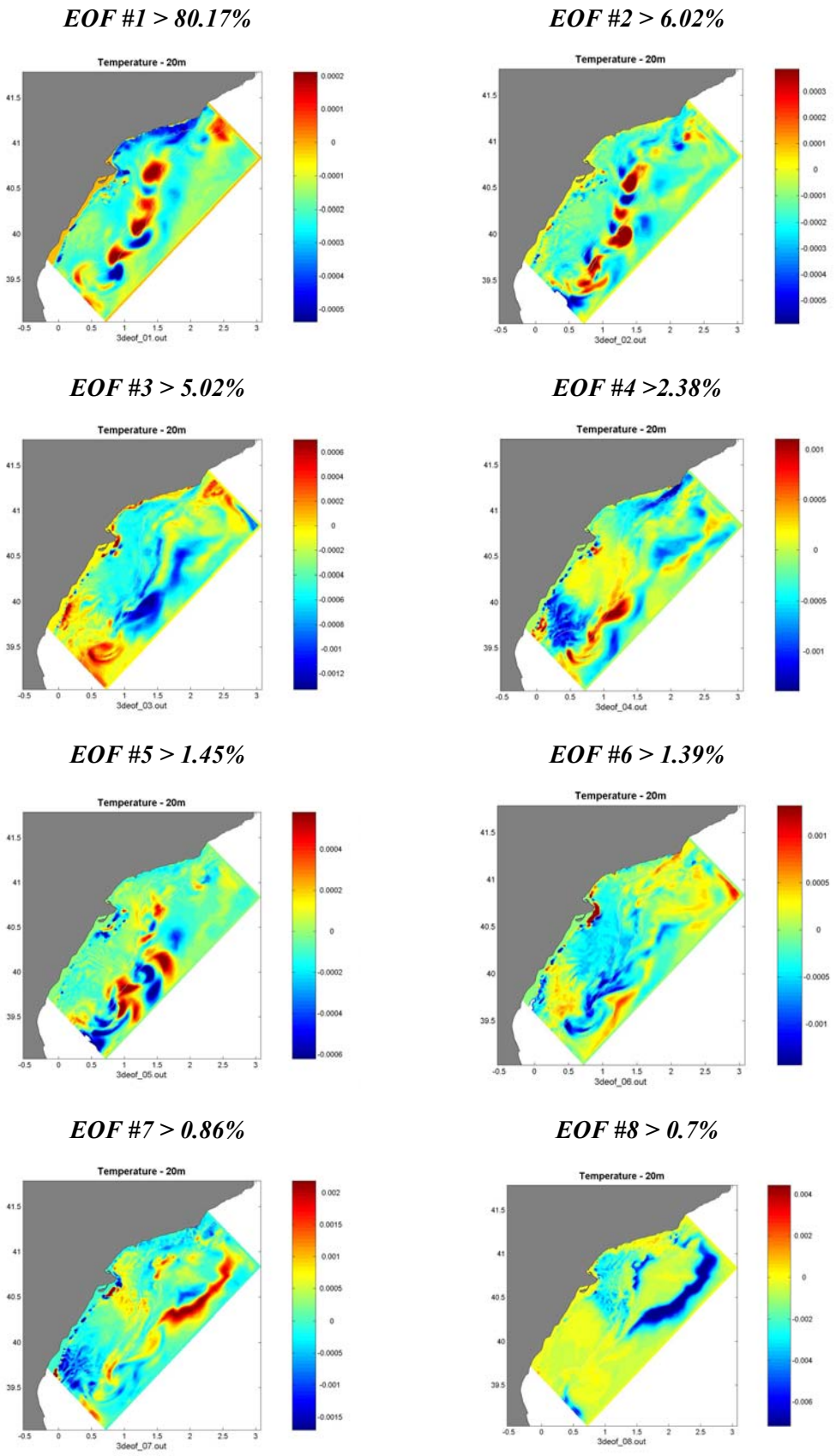

Fig 4. 37: As in Fig 4. 36 but for the temperature at 20m.

4.8 SINGLE MODE EXPERIMENTS

In order to have more insight into the properties of the selected base, we ran several Single Mode Experiments (SME). These experiments consist into compute the model correction for a single observation associated to a certain EOF and to let the corrected model state evolve with time. This kind of experiments allows us to see what the model response to the EOF base chosen is. In our case, the motivation of the SME is purely technical. We want to test stability of model after the correction, the duration of transients and the interaction with the open boundaries.

We ran a large number of SME with different combinations of observed variables, locations and observational errors but for the sake of clarity we will base our discussion in just two different configurations that will allow us to summarize the basic behaviour found in all the experiments.

In both configurations we assumed that the measurement point was located over the slope in the widening area and that the measure was temperature at 20m depth. We considered an increment between observation and model of 0.5ºC with an observational error of 0.01ºC. In the first case we used the first EOF obtained from the wind ensemble (see Fig 4. 32) while in the second we use the first EOF obtained form the current ensemble (see Fig 4. 30). A summary of the correction parameters is presented in Table 4. 5.

Measurement: Temperature at 20m in the widening area	δT=0.5ºC	ε obs = 0.01ºC
Pertur-1 > 1st EOF - ENS5 base		
Pertur-2 > 1st EOF - ENS1 base		

Table 4. 5: Summary of the parameters used in the SME

As we use a single observation the formulation of the correction is reduced to:

$$\delta \mathbf{x}_i = \frac{< T_0, \mathbf{x}_i >}{< T_0, T_0 > + \varepsilon_{obs}^2} \delta T_0 \qquad \textbf{(4.47)}$$

where $\mathbf{x}_i$ is the state vector and <,> represents covariance. In our case the covariance $<T_0,\mathbf{x}>$ is represented by the single EOF chosen.

What we realised with the SME is that with the same increment and observational error, the correction we have is strongly dependent on the EOF chosen. It can be seen in Fig 4. 38 how the correction in the two cases is quite different. When using the wind EOF, there is a increasing of

the free surface elevation over the shelf and a slight reduction of temperature at 50m depth. On the other hand, if the current EOF is used to project the correction over the model state, a meandering of the slope current is generated and the base of the current is raised from 250m to 200m with the consequent change in the density structure.

The three-dimensional aspect of the corrected field is linked with the aspect of the mode chosen. This is important to highlight as the correction is global and multivariate, and it is possible to have strong corrections of a non-observed variable far from the observational point. We have already discussed this issue previously but we wanted to remind that this is one of the main features of the use of EOFs. It can be a great advantage if the error to be corrected is included in the error subspace but if not it is a shortcoming of the method.

Another point is that the correction depends on the measurement point. Namely, it depends on the variance estimated there. When we use the statistics obtained from the wind ensemble, the variance in the point of observation is smaller than when the statistics is obtained from the current ensemble. This implies that correction will be more important in the latter case than in the former.

Finally, the magnitude of the correction also depends on various factors summarized in equation (4.47) and explained in section 4.5. In our case, where δT and ε obs are the same in both experiments, the difference is linked to the eigenvalue of the EOF chosen, which is a measure of the magnitude of the covariances. In the first case (Pertur-1) the covariances are 5 times smaller than in the second case (Pertur-2). Consequently, the corrections in the first case are much smaller than in the second one.

Once the basic features are explained, we can consider that Pertur-1 case is a typical case where the correction is reasonable. On the other hand, the correction induced by the Pertur-2 configuration is much greater and can be considered as an extreme case. Other configurations (not shown) implied still greater corrections but they were too unrealistic, so we didn't consider them. In a real case, we do not expect to have to impose a strong correction to the model. It should be kept on mind that assimilation has been formulated in a linear case, so it is intended to generate small corrections.

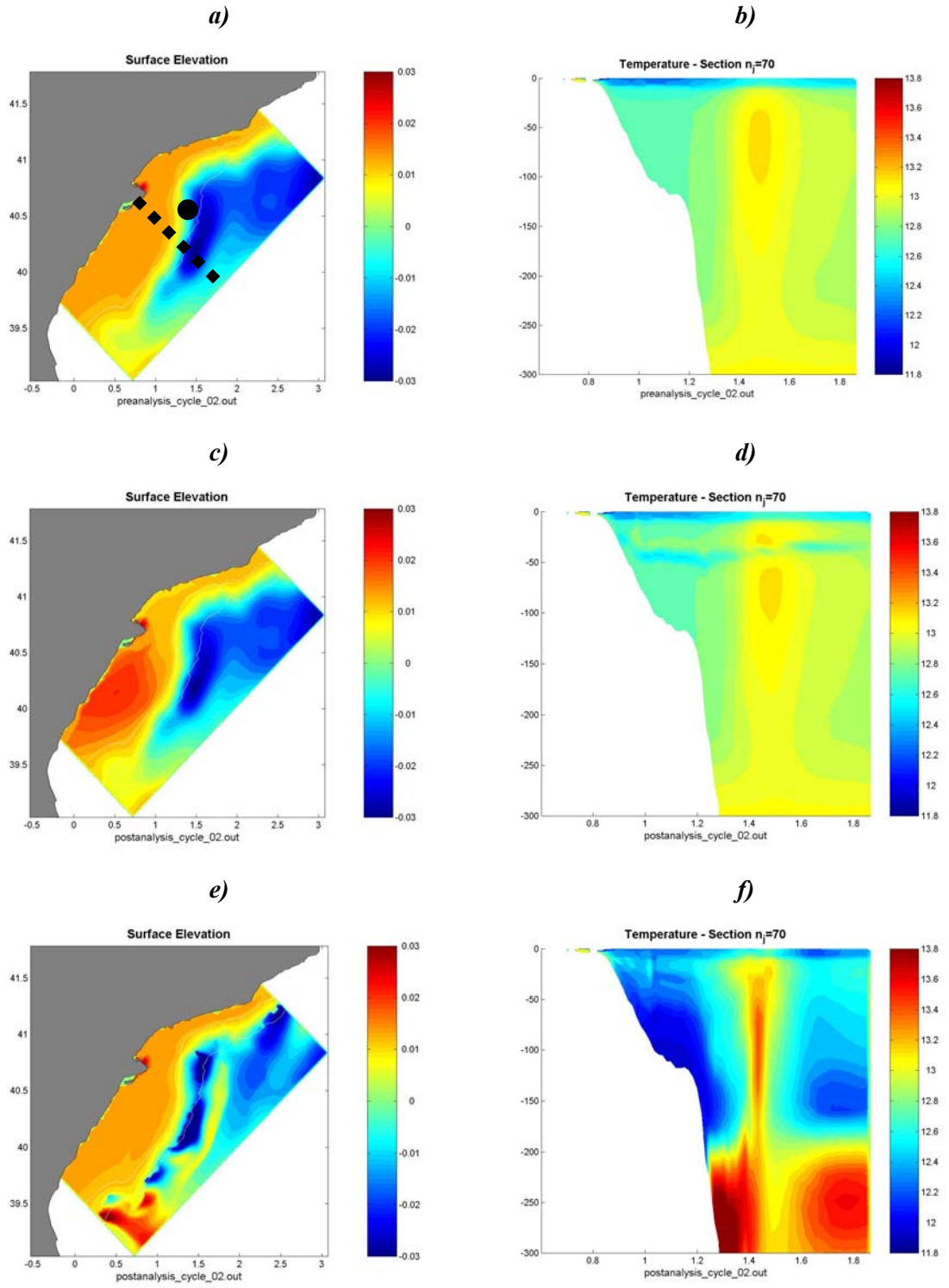

Fig 4. 38: Model state before correction (a-b), after a standard correction is applied (c-d) and after a strong correction is applied (e-f). The variables showed are free surface elevation (a,c,e) and a vertical section of temperature (b,d,f). The black dot in (a) indicates the measurement point and the dotted line shows the section location

In order to have an idea about the time evolution of the corrected model state, we look at the time series of several averaged quantities for both corrections (see Fig 4. 39). The first thing that can be seen is that, in both cases, correction induces external gravity waves which radiate away during the first day. This kind of transients has already been reported by Auclair et al. (2000) related to the initialization of a coastal model from unbalanced fields. In our case this problem is not critical as the other fields are not affected by the transient and the model behaves properly. Nevertheless, if this transient phase became a problem, a balancing method as VIFOP (Auclair et al., 2000) could be used to adjust the correction to the model dynamics.

After the correction is done the Pertur-1 case evolves smoothly following the same trajectory than the uncorrected model with just a small bias in the temperature and salinity fields. On the other hand, when the correction is important (Pertur-2), the gap between both trajectories is important. The correction generated an important change in the water masses properties as it can be seen in the time series and in Fig 4. 38. Finally it also induced a sudden increase of the kinetic energy due to a modification of the velocity field and to the subsequent baroclinic conversion of energy. Nevertheless, it must be noted that after the first two days, the model trajectories keep a constant bias in all the variables. In other words, the final state reached after the correction is in the same attractor of the model. This is probably due to the fact that the EOFs used come from the model results.

In summary it can be said that in normal conditions the model reacts well to typical corrections with slight changes of its integral quantities. In some particular cases where the correction is restricted to the river plume or when it is specially weak the model converges to the uncorrected state. In the other cases the model trajectory remains near but not exactly at the same place than the uncorrected one.

Strong corrections are not expected but if they are present they can induce a model blow up. It has been also found that strongly corrected model trajectories can also evolve near the original model trajectory, meaning that they are still in the same model attractor.

A comment that arises from the SME analysis is that the use of a single observation (or a reduced number of them) is a danger that must be avoided. An insufficient number of measurements will imply that the assimilation system will not be able to properly select the EOFs to project the correction and the result can be unphysical.

Finally, we want to mention that the use of model EOFs to project the correction enhance the stability of the corrected model and allows, in most of the cases, to keep some properties as the trends or the integral quantities near unaltered

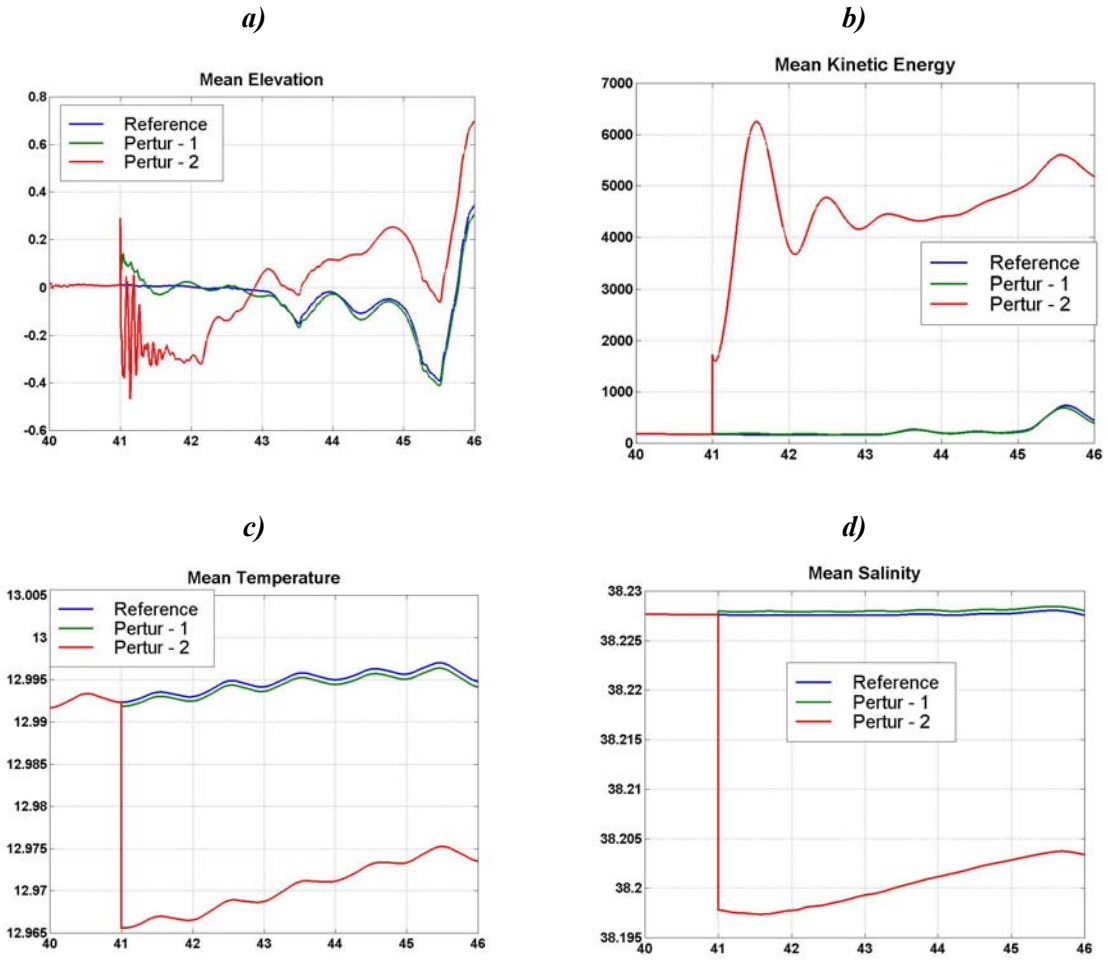

Fig 4. 39: Time evolution of some averaged variables in the reference case (blue), when a typical perturbation is applied (green) and when a strong correction is applied (red). The represented variables are (a) mean free surface elevation (b) mean kinetic energy (c) mean temperature and (d) mean salinity.

4.9 CONCLUSIONS

The goal of this chapter is to setup a data assimilation system well suited for coastal and shelf applications. In our case, we have chosen the SEQUOIA data assimilation system with the MANTA analysis kernel which is based in a Reduced Order Optimal Interpolation scheme where the order reduction is done using 3D EOFs. In our implementation those EOFs have been obtained from ensemble modelling.

After the work carried on in chapters 2 and 3, we have identified the main sources of error as the characterization of the slope current and the wind field, which are two of the main dominant physical features in the region. We have also selected several dynamical conditions (wind regime, stratification, current depth) and we have run several ensembles in those different

scenarios perturbing the characteristics of the current and the wind field. We have found that different scenarios lead to similar structures of error.

When current characteristics are perturbed the variability structures are associated to the current meandering. The final ensemble distributions are asymmetrical due to the different response of the slope current if it is shallower or deeper than the shelf break. The dispersion in the results due to errors in the current has been found to be highly stationary as it is linked to quasi-geostrophic structures which are very stable.

When errors in the wind field have been considered, all the dispersion of the results concentrates in the surface mixed layer. The distributions therein are highly simmetric showing a Gaussian behaviour. On the other hand, the error structures are linked to the specific wind regime, so being non-stationary. The time evolution of those structures has been found to be fast (~1-2 days) and with a low rate of "memory" (the different states forget their initial conditions in 2-days).

The ensemble simulations allow us to obtain the representers which are a way to measure the influence of a given variable in a given location over all the other model variables. Our results confirm the results found by Echevin et al. (1999) and Mourre et al. (2004) where the representers showed an anisotropic and non-homogeneous behaviour and even non-stationarity. In addition to that, we find that those influence functions depend on the error process where the statistics is based. The processes linked to the slope current induce a clear separation between shelf and open sea while the processes linked to the wind have a more complicated structures depending on the region and the wind regime.

The ensemble covariances have been used to compute the EOFs. In both ensembles, the eigenvalues spectrum is quite red and few EOFs (~5) captures almost 99% of the variance. The current ensemble EOFs basically represent the different 3D density structures associated to different slope current depths and the meandering of the slope current. As it was expected the wind ensemble EOFs are non stationary and their aspect depends on the wind regime.

For assimilation purposes, a new EOF base has been created mixing members of both ensembles at different times in order to capture the maximum number of dynamical processes.

Finally, several Single Mode Experiments have been carried on in order to test the stability, advantages and shortcomings of the approach chosen. In normal conditions the corrections induced in the model are well assumed and the model doesn't diverge. On the other hand, strong corrections can significatively change the model trajectory but without going out of the model attractor. Obviously, exaggerated corrections lead to dynamical inconsistencies that the model is not able to assume.

DATA ASSIMILATION IN THE EBRE REGION.
PERFORMANCE OF DIFFERENT OBSERVATIONAL NETWORKS

"Much less errors are made using
wrong data that using no data at all"
(Charles Babbage)

5 DATA ASSIMILATION IN THE EBRE REGION. PERFORMANCE OF DIFFERENT OBSERVATIONAL NETWORKS

5.1 Introduction

Once the error dynamics has been characterized, we can implement and evaluate the data assimilation scheme presented in chapter 4. We want to have an insight into its characteristics and its performance depending on the choices adopted and, although we work in a particular region, we expect the conclusions can be extrapolated to other regions or other implementations of the system.

The framework is the study of the performance of several observational networks for correcting errors in the wind and the slope current. We are interested in comparing how different networks among the possible configurations would perform, and how the information provided by them could be used to correct the model trajectories.

First of all, in section 5.2, the assimilation procedure and the experiments protocol are presented. Then, we present the analysis tools used to diagnose the skills of the assimilation in the different contexts (section 5.3) and the set of observational networks that will be tested (section 5.4). In the following sections (5.5-5.7) we show the results in three different regimes where the errors are linked to the slope current characterization, the wind uncertainties or a mixed situation, respectively. Afterwards, in order to gain insight into the characteristics of the assimilation and its limitations, we perform several sensitivity tests (section 5.8). Finally we discuss the main results in section 5.9 and present the conclusion in section 5.10.

5.2 Experiments protocol

As it was presented in the previous chapter, SEQUOIA is a data assimilation system, which has been designed to manage all the steps of the assimilation procedure. It manages the data available for the assimilation, controls the forecast stage integrating the model forward in time and the analysis stage computing the correction of the model state depending on the differences between model-observation and the error forecasting scheme chosen. The analysis stage is done in the analysis kernel, which can be exchanged or improved in different implementations. In our case we use the MANTA kernel, which is a Reduced Order scheme. The error forecasting scheme is replaced by stationary reduced-order statistics inferred from ensemble modelling. In consequence, the implementation we use is a Reduced Order Optimal Interpolation. To help the

discussion in the chapter, Table 5. 1 summarizes the definitions used in the data assimilation framework.

Formule	*Description*
$\mathbf{x}^{\mathbf{f}}$	Model state vector
$\mathbf{y}^{\mathbf{0}}$	Observation vector
$\mathbf{S}$	Reduction operator formed with the multivariate EOFs
$\mathbf{Hr} = \mathbf{HS}^{\mathbf{T}}$	Reduced order observation operator
$\mathbf{d} = \mathbf{y}^{\mathbf{o}} - \mathbf{Hr}\,\mathbf{x}^{f}$	Difference between the observations and the model state in the observation space
$\delta\mathbf{x}^{f} = \mathbf{K}^{ROOI}\,\mathbf{d}$	Correction of the model state
$\mathbf{Kr} = \left(\mathbf{Br}^{f}\right)^{1/2}\left(\mathbf{I} + \boldsymbol{\rho}\mathbf{r}\,\mathbf{Rr}^{-1}\boldsymbol{\rho}\mathbf{r}^{\mathbf{T}}\right)^{-1}\boldsymbol{\rho}\mathbf{r}$	Gain Matrix in the reduced order space
$\mathbf{B} = \mathbf{S}^{\mathbf{T}}\,\mathbf{Br}\,\mathbf{S}$	Background error covariance matrix
$\mathbf{Rr} = \mathbf{R} + \bar{\mathbf{H}}\mathbf{r}\bar{\mathbf{B}}\mathbf{r}\bar{\mathbf{H}}\mathbf{r}^{\mathbf{T}}$	Observational error covariance matrix
$\boldsymbol{\rho}\mathbf{r} \equiv \left(\mathbf{Br}^{f}\right)^{1/2}\mathbf{Hr}^{\mathbf{T}}$	Reduced-order representer matrix

Table 5. 1: Summary of definitions used in the chapter.

The assimilation procedure is presented in the Fig 5. 1. During an assimilation cycle ($t \in (t_1, t_3)$) all the available data is compared with the model results and the differences $\mathbf{d} = \mathbf{y}^{\mathbf{o}} - \mathbf{H}\,\mathbf{x}^{f}$ are stored in memory. At the end of the cycle, all the differences in **d** are used to compute the model correction at time t_2. The corrected model state is then integrated again forward in time in the next assimilation cycle in an iterative procedure.

SEQUOIA can work in two different modes: filter or smoother. In the ***filter*** mode, t_2=t_3 (see Fig 5. 1a), the correction of model state is done at the end of the cycle, so the analysis is done using past data. In the ***smoother*** mode $t_1 < t_2 < t_3$ (see Fig 5. 1b), the model correction is done at t_2 using past and future data (between t_1 and t_3). It must be noted that in this case the data between t_2 and t_3 is re-used in the following assimilation cycle.

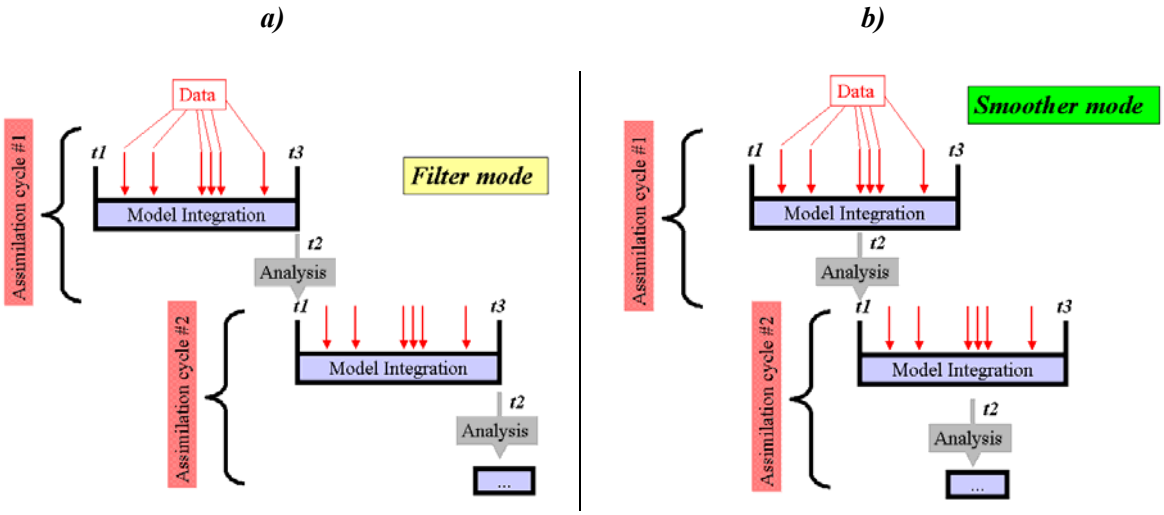

Fig 5. 1: Sketch of the assimilation in the (a) filter mode and the (b) smoother mode.

There are several parameters and variables that must be prescribed by the user and, as it will be shown later, will have a strong impact into the assimilation performance.

The first is the length of the assimilation window, which in this implementation is set constant during all the assimilation procedure. This parameter has a significant importance and it should be chosen carefully. First of all it must not be forgotten that the MANTA kernel doesn't consider the "age" of the observations. Each difference d_i is calculated at the right time but there is no covariance decay with time. This is equivalent to considered than all the distances d_i are representative of the same error structure. If the assimilation cycle is too long this can causes a problem: the information contained in the older observations could not be significant to correct the model state long time after. On the other hand, the system needs enough data to be able to project the information into the correct set of EOFs, so too short assimilation cycle could be counterproductive.

The second thing that must be prescribed is the form of the reduction operator S (see equation 4.16) and the forecast errors in the diagonal matrix Br^f. This information is obtained from the EOF decomposition presented in the previous chapter. The reduction operator S is formed by the spatial modes of the EOF base, which will establish the spatial structure of the error modes. The variances of forecast errors in the reduced order space are obtained from the corresponding eigenvalues λ_i being $\sigma_i^f = \sqrt{\lambda_i}$. These are a measure of the variance associated to each error mode, so giving a measure of the error associated to each mode. When the correction in the reduced order space will be established, they will play the role of weight the different EOFs.

Finally, the data that will be used must be provided to the system as well as the observational errors associated to the measurements.

In our case we work in a twin experiments framework where the truth is considered to be a reference simulation (the ***control run***). In order to simulate different observational networks, different kinds of data in different locations are obtained from this run and perturbed adding white noise with a null mean and variance consistent with the observational error prescribed. A second run with different initial conditions and/or wind forcing is used as the ***free run***. This run is the one that is intended to be corrected with the assimilation. The simulation where data is assimilated will be called the ***assimilated run***.

In the basic configuration, the system is run in the smoother mode with an assimilation cycle of 4 days. The procedure begins in February 10th and data is assimilated during 8 days until February 18th. Afterwards, the model runs without any assimilation from day 18th to day 26th in order to evaluate the persistence of the correction provided by each network.

The assimilation experiments will be run in different scenarios to test the performance in various error regimes. Namely, these are the current errors, the wind errors and the mixed errors.

· In the ***current errors regime***, the free and control runs are members of the current ensemble (ENS1) and the EOFs used are those obtained from that ensemble.

· In an analogous way, in the ***wind errors regime*** the free and the control run and the EOFs are obtained from the wind ensemble (ENS7). Finally, we are interested into test the system performance in a more complex situation where both kinds of errors are present.

· In the ***mixed errors regime***, the control run is a member of the current ensemble and the free run a member of the wind ensemble. In other words, both runs differs in the initial conditions (the characterization of the slope current) and the wind forcing applied. The EOFs used are the mixed base where members of both ensembles have been used to generate it.

The original idea behind MANTA is to provide a data assimilation scheme cheap (necessary for operational purposes) and yet physically consistent and multivariate. This last part is ensured with the use of the multivariate EOFs. On the other hand, in the present configuration, the assimilation step costs, in average, the 10% of the computer time needed for one day of simulation. Namely all the assimilation experiment needs 11h22' in the smoother mode and 5h46' in the filter mode.

5.3 Diagnostic tools

The analysis of the results can be done from different points of view depending on what the parameters of interest are. It is not possible to find a unique magnitude that measures in an absolute way the quality of the assimilation system or the skills of an observational network. In consequence we use different analysis tools to evaluate the quality of the results.

The data assimilation is a technique that tries to bring the model trajectory close to the observations minimizing the distance between them from a statistical point of view, so it is natural that the parameters used to evaluate the quality of the experiments are also statistical.

RMS and Correlation

The first parameter that is usually introduced is the root mean square distance (rmsd, E). It measures the distance between the model results and the truth, which in our case they are the assimilated run and the control run. The rmsd is defined as:

$$rmsd(A,B) \equiv E_{A-B} = \frac{1}{n}\sqrt{\sum_{j=1}^{n}\left(\phi_A^j - \phi_B^j\right)^2} \qquad (5.1)$$

where ϕ is a certain field, A and B are the two states that will be compared, j represents each point where fields are compared (in our case they are the grid points) and n is the dimension of the model state (in our case the number of grid points).

The RMS gives an absolute measure of the distance between the two fields and we compute them for each variable as it is expected that different measures will have a different impact in each variable of the model.

Another parameter that is useful is the correlation (R) between two fields. It is defined as:

$$corr(A,B) \equiv R_{A-B} = \frac{1}{n}\frac{\sum_{j=1}^{n}\left(\phi_A^j - \overline{\phi}_A\right)\left(\phi_B^j - \overline{\phi}_B\right)}{\sigma_A \sigma_B} \qquad (5.2)$$

where σ represents the standard deviation of the field ϕ.

The correlation measures the coincidence of the spatial patterns between two fields. It is interesting to note that a perfect correlation (corr ~1) doesn't imply that both fields are exactly the same. It means that the structures are identical but it can be that the magnitudes are quite different. At the same time, a low value of the rms doesn't imply that both fields have the same structure, so although both parameters give a valuable objective information it is important to not focus just on them to evaluate the results.

As the assimilation takes place in several assimilation cycles we will look at the time evolution of the rms and correlation. To compare the performance of different observational networks we will also use the ratio of rms (correlation) of a given experiment by respect to the rms (correlation) of the experiment without assimilation, so values lower (greater) than 1 will imply an improvement (worsening) of the results.

The Taylor diagram

Another way to summarize the performance of different experiments in a single diagram is the Taylor diagram (Taylor, 2001) and an example can be found in Fig 5. 11.In this kind of

diagram, a polar plot is used where the angle represents the degree of correlation and is usually defined between -1 and 1. In our case, and due to the short duration of the runs and the special way the members have been initialized, the correlation values are always near 1, so the azimuthal limits will be zoomed to clearer represent the set of data. In the radial direction it is represented the ratio of model standard deviation respect the standard deviation of the reference (the control run): $\gamma = \frac{\sigma_{assim}}{\sigma_{ref}}$

In fact, with these two parameters, a good description of the model performance can be provided. The correlation gives, as it was mentioned before, an idea of the coincidence of spatial patterns. The ratio of standard deviations γ gives a measure of the relation between magnitudes in both fields.

As the RMS is the typical parameter to define the quality of a model result it could be useful to include it in the diagram. In fact there is a relation between the RMS, the correlation and the parameter γ. Following Taylor (2001):

$$E' = \sigma_A^2 + \sigma_B^2 - 2\sigma_A\sigma_B R \qquad (5.3)$$

where E' is the centered pattern of correlation where the difference between mean fields of A and B have been removed. This is $E^2 = \overline{E}^2 + E'^2$ and $\overline{E} = \overline{\phi}_A - \overline{\phi}_B$.

In consequence, isolines of rms could be overimposed in the Taylor diagrams. It must be noted that other parameters could be defined to measure the skills of the experiments. If the correlation between structures is more important than the magnitudes (or viceversa) other expressions could be used (i.e: see Taylor, 2001).

T-S census

The assimilation process could significantly modify the water mass structure represented in the model. On the other hand, as we are working in a limited area in short time periods, we do not expect to need to alter the distribution of water masses to much (heat fluxes and advection have no time to effectively act). To diagnose if this happens we use a 3D T-S diagram where a census is performed. We define different T-S classes and plot the volume of each class to clearly see if some different water masses have been introduced (see Fig 5. 6). It is undoubted that in larger domains or longer simulations these kind of diagrams would become much more useful to understand the effects of assimilation.

Structure of correction in the reduced order space

In the analysis step the correction of the model state (δx) is done in the reduced order space (dx_{ro}). The distances d_i between model and observations are projected over the 3D multivariate EOFs that conform the reduction operator S to find the best combination of error modes, which

adjusts to the distances. In consequence, it could be useful to look to this projection to see which are the modes used to create the correction and compare it between the different observational networks to better understand their behaviour.

Observability of the error subspace

The knowledge of the forecast error structure allow us to have an idea of its observability by the different observational networks. As it was shown in the previous chapter, we can introduce the representers in the equations of the gain matrix which represent the influence structure of a given measurement or set of measurements. The expression of the representers in the reduced order space is

$$\boldsymbol{\rho r} \equiv \left(\mathbf{Br}^{f}\right)^{1/2} \mathbf{Hr}^{\mathbf{T}} \qquad (5.4)$$

where the forecast errors are included in matrix $\mathbf{Br^f}$ and the characteristics of the observational network is described by the observation operator in the reduced space **Hr**.

Assuming this, it can be easily seen that the correction of the model state as a function of the distances model-observations d_i, expressed as a vector **d,** and the forecast error and observation error covariance matrices is:

$$\delta \mathbf{x} = \frac{\mathbf{Br}^{f}\mathbf{Hr}^{\mathbf{T}}}{\mathbf{HrBr}^{f}\mathbf{Hr}^{\mathbf{T}} + \mathbf{R}}\mathbf{d} \qquad (5.5)$$

Depending on the relation between both terms in the denominator, the correction will be more or less important. In particular, if the product $\mathbf{HrBrHr^T} << \mathbf{R}$, the correction will tend to zero. In other words, if the forecast error that can be seen by the observations were much smaller than the observational error the system would not correct anything.

To compare both terms we can construct a new matrix :

$$\chi = \mathbf{R}^{-1/2}\mathbf{HrBr}^{f}\mathbf{Hr}^{\mathbf{T}}\mathbf{R}^{-1/2} \qquad (5.6)$$

and using equation (5.4):

$$\chi = \mathbf{R}^{-1/2}\boldsymbol{\rho}\mathbf{r}^{\mathbf{T}}\boldsymbol{\rho}\mathbf{r}\mathbf{R}^{-1/2} \qquad (5.7)$$

Inspired in the work of Bennett et al. (2000), we can compute the eigenvalues of this matrix and compare them to unity to see how many forecast error degrees of freedom can be constrained by observations. In our case we will equate these forecast error degrees of freedom with the number of error EOFs that could be constrained by the different networks. It must be noted that the results depend both on the characteristics of the network and on the error statistics which is represented by the EOFs. This last point is quite logical if we consider than errors induced by the wind field or by the slope current don't necessarily have the same structure, so

the same network can better perform for one kind of errors than the other (i.e. deep measurements could not correct the effects of the wrong wind fields).

In section 5.4 we compute the spectrum of the *scaled representer matrix* χ for the different networks and error regimes.

Diagnostic of the cost function minimum

The base of the data assimilation scheme is the BLUE (Best Linear Unbiased Estimation). This estimation can be formally obtained from the minimization of a cost function (J) that measures the distances between the model state and the observations.

This is:

$$\frac{\delta J}{\delta \mathbf{x}^a} = \mathbf{0} \qquad (5.8)$$

where the cost function of the analysed state can be expressed as the addition of two terms: the measure of the distance between the analysed state and the background field (which in our case is the forecast field) and the distance between the analysed state and the observations:

$$J(\mathbf{x}^a) = \frac{1}{2}\left[\left(\mathbf{x}^a - \mathbf{x}^f\right)^T \left(\mathbf{B}^f\right)^{-1} \left(\mathbf{x}^a - \mathbf{x}^f\right) + \left(\mathbf{H}\mathbf{x}^a - \mathbf{y}^o\right)^T \mathbf{R}^{-1} \left(\mathbf{H}\mathbf{x}^a - \mathbf{y}^o\right)\right] \qquad (5.9)$$

$$J(\mathbf{x}^a) = J_b(\mathbf{x}^a) + J_o(\mathbf{x}^a)$$

Following Talagrand (1998) and Sadiki (2005), an expression for the statistical expectation of the cost function can be deduced. Talagrand found that the expectation of the term, which represents the distance to the observations, J_o is:

$$E\left[J_o(\mathbf{x}^a)\right] = \frac{1}{2} Tr\left(\mathbf{I}_{p*p} - \mathbf{HK}\right) \qquad (5.10)$$

where **K** is the gain matrix and $\mathbf{I_{p*p}}$ is the identity matrix with dimension p (the number of observations).

On the other hand, the statistical expectation for the term that represents the distance of the analysed field to the background, J_b is:

$$E\left[J_b(\mathbf{x}^a)\right] = \frac{1}{2} Tr\left(\mathbf{KH}\right) \qquad (5.11)$$

Combining both, it is found that:

$$E\left[J(\mathbf{x}^a)\right] = E\left[J_b(\mathbf{x}^a)\right] + E\left[J_o(\mathbf{x}^a)\right] = \frac{1}{2} Tr\left(\mathbf{I}_{p*p}\right) = \frac{p}{2} \qquad (5.12)$$

This indicates that the minimum of the cost function (in a statistical framework) would be proportional to the number of observations if the error statistics (both the forecast and

observation) is properly described. On the other hand, the deviations from this value will be the sign that a bad definition of the covariance error matrices has been done.

5.4 Observational networks

The different observational networks considered here have been chosen to be representative of the most used configurations in observational systems both for research and operational purposes. We try to combine the different factors that are usually taken into account when the networks are designed: the spatial coverage, the time needed to complete the measurements and the cost of the survey. Obviously, the details of each network could be redefined but we do not expect that they change the main conclusions.

The first configuration considered is the ***classic*** network, representative of a typical research survey with CTD and ADCP. The CTD measures temperature and conductivity (which is transferred to salinity) with a high degree of accuracy reaching deep levels (usually it is get down until near the bottom). Although it measures continuously, its measures are averaged in vertical bins of 5m. This accuracy and vertical coverage and the fact that the ship must be stopped in each station make this configuration to take a long time to be completed. To complement the temperature and salinity data, velocity measurements are usually obtained with an ADCP (Acoustic Doppler Current Profiler) mounted in the vessel. Its configuration can be highly variable but in a standard set up it measures velocities until 300m with a vertical resolution of 16m. It has a significant error both in the current intensities and directions, greater than a typical current meter. We have considered the same stations map used in the FANS project with 98 stations covering the shelf and slope region near the Ebre delta (see Fig 5. 3) in 6 days.

An alternative to the typical CTD based campaigns is presented with the use of the ν-shuttle. This instrument is an ondulating CTD (similar to the SeaSoar), which is dragged by the ship while it goes up and down (an sketch of this procedure is presented in Fig 5. 2). It measures temperature and conductivity continuously in the first 150m of the water column with less precision than the classic CTD. On the other hand it provides a good spatial coverage as it ascending/descending velocity is around 20m/minute and can operate with the vessel moving at 6-9 knots. As the ship doesn't need to stop the campaigns based in the ν-shuttle are much faster than those based in the CTD. The ***fast*** network defined here covers all the slope and part of the shelf in the Ebre region area (see Fig 5. 3) doing 250 profiles in 2 days. The temperature and salinity measurements are complemented with the same ADCP measurements presented in the classic network.

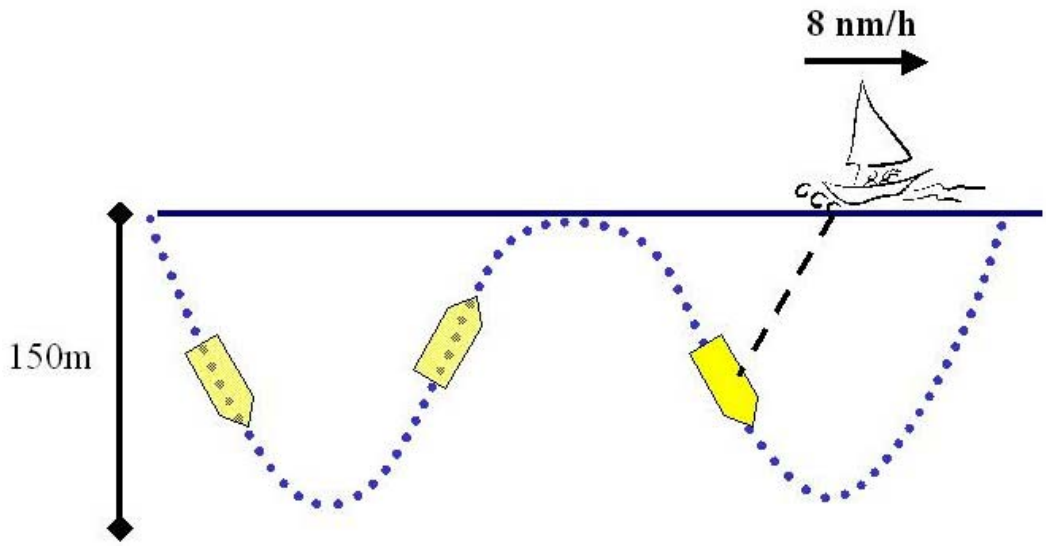

Fig 5. 2: Sketch of the undulating CTD operation.

The works in the sea are usually expensive and some times cheaper alternatives must be considered. In our case we have define a ***cheap*** network, which consists on ν-shuttle and ADCP measurements taken into a limited area around the Barcelona harbor. As the area to cover is small and all the procedure could be finished in few hours, it could be done in a vessel smaller than the previous networks, so reducing the costs. We have also considered that this survey is repeated one week later the first one. The ship trajectory is showed in Fig 5. 3 and 54 profiles are obtained in 12 hours of work.

The next configuration proposed is the one based in the moorings measuring currents and temperature at different depths in a continuous way. In the operational networks the mooring lines represent one of the most popular alternatives as it can be relatively easy implemented and can provide data in near-real time during long periods. The problem is that they provide punctual measurements, which could be insufficient to sample complex structures. On the other hand the continuous behavior of their measurements is an attractive counterpart. Our ***cmeter*** network is formed by 5 mooring lines, which measure currents and temperatures every hour at four depths (5-50-100 and 300m) over the slope and at two depths (15-50m) over the shelf. We have placed three mooring lines over the slope upstream, over and downstream the shelf widening and two more over the wide shelf.

Identifier	*Main characteristics*	*Spatial coverage*
CLASSIC	*CTD +ADCP* *Done in 6 days*	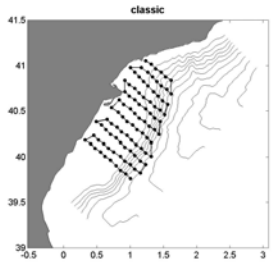
FAST	*SEASOAR +ADCP* *Done in 2 days*	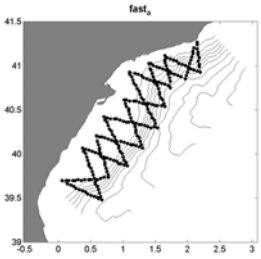
CHEAP	*SEASOAR +ADCP* *Done in 12 hours* *Repeated one week later*	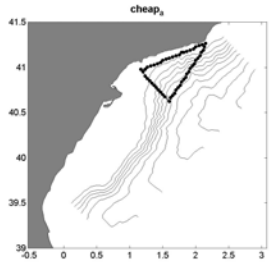
CMETER	*Moorings measuring Temperature and Currents at 5 depths every hour.*	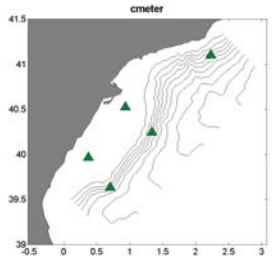
SATELLITE	*SST + ALTIMETER* *Daily SST and weekly altimetry*	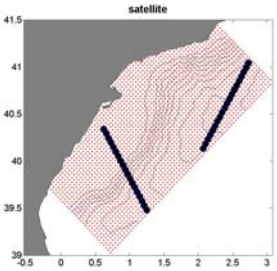

Fig 5. 3: Summary of the observational networks considered.

Finally we wanted to test the performance of satellite data. These data could be used to complement any of the previous networks but we prefer to consider it separate to evaluate its single contribution. The ***satellite*** network is formed by daily SST data covering all the domain with high resolution (1km) and weekly altimeter data provided over the two altimeter tracks that cross our domain (see Fig 5. 3). This configuration is obviously the cheapest one and the data can be obtained in near-real time with good temporal and spatial resolution, but it just provides surface information.

The observational error definition is a key issue into the data assimilation procedure as it has been shown in the previous chapter. The reliability of the data conditions the correction done in the analysis stage: better measurements have bigger influence than worst ones. On the other hand, the observational errors covariance matrix R contains several contributions as it was commented in section 4.1. Loosely speaking it could be said that R measures the distances between the observations and the best approximation of the model in the observational space. So, there are the instrumental errors, what is usually considered as the errors of precision (F), the representativity errors (E) and also the errors in the observation operator (E_H). In addition to that, the assimilation procedure is done in a reduced order space, so the errors done truncating the space must also be included. Re-writing equation 4.20 this is:

$$\mathbf{Rr} = \mathbf{R} + \bar{\mathbf{H}}\mathbf{r}\bar{\mathbf{B}}\mathbf{r}\bar{\mathbf{H}}\mathbf{r}^{\mathbf{T}} \qquad (5.13)$$

In conclusion, the error covariance matrix must include not just the instrumental errors, but also all the other contributions that separates the observations $\mathbf{y^0}$ from the projection of the true model state in the observational space $\mathbf{Hx^t}$.

$$\mathbf{Rr} = \mathbf{F} + \mathbf{E} + \mathbf{E_H} + \bar{\mathbf{H}}\mathbf{r}\bar{\mathbf{B}}\mathbf{r}\bar{\mathbf{H}}\mathbf{r}^{\mathbf{T}} \qquad (5.14)$$

For the instrumental errors we use the known precision of each instrument while for the rest of the contributions we have no information at all, so the estimation we do is arbitrary and will be revisited in the sensitivity tests (section 5.8.5). The summary of the errors assumed for each data source is presented in Table 5. 2.

Once the observational networks have been defined as well as the observational error covariances we can compute the eigenvalues of the scaled representer matrix χ for the different networks and error regimes, as it was explained in the previous section. To compute them we have considered that all measurements were simultaneous (altough this can be relaxed using space-time EOFs in ρ_r). In case of a non-stationary error regime this could be questioned but as it is just an orientative diagnostic we can assume it. This diagnostic should be seen as a crude

estimation of the degrees of freedom that can be seen by an observational network in an assimilation cycle. Afterwards, it should be evaluated if this is enough or not depending on the frequency of the observations and the variability of the error structures.

Data source	*Instrumental error*	*Error assumed in Rr*
CTD - Temperature	0.01 ºC	0.02 ºC
CTD - Salinity	0.03 psu	0.05 psu
ADCP - Current intensity	0.05 m/s	0.08 m/s
ADCP - Current direction	20 º	30 º
ν–Shuttle - Temperature	0.02 ºC	0.03 ºC
ν–Shuttle - Salinity	0.05 psu	0.08 psu
Current meter - Current intensity	0.005 m/s	0.01 m/s
Current meter - Current direction	10 º	15 º
Current meter - Temperature	0.005 ºC	0.01ºC
Satellite SST	0.2 ºC	0.8 ºC
Altimeter - Surface Elevation	0.05 cm	0.1 cm

Table 5. 2: Summary of the errors assumed as the reduced order observational errors (Rr) for the different data sources simulated in the experiments.

In Fig 5. 4 there are the results for the five networks in the current errors regime and the wind errors regime. The first comment that arises from them is that the networks which are not 3D (cmeter and satellite) have almost all the modes below the limit of observability. Although this is not a conclusive result, it gives a good flavor about what will happen with the assimilation. The punctual measurements in the current meters are not enough to capture the errors in the 3D structure of the slope current even if they are placed in maximum variance regions. Similarly the surface temperature gives low information as the surface mixed layer masks the surface signal in temperature of the 3D errors below. The altimeter data has also little information about the errors in the current depth because if the current transport is maintained the surface elevation gradients are the same for all the current depths.

When errors in the wind field are considered the performance of these networks is the same but probably for different reasons. It is probable that the problem with the current meters arise from the fact that there is not much information in the upper levels where the error structures associated to the wind have larger values. On the other hand the SST measurements could contain useful information, but the error associated to them is comparable (if not larger) than the surface temperature errors induced by the wind.

The other observational networks (classic, fast and cheap) give a better performance allowing more than 8 degrees of freedom, which seems enough to capture most of the variability (it must be remembered than the EOF spectra was quite red). It must be noted that during the assimilation the observability is not enough to ensure a good correction because the temporal dimension will play a crucial role. Namely constant EOFs are not representative of the model error subspace in response to wind perturbations as it will be shown later.

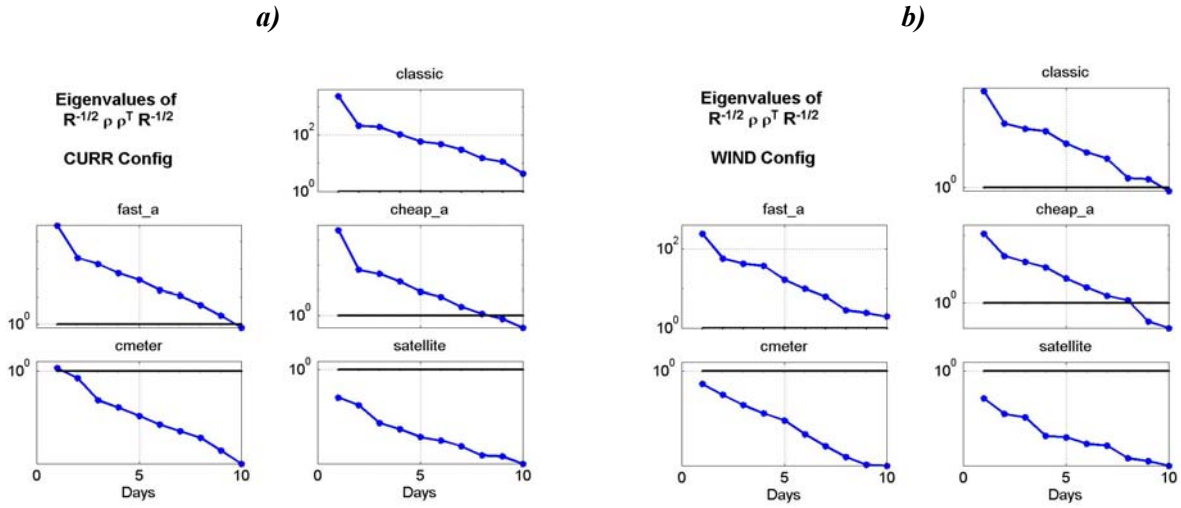

Fig 5. 4: Eigenvalues of the scaled representer matrix for the different observational networks in (a) the current errors regime and (b) the wind errors regime. The black solid line indicates the unity.

5.5 Results regime 1-Correction of slope current errors

Free run statistics

The first thing that we can look at is at the time evolution of the rms and correlation of the free run respect to the control run (see Fig 5. 5). As it can be seen, the rms has a non-zero value at the initial time (we are perturbing the initial conditions) and grows monotonically in all the variables. The error in the free surface elevation begins to grow before the other variables when the first winds start to blow (at day 12) because it is the most sensible variable to the wind. The density field seems more or less stationary during the first 10 days of simulation because the initial error is big enough to mask the small deviations that are generated. It is after day 20 when the errors in the density structure increase due to the triggering of a current meandering which has different properties depending on the current depth (see chapter 4 for a description of the behaviour of different members in ensemble ENS1).

The correlations are very high in all the variables due to the way the system has been perturbed. The initial barotropic streamfunction is quite similar in all the members (their main

difference is in the vertical structure of the current) so the structure of the density field resulting from the initialization method (see chapter 3) is near the same in all the members.

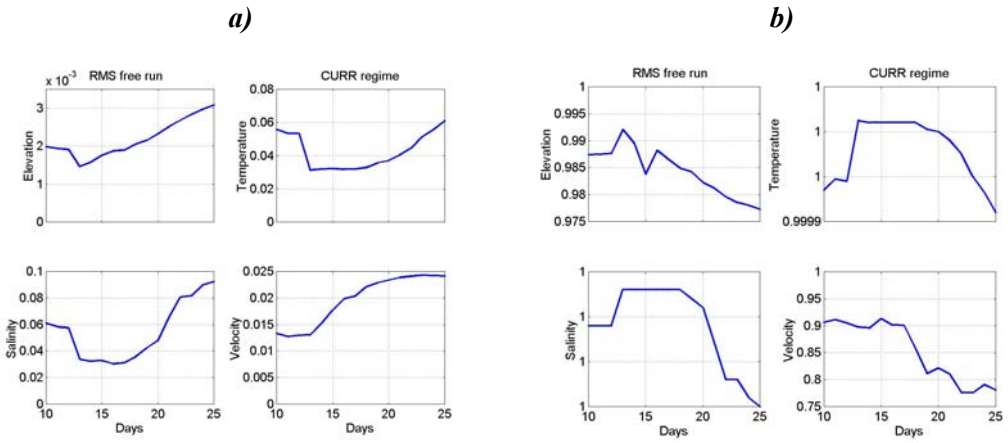

Fig 5. 5:Time evolution of the rms (left) and correlation (right) of the free run with respect to the control run in the current regime for different variables..

Water masses

As it was mentioned in section 5.3 we want to know if the assimilation introduces significant changes in the water masses. The best way to look at this is the volumetric TS diagram (see Fig 5. 6). It represents the amount of water in each cell of given TS characteristics. The comparison of those diagrams for the different runs allow to see which water mass has changed and how much. It can be seen that assimilation doesn't introduce spurious water masses. The aspect of the vol-TS diagram for the assimilated run is quite similar to the control run diagram showing how the analysis have change the distribution of the water masses (compare with the free run diagram). In particular, the analysis has not introduced new water masses but it has changed the volume of each one. The depth of the slope current has been corrected and the distribution of the density field has changed.

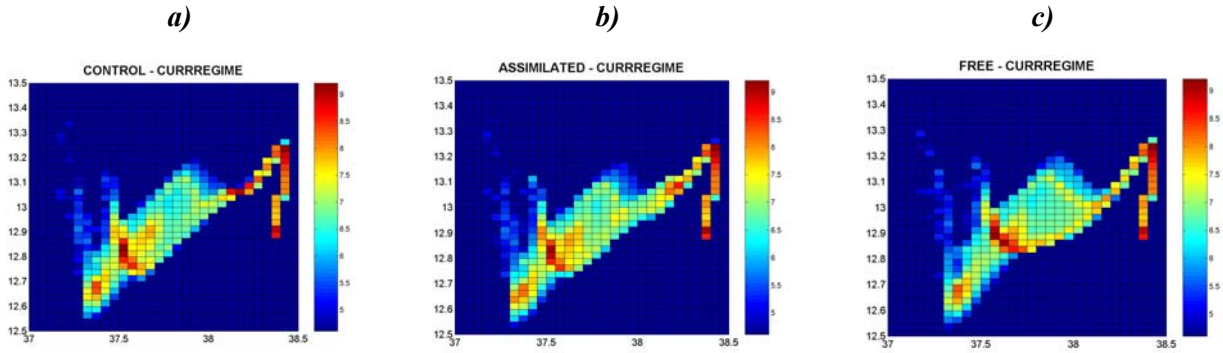

Fig 5. 6: Volumetric θ–S log diagram for the (a) control run (b) assimilated run using the classic network and (c) free run.

Spatio-temporal structure of the corrections

Fig 5. 7 shows the comparison of different fields in the control, assimilated and free runs in order to have an idea about the structure of the corrections performed. It can be seen that the assimilation does a good job approaching the free run towards the reality (in our case this is a synthetic reality represented by the control run). In the free surface and the velocity fields it is clear how the oscillations in the slope current are introduced. As it is a multivariate analysis with the EOFs obtained from the model, the meandering introduced by the assimilation is in equilibrium with all the variables (temperature, salinity and elevation). In addition to that, the vertical structure of the density field is also corrected and the base of the current is placed at 200m.

Over the shelf there is no correction at all because in the ensemble used to generate the error structures there is no variability there. This is coherent with our goal of just correcting the current depth leaving the shelf unaltered.

It must be noted that we are placed in an extremely favorable framework where the free and the control runs come from the same ensemble from where the EOFs have been obtained. In other words, the errors in the free run are almost completely included in the error subspace, so a good correction was expected. Nevertheless we are not obtaining a perfect correspondence between the assimilated and the control runs because of the observational errors and the part of the errors structure that are not included in the error subspace.

The following that can be looked at is the evolution of the assimilated run some time after assimilation is stopped. It is important to know if the improvement provided by the assimilation lasts for some time or not. In Fig 5. 8 a comparison is presented for the fields at the end of the run eight days after all the assimilation is finished. It seems that the run with assimilation keeps part of the improvement, especially in the vertical structure where the current depth is the same that just after correction. The velocity field shows more meandering than the free run but this is not located in the same place than in the control field.

It is also interesting to note that the assimilated model generates some structures similar to those in the control run (i.e. aspect of the temperature maximum at 50m in Fig 5. 8) but which are not present at day 18 (i.e. not introduced by assimilation). This means that the trajectory of the run with assimilation is similar to the trajectory of the control run even when assimilation is finished. In other words, the correction performed placed the model on the right path.

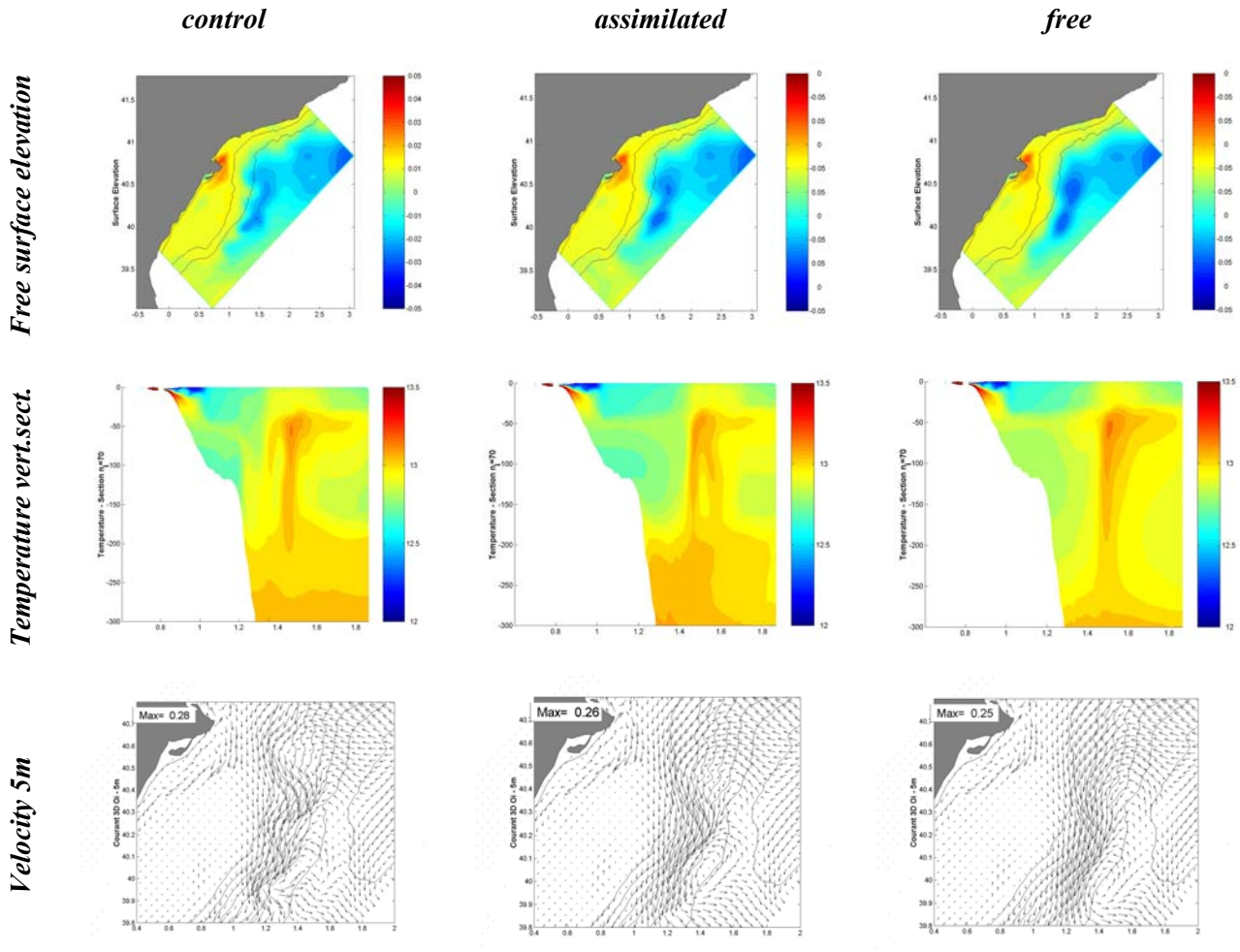

Fig 5. 7: Comparison of the control, assimilated and free runs for day 18 when the classic network is used.

Once we have seen the structure of the fields at two different times, it is interesting to see the time evolution of the model trajectories. Fig 5. 9 displays the time evolution of the free surface in a point located in the open sea. The assimilation approaches the values to those of the control run every time an analysis is performed. As it was shown in chapter 4 a transient is generated but just in the external mode. The internal mode variables are quite stable and no significant transients are detected. The point of interest of this plot is to note that there is a step-like behaviour with each assimilation cycle, which has no physical sense. This should be kept in mind if the assimilated results have to be used for physical interpretations. A way to solve this could be to use the Incremental Analysis Update (Bloom et al., 1996). In this case, once the analysis is done the assimilation cycle is re-run and the correction is shared every time step instead of doing it once at the end, so the time evolution of the variables is much smoother without sudden changes.

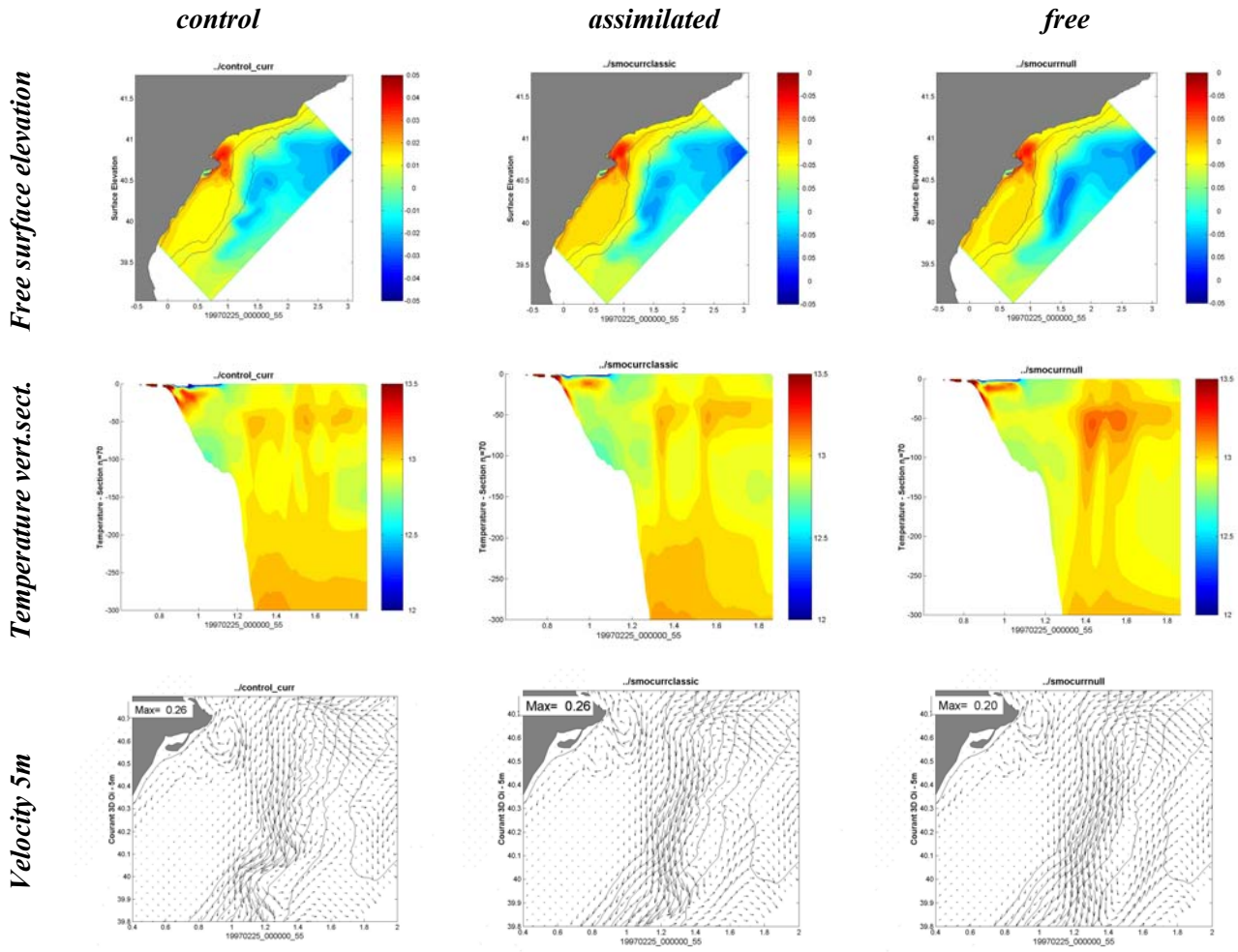

Fig 5. 8: As Fig 5. 7 but at the end of the run, 8 days after assimilation stops.

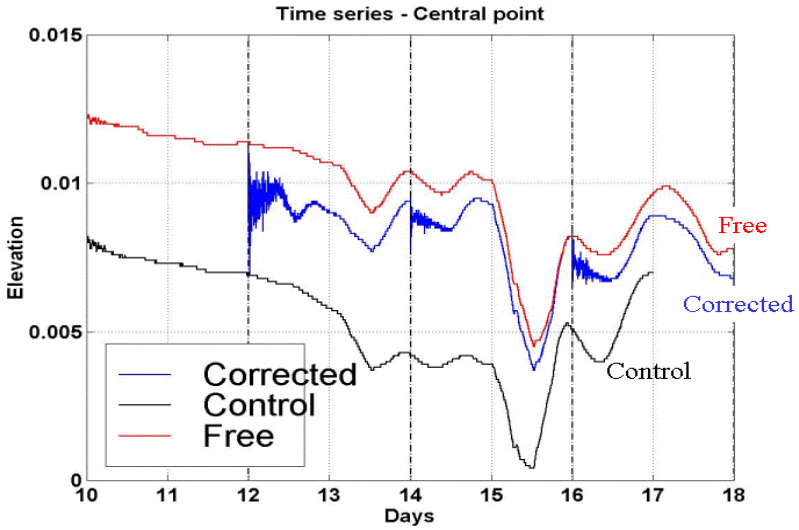

Fig 5. 9: Time evolution of the free surface elevation in a point located in the center of the domain. The dotted lines indicate the assimilation cycles.

Performance of different networks

The general characteristics of the assimilation when the other observational networks are used are quite similar, so instead of describing precisely each network we show a statistical summary of the results. In Fig 5. 10, the ratio of rms of the different networks respect to the rms of the free run is displayed.

In all variables, except the velocity, the rms difference is reduced from a 30% to 50% thanks to the assimilation. Obviously, the way this reduction is done depends on the observational network and the moment the data are available. Namely, the ship-based networks (classic, fast and cheap) quickly correct the model trajectory because enough data is available in a short period. On the other hand the network based on the current meters needs more time to have enough information and the correction is done gradually. Finally, the performance of the satellite network is similar due to the big observational errors and the fact that sea surface temperature is not too useful in the study period as far as the mixed layer reduce the signal in surface of the errors in the current depth.

If we look precisely at each variable we see different performance and evolution because the characteristics of each field are intrinsically different. For instance, the surface elevation is more sensitive to the fast processes (i.e. adjustment to the wind), while the temperature and salinity evolve more slowly.

For the temperature and salinity the fast and classic networks work best because they provide a good coverage of the entire region. The fact that measurements in the fast survey are limited to the first 150m is not a problem because the information obtained is enough to correct the whole structure thanks to the use of the 3D EOFs. The time spent to do the survey is not a problem as far as the error process associated to the current depth is stationary (or almost), so the moment the data is obtained is unimportant. The cheap survey also gives good results showing again that the use of 3D EOFs allows global correction even if data is limited to a certain area. The best agreement with the control run is in the area where data is available while far away from this region there are some small-scale structures than worsen the solution downstream.

In the case of errors in the slope current, this globality of the correction is consistent with the fact that the structure characteristics are highly correlated in different places. In consequence, it is logical than if we know that the current depth in one part of the domain must be corrected it should also be corrected downstream.

The structures in the elevation field evolve faster than in the tracers field. The networks, which are more continuous in time as the classic network, which takes one week to complete the measurements or the current meters, are better placed to correct those structures.

The velocity field is not satisfactorily corrected. The assimilation improves little or even worsens the results. There are two possible explanations to this feature. First, the current meandering is introduced but not in the exact place so the differences with the control would be important. In this case it is interesting to note that the assimilation introduce an important feature as the meandering and, even if it is not in the right place and the rms is bad, its presence is already an important improvement. With this we want to highlight that objective parameters as the rms or the correlation are not perfect indicators of the assimilation skills.

The second possible reason to the low improvement in the velocity field is that this field is dominated by inertial oscillations. This means that a slight phase lag between assimilated field and the control would induce a big error. This problem is linked to the fact that no filtering of velocity data to extract the low frequency component has been done. The high frequency part is difficult to correct and should be excluded from data and from the characterization of the error structures.

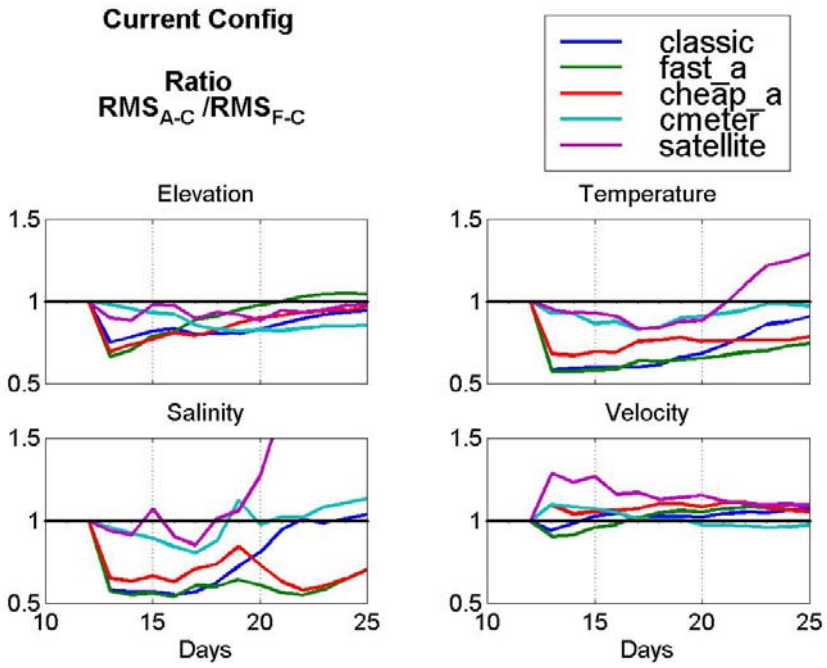

Fig 5. 10: Ratio of the rms (assimilated-control) with rms (free-control). Gives the fraction of rms reduced thanks to the assimilation. Values <1 means improvement.

Now we can focus on the time evolution of the corrected state once the assimilation is finished (after day 18). In all cases, the solution begins to worsen although in some cases this worsening is quite slight. When the fast and the cheap networks are used, the solution after the assimilation maintains more or less its quality while the correction provided by the classic network doesn't last for long time. The reason is that both the cheap and the fast networks

corrected the model solution upstream while the classic network was focused on the center of the region (see Fig 5. 3). Although the 3D EOFs provide a global correction, the quality of this correction far from the place were data is available is lower. In the classic case, the results upstream are not so good than in the fast case, so when current advects this information downstrem the results worsen.

The solution corrected with the current meters also worsen once the assimilation is stopped although the worst case is when satellite data is used where the solutions at the end of the run are even worse than the free run. One explanation to this is that we are not able to bring the model to the right trajectory when satellite data is used. In consequence, it is not guaranteed that its evolution in time will be the correct one.

A different way to look at the results are the Taylor diagrams already presented in section 5.3. They give a compact overview of the results of the different networks compared to the control run (see Fig 5. 11). It can be seen that for the temperature and the salinity, the performance of all the networks and the free run is quite similar. This is due to the short duration of the runs and the special way the fields have been initialized. Correlations are, by construction, especially high in the density field and there is no time to present important variations of the std. The free surface elevation and the velocity evolve faster and present more differences. For the surface elevation all the networks performs better than the free run, except the fast network that is comparable. The opposite happens with the velocity field where almost all the networks present a worsening of the results. In any case the range of values presented difficult a clear judgement of the quality of the results.

A clearer way to diagnose the behaviour of the different networks is to show the correction performed in the reduced order space. Namely, we can look at the combination of EOFs used to generate the correction (Fig 5. 12 displays it for each assimilation cycle). If we look at the first cycle (black line), it can be seen that the three networks that perform the best have a similar contribution of the different EOFs while the satellite network is quite different. In that case the first EOF dominates in the correction while in the other networks its contribution is negligible. This means that the structure of the correction provided by the satellite data is not the correct one, so it is not strange that the model solution diverges from the reference solution with time.

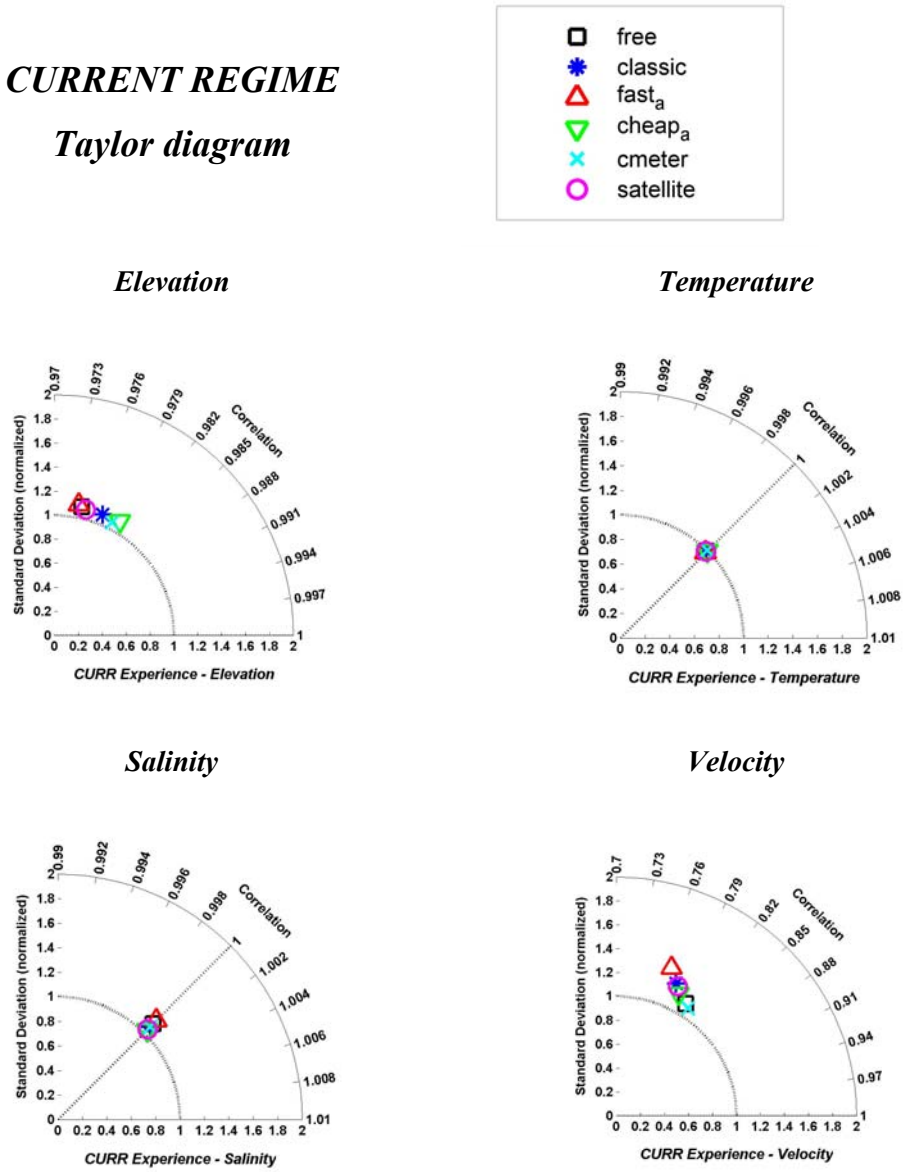

Fig 5. 11: Taylor diagrams for the different fields at the end of the assimilation period in the current regime.

Another information that can be obtained from this graphics is that most of the correction is done in the first cycle, when most of the data is available. In the following cycles the behaviour of all the networks is more or less similar although there are small differences that can be the responsible of the differences in time. It must also be noted that in all cases the assimilation just uses 6 modes (consistent with the extremely red spectrum of the EOF base).

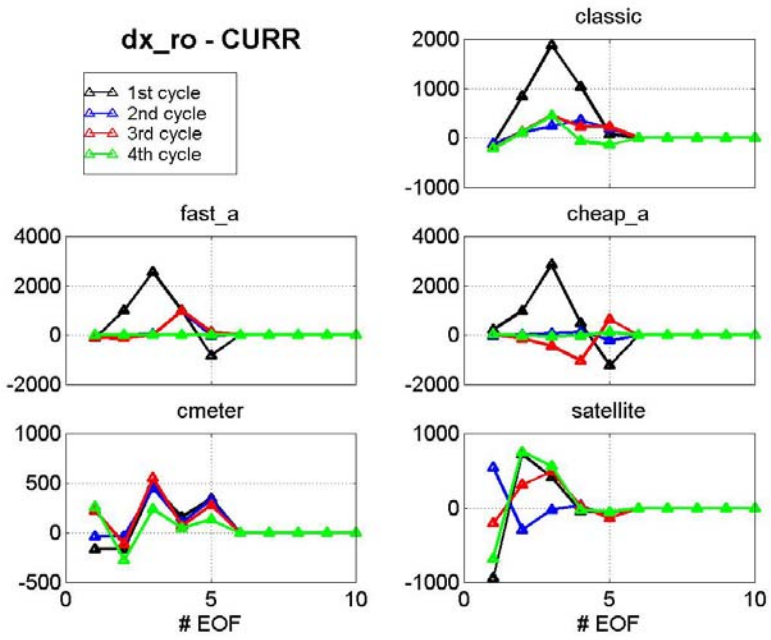

Fig 5. 12: Correction in the reduced order space for the different assimilation cycles and the different observational networks

Finally we can see the values of the cost function normalized by the number of observations (J_a/p) to see if the condition of optimality proposed by Talagrand is accomplished. Even if it is neither necessary nor sufficient it gives a flavor about optimality. In Fig 5. 13 the time evolution of the cost function is shown for the different observational networks. It is clear than in almost all cases the assimilation is suboptimal (Ja/p > 0.5). One possible reason is that we have underestimated the observational error, so the computation of Ja in (5.9) is no longer the optimal one. The problem lies in the fact that we have not quantified correctly the errors in Rr. As it was mentioned previously, one of the parts that should be included there is the representativity error induced by the truncation of the subspace S (the EOFs that we have not considered). The suboptimality comes from the no inclusion of that part. In fact, if we look at the eigenvalues in Fig 5. 4, it can be seen that networks able to "see" more than 10 EOFs, are those, which are further away from optimality. In other words, as we have lot of measurements, there are more modes of error that could be observed and the modes not included are comparable to Rr, so its lack becomes important. On the other hand, in a network with few observable modes (i.e. satellite) the truncation of the EOF base has no importance, as all the modes are much less important than Rr. In that case the optimality criteria is satisfied (J_a/p ~0.5) hinting at the fact that we have described correctly the matrix Rr and Br.

Finally, a last remark should be done about the fact that the criteria of Talagrand must be accomplished in a statistical framework. Strictly we should re-do the computation for different

pairs of free-control simulations but in practice we do not think that the conclusions significantly change.

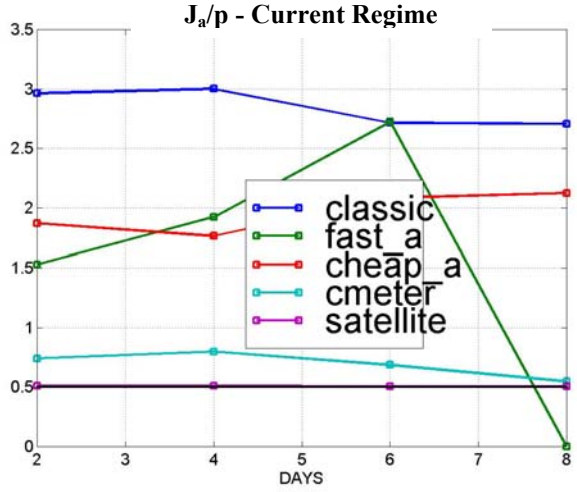

Fig 5. 13: Time evolution of the cost function divided by the number of observations (J_o/p) for the different observational networks in the current errors regime. The 0.5 value indicates optimality.

5.6 Results regime 2-Correction of wind errors

Free run statistics

In this regime, where the errors are in the wind field, the evolution of the rms and the correlation is different than in the previous case (see Fig 5. 14). At the initial time the rms (correlation) of the free run respect to the control run is null (equal to 1) because the initial conditions are the same. Then they begin to gently grow in time until 15th February when the strong Mestral wind burst appears. In that moment, the differences between the free and the control run abruptly increase both in terms of structure and magnitude. When the wind stops both runs converge again: the rms is reduced and the correlation increases. This behaviour matches the ensemble variance evolution (cf chapter 4).

As it was expected, with strong winds the effect of the errors is much more noticeable. What is interesting to note is that after the wind stops, the errors in the sea state are reduced, or at least it seems they are. The variables, which are more sensible to the wind effects as the free surface elevation or the velocity, converge to the reference values after the burst. The other variables as the temperature and salinity, which has more inertia and need more time to adjust, do not come back to the previous values of rms or correlation but they still increase (although

slowly). The peak in the salinity is linked to the river plume, which also adjusts fast to the wind, but if we look to the general trend there is also an increase.

In conclusion, there is a strong error around day 15, when the Mestral wind blows. After it, the error is reduced in the variables that are more dependent to the wind, but errors in the temperature and salinity continue increasing with time.

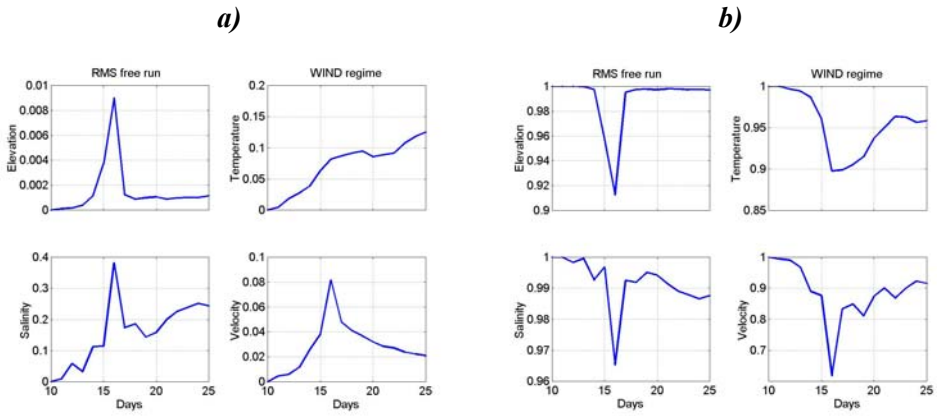

Fig 5. 14:Time evolution of the rms (left) and correlation (right) of the free run in the wind regime for different variables.

Water masses

In this regime, the corrections are limited to the first 50 meters, so affecting the water masses therein (see Fig 5. 15). This is why the amount of Winter Intermediate Deep water and Levantine Intermediate Water are not changed. The differences are present in the waters with lower salinities placed in the surface mixed layer. Also shelf waters influenced by the river plume are changed. Nevertheless, the amounts of water masses introduced by assimilation are negligible, which is the desired effect.

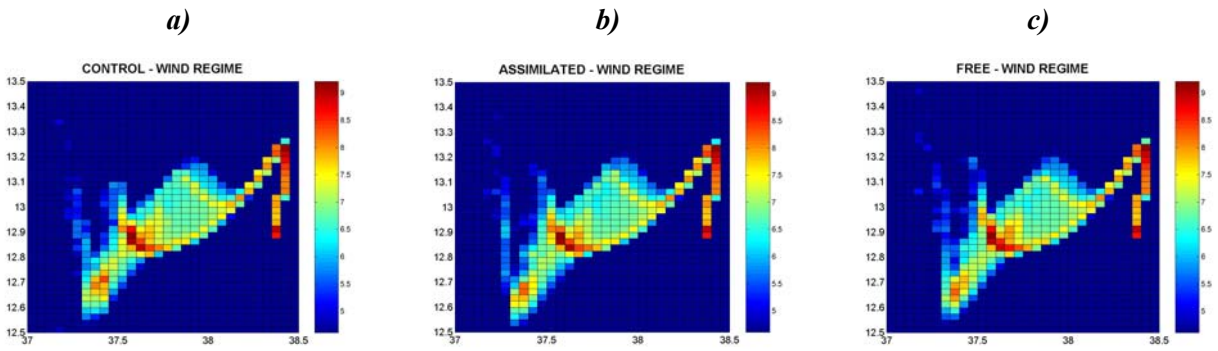

Fig 5. 15: Volumetric TS log diagram for the (a) control run (b) assimilated run using the classic network and (c) free run.

Spatio-temporal structure of the corrections

In Fig 5. 16 the aspect of some fields is shown in order to visualize the effects of the assimilation. Contrary to what happened in the current regime, here it is more difficult to find a significant correction at day 18. One of the reasons for the low corrections is that in the assimilation window there are different error processes superimposed. In other words, the distances model-observation in the matrix **d** maybe do not correspond to the same error structure. In addition to that, the assimilation method doesn't take into account the "age" of the observations, so to do the analysis all data is used with the same weight. In consequence, the information used in the analysis could be a mixing of different processes, so leading to a bad correction.

A sketch of this process is showed in Fig 5. 17. At two different times t1 and t2, the difference between model and observation can be different meaning that the error structure has evolved with time. In an extreme case as the one depicted in the figure, d1 and d2 could be the opposite (d1= -d2). If the two times are in the same assimilation window, the two distances d1 and d2 will be part of the innovation vector **d**. In that case, the system would have two pieces of information indicating the opposite, so no correction would be done. So, we have an example where the fact of having more information doesn't mean to have better results because the error process varies in a shorter time scale than the length of the assimilation window. We think that this is the main reason why the corrections provided by the assimilation are so small. Another possible reason, which could complement the main one, is that the error modes included in the EOF base are not representative of what happen when data is available. With this, we mean that if the errors change a lot, is possible than a EOF base with just 10 modes would not be enough to capture all the possible error structures present in the system. We will come back to this issue in section 5.8.

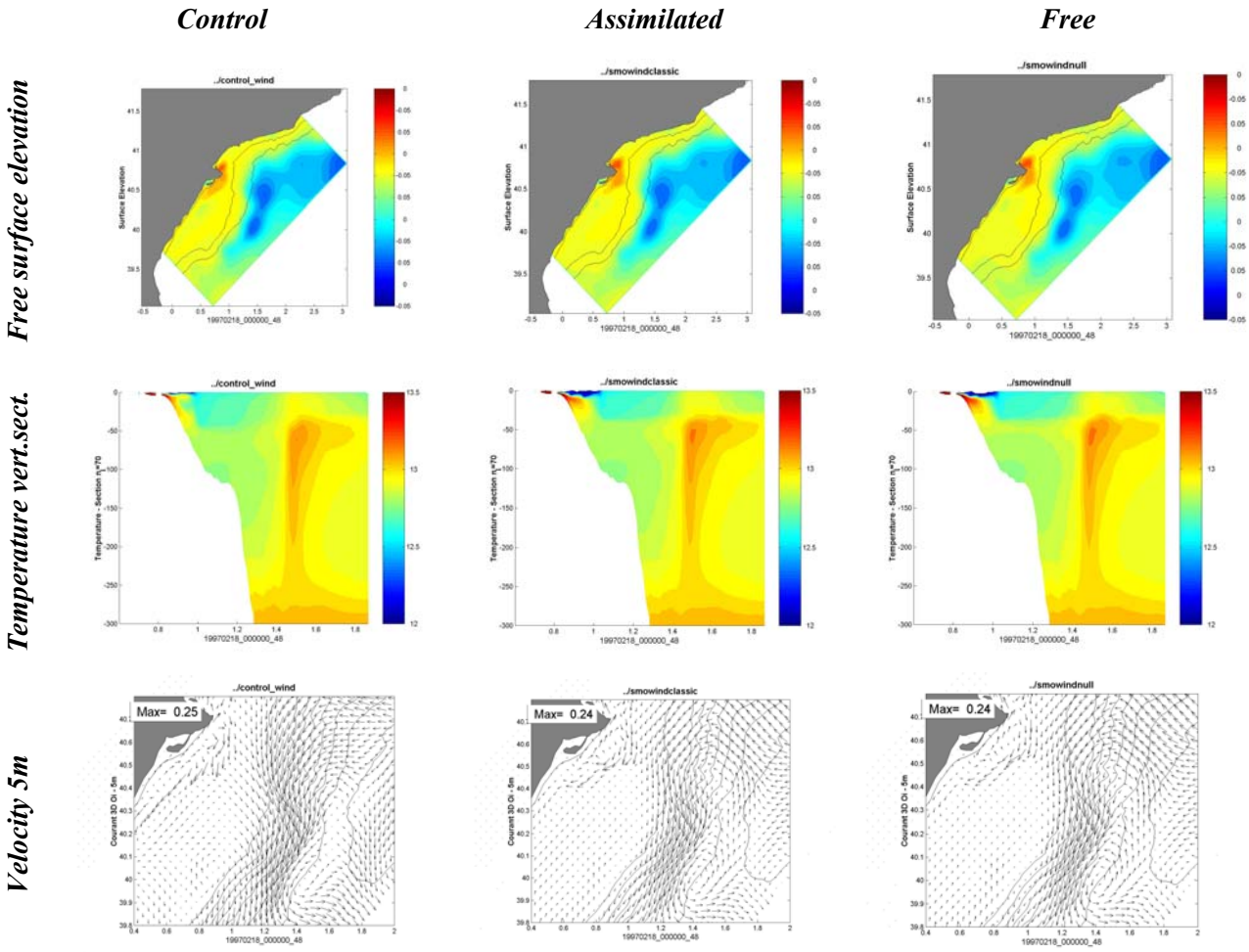

Fig 5. 16: Comparison of the control, assimilated and free runs for day 18 when the classic network is used to correct errors in the wind field.

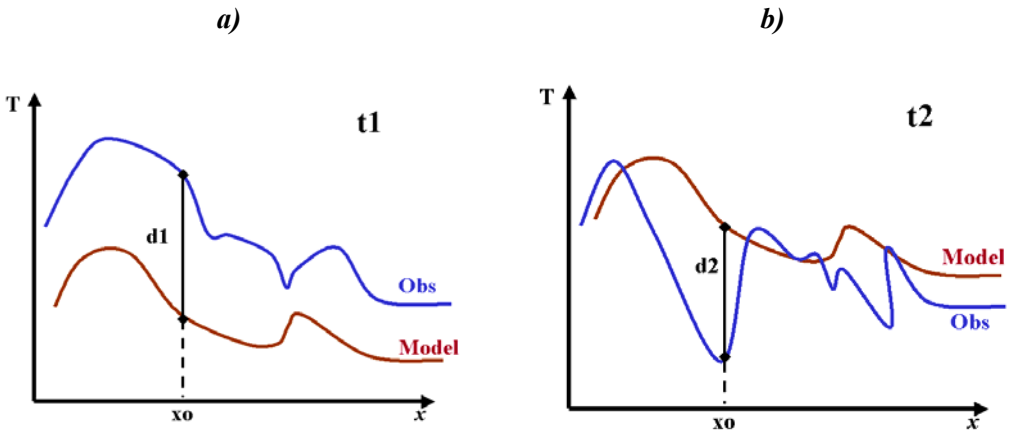

Fig 5. 17:Sketch of the evolution with time of the errors in temperature at a given location xo.

In Fig 5. 18, it is presented the time evolution of elevation and temperature in a single point in the open sea near the surface. It can be seen how the divergence between the control and the free run increases between days 14-16, when the Mestral wind blows and how, after day 18, the inertial oscillations dominate the variability. It is clear how the assimilation seems to do a good job correcting in the right sense but it must be noted that a single point is not significant of the overall performance (see Fig 5. 19).

The elevation field suffers again a transient period of 1 day after each analysis but it is not noticeable in the other fields. The model trajectory is corrected step by step each assimilation cycle and, at the end of the assimilation, it is quite near the control values. The interesting point is that the evolution of the assimilated run, after the assimilation is finished, has converged quite well to the control run before the free run did.

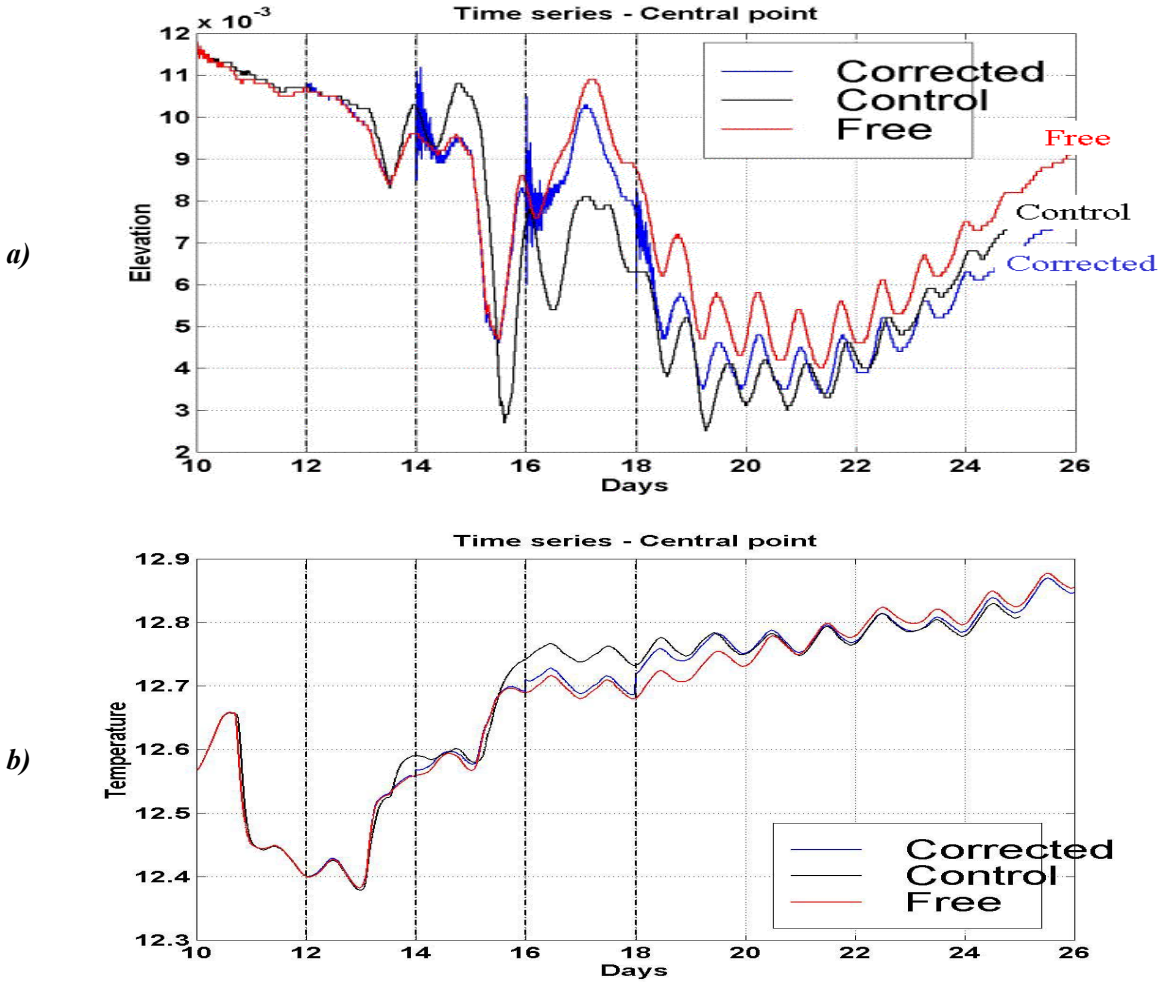

Fig 5. 18: Time evolution of (a) elevation and (b) temperature in a point located in the open sea in the center of the domain. The dashed lines indicate the analysis time. The assimilation

Performance of different networks

The time evolution of the rms ratio for the different observational networks is showed in Fig 5. 19. It can be seen that the improvements in this regime are lower than in the current regime. The rms reduction with the best network is just around 20% and, in some cases, assimilation even worsen the solution especially during the first days of simulation.

In the first part of the period, before day 15, the assimilation is not effective because a joint effect of what was mentioned before. On one hand there are different error structures in the same vector d, and the winds are weak,so the differences between the control and the free run are comparable to the observational error in the measurements. In consequence, the corrections induced are very low.

At day 15 the wind burst enhances the differences between the free and the control run and is then when assimilation could do a better job. The problem there is that there are no available measurements for some of the networks. The fast network is already finished and the classic network is near the end, so few data is obtained after the wind burst. On the other hand, the cheap network, which has its second passage at day 16, is the network that performs the best because, is the one that provides more measurements after the wind burst.

The problems with the variability of the error structures are more noticeable with the river plume. It is quite sensible to the wind direction and intensity and errors in that field are directly translated to errors in the plume extension or mixing. In addition to that, the density gradients linked to the plume are important, so errors in the plume position lead to important differences of salinity or temperature.

The network based in current meters worsens the results for all the variables. This is probably due to the fact that there is no enough data to correct the errors in the wind field. It must be noted that the variance observed in the wind ensemble (see chapter 4) was localized in the first 50m, so there are just 4 useful points of measurement when the current network is used. This has already been announced when we showed that this network could just force one EOF at most (cf 5.4).

Finally, the satellite based observational network just slightly improves the temperature field. The observational error is too big compared to the model variance obtained from the ensemble simulations from where the forecast error is defined. In other words, the reliability of the satellite data is comparable to the realibility of the model, so the assimilation scheme tends to do smaller corrections than in the other networks.

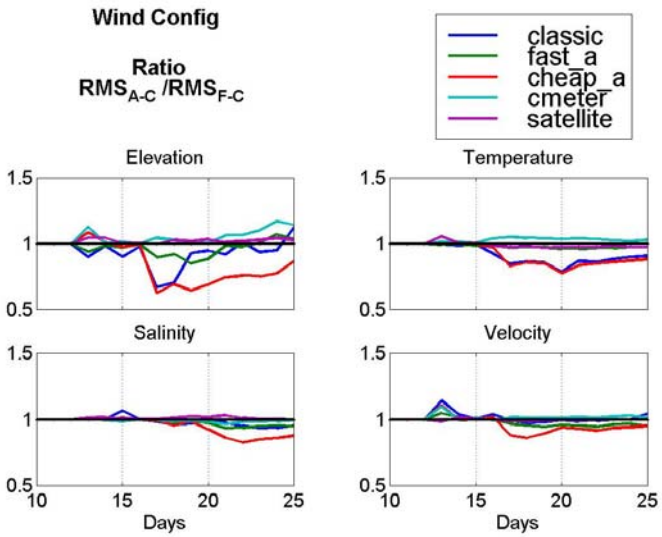

Fig 5. 19: Ratio of the rms (assimilated-control) with rms (free-control). Gives the fraction of rms reduced thanks to the assimilation. Values <1 means improvement.

In the wind regime the Taylor diagrams offer more variability than in the current regime although the range of variations is still small for the above-explained reasons. In this case all the runs present a perfect correspondance of the std values meaning that the variability of all the fields is the correct one and that assimilation do not generate strong spurious structures. About the correlation, the results are the same that those observed in the rms computations. The cheap and the classic network are those performing the best while the current meter and the satellite do not show any improvement respect to the free run.

When looking to the correction in the reduced order space we find a different behaviour than in the current regime (see Fig 5. 21). The number of EOFs used to do the corrections is greater, which means that there are a greater variety of error structures. This was already expected as the errors associated to the wind are non-stationary and their structure is highly variable with time (cf. chapter 4). In consequence, it is not strange to find that different EOFs are implied in each assimilation cycle.

The most interesting from that plot is that each observational network uses different combinations of EOFs to describe the same error structure. In consequence the corrections performed by each system will be quite different. In other words, the characteristics of the different observational networks lead to different analysis to correct the same error. This is due to the fact that each network has different capabilities of observing the errors due to its location and time. This is closely linked to the observability of the error space commented in section 5.3.

It must be noted that this feature is not desirable and means that the system configuration is not able to find the optimal solution which is unique by definition.

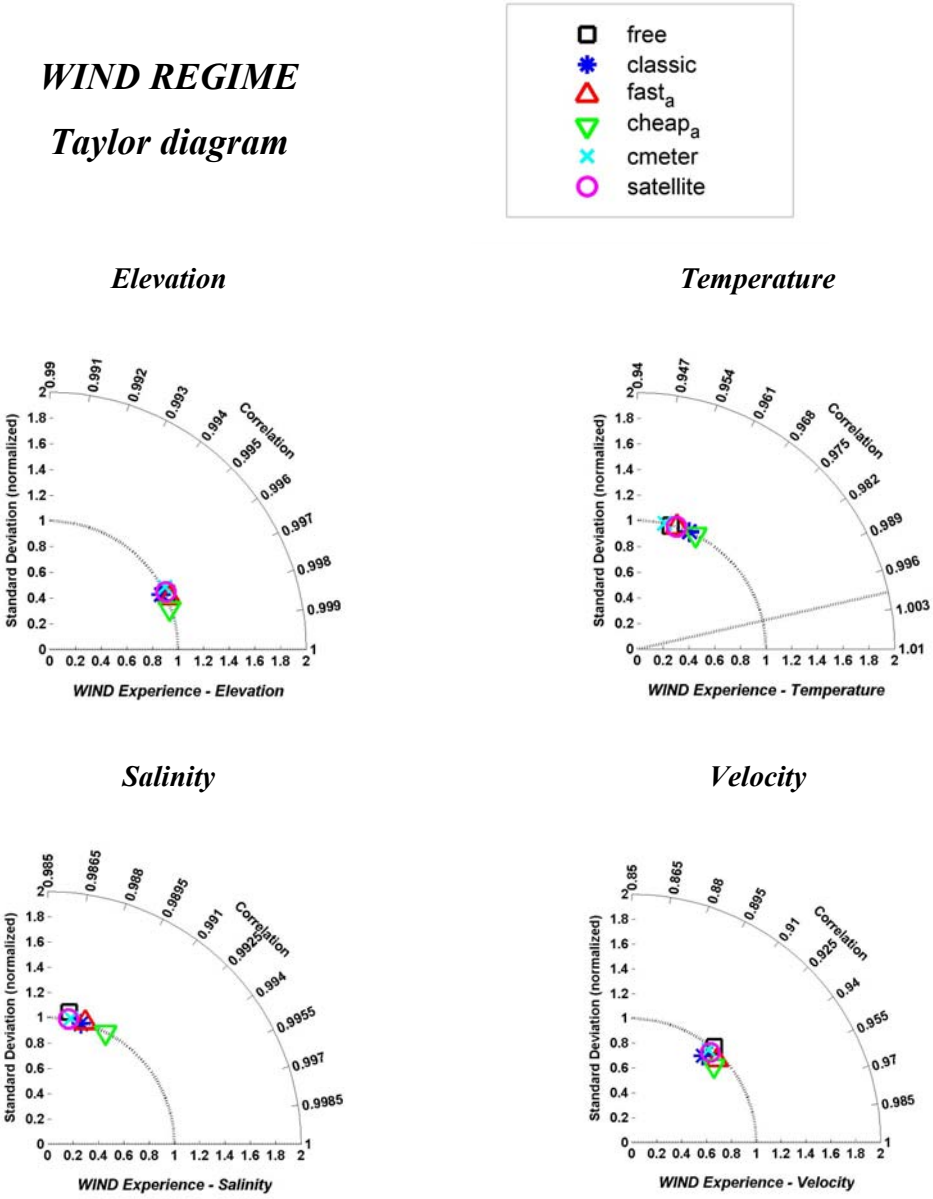

Fig 5. 20: Taylor diagrams for the different fields at the end of the assimilation period in the wind regime.

About the concrete results, it can be said that in the first assimilation cycles the corrections are small because the distances model-obs before the wind burst are small. The satellite and the current meter networks predominantly use the first EOF while the classic and the cheap, which perform the best, use higher order modes. The reason of using just the first mode is linked to the fact that, with the available data provided by the current meters or the satellite, the assimilation is not able to chose which is the best EOF. They are not able to force any EOF (see the

representer matrix svd analysis in 5.4), so the weight for each element of the base is defined by the forecast error fixed by us. In consequence, the priority is given to the first mode.

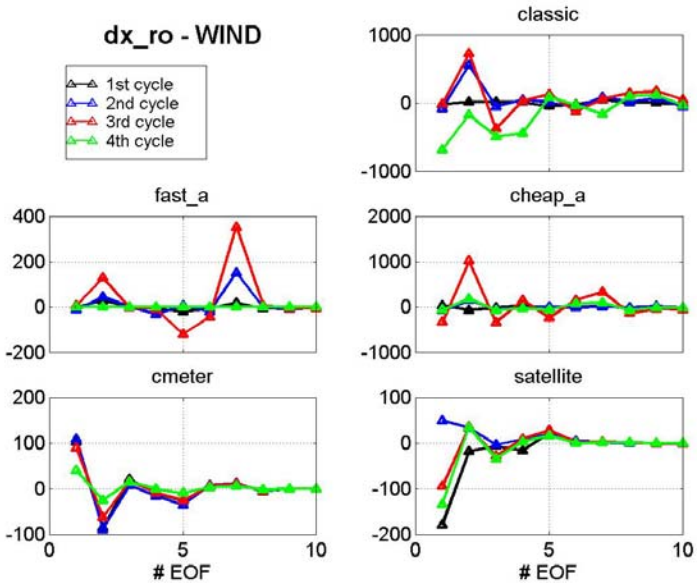

Fig 5. 21: Correction in the reduced order space for the different assimilation cycles and the different observational networks

The optimality of the assimilation can be checked again looking at the values of Ja/p (see Fig 5. 22). For the classic network the assimilation is largely suboptimal probably due to the truncation of the EOF base. On the other hand all the other networks are much nearer the optimality than in the current regime.

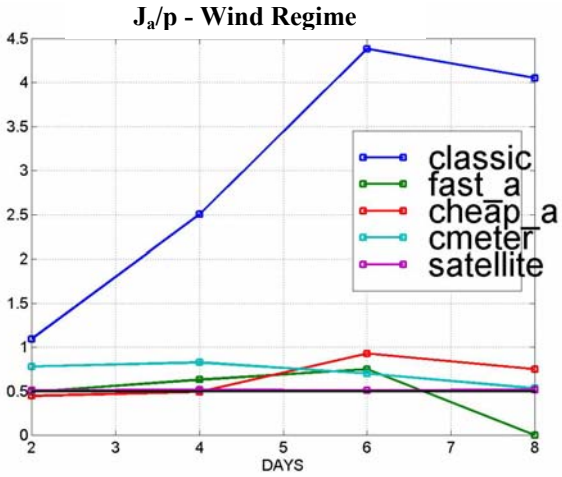

Fig 5. 22: Time evolution of the cost function divided by the number of observations (J_o/p) for the different observational networks in the wind errors regime. The 0.5 value indicates optimality.

5.7 Results of regime Mixed

Free run statistics

In this regime we consider both sources of error in order to see which one dominates and if we are capable to define a good EOF base which works fine. The rms and the correlation of the free run with respect to the control run is showed in Fig 5. 23. There is an initial error due to the different initial conditions. During the first two days, this error decreases as it happened in the current regime. The reason is that, in this spin-up period, non-linearities begin to act and reduce the difference between both runs. After this short period, the error grow monotonically except during the wind burst where it is suddenly increased. The correlation is again quite high due to the intialization method and its behaviour is the same as in the rms.

Comparing the Fig 5. 23 with Fig 5. 5 and Fig 5. 14 it can be said that the evolution of the errors in this regime is a mixing of the effects of both sources of error. The errors in the characterization of the slope current are translated into errors in the initial conditions and the whole 3D structure. Overimposed to them there is the effect of the errors in the wind field, which are increased after the wind burst at day 15.

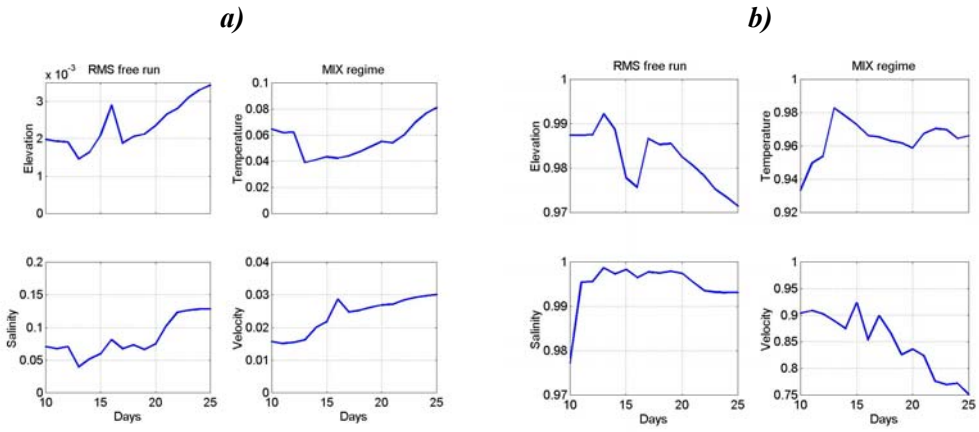

Fig 5. 23:Time evolution of the rms (left) and correlation (right) of the free run in the mix regime for different variables.

Spatial structure of the corrections

When looking to the aspect of the fields at the end of the assimilation period (see Fig 5. 24) we find something quite similar to what was found in the current regime. The errors in the slope current dominate over the uncertainties in the wind field. The assimilation is able to correct those errors with a similar level of efficiency than in the current regime. In other words, the system has found the suitable modes to correct the main structures of error.

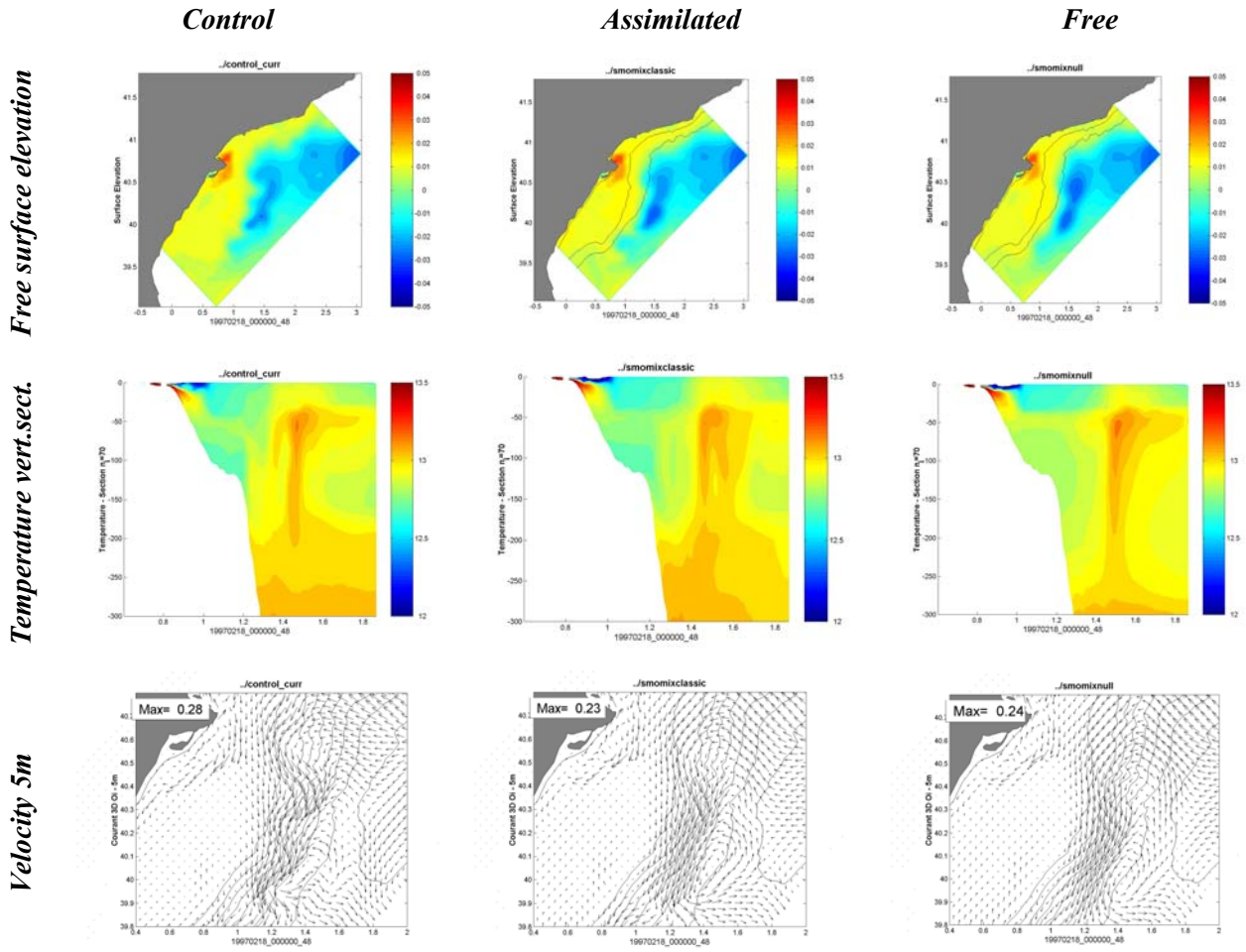

Fig 5. 24: Comparison of the control, assimilated and free runs for day 18 when the classic network is used to correct errors in the wind field.

Performance of different networks

If we look to the time evolution of the errors (see Fig 5. 25) we can better interpret what happens with the different processes of error. In the first period, before the wind burst, the errors in the wind field are not important and the system performs as in the current regime. When the Mestral burst appears the errors linked to the wind uncertainties increase and the solution is degraded until the similar levels observed in the wind regime.

Fast, classic and cheap are the networks that perform the best, as it was expected since they are the most suitable for correcting the 3D density structures. Nevertheless the corrections introduced by them don't last for so long time as in the current regime. The increasing importance of the wind errors induces a decay of the quality after the wind burst at day 15. This means that the system is not able to reproduce the actual error structure from the different modes. We think that this is due to the high variability of the wind error structures.

In conclusion, what we find in this regime is that the results are a combination of what has been found previously. Depending on the relative importance of each error, the system performs as it has been seen before for each error regime.

One interesting thing that should be noticed is the different performance respect the free surface elevation if we compare the results in the mixed regime with those in the current regime. We have commented before than errors in the slope current dominated, and the system acts as if we were in the current regime. The performance for correcting temperature and salinity in both regimes is quite similar, at least before day 15 (compare Fig 5. 10 with Fig 5. 25) but the performance for the free surface elevation is not so similar.

The reason is that a given error can have more influence over one variable than over another. For instance, the errors in the slope current have a great influence in the density structure but not over the free surface elevation. On the other hand, the errors in the wind field have no influence at all over the density structure below 50m but affect a lot the surface elevation. When a multivariate analysis is performed, the modes of error include all the variables and it is not possible to separate the error process in the different variables. In consequence, if the temperature and salinity field dominate, the error structure that will be corrected is the one that corresponds to the slope current errors, even if this means that the quality of the elevation field will be degraded.

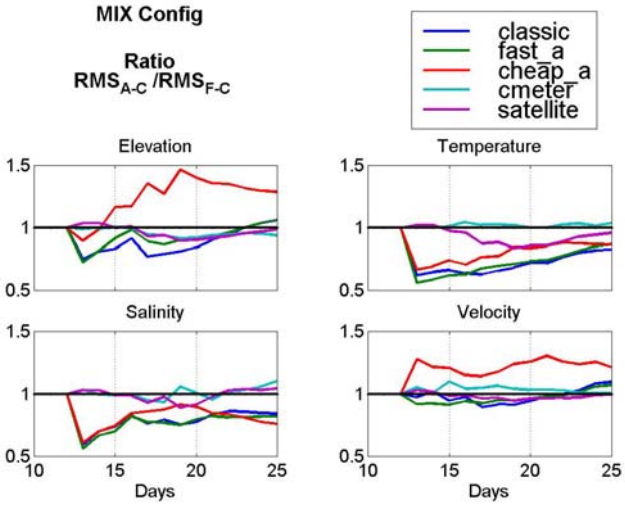

Fig 5. 25: Ratio of the rms (assimilated-control) with rms (free-control). Gives the fraction of rms reduced thanks to the assimilation. Values <1 means improvement.

In the mixed regime, the Taylor diagrams present a wider dispersion than the other ones. It is interesting to note how, in this case, those diagrams offer a different point of view about the results. For instance, in terms of salinity, it seems that all the networks have similar values

denoting a similar performance (note the different azimuthal scales in the different diagrams), while in the rms plots there were clearer differences between the networks. Also for the elevation field, the cheap network is the worst in terms of correlation. In fact in all the variables there is a good agreement in terms of std except in the velocity field, as usual, where all the networks worsen the results both in terms of correlation and std.

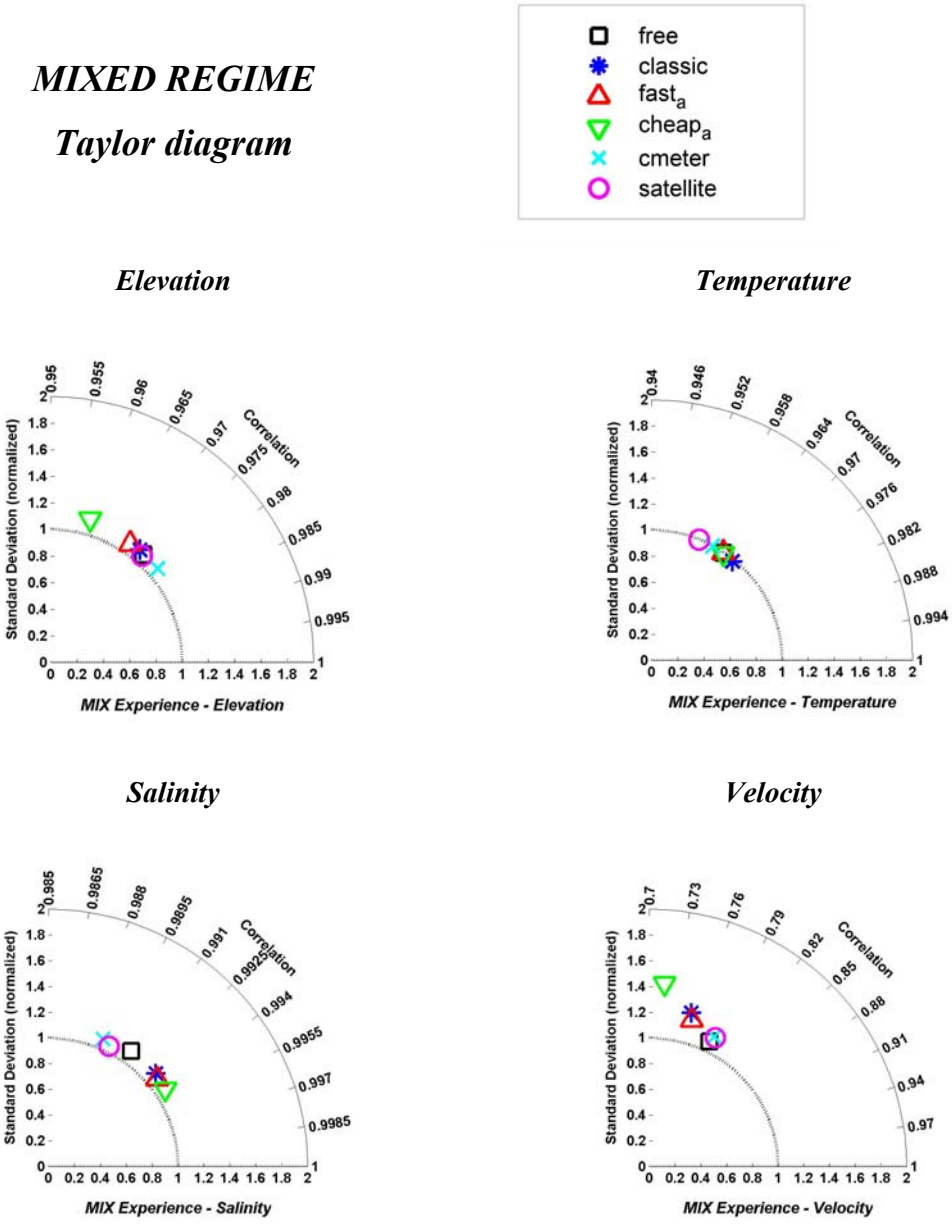

Fig 5. 26: Taylor diagrams for the different fields at the end of the assimilation period in the mixed regime.

The plots of the correction in the reduced order space are really useful in this regime to see the behaviour of the EOF base used for the assimilation (see Fig 5. 27). All the EOFs of the base

have been used so suggesting that a larger base could be used including more modes of error. In the first assimilation cycle the combination of modes is the same in the networks that perform the best (cheap, fast and classic). When data is available in the following cycles (if no data is available there is no correction), a different combination of modes is used indicating that more structures of error have been identified (i.e. see the cheap network).

The current meters induce the use of the same EOFs in all the cycles. This is motivated by the fact that the current meters are better placed to observed the structure of errors in the density field, which are stationary. In consequence, they observe mainly the same structure, so it is logical they always use the same combination of modes. On the other hand the network based in satellite data has again problems to correctly observe the errors and to decide which is the best combination. Consequently, the weight is given by the prescribed forecast error.

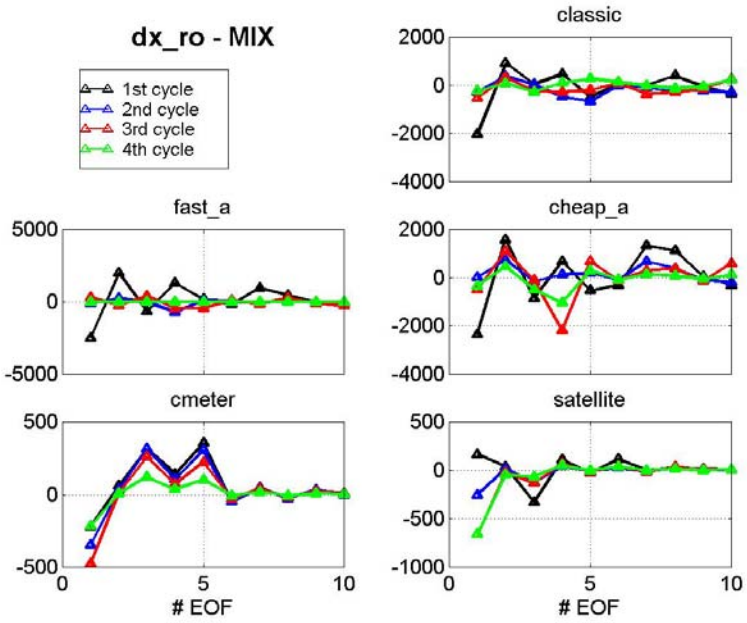

Fig 5. 27: Correction in the reduced order space for the different assimilation cycles and the different observational networks

Looking at the optimality of the assimilation we find that it is quite similar to the optimality of the current regime. This was already expected as all the other parameters already indicate that the assimilation performs as the current regime. The classic, fast and cheap networks are quite suboptimal, probably due to the importance of the truncation of the error subspace, while the current meter and the satellite networks are much nearer the optimality due to the same reasons explained previously for the current regime.

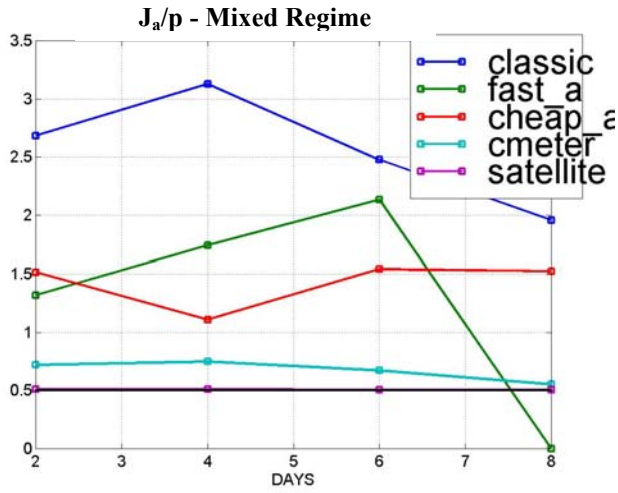

Fig 5. 28: Time evolution of the cost function divided by the number of observations (J_o/p) for the different observational networks in the wind errors regime. The 0.5 value indicates optimality.

5.8 Sensitivity of the results

Most of the results obtained in the previous sections are dependent on the configuration chosen. In order to obtain more generic conclusions we perform several tests to evaluate the sensitivity of the results and to elucidate which of them are robust and which are particular of our study case. In consequence we test the influence of the definition of the error subspace, the prescription of the forecast and observational errors and the assimilation protocol (assimilation cycle, smoother vs. filter and stationarity of the error subspace). We also looked at the influence of the members used as control and free runs but the results were uninteresting. The conclusions obtained using different members were the same so we don't show them.

5.8.1 Assimilation period

When errors are stationary, as in the current regime, we have shown that the time dimension for obtaining the data is unimportant. On the other hand, for variable regimes, as is the case for errors in the wind field where the error structures are non-stationary, the time scale gains importance. We have shown how the fast network has a poor performance due to the fact that all data is obtained before the wind burst, which enhances de variance in the system. In order to enlight this fact we perform a test with the same observational network but delayed two days, so most of the data is obtained during the period of maximum error.

In Fig 5. 29, the rms ratio using the original fast network and using the same network delayed two days is presented. It can be seen how the performance is much improved, as it was

expected, when data is obtained in the moments of maximum variance. The improvement is obtained in all the variables although for the velocity the performance is still poor due to the reasons explained previously. The slight worsening present around day 12 is linked to the use of the smoother mode where data from a broad period is used.

Even with those two remarks the improvement is quite significant denoting the importance of having the data in the moments when the variance is more important. The same conclusion could be applied to the spatial location: the use of data obtained in regions of low variance will not provide any useful information.

The recommendation for the observational networks in this case would be, when possible, to plan the campaign just after important events that could enhance the variance of the system. (for instance, a strong storm).

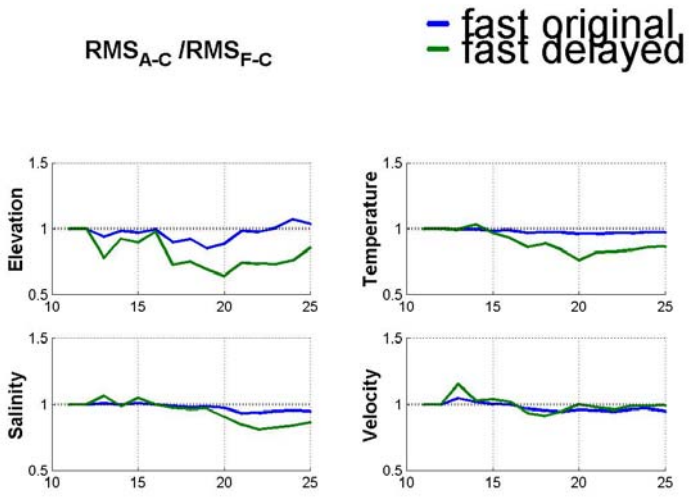

Fig 5. 29: Comparison of the rms ratio obtained with the original fast network (blue) and with the fast network delayed 2 days (green).

5.8.2 EOF base

From several tests (not shown) we have seen that the use of an EOF base, which describes the modes of error associated to the current structure, is useless to correct the errors linked to the wind field and viceversa. It is important to provide the system with the correct "tools" (modes in the base) to correct the different error structures.

In the mixed regime we have a combination of two sources of errors (current and wind) and the EOF base is obtained from a combination of members of different ensembles at different times (cf. chapter 4). The results are quite robust to different combinations of the EOF base.

Namely, the system is "intelligent" enough to select the correct modes with the available data. The important thing is to have the correct "tools" in the base.

In order to generate this base and to include all the modes we have two possibilities, as it was mentioned in chapter 4. The first one, which has been adopted in the mixed regime experiments, is to combine members of the different ensembles at different moments. This will generate an orthonormal base with all the error structures present in each ensemble and, maybe, some other modes arising from the combination of different error processes.

The problem is that some error structures could be shared in different modes. An example of this is presented in Fig 5. 30. The temperature of the multivariate 7th and 8th modes of the mixed EOF base are presented. It can be seen a strange structure in both modes which has no physical sense. In fact, the combination of both modes induces this structure to dissappear. The problem is when one of both modes is not included in the base because of truncation. In that case, if the assimilation system used just one of those EOFs, the correction would be unphysical and the performance of the analysis will be reduced.

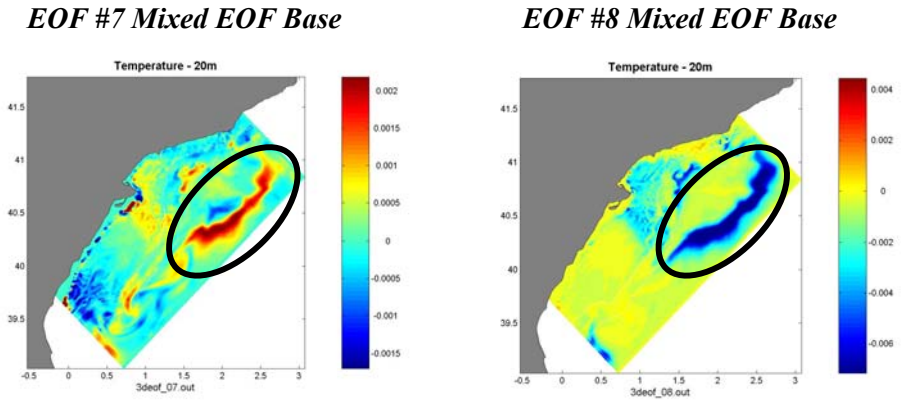

Fig 5. 30: Temperature at 20m of two multivariate modes of the mixed EOF base. The circle indicates an unphysical structure.

A way to solve this issue is to include a large number of EOFs to be sure that all the error structures are completely described. It must be noted that mixing different ensembles some of the error structures that are interesting can appear in high order modes with low values of explained variance associated, so the size of the base should be quite bigger.

An alternative is to simply juxtapose the modes obtained for each ensemble independently. By this way, the error structures are better described and even can be selected "by hand". In addition to that, some modes obtained from different computations as variability EOFs or modes obtained with a special normalization (i.e. to highlight the plume structures) could be used to enrich the base. The main problem of doing this is that the resulting base would not be orthonormal. This could present problems if an observational network sees two modes as

collinear. Nevertheless, we have the feeling, after the experiences carried on, that this is not a real problem in practice.

In order to see if the juxtaposed base introduces any improvement, we run the twin experiments in the mixed regime (errors in the current and the wind fields). Data is obtained from the classic network and the error subspace is defined with a "*juxtaposed*" base where the five dominant modes of the bases used in the current and wind regimes are put together.

Results from this experience are showed in Fig 5. 31 comparing them with the results using the mixed base. It can be seen how the improvement is clear in all the variables. This improvement comes from the inclusion of modes of error that are clearly defined. As it was shown in the chapter 4, the EOF base obtained from each ensemble is more easily assimilated to a physical process than in the mixed base and the resulting corrections are more coherent with the dynamics.

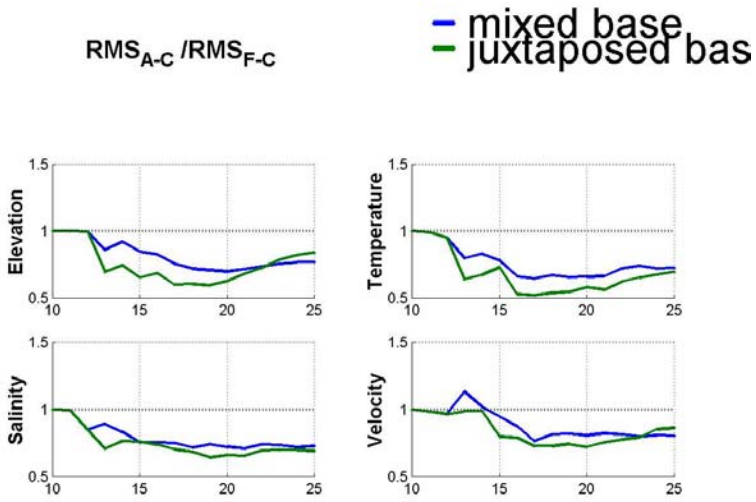

Fig 5. 31: Comparison of the rms ratio obtained in the mixed regime using the mixed EOF base (blue) and using the juxtaposed EOF base (green).

5.8.3 Forecast error

The forecast errors variances have been prescribed a priori from the information given by the eigenvalues of the EOF base used for assimilation. This is equivalent to weight each mode by the variability explained by it, which is a concept coherent with the way the error dynamics has been defined. Nevertheless, we have found that although the spatial structures (the EOFs) are quite robust, the eigenvalues are quite dependent on the way the ensemble has been created and the strength of the perturbations introduced to generate the different members. In other

words, we can be more or less confident on the structure of the errors but not about the variability associated to them, and in consequence, to the values used for the forecast errors.

To quantify the influence of the choice adopted we run several tests varying the values of the forecast errors. We have tested increasing or reducing by a factor 10 the forecast errors used in several twin experiments but the results were mainly unaffected. The forecast errors prescribed act as a weighting factor when the correction is projected over the different EOFs. If there are enough data this weighting is useless because data do the job and just the relation between the different modes is important. In consequence, the fact of increase or reduce the values has no practical influence.

Another possibility could be to use the same forecast error for all the modes but this would give more weight to higher order modes and the corrections would become much more noisy.

In summary, we have seen that the values used for the forecast error are not crucial and the relation between the values associated to the different modes is more important.

The other point that should be addressed is the stationarity of the forecast error spectra. If the error dynamics is non-stationary it is logical to expect that the forecast errors should evolve in time following the error dynamics. To test if this has an influence in the assimilation we run a test where the error forecast spectra evolves with time.

The time evolution can be directly obtained from the ensemble run. The forecast error ε_f can be expressed as the variance of the projection of the different members of the ensemble over a given EOF (Auclair et al., 2003):

$$\varepsilon_j^f(t) = \frac{1}{n\,m}\left[\sum_{i=1}^{n}\left\langle x_i^f(t) - x^c(t), \phi_j\right\rangle^2\right]^{1/2} \qquad (5.15)$$

where x is the model state, superscript f and c denotes forecast and reference, respectively, and ϕ_j is the j^{th}-EOF considered as constant.

Using this approach we project all the members of the wind ensemble over the EOF base used in the wind regime at different moments (see Fig 5. 32). It can be seen how the spectra of the forecast error are very variable in time. The importance of the different modes change along the simulation as it was expected since the error dynamics is non-stationary.

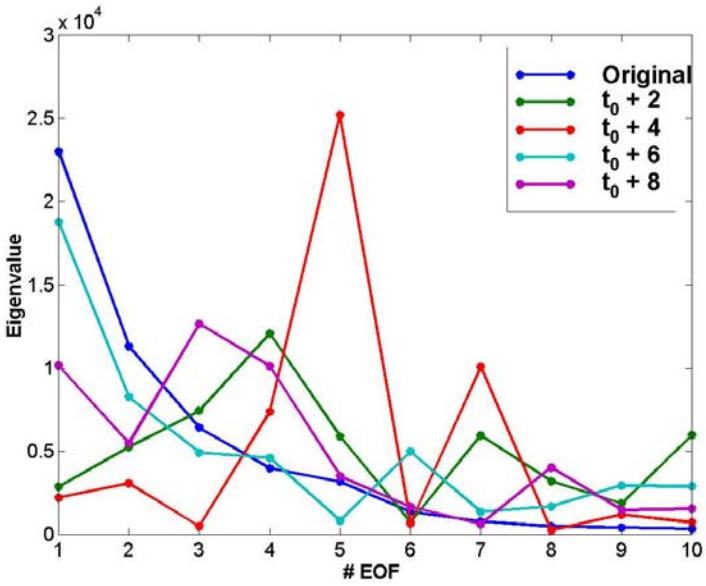

Fig 5. 32: Forecast error computed using (5.15). The members of wind ensemble have been projected over the EOF base. The forecast error spectra obtained at different moments is compared with the original spectra used in the wind regime experiments.

After seeing this variability, it seems that fixing the error forecast spectrum is a crude approximation that must be evaluated. To do this we modify the error forecast spectrum every assimilation cycle to follow the results showed in Fig 5. 32. We apply this method in the wind regime assimilating data from the fast network delayed two days. We have chosen this configuration because ,a priori, it seems the most sensible to changes in the EOF base.

The results of this experience are shown in Fig 5. 33 and it can be seen that there is no clear improvement. The only advantage is that the worsening observed in the first days with the fixed forecast error spectrum is reduced but at the same time there is less improvement in the temperature and elevation fields. It seems that what is happening is that the scheme of assimilation is able to decide which are the more suitable modes and to weight them properly just using the information contained in data.

In conclusion we have seen that the values used for the error forecast spectra are not really influential into the assimilation procedure if there are enough data. In cases where there are few data or the information provided by them is contradictory (i.e. if they correspond to different error processes), the choice of the error structures will be more influenced by the forecast errors used, and, consequently, this approach could be considered.

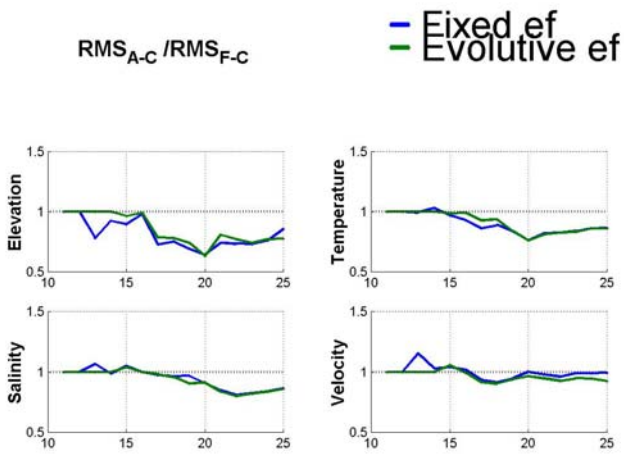

Fig 5. 33: Comparison of rms ratio using the fixed values for the forecast errors (blue line) and using the pre-computed evolution for the forecast errors. The assimilation is done using the fast network in the wind regime.

5.8.4 Is the EnKF a good alternative?

To solve the problems showed above the most natural possibility is to use the Ensemble Kalman Filter. This filter works in the following way: Instead of explicitely compute the evolution of the forecast error covariance matrix, which is too expensive and do not guarantee optimality in highly non-linear regimes, an ensemble of model states is evolved in time and the error statistics is computed from the ensemble of results. The main advantage of this filter is that the error statistics evolve in time in a natural way solving the problems showed above. On the other hand, the main shortcoming of this option is the way the members of the ensemble are perturbed.

In order to test if the EnKF is a viable option we implement a "pseudo" EnKF where we run an ensemble of 20 simulations. Data is assimilated with the SEQUOIA system in all the members until day 16 (just after the wind burst). At day 16 we compute the EOFs from the ensemble of model results and we use them to assimilate data in the free run. In other words, the EOF base used for assimilating data after the wind burst is obtained from and ensemble of model results. The difference with the actual EnKF is that in the original formulation there is no order reduction via the EOF base. Nevertheless, being the EOF spectra quite red, the problem become comparable and our configuration is equivalent to the actual EnKF. A sketch of the procedure is shown in Fig 5. 34

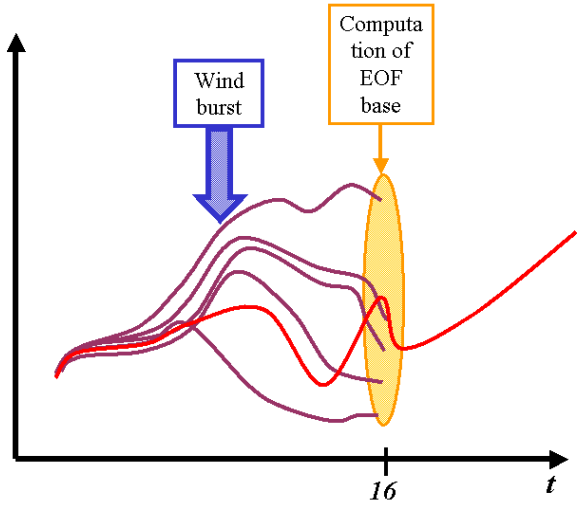

Fig 5. 34: Sketch of the pseudo EnKF strategy followed. An ensemble of model states is evolved in time until day 16 where the variance is maximum. Then, an EOF base is computed and data is assimilated in the red trajectory using it.

The errors associated to the current characterization are quite stationary, so we carry on the test considering errors in the wind forcing. The ensemble of models is directly obtained from the wind ensemble (cf. chapter 4) and the data has been obtained from the classic network because it provides enough information during all the assimilation cycles.

Fig 5. 35 displays the comparison of the rms ratio using the pseudo EnKF and the standard procedure in the wind regime. EOFs from the ensemble of 20 members have been obtained just at the moment of the assimilation in the third cycle. They have been used for assimilating in that cycle and the following. It can be seen how at day 16, when those EOFs have been computed and used, the improvement is really important in temperature and salinity, which in our case are the main variables as they represent the low frequency component of the variability. This means that the pre-computed EOF base doesn't contain all the necessary structures. After that assimilation cycle the results get worse quite fast. The reason is that the modes obtained are not at all representative of the processes present later on.

To sum up, it seems that the EnKF would introduce an interesting benefit but it should run continuously because the error modes are just representative of the error structures at a given time. As the main handicap of this approach is how to define the perturbations of the ensemble, another possibility could be to keep one fixed base, which would include mainly stationary error structures, and to enrich it with the modes obtained from reduced ensembles where the non-stationary part would be investigated.

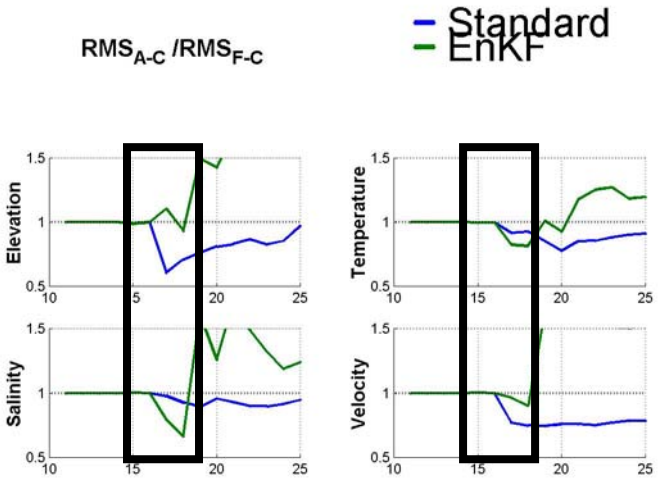

Fig 5. 35: Comparison of the results using the standard configuration for assimilating data of the classic network (blue) and when using the pseudo-EnKF (green). The frame shows the period when the EOFs from the small ensemble have been computed.

5.8.5 Observational errors

The values used for the observational errors are mostly instrumental. On the other hand, it has already been mentioned in section 5.4 that we should also include representativity errors due to the non inclusion of the null subspace. The problem is how to quantify these errors. In our case we have done crude estimations of them so it would be interesting to see what happens if those values are modified. When they are increased, the corrections become weaker as it was expected, and the assimilation doesn't introduce a clear gain.

More interesting is the case where the observational errors are reduced. In particular, we focus into the case of the satellite network. It has been mentioned before that one of the reasons (if not the main one) of the poor performance of this network was the big observational error associated to the SST measurements compared to the model variability. We think that the values used are quite reasonable (0.8ºC) considering both the instrumental and the representativity errors. Nevertheless, the precision of an instrument is something that can easily evolve with the technological improvements. In consequence, we wanted to test what would be the performance of the satellite network if the errors in the satellite measurements were reduced. We run in the current and wind regimes with the same satellite network configuration but using an observational error for the SST of 0.1ºC and 1cm for the altimeter measurements.

Fig 5. 36 displays the comparison of the rms ratio when using the standard configuration and when using the reduced errors. In the current regime, the fast evolving components (elevation and velocity) show a worsening in the results while the low components (temperature

and salinity) show a significant improvement. In the wind regime the corrections are more important than when the standard values were used. Before the wind burst (day 15) the results worsen while after it the assimilation introduces a clear improvement.

These differences between the use of both values for the observational error come from the fact that the typical error was comparable to the ensemble variability, so inducing low corrections. When that value is reduced, the information provided by the measurements is taking in consideration and assimilation becomes useful.

In conclusion, we see that the observational errors have a maximum value, which limits their range of usefulness. If those errors are too big (compared to the system variability), the data will not be taken in consideration and assimilation will be useless. In the particular case of the satellite network, it has proven to be effective specially for correcting the temperature field. Nevertheless, surface information is still insufficient to properly correct the 3D structure, especially in cases were the surface mixed layer significantly uncouples surface and sub-surface processes.

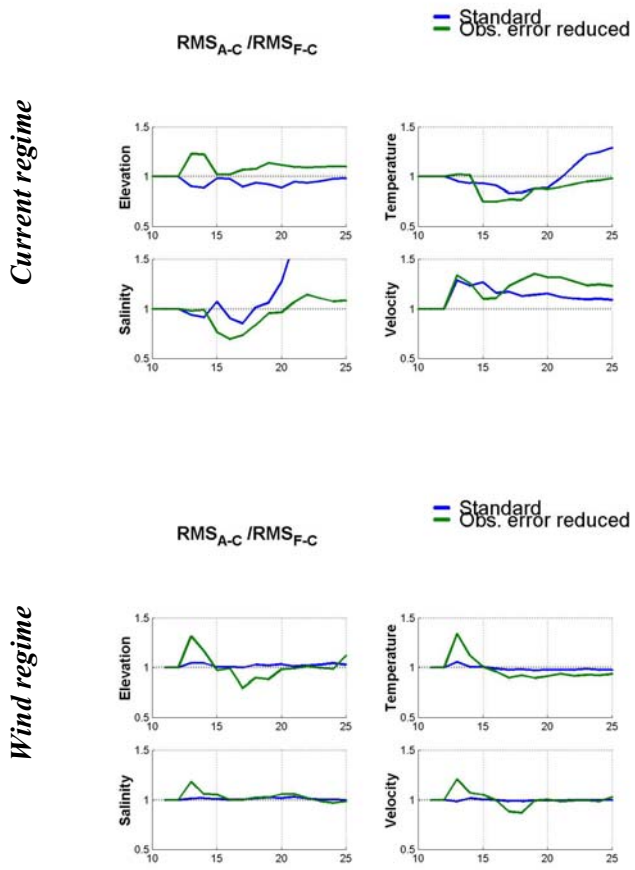

Fig 5. 36: Rms ratio when the observational error associated to the satellite measurements is reduced in the current regime (top) and the wind regime (bottom)

5.8.6 Use of smoother/filter mode

The next sensitivity test is to evaluate if the smoother mode improves the assimilation in front of the filter mode. It must be noted that in our case the smoother has not the same properties as the typical Kalman smoother (for instance) as the forecast error covariance matrix is fixed and the future information is not used to improve that matrix in the present time. The difference between both modes in our case is linked to the quantity of data used to do the analysis. In the smoother mode more data are used (past and future) and, in practice, it is similar to consider an assimilation cycle of double length.

Fig 5. 37 shows the comparison between the smoother and the filter mode when assimilating data from the classic network in the wind regime (in the classic regime the results of both modes are quite similar). The performance of the filter is higher because the information obtained in each assimilation cycle probably corresponds to the same error structure while in the smoother mode the information can come from different error processes (see discussion in section 5.6).

Consistent results are obtained when a shorter assimilation cycle is used. For regimes with a highly variable error dynamics it is more recommendable to assimilate more frequently if enough data is available. Doing this we ensure that the error structure captured by the different observations correspond to the same process and, therefore, the analysis is more optimal. It must be noted that enough data should be available to do a proper analysis, so an extremely short assimilation cycle would not be useful because there would be not enough data to select the adequate EOFs.

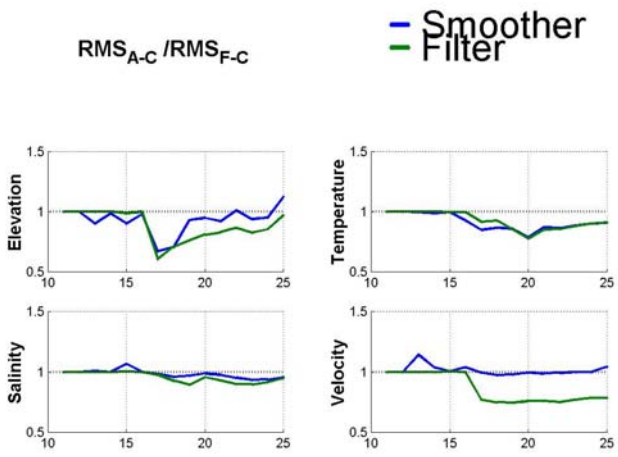

Fig 5. 37: Rms ratio when assimilating in the smoother mode (blue) and in the filter mode (green). The classic network has been used in the experiment.

5.9 Discussion

Limitations of the experimental protocol

The main thing that must be discussed about the work presented above is the limitations of the experiment protocol used. It is important to remark until which point the work done and the conclusions obtained are dependent on the choices adopted or if they can be extrapolated to other similar systems.

The first big issue is if the error dynamics has been correctly described. We think that the method adopted with the ensemble simulations is quite robust and provides enough information to characterize the error dynamics. Its shortcomings are linked to the model configuration, which has some limitations as the lack of imported variability. In consequence we focus in the local effects of the current depth. Nevertheless, even in our simplified configuration, we consider that the main characteristics of the error sources have been captured.

In the case of the errors in the characterization of the slope current, we have found that they have a small impact over the free surface elevation. If the current transport is similar, the gradients of the surface elevation would be the same and it would be difficult to trace the current in the elevation field. In addition to that, this field is much more influenced by the wind instantaneously masking the signal of the current in surface. Also the surface mixed layer reduces the density gradients associated to the current, so masking again their trace in the surface temperature or salinity.

The characterization of the errors induce by the uncertainties in the wind dynamics is also adequate although maybe insufficient. We have seen that they are non stationary and highly dependent on the wind regime. In consequence it is very difficult to define a EOF base, which includes all the cases (i.e. all wind regimes) to ensure that the base is general enough.

In addition to the limitations of the description of the error dynamics, there is the fact that the twin experiments is an over-optimistic framework. We agree that the improvements observed would not be so good in a real case but the behaviour of the assimilation procedure would be the same. Also, for the goal of the work, which is to evaluate the performance of different observational networks, this over-optimism is not a problem.

A real limitation of the work done is that the conclusions obtained are linked to the defined error sources (which we consider that are the most relevant) but we cannot directly extrapolate our results to other error sources as the bathymetry or some model parametrizations.

Another issue that must be addressed is the choice of the assimilation scheme, why we have adopted a reduced order interpolation method instead of other possibilities as the SEEK filter or the EnKF. The main advantage of the MANTA kernel is that it is very cheap. The

computational burden is almost unaltered by assimilation. Another positive feature is that error dynamics is obtained from ensemble simulations specially designed to characterize them. The variability EOFs are easier to obtain but they do not ensure a good representation of the error modes.

The main handicap is the stationarity of the error covariance matrix. We have shown how, in non-stationary error regimes, the quality of the assimilation is reduced mainly because the EOF base doesn't have the correct modes to describe the errors. In that case, we think that the best alternative would be to use an EnKF to carry on the evolution of the non-stationary part of the error dynamics. In other words, we could use a fixed EOF base as complete as possible and to enrich it with the results of a small ensemble.

Finally, there is the problem of the step-like evolution of the variables. This is a typical feature of the sequential assimilation that could be solved using the Incremental Analysis Update (Bloom et al., 1996). In that case the correction is partially applied every time step in the assimilation cycle, so ensuring a smoother transition of the variables. Nevertheless there is no guarantee that the model trajectories are physical, so maybe the method could be improved if the correction is forced to follow some physical rule as the geostrophic balance.

System configuration

Once the main limitations of the experimental protocol have been enlightened, we can discuss the features of the assimilation.

First of all, the EOFs used to define the error subspace must be adequate to the problem that is addressed, and they must be able to describe the error dynamics that is expected to be present in the system. In consequence, some practical issues as the normalization or convergence must be considered carefully (see chapter 4 for extensive discussion about that). For instance, if the processes in the river plume dominate the EOF they will not be able to correct anything else than the plume.

Another point to be considered is that if the error processes included in the base are not those present in reality, the assimilation would be useless. If there are enough data, the projection of the distances model-obs over the modes would be null. In case of having few data there is the risk of introduce unrealistical corrections.

A way of overcome this problem is to have the most complete EOF base. We have seen that the juxtaposed base is a feasible alternative, so the best we could do is to put together different modes of error obtained from the ensemble simulations. Even, it could be possible to enrich it with modes of variability, if they are available, or with modes obtained from special normalizations (i.e. to extract information about the plume or processes in certain regions).

Once the EOF base is well suited for the assimilation problem, they provide some useful properties to the corrections. First of all, the corrections are quite stable and there are just some

transients in the surface elevation, which damp after one day. This is because the modes are multivariate and have been obtained from model results, which helps to the corrections be in equilibrium with the model dynamics.

The second main property is that corrections are global. In other words, data limited in space can be used to correct the model state in other regions. In coastal implementations this is a quite good feature because in small areas all the processes are more or less related. For instance, the slope current characteristics upstream and downstream are closely linked, and the wind structures (and therefore the error structures linked to it) usually have a size comparable to the model domain. On the other hand, for bigger regions this globality of the corrections could become a shortcoming. In regional or basin scales it is not realistic to allow corrections at long distances, so a localization function should be introduced to avoid the long distance effects.

Finally, the third main property, and probably the most important, is that corrections are multivariate. This property is coherent with the physical characteristics of the problem as far as in reality all the variables are linked, so information from one of them can help to correct the others. Consequently, we have seen how temperature data can help to correct salinity or surface elevation. This feature is quite powerful but some considerations must be done. The most important is that we have to be sure that the errors that affect different variables are the same. For instance, an error in the wind field would affect the surface elevation but will have small impact on the subsurface density structure. If data is telling us that the error is in the 3D density structure, it will correct the surface elevation coherently even if that variable is dominated by the errors in the wind field. In consequence, the solution in that field could be degraded.

Another choice adopted is the forecast errors, which, in our case, have been defined from the eigenvalues associated to the EOFs. We have seen that the choice is not too important if there are enough data. In that case, the data would "decide" which are the suitable modes to be used and the weight given by the forecast error would be useless. In that case the most important is the relation between the different modes, more than the concrete value they have. The problem appears when there is not enough data. In that case, the system would give priority to the modes with a bigger forecast error associated, so the choice adopted would be more relevant.

We have also seen that the time evolution of the forecast error spectrum is not a crucial issue (considering again that enough data is available).

Finally, there is the choice of the assimilation cycle length, which defines the amount of data that is included to do the analysis. If we deal with stationary processes it is unimportant but for processes, which are highly non-stationary, as those associated to wind errors, the duration of the assimilation cycle is a key point.

On one hand, it is important to have a cycle long enough to include enough data to properly do the analysis. Also, a cycle that is shorter than the transient period, which appears after each analysis, is dangerous (i.e. if there are important oscillations of the surface elevation due to the transients, the distance model-obs would be meaningless and could introduce lot of noise).

On the other hand, if the cycle is too long we would include different error structures in the same analysis and this would be suboptimal. An example could be if the wind changes its direction during the same cycle. Some of the data would have information about the errors associated to a Mestral event (for instance), while the rest would describe the errors associated to a Llevant regime. When doing the analysis, both pieces of information would be together and it would not be possible to define which one is the error that must be corrected.

Finally, we wanted to comment the possibility mentioned above about using an Ensemble Kalman Filter. We have shown how its performance is higher than the conventional filter and how it is better suited for evolving error structures. Nevertheless it must be kept on mind that it is much more expensive, and the problem of defining the error sources (the perturbations of the ensembles) is still present. A possible way to marry both approaches would be the one already presented above. It can be imagined to define a quite complete EOF base describing much of the stationary error processes, as those linked to the current characteristics, or the most typical error structures. Then, a small ensemble of model runs should be carried on to define the structure of the errors associated to variable error sources (i.e. the wind). That description would complement the information present in the fixed EOF base. In that case a reduced number of members would be enough reducing significantly the cost of the assimilation procedure. On the other hand most of the problems of using a fixed base would be overcome.

The observational networks

The different experiences done suggest that the quality of the different networks depends on the kind of error that must be corrected (i.e. deep moorings would be useless to correct the effects of errors in the wind field, which are restricted to the first 50m). In consequence, it is important to have a good estimation of which are those errors to properly design the observational program.

Another point that must be considered is that different networks are better suited to correct some variables than others. It should be decided which are the most important fields and the time scales of interest.

Finally, another parameter that should be kept on mind is the characteristics of the model configuration. For instance, if the model is not able to properly solve the surface mixed layer it is useless to try to correct the results there in because the model will degrade the solution

quickly. The assimilation must be viewed as a tool to correct small errors and not as a magical engine capable to convert a simple model into a perfect forecasting system.

From the results obtained by the twin experiments, and always within the limits of our experimental protocol, we can sum up the characteristics of the different networks looking at each kind of error separately.

To **correct errors in the slope current** 3D measurements are needed. As the current is associated to the 3D field, surface or point data are not enough. Satellite data has a too big observational error associated and the surface mixed layer difficults the extrapolation of information from surface to deeper layers. On the other hand, punctual data as the current meters can help but they provide a limited coverage, which reduces its effectiveness, and a longer time period of assimilation is needed.

There are also indications that the area covered by the network is of secondary importance. Data localized in a small area can allow the correction of the slope current characteristics in all the domain. This is coherent with the fact that the slope current error is a structure present in all the domain, which induce strong correlations between upstream and downstream. It is therefore logical than data of the current in one part of the domain affects the characteristics in the other parts. So, the location of the data is not important and it is just important to be 3D.

Finally, the time spent to take the observations is also unimportant. As the error dynamics associated to the slope current is quite stationary, the time dimension has no effect. In consequence the three networks with 3D measurements (classic, cheap and fast) but with different durations have similar performances.

To **correct errors due to the wind uncertainties** data should be obtained frequently and specially during (or just after) strong wind events. It is important to have data in places and moments where the variance is important. If there is no model variance, the assimilation cannot correct anything. This is why it is more interesting to have data when (or where) uncertainties are more important. On the other hand the error dynamics associated to the wind is highly non-stationary, so it is important to have data frequently enough to be able to capture the different error processes.

The effect of the wind uncertainties is restricted to the first 50m, so deep data is not necessary. Deep CTD measurements or deep current meters would not help to correct the effects of the wind errors. On the other hand, satellite data is again not enough since its observational error is too important compared to the model variability.

About the satellite data some remarks must be done. In coastal applications the altimetry gives a poor resolution (at least in the present configurations) both in time or space and its observational error is comparable to the anomalies of sea level that are expected to be observed. In other words, the signal of the currents in the spatial scales (limited domains) where we are

working are of the same order of magnitude than the observational error associated to the altimeter (5cm), so this source of information is not quite useful. In addition to that, for a limited domain there will be just one or two altimetric tracks passing across the domain with a temporal resolution of 10 days. If we consider that data near the coast cannot be used, we find that the total amount of data is quite limited. In consequence the present available altimeter configuration cannot help too much the coastal models. It must be noted that new satellite configurations providing more and more reliable data could overcome those limitations. Also, for greater domains (regional scales), altimetry could probably has a greater contribution.

The SST data is more useful as it provides a good spatial resolution (~1km) with a high frequency (12h-24h). The problem is that its observational error is again too important compared to the model variability in the coastal models. On the other hand, we have seen that an improvement of the quality of SST data could convert this data into an useful source of information. Nevertheless it must not be forgotten that it is just surface information, so the representativity errors will be also present, and some physical processes as the surface mixed layer can difficult the extrapolation of information from surface to deeper layers.

Finally a last remark must be done about the use of one or other observational network. Although it seems a trivial conclusion and a bit disappointing after all the work presented before, we just can say that there is not possible to do an unique and universal recommendation: the choice of the best suited observational network is problem dependent.

Different suggestions could be done if the network is planned to sample a given physical process, to be assimilated into a numerical model or to be used for operational purposes.

For sampling a concrete process its characteristics should be very present when the network is design. Spatial coverage, sinoptic problems and the temporal scales should be defined according to the features of the process.

If data will be assimilated in a numerical model in a non-operational framework the requirements are different. The spatial coverage is not a determinant issue as the model can physically interpolate the data. The temporal dimension and the sinopticity is not a problem either because the model also interpolates in time. The main issue that should be addressed is what are the errors in the model, what do we want to correct. Then, the necessary data can be defined. We can know if it is more interesting to have 3D data, if deep information is needed or if a continuous sampling is desirable. Usually, a network with a good spatial coverage and a good temporal coverage is preferred. A high horizontal resolution is probably not needed and it would be better to cover a greater extension. It is also recommendable to cover a long period or to repeat the measurement stations in order to better constrain the temporal evolution of the model.

Finally, for an operational system there are several criteria to put together. First of all there are the practical issues, which are the most limiting. For instance it must be considered the cost of the system or the facilities for the maintenance. A second issue would be which are the variables or processes in the operational system that is intended to be corrected. It is not the same to try to correct the surface circulation in a bay that to correct the thermocline depth in the Mediterranean basin. As it was mentioned before, from that approach the characteristics of the network could be defined. Finally, the performance of the different networks can be considered. This is linked to the quality of the available data, its location in time and/or space and the needs of the modelling system.

5.10 Conclusions

In this chapter we have implemented a data assimilation system especially well suited for the shelf and coastal regions. Although the implementation is particular for the Catalan continental shelf, the methodology and most of the general conclusions of the assimilation are extrapolable to other coastal areas.

We have implemented a reduced order optimal interpolation code (the MANTA kernel of the SEQUOIA data assimilation system) interfaced with the SYMPHONIE model. The reduced order space is defined using EOFs obtained from ensemble simulations (cf. chapter 4) and the spectrum of forecast error are prescribed from the eigenvalues of the base and are fixed constant during all the assimilation.

The system has been tested in different twin experiments configurations in order to evaluate the characteristics of the assimilation procedure and the performance of different observational networks. The assimilation works well being quite stable and just some transients are present in the free surface elevation field during one day after the analysis.

After carrying on several sensitivity tests we have found that the EOF base should be viewed as a toolbox where different modes of error can be put together to provide the assimilation procedure with enough resources to characterize the error structures. Then, if enough data is available, the assimilation is able to select the correct combination of modes.

The problem of non-stationary errors leads us to suggest that the best configuration for coastal problems would be the use of a hybrid system. This system would be formed by a fixed EOF base, which would contain most of the stationary error structures and complemented with the information provided by an ensemble Kalman Filter with a small number of runs, which would describe the non-stationary error dynamics.

Applying the system to the different observational networks, we have seen that their performance depend on the kind of errors that have to be corrected. To correct errors in the

slope current characterization 3D measurements are needed at any time while for the wind errors a frequent sampling in the surface layer is recommended.

If a real monitoring network should be designed, new experiments should be done using different combinations of the elements showed here. In any case, it would be necessary to have a validated modelling system and enough data to characterize the errors of the system.

CONCLUSIONS, PERSPECTIVES AND FINAL THOUGHTS

"La vida es siempre urgente. Y la cultura,
que no es sino su interpretación, no puede
tampoco esperar"
(Ortega y Gasset)

"L'educació científica dels joves és
al menys tan important, inclús més,
que la pròpia investigació"
(Glenn Theodore Seaborg)

6 CONCLUSIONS, PERSPECTIVES AND FINAL THOUGHTS

Conclusions

The main objective of the thesis was to implement a suitable data assimilation scheme into a numerical model of the Catalan continental shelf. This goal has been successfully achieved as far as the SEQUOIA data assimilation system has been coupled to the SYMPHONIE model, implemented in the study area and tested in realistic configurations. Nevertheless, this is too simplistic and a more detailed review of the steps done until reaching that goal must be done.

In a first phase we wanted to characterize the dynamical processes in the region but not just using the information in literature. We have retrieved several underused datasets from the FANS and YOYO projects and analysed them trying to confirm and complement the previous work done in the region. Namely, we had current meter and temperature time series for the period between 1996-1999 in different locations over the shelf and the slope. Using this data and some complementary information from CTD campaigns and satellite images (SST, SeaWifs) we could do a complete review of the dynamics in the shelf and slope areas.

Over the slope there is a quasi-permanent current in geostrophic equilibrium strongly constrained by the topography. Its vertical structure is mainly barotropic with a certain contribution of the first Kelvin mode. The high frequency variability is controlled by near-inertial processes, and below 100m only several isolated wind events have some effect. Also, we have tracked the apparition of gyroscopic waves in periods when the water column is homogenized. The low frequency variability is mainly in semi-geostrophic equilibrium and neither the wind nor the pressure has a remarkable effect over it. We have also proposed resonance phenomena as the explanation for the 14 days current oscillations. Finally we have shown the propagation of waves along the slope and the advection of anticyclonic eddies and how in certain periods, the current can be reversed.

Over the shelf there is no clear dynamical pattern and the vertical structure of the circulation is well represented by the barotropic mode and the first Kelvin mode. The apparition of the thermocline in summer unlinks the processes between surface and bottom. The variability is dominated by the oscillations in the inertial-diurnal band induced by the wind, although we have also observed the effects of the slope circulation. The Ebre river plume doesn't seem to be responsible of the movements in the observing points but it has an influence in the interaction of surface processes with what happens in deeper levels.

The next step in the way fixed in this thesis was to implement a numerical model of the shelf-slope region. It should be realistic enough to reproduce the main processes observed from data. The SYMPHONIE model has been implemented in the southern Catalan shelf in a high-resolution configuration. The initial and open boundary conditions have been obtained from the MPV method and real atmospheric forcing has been applied. The validation against data has shown that model reproduces the slope current and the main processes over the shelf although the lack of slope current variability is a shortcoming.

The model has been used to characterize the evolution of a topographic Rossby wave over the shelf widening and its implications over the shelf dynamics. The 3D circulation induced by the principal wind regimes has also been described as well as the effects of a narrow wind over a shelf region. Finally, we have characterized the shelf-slope exchanges depending if the forcing factor was the wind or the slope current variability.

Once the modelling system was set up, the next phase was to explore its errors and to characterize them spatially and temporally. To do that we have used stochastic modelling .The underlying idea is to take a reference simulation that we consider is a good representation of reality and to apply some perturbations to a model parameter. The introduced perturbation (i.e. in the wind or slope current characterization) can be considered as a system error and we can see how this perturbation/error evolves in time. In order to be able to do a statistical description of the dynamics of that error, we run an ensemble of model realizations were the parameters have been randomly perturbed. Thus, even if we do not know the actual error we can characterize its statistical properties.

We have identified as the main sources of error the characterization of the slope current and the wind field. Both kinds of error have different properties. The errors in the slope current are stationary but non-linear while the uncertainties in the wind field induce errors with a linear behaviour but highly non-stationary. The EOF decomposition of the error structures allowed us to define the reduction operator S that would be used in the data assimilation scheme. A key point is that the reduced order subspace is defined from multivariate EOFs obtained from model results, which is a significant improvement related to the usual simplified schemes.

The last step has been to couple the SEQUOIA data assimilation system with the SYMPHONIE model using the error characterization obtained from the ensemble modelling approach. To test its performance we have run the system in a twin experiments framework to study the capabilities of different observational networks to correct errors in the wind or the slope current characterization.

The assimilation worked well from a technical point of view and allows us to better understand the advantages and shortcomings of the system. We have found that the EOF base should be viewed as a toolbox where different modes of error can be put together to provide the assimilation procedure with enough resources to characterize the error structures. If enough data is available, the system is able to select the correct combination of modes, which describes the error of the modelling system. Applying the assimilation system to different observational networks we have seen that their performance and suitability depend on the kind of errors to be corrected. The errors in the slope current structure need 3D data but its location and time of acquisition are not important, as they are global and stationary errors. On the other hand, the uncertainties on the wind field introduce non-stationary and more local errors, so the requirements for the observational network are different. Data can be obtained in the shallower layers but a continuous acquisition is needed to constraint the evolving error structures.

Perspectives

All this work has allowed to explore different ways of study the shelf-slope dynamics and has provided us with some useful tools for monitoring and forecasting the coastal region. At the same time, there are several unresolved questions that could be considered to define new work lines to improve the knowledge of the Catalan continental shelf dynamics and the data assimilation systems for coastal regions.

First of all, the propagation of structures along the slope is not well understood yet. There are some evidences of waves propagation or eddies advection but the interaction of those processes with the local dynamics is not well established. On the other hand, the dynamics over the shelf is not completely explained by the wind and river forcing so more efforts in that sense should be done.

A basic point to solve these issues is to have good datasets. Namely, a dense network of moorings covering the shelf and slope before and after the shelf widening would definitively help to clarify those questions. In addition, it would help to understand the shelf-slope exchanges and the mutual influence between the shelf processes and the open sea dynamics.

The validated modelling system is also still useful and could be exploited to properly characterize the plume dynamics establishing a complete set of scenarios where all the basic forcings (wind, river runoff, slope current) act in a realistic way. On addition to that it could be used to complement the understanding of the advection of structures and their influence in the shelf-slope exchanges.

Nevertheless, for progressing into the modelling work it should be noted that the configuration used is realistic but has a main shortcoming, which is the lack of imported

variability through its boundaries. To solve this, the model could be easily nested into a coarser resolution model which resolves the general dynamics of the NW-med and which provides a correct variability through the boundaries. Until now this was not possible to do because the available regional models didn't properly solve the characteristics of the region but in the frame of some on going operational programs (MFS, ESEOO) this could be sorted out. When this happens it will be straightforward to implement in the nested model the developments done in this thesis.

Finally, the future work that should be done in the data assimilation in coastal regions is quite extensive.

First, the characterization of the error dynamics should be reviewed using a more general model configuration. Namely using a nested model, which would provide a richer dynamics. In any case we think that it would be worthless to re-do the work if the new modelling system has not been validated and has not proven to do a good job in modelling the shelf-slope processes.

Once those requirements were fulfilled, the exploration of the error-subspace could be done increasing the length of the simulations periods and the number of parameters to perturb. Namely it would be interesting to explore, for instance, the effects of the bathymetric errors, the variability of the slope processes and the plume related parameters.

The following step that could be done in the errors characterization should be to use real data to evaluate the model performance. To do this extensive datasets should be used in long periods, and special care should be taken about the 3D structure of the errors. The new GLIDER programs (autonomous submarines) would probably help significantly to this.

A second line of work to improve the assimilation in coastal areas would be to review the data assimilation scheme. The stationarity of the EOF base has proven to be insufficient for non-stationary error regimes, as those expected in shelf-slope areas. The EnKF seems a good alternative but it also has some shortcomings. Our proposal would be to use a hybrid filter were a fixed EOF base would describe the stationary part of the error subspace and a small ensemble of model realizations would provide the description of the non-stationary errors.

Final thoughts

In these lasts paragraphs of the thesis I forget the royal we (customary in the scientific speech) because I do not want to talk about science but about how do we do science. A thesis is much more than just several hundreds of pages. It is a path of several years of work where the person who does it invests more than just his time. In consequence, I consider that the book that summarizes the scientific results of these years is the correct place to summarize some of the non-scientific experience gained along this period. Obviously these are just some considerations from the humble point of view of somebody who have just started on that business, but if you, the reader, are not agree, I am open to discussion as I am for the rest of the thesis.

First of all I wanted to comment something that I'm thinking about since I read the Umberto Eco's book "Come si fa una tesi di Laurea" (quite recommendable lecture): The role of the researchers in training period (also called PhD students) in the scientific community.

Usually, these people decide to "taste" the science beginning a PhD thesis. To do that they become part of a scientific team and, automatically, a mutual relation is established between the student and the group receiving him (or her). On one hand the team provides the resources to the student to develop his scientific skills. On the other hand he provides his work and efforts to develop some research lines that otherwise would not be possible to develop due to the lack of human resources.

Until here it seems quite fair. The exchange of work for knowledge is a good compromise and lots of times it is quite satisfactory for both parts.

Sometimes it is not.

It is a clear fact that nobody does a PhD, especially in Europe, neither for the social recognition nor for the economic benefits. It is almost done for a personal profit. In addition to that, to successfully finish a PhD, a strong load of motivation and enthusiasm is needed. Consequently, it is common that the person who begins a thesis tries to do his best working hard. So, a priori, the student usually fulfills his part of the agreement providing his work to the team. One evidence of this is that the researchers in training period participate in the 80% of the scientific publications in Spain (I have no information about the rest of Europe).

On the other side of the agreement there is the formation that he should receive. The problem often appears when the team that accepted this person forgets the implicit commitment acquired and the scientific formation of the student is no longer a priority. He is considered as another researcher (obviously low qualified and usually quite cheap). In consequence, the student (who no longer studies) doesn't receive the adequate training that would allow him to continue an independent scientific career once the PhD period will be finished.

When this situation is reached, the initial agreement is no longer fair for obvious reasons.

On addition to that, the serious question is that people who decide to start a thesis do not think on it as a common job, and they do not just invest their time. They also invest lots of energies and hopes, so the disappointment is much greater.

In this kind of situations, it is never the fault of a single person but it is usually due to the dynamics of a group, to the inertia of a working system imposed for different reasons. Also, it is not exclusive of a university or a country. I have met quite a lot of people coming from very different backgrounds who were in such a situation. In any case, the fact that certain behaviour is generalized does not mean that it is right.

To finish this issue I just wanted to do a simply reflection.

I would request, that the first meeting between the student and his supervisor was to define the role of each one, its rights and its duties. As well as the student undertakes to work hard, the team who receives him should undertake to do its best to ensure his formation. On the other hand, if the student just will work in some scientific projects without any guarantee about his formation, then, simply, he should not be called student but (cheap) researcher.

The other subject I wanted to talk about is much more important.

We have commented in the introduction of the thesis that it is important to know and to monitorize the state of the sea. This has been the base of our approach. However, it wouldn't be useless to think during a while about what does *important* mean.

In the global context of societies, what we call problems from our privileged and well-off position are simply anecdotes. Doing a sincerity effort, we have to recognize that the applications that motivate our work are luxuries, and without them our life would not change significatively.

However, there are lots of places in the world where the problem of the water quality is not translated into a reduction of the tourism like here but into a matter of life and death. There are regions extremely sensitives to the sea state where the knowledge and the forecast of the sea caprices would clearly improve the quality of life.

With all this speech, I do not aim to depreciate what we are doing. It **IS** important, but maybe it is not applied were it should. Consequently, I would like to introduce a proposal.

The scientific world is made up of individuals that, due to their education and their social position, cannot hide behind the unconsciousness or ignorance to justify their passivity respect to what is happening in the world. As well as we have the privilege of working on science and to enjoy it, I think we have the obligation of finding the way to transmit what we learn to the places were research is just science-fiction because it is in that places where what we do would be really useful.

This obligation is even greater if we realize that our privileges are maintained over their penuries.

In consequence, I think that we all should be more conscious, from the PhD student to the education minister, that its neither fair nor logical to think that development is just a right for who can pay for it.

Between all the different levels of the scientific community, we should try to transmit our privileges to those who were not born with them. Obviously, the most convenient would be that the governments launch cooperation projects, but it is also important that each individual apply for the projects and take profit of the existing resources.

There is always a way to what is fair.

APPENDIX

VALIDATION OF ARPEGE WIND AND PRESSURE FIELDS

APPENDIX : VALIDATION OF ARPEGE WIND AND PRESSURE FIELDS

The ARPEGE model is an atmospheric model that is run operationally by Météo France (*www.meteofrance.fr*) since 1994. It provides 6-hours forecasts of the meteorological variables with a spatial resolution of ~25km in our region.

To validate the results of ARPEGE wind fields we compare its results with the data obtained in the Casablanca station (open sea). The atmospheric pressure time series (see Fig A. 1) shows a high agreement between model and observations with just a constant bias of 12mbar. This bias could be produced by a default in the instrumental calibration or by a mismatching in the measurement height. In any case, the mean value has no influence over the results and just its variability is important. The results for other stations over the coast and in different locations show the same agreement, so we can be confident enough on the spatial structure of the ARPEGE results for the atmospheric pressure.

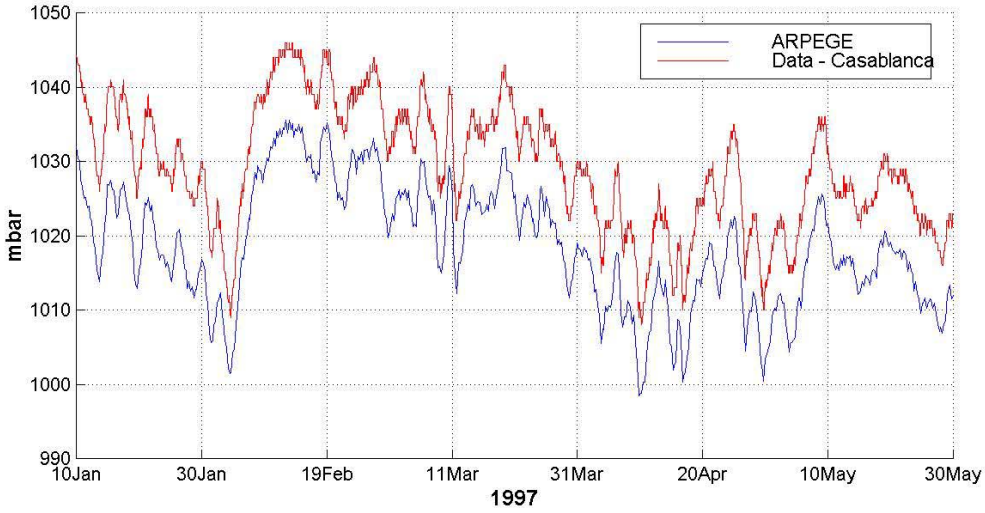

Fig A. 1: Comparison of atmospheric pressure in the Casablanca station (open sea).

The wind field results are not so good (see Fig A. 2). Most of the events are reproduced but the ARPEGE winds are, in general, a bit weaker than measurements. On the other hand the wind direction presents some problems (i.e.: see disagreements in the NS component where it seems the model has the opposite sign).

The comparison with coastal stations results worse, mainly due to the coarse resolution of ARPEGE and its difficulties to properly resolve the local orography. Nevertheless the quality of

ARPEGE results in the open sea is enough to guarantee a realistic atmospheric forcing of the coastal model.

The errors in the ARPEGE directions will not be a problem in the frame of this thesis. When we use the ARPEGE data to fill gaps in the measured wind time series (chapter 2), we just use the intensity of the wind, which is of quite acceptable quality. In the modelling part, meteo model results are used to do a realistic (but not real) forcing of the model. Although the wind structures are not perfectly place, they provide a realistic variability.

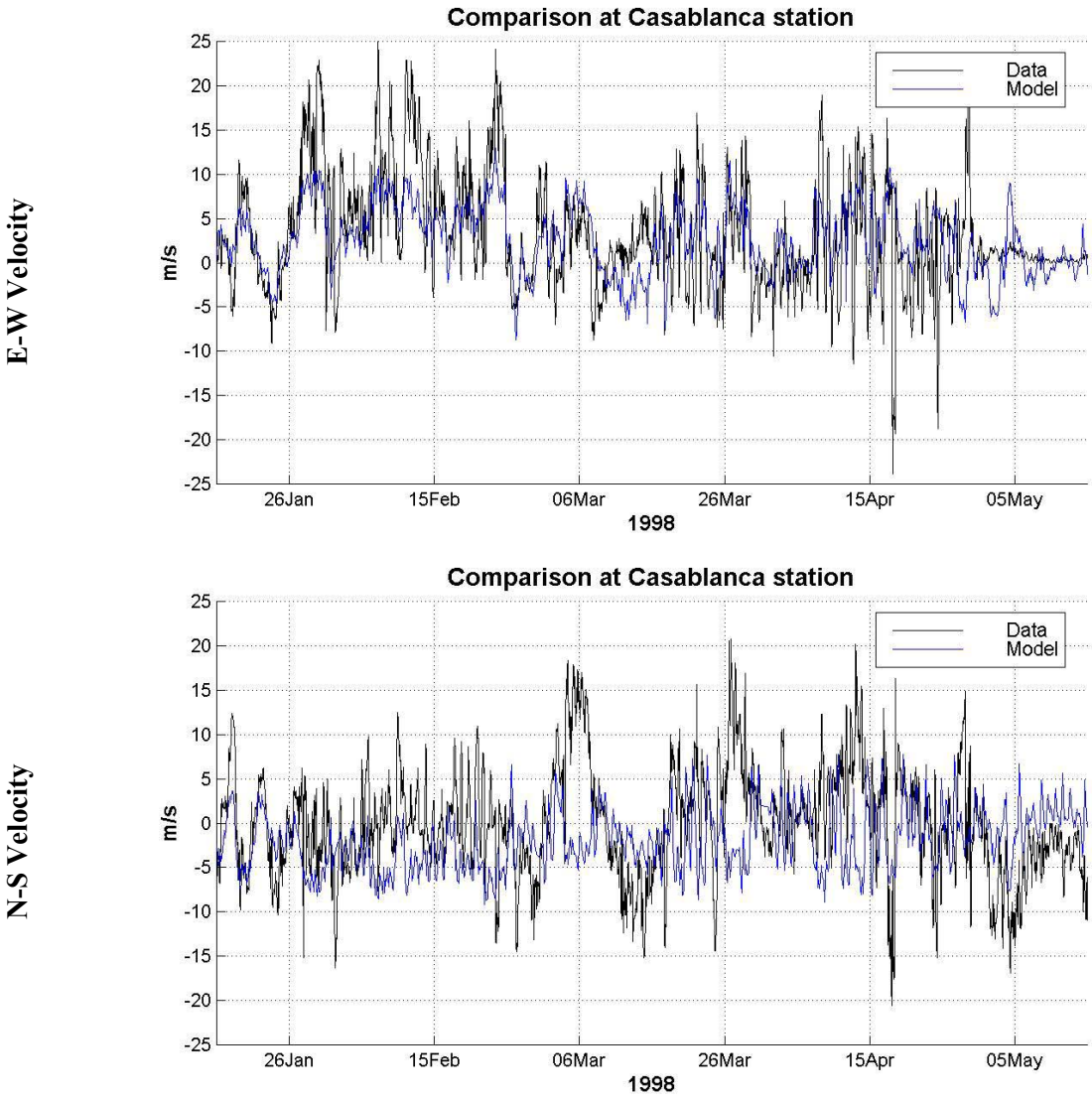

Fig A. 2: Comparison of atmospheric pressure in the Casablanca station (open sea).

REFERENCES

REFERENCES

Alberola,C. C. Millot and J. Font, On the seasonal and mesoscale variabilities of the Northern Current during the PRIMO-0 experiment in the western Mediterranean Sea, *Oceanol. Acta*, 18 (2), 163-192, 1995.

Arakawa, A.and M.J. Suarez, Vertical differencing of the primitive equations in sigma coordinates, *Mon. Weath. Rev.*, 111,pp. 34-45, 1983.

Arnau del Amo, P.A., Aspectos de la variabilidad de mesoescala de la circulacion marina en la plataforma continental catalana, *Tesis doctoral,*Universitat Politècnica de Catalunya, 2000.

Asselin, R., Frequency filters for time integrations, *Mon.Weath. Rev.,* 100, pp. 487-490, 1972.

Auclair F., Casitas S., Marsaleix P. Application of an inverse method to coastal modelling. *Journal of Atmospheric and Oceanic Technology*. 17, 1368-1391, 2000.

Auclair, F., P.Marsaleix, and P. de Mey, Space-time structure and dynamics of the forecast error in a coastal circulation model in the Gulf of Lions, *Dyn. Atmos. Oceans*, 36(4), 309-346, 2003.

Beckers, JM., Application of a 3D model to the Western Mediterranean, *Journal of Marine Systems*, 1:315-332, 1991.

Beckers J.M., 1994 b : On destabilizing implicit factors in discrete advection-diffusion equations. *J. Comp. Physics*, 111, pp.260-265.

Bennett, A.F.. Inverse Methods in Physical Oceanography. Cambridge University Press, Cambridge. 1992

Bennett, A. F., B. S. Chua, D. Ed. Harrison and M. J. McPhaden,: Generalized Inversion of Tropical Atmosphere-Ocean Data and a Coupled Model of the Tropical Pacific. II. The 1995-96 La Nina and 1997-1998 El Nino. *Journal of Climate*, **11**, 2770-2785., 2000.

Bethoux, J.P., X. Durrieu de Madron, F. Nyffeler and D. Tailliez, Deep water in the western Mediterranean: peculiar 1999 and 2000 characteristics, shelf formation hypothesis, variability since 1970 and geochemical inferences, *J. Mar. Syst.*, 33-34 (C), pp 117-131, 2002.

Bloom, S., L.L. Takacs, A. M. da Silva, and D. Ledvina, Data assimilation using incremental analysis updates. Mon. Wea. Rev., 124, 1256-1271., 1996

Blumberg, A.F. and G. Mellor, A description of a three dimensional coastal circulation model, in *Three-dimensional coastal ocean model*, edited by N. Heaps, 208 pp., 1987.

Bougeault, P. and P.Lacarrere, Parameterisation of orography-induced turbulence in a meso-beta scale model, *Mon.Weath.Rev.*, 117, pp 1872-1890, 1989.

Bouttier F., and P. Courtier Data assimilation concepts and methods ECMW technical reports http://www.ecmwf.int/newsevents/training/rcourse_notes/ 1999

Brink K. and D. Chapman, Programs for Computing Properties of Coastal-Trapped Waves and Wind-Driven Motions Over the Continental Shelf and Slope, *Technical Report Woods Hole Oceanographic* Institute, Massachusetts, 1987

Canals, M., J. Serra and O. Riba 1982. Toponimia de la Mar Catalano-Balear. *Boll. Soc. Hist. Nat. Balears*, 26:169-194

Carrère L., Le Provost C., Lyard F. On the statistical stability of the M2 barotropic and baroclinic tidal characteristics from along-track TOPEX/Poseidon satellite altimetry analysis *Journal of Geophysical Research*, 109, C03033, 2004

Crépon, M., L. Wald and J. M. Monget, Low-frequency waves in the Ligurian Sea during December 1977, *J. Geophys. Res.,* 87 (C1), 595-600. 1982

Daley, Roger. Atmospheric Data Analysis. *Cambridge University Press*. 1991

De Mey, P. and M. Benkiran, A multivariate reduced-order optimal interpolation method and its application to the Mediterranean basin-scale circulation, in *Ocean Forecasting: Conceptual basis and applications*, N. Pinardi and J.D. Woods, Eds. Springer Verlag, 2002.

Demirov, E. and N. Pinardi,. The Simulation of the Mediterranean Sea circulation from 1979 to 1993. Part I: The interannual variability. J. Marine Systems, 33-34, pp. 23-50., 2002

Demirov E., N. Pinardi, C. Fratianni, M. Tonani, L. Giacomelli, P. De Mey, Assimilation scheme of the Mediterranean Forecasting System: operational implementation. *Annales Geophysicae*, 21: 189-204., 2003

Dufau-Julliand,C. , P. Marsaleix, A. Petrenko and I. Dekeyser, Winter Hydrodynamical 3D Modelling in the Gulf of Lion, North Western Mediterranean: Dense Water Formation over the Continental Shelf during January 1999 (MOOGLI3 Experiment) and Late Winter, *J.Geophys. Res*.109, C1102, 2004.

Durand N.; Fiandrino A.; Fraunie P.; Ouillon S.; Forget P.; Naudin J.J. Suspended matter dispersion in the Ebro ROFI: an integrated approach *Cont. Shelf. Res*. , 22 (2), 2002

Echevin, V., P. D. Mey, G. Evensen, Horizontal and vertical structure of the prepresenter functions for sea surface measurements in a coastal circulation model. J. Phys. Oceanogr., 30, 2627-2635-, 1999

Echevin, V., L. Mortier and M. Crépon, 2003. Interaction of a coastal current with a shelf topography, application to the gulf of Lions shelf, *Journal of Physical Oceanography*, 33,1,188-206.

Evensen, G. Sequential data assimilation with a nonlinear quasigeostrophic model using Monte-Carlo methods to forecast error statistics. *J. Geophys. Res.*, 99 (C5), 10143-10162.

Evensen, G. The ensemble Kalman filter: Theoretical formulation and practical implementation. Submitted to Ocean Dynamics., 2003

Estournel C., Broche P., Marsaleix P., Devenon J.L., Auclair F. and Vehil R The Rhone river plume in unsteady conditions : numerical and experimental results. *Estuarine, Coastal and Shelf Science*. 53, 25-38. 2001

Estournel, C., X. Durrieu de Madron, P. Marsaleix, F. Auclair, C. Julliand and R. Vehil "Observation and modelization of the winter coastal oceanic circulation in the Gulf of Lions under wind conditions influenced by the continental orography (FETCH experiment)", *J. Geophys. Res*. 108(C3), 8059, doi:10.1029/2001JC00825, 2003

Espino M., A.Sanchez-Arcilla, M.A.Garcia. . Wind-Induced Circulation Off The Ebro Delta, Nw Mediterranean: A Numerical Study. *Journal Of Marine Systems* , 16 235-251., 1998

Flexas M.M., X. Durrieu de Madron, M.A. Garcia, M. Canals and P. Arnau, Flow variability in the Gulf of Lion during the MATER HFF experiment (March-May 1997), *J. Mar.Syst.,* 33-34, pp. 197-214, 2002.

Flexas M.M., G.J.F. van Heijst, G. Jordà and A. Sánchez-Arcilla, Numerical simulation of barotropic jets over a sloping bottom: Comparison to a laboratory model of the Northern Current, *J. Geophys. Res.*, 109, C12039, 2004

Flexas M.M., G.J.F. van Heijst, R.R. Trieling, The behaviour of jet currents over continental slope topography with a possible application to the Northern Current, *J. Phys. Oceanogr.* In press

Font, J., García-Ladona, E., Górriz, E.G., "The seasonality of mesoscale motion in the Northern Current of the Western Mediterranean:several years of evidence". *Oceanological Acta* 18 (2), 207-219, 1995.

Fukumori, I., J. Benveniste, C. Wunsch and D. B. Haidvogel,
Assimilation of sea surface topography into an ocean circulation model
using a steady-state smoother, *Journal of Phys. Oceano.* 23, 1831-1855., 1993

Garcia, M.A. and Ballester, A. Notas acerca de la meteorologia y la circulacion local en la region del delta del Ebro (1980-1981). *Investigacion Pesquera*, vol. 48 (3)., 1984

García-Ladona E., A. Castellón, J. Font, J. Tintoré The balearic current and volume transports in the Balearic basin *Oceanologica acta*,19, 5, 489-497, 1996

Garret , C.J.R. and W.H. Munk Space-time scales of internal waves. *Geophys. Fluid Dyn.,* 2, 226-64, 1972.

Gaspar, P., Y. Gregoris, and J. M. Levevre, " A simple eddy kinetic energy model for simulations of the oceanic vertical mixing: Tests at station Papa and long-term upper ocean study site", *J. Geophys. Res*., 95, 16,179-16,193, 1990.

Gelb Q.. Applied Optimal Estimation. *MIT Press*, Cambridge, MA, 1974.

Gill, A.E., 1982. Atmosphere-Ocean Dynamics, Academic Press, New York, 662 pp.

Gjevik,B., H. Moe and A. Ommundsen, Idealized model simulations of barotropic flow on the catalan shelf, *Cont. Shelf Res*., 22, pp 173-198, 2002.

Haney RL, 1991: On the pressure gradient force over steep topography in sigma coordinate models. *J. Phys. Oceanogr*., 21, 610-619.

Jordà G., M. Espino, P. Marsaleix, Implementation and validation of the south catalan shelf model . The Scientific Validation Period Experiment. *MFSTEP Report*. 2004

Kantha, L. H., and C. A. Clayson, Numerical Models of Oceans and Oceanic Processes, *Academic Press*, pp. 956., 2000

Kroll J., The propagation of wind-generated inertial oscillatiosn from the suface into the deep ocean. *J. Mar. Res.*, 33, 15-51, 1975

Kundu,P.K.,Allen, J.S. Some three-dimensional characteristics of low-frequency current fluctuations near the Oregon coast. *J. Phys. Oceanogr.* 6 (2), 181–199, 1976

Large W.G. and S. Pond, Open Ocean Momentum Flux Measurements in Moderate to Strong Winds *Journal of Physical Oceanography* Vol. 11, No. 3, pp. 324-336.

LeBlond P.H., Mysak, L.A., Waves in the Ocean. *Elsevier*, Amsterdam, 1978

Luyten P.J., J. H. Simpson and T. P. Rippeth. Comparison of turbulence models for homogeneous and stratified flows with turbulence measurements in the Irish Sea,. *Paper presented at the MAST Workshop on Turbulence Modelling*, Bergen, Norway. August 1996

Maas, L.R.M., Wave focusing and ensuing mean flow due to symmetry breaking in rotating fluids. *J.Fluid Mech.*, 437, 13-28, 2001

Maidana, M.A.; Naudin, J.-J.; Espino, M.; García, M.A.; Sánchez-Arcilla, A Feasibility and usefulness of steady-state calculations of the mean circulation in the vicinity of the Ebro mouth. Model tests against field data. *Cont. Shelf. Res.* , 22 (2), 2002

Marchesiello, P., J.C. McWilliams, and A. Shchepetkin, Open boundary conditions for long-term integration of regional ocean models. *Ocean Modelling* 3, 1-20, 2001

Marsaleix, P., C. Estournel, V. Kondrachoff and R. Vehil, A numerical study of the formation of the Rhone river plume, *J. Mar. Syst.,*14, pp 99-115, 1998.

Millot, C., . "Circulation in the Western Mediterranean Sea". *J. Mar. Syst.* 20, 423-442, 1999.

Mellor, GL, and T. Yamada, Development of a Turbulence Closure Model for Geophysical Fluid Problems. *Rev. Geophys. Space Phys*., 20: 851-875 , 1982

Mestres, M., J.P. Sierra, A. Sánchez-Arcilla, J. González del Río, T. Wolf, A. Rodríguez and S. Ouillon Modelling of the Ebro River plume. Validation with field observations *Scientia Marina*. 67 (4): 2003

Mooers, C. N. K. Several effects of a baroclinic current on the cross-stream propagation of inertial-internal waves. *GeophysicalFluid Dynamics*, *6*, 245–275., 1975

Morrow, R.A., and P. De Mey: An adjoint assimilation of altimetric, surface drifter and hydrographic data in a QG model of the Azores current. *J. Geophys. Res.*, 100(C12), 25007-25025., 1995

Mourre B., P. De Mey,. F. Lyard, C. Le Provost, Assimilation of sea level data over continental shelves: an ensemble method for the exploration of model errors due to uncertainties in bathymetry. *Dyn. Atmos. Oceans.* 38, 93-121, 2004.

Noble, M.A., Ramp, S.R.,. Subtidal currents over the central California slope: evidence for offshore veering of the undercurrent and for direct, wind-driven slope currents. *Deep-Sea Res.* II 47, 871–906, 2000.

Palanques, A., Garcia-Ladona, E., Gomis, D., Martín, J., Marcos, M., Pascual, A., Puig, P., Gili, J.M., Emelianov, M. , Monserrat, S. , Guillén, J., Tintoré, J. ,Segura, M. ,Jordi, A. , Ruiz, S., Basterretxea, G., Font, , J., Blasco, D., Pagès, F. General patterns of circulation, sediment fluxes and ecology of the Palamós submarine canyon, north western Mediterranean*, Progress in Oceanography*, (in press) 2004

Palma, E. D., and R. P. Matano, 1998: On the implementation of open boundary conditions to a general circulation model: The barotropic mode. *J. Geophys. Res*. 103, 1319-1341.

Pascual, A., Buongiorno Nardelli, B., Larnicol, G., Emelianov, M. & Gomis, D.. A case of an intense anticyclonic eddy in the Balearic Sea (western Mediterranean). *J. Geophys. Res.*, 107 (C11).2002

Pedlosky, J., *Geophysical Fluid Dynamics*, second edition, Springer-Verlag, 710 pp., 1987.

Pham, D., J. Verron, M. Roubaud, A singular Evolutive Extended Kalman filter for data assimilation in oceanography *J. Mar. Sys*, 16 (3-4), 323-340, 1998.

Pinot J.M., Tintoré J., Gomis D. Multivariate analysis of the surface circulation in the Balearic Sea. *Progress in Oceanogr*., 36, 343-376 1995

Pinot J.M, J.L. López-Jurado and M.Riera, The CANALES experiment (1996-1998). Interannual, seasonal and mesoscle variability of the circulation in the Balearic Channels, *Prog. Oceanog.* , 55, 335-370, 2002.

Puig P., A. Palanques, J.Guillén, E. García-Ladona, Deep slope currents and suspended particle fluxes in and around the Foix submarine canyon (NW Mediterranean) *Deep-Sea Res.* I 47 343-366, 2000

Rippeth, T. P., J. H. Simpson, R. J. Player and M. Garcia, Current oscillations in the diurnal-inertial band on the Catalonian Shelf in Spring, *Cont. Shelf. Res.*, 22, pp 247-265, 2002

Rubio A., P. A. Arnau, M. Espino, M.M.Flexas, G. Jordà , J. Salat, J. Puigdefàbregas, and A. S.-Arcilla A field study of the behaviour of an anticyclonic eddy on the Catalan continental shelf (NW Mediterranean) *Prog. Oceanogr.* in press, 2005

Sadiki , A posteriori verification of analysis and assimilation algorithms and study of the statistical properties of the adjoint solutions *PhD. Thesis, Université Paul Sabatier*, Toulouse, 2005

Salat, J. and A. Cruzado, 1981. Masses d'eau dans la mer Catalane. *Rapp.Proc.Verb.CIESM*, 80:5-6

Salat, J., J. Tintoré, J. Font, D.P. Wang, M. Vieira, Near-inertial motion on the shelf-slope front off northeast Spain, *Journal of Geophysical Research* 97, C5, 7277-7281, 1992

Salat, J., M.A.Garcia, A. Cruzado, A. Palanques, L.Arin, D.Gomis, J.Guillen, A.de Leon, J.Puigdefàbregas, J. Sospedra and Z.R. Velasquez, Seasonal changes of water masses structure and shelf slope exchanges at the Ebro Shelf (NW Mediterranean), *Cont.Shelf Res.*, 22, pp 327-348, 2002.

Sammari, S., C. Millot and L.Prieur, Aspects of the seasonal and mesoscale variability of the Northern Current in the western Mediterranean Sea inferred from PROLIG-2 and PROS-6 experiments, *Deep Sea Res. I,* 42(6), pp 893-917, 1995.

Sanchez-Arcilla, A. and Simpson, J.H. The narrow shelf concept: couplings and fluxes. *Continental Shelf Research*, 22, 153-172., 2002

Schepetkin, A.F. and J.C. McWilliams, The Regional Ocean Modeling system (ROMS): A split-explicit, free-surface, topography-following coordinates ocean model, *Ocean Modelling,* 9, 347-404, 2005

Talagrand. A posteriori verification of analysis and assimilation algorithms.*In Proceedings of the ECMWF Workshop on Diagnosis of Data Assimilation Systems*, 2-4 November pages 17--28, Reading., 1999.

Taylor, K. E., Summarizing multiple aspects of model performance in a single diagram.*J. Geophys. Res.*, 106, 28033-28059, 2001

Testut,C.E., Assimilation de données satellitales avec un filtre de Kalman de rang réduit dans un modèle aux Equations Primitives de l'ocean Atlantique., *PhD. Thesis, Université Joseph Fourier*, Grenoble. 2000

Toumazou V. and JF Cretaux , "Usign a Lanczos Eigensolver in the Computation of Empirical Orthogonal functions, *Month. Weather. Review* Vol.129. No.5. 1243-1250, 2001.

Vitorino J., A. Oliveira , J.M. Jouanneau , T. Drago, Winter dynamics on the northern Portuguese shelf. Part 1: physical processes, *Prog. in Oceanogr* 52 129–153, 2002.

Van Haren, H. Millot, C. Rectilinear and circular inertial motions in the Western Mediterranean Sea. *Oceanol. Acta* (in press), 2003

Wu, J. Wind-stress coefficients over sea surface near neutral conditions - A revisit. *J. Phys. Oceanogr*. 10 727-740, 1980

Xing, J. and A.M. Davies, Influence of topographic features and along shelf flow upon the Ebro plume, *Cont. Shelf. Res.,*22, pp 199-*227*, 2002

Zavatarelli M., Pinardi N., Kourafalou V. H., Maggiore A. Diagnostic and prognostic model studies of the Adriatic Sea general circulation. Seasonal variability. *Journal of Geophysical Research*, 107(C1), 4-1 - 4-20., 2002